ScuDo
Scuola di Dottorato ~ Doctoral School
WHAT YOU ARE, TAKES YOU FAR

Doctoral Dissertation
Doctoral Program in Environmental Engineering (29th Cycle)

Hydro-Mechanical Behaviour of Tailings in Unsaturated Conditions

By

Gianluca Bella

******

Supervisors:
Prof. M. Barbero, Supervisor
Prof. F. Barpi, Co-Supervisor
Prof. G. Musso, Co-Supervisor

Doctoral Examination Committee:
Prof. Corrado Fidelibus, Politecnico di Bari, Italy
Prof. Daniele Costanzo, Politecnico di Torino, Italy
Prof. Gabriele Della Vecchia, Politecnico di Milano, Italy
Prof. Maria Claudia Barbosa, Universidade Federal do Rio de Janeiro, Brazil
Prof. Rafaela Cardoso, IST - Técnico Lisboa, Portugal

Politecnico di Torino
2017

Declaration

I hereby declare that, the contents and organization of this dissertation constitute my own original work and does not compromise in any way the rights of third parties, including those relating to the security of personal data.

Gianluca Bella

Torino. June 28th, 2017

* This dissertation is presented in partial fulfillment of the requirements for **Ph.D. degree** in the Graduate School of Politecnico di Torino (ScuDo).

I would like to dedicate this thesis to my nephews Leonardo and Beatrice

Non è importante aggiungere anni alla vita, ma vita agli anni.

Rita Levi Montalcini (1909-2012)

Contents

Acknowledgments

I am grateful to my Italian Tutor Prof. Monica Barbero, Co-Tutors Prof. Fabrizio Barpi, Prof. Guido Musso, and to Brazilian Professors Terezinha Esposito and Fernando Soares Lameiras for their valuable supervision and suggestions throughout all the research period. Their recognized experience in different scientific fields, their recommendations for the experimentations and their discussions of the tests results were always invaluable and helpful for me. They improved my research skills and my in-depth understanding of unsaturated soil mechanics. Thanks to Prof. Renato Lancellotta for introducing me into geotechnical study some years ago.

Many experiments in this research work, carried out at Politecnico di Torino (Italy), have been possible with the technical support of Mr. Giovanni Bianchi and Dr. Oronzo Pallara. My special appreciation goes to a very big friend and colleague, Dr. Arash Azizi for teaching me all the experimental techniques from the practical point of view. His patience, friendly guidance and our discussions of the tests results were fundamental for me. My appreciation is also for the current staff of DISEG and Geotechnical laboratory of Politecnico di Torino, especially Francesco Macario, Edoardo Nocera and Sara Sacco for helping me with some laboratory activities.

All the characterization tests carried out at Centro De Desenvolvimento de Tecnologia Nuclear (Brazil), have been possible only with the scientific and technical support of Prof. Ana Maria Matildes dos Santos, Prof. Monica M.A.M. Schvartzman, Prof. João Batista Santos Barbosa, Prof. Lúcio Carlos Martins Pinto, Sérgio Carneiro dos Reis, Prof. Tércio Assunção Pedrosa and Prof. Vanessa de Freitas Cunha Lins.

I would like to acknowledge lots of friends I have made in this research period. I am grateful to Giovanni Anglani, Prof. Alice di Donna, Alessandra Insana, Dr. Francesco Antolini, Matteo Baralis and Dr. Fabio Bazzucchi. You are the best friends and colleagues I could never wonder. With your friendship, you make my days much more happy. I am very grateful to Angela Carboni, Elisa Procopio, Dr. Miriam Pirra, Riccardo Ceccato and Andrea Barbato for your sympathy during our funny lunches. I also would to acknowledge the friends I made during my research activity in Brazil, especially Cristina Isabel Salerno, Mr. Henrique and Bernardo Lameiras, Bruna Drummond, Giovanna Larissa and Isabela Campos.

Thanks to Prof. Alberto Sapora and Dr. Giacomo Boffa for their friendships.

Last but not least, I am most grateful for the love and understanding from my mother Gianna, my father Franco, my grandmother Marianna, my sister Eleonora, her husband Giuliano and their babies Leonardo and Beatrice. All of you supported me in this period. I love you.

Abstract

Many geotechnical problems are related with soils and structures in unsaturated conditions. Among them, a significant role is played by tailing dams that represent complex geotechnical systems. Because of their wide extension, tailing storage facilities are subjected to many external actions and interactions with the atmosphere, whose effects governing the position of phreatic surface. Hence, the low permeability deposited tailings are subjected to drying-wetting processes, leading variation in the extensions of the unsaturated zone above the phreatic surface with a significant role in stability of the embankment.

The current research is aimed to study the hydro-mechanical behaviour and the water retention response of unsaturated silt and silt-sand tailings mixtures, respectively, in order to extend a previous characterization of the same soil performed in saturated conditions. This research is also aimed at investigating the occurrence of the critical state in unsaturated conditions, showing the range of state variables leading the static liquefaction. Finally, irradiation by means of gamma rays is proposed as an accelerated technique in order to simulate the natural ionizing radiations acting on stored tailings that, in many countries, are beginning to be re-used as backfill, landscaping material or feedstock for cement and concrete. Wet and dry silty samples were exposed to gamma rays and then characterized in order to study any possible physical and chemical modifications of the exposed matter.

The starting point of this research is an available hydro-mechanical characterization of saturated tailings coming from Stava tailing dams collapsed in 1985 (Italy). The first series of experimental tests was carried out to study the hydraulic behaviour of the Stava tailings by means of water retention tests. To account for the heterogeneity of the tailing material within the basin, the dependency of the water retention relationship on grain size distribution and void ratio was investigated. In order to extend the limited range of matrix suction allowed by the axis translation technique, the water retention curves were also implemented with data obtained by indirect soil suction measurement and soil suction controlling methods, dew point technique and vapour equilibrium technique, respectively.

Since the pre-shearing state of the soil has a relevant effect on the behaviour shown during shearing before reaching the critical state conditions, a second campaign of experimental tests, consisting in five mono-dimensional compression tests, was performed. Results were compared with those in saturated conditions obtained by Carrera (2008) in order to investigate the dependency of preconsolidation stress and stiffness of the soil on suction. Aimed to extend the hydraulic characterization and to approach the possible critical

state in unsaturated conditions from drying and wetting sides, a third campaign of experimental tests was carried out by using a suction controlled triaxial cell and imposing different hydro-mechanical stress paths. Statically compacted silty samples were subjected at different suction levels, then isotropically consolidated at different net stresses, and finally sheared at constant water content or constant suction level by means of the axis translation technique or the vapour equilibrium technique.

Finally, due to the importance of the static liquefaction phenomena in stability problems of tailing dams, a fourth series of experimental tests was performed by means of a triaxial cell. Silt specimens were tested in unsaturated or close to saturated conditions, in order to investigate some of the main factors (degree of saturation, initial density and preparation technique) that are supposed to influence the liquefaction response.

List of figures

List of symbols and abbreviations

A, A_0	Area, initial area
AEV	Air entry value
A_γ	Activity of gamma ray
B	Skempton parameter
B_w	Skempton parameter at the end of saturation phase
CSL	Critical State Line
CSR	Cyclic strength stress ratio
d, d_0	Diameter, initial diameter
Dr	Relative density
$e, \Delta e, e_0$	Void ratio, variation of void ratio, initial void ratio
e_w	Water ratio
e_{min}, e_{max}	Minimum and maximum void ratio
e_{wm}	Microstructural water ratio
e_c	Void ratio at the end of consolidation phase
E_γ	Photon energy of gamma ray
fc	Fine content
F	Axial force
$g(s)$	Intercept of the Hvorslev surface
Gs	Specific gravity
h, h_0	Height, initial height
h_c	Capillarity height
$h(s)$	Slope of the Hvorslev surface
ICL	Isotropic Compression Line
I_γ	Intensity of gamma ray
K_w, K_a	Bulk modulus of water, bulk modulus of air
K_{fV}, K_{fR}	Voigt bound of the fluid modulus, Reuss bound of the fluid modulus
K	Bulk modulus of the solid skeleton
LRR	Liquefaction resistance ratio
M	Stress ratio at critical state
M, M_s, M_w	Total mass, dry mass, mass of water
NCL	Normal Compression Line

p'	Mean effective stress
p'_B	Mean Bishop stress
p'_c	Mean effective stress at the end of consolidation phase
p'_e	Equivalent pressure
p_{net}	Net stress
PI	Plasticity index
PSD	Pore size distribution
P_γ	Emitted power of gamma ray
q	Deviator stress
q_{res}, q_{max}	Residual and maximum deviator stress
r, r_0	Radius, initial radius
r_1, r_2	Principal radii of curvature
R	Universal gas constant
RH	Relative humidity
s, s_i	Matric suction, initial matric suction
S_a	Degree of saturation of air
Sr	Degree of saturation
Sr_{eff}	Effective degree of saturation
Sr_M	Degree of saturation of the macropores
Sr^{res}	Residual degree of saturation
Sr_w, Sr_C	Degree of saturation at the end of saturation phase and at the end of consolidation phase
S_{us}	Residual strength
$SLRR$	Static liquefaction resistance ratio
$t, t_\gamma, t^{uv}{}_{sun}$	Time, Gamma and UV-sun exposition time
$t^{uv}{}_{sun,est}$	Real sun exposition time
T_s	Surface tension
T	Absolute temperature
u_a	Air pressure
u_w	Pore water pressure
v	Specific volume
v_γ	Frequency of gamma ray
$V_{w,flu}$	Water volume exchanged due to flushing
$V_{w,vol}$	Water volume exchanged with volume-meter
V_v, V_{v0}	Volume of voids, initial volume of voids
$V_w, V_{w0}, \Delta V_w$	Volume of water, initial water volume, water volume change
V, V_0	Total volume, initial volume
w, w_0	Water content, initial water content
w_L, w_P	Liquid and plastic limit
WRC	Water retention curve
α, n, m	Van Genuchten parameters
Φ, ψ, n, m	Gallipoli parameters
$\Delta h, \Delta r$	Axial and radial displacement
$\Delta p'$	Change in mean effective stress

$\Delta\varepsilon_v$	Change in volumetric strain
Δu	Change in pore pressure
$\Delta\sigma_3$	Change in cell pressure
ε_a, ε_r, ε_v	Axial, radial and volumetric strain
ε^*_v	Potential volumetric strain
φ	Friction angle
γ_w, γ_d	Unit weight of water, dry weight
Φ_{cv}	Friction angle at critical state
η	Stress ratio
λ	Compressibility index
θ	Volumetric water content
$\rho_{\gamma,}$	Energy intensity of gamma ray
$\rho^{uv}{}_{sun,}$ $I^{uv}{}_{sun,}$	Energy intensity and intensity of UV radiations
σ_a, σ_r	Total axial and radial stress
σ'_a, σ'_r	Effective axial and radial stress
ξ	Bonding factor

List of tables

1 Introduction and organization

A large number of engineering problems is related to the behaviour of soils in unsaturated conditions. A state where soil pores are filled with two or more fluids, generally water and air, is known as unsaturated. Unsaturated conditions can be found in natural environments or in artificial structures subjected to variations in the level of phreatic surface. These conditions are very common in soil slopes or in many civil engineering structures, i.e. tailings dams, earth water retention embankments or cutting, while many other structures like tunnels, highways, retaining walls, road subgrades and shallow foundations are built on unsaturated soil layers. Due to the fact that these structures are placed above the groundwater table, their behaviour involves soil layers having negative pore-water pressures, which are usually unsaturated. The consequences of negative pore-water pressure distribution are often neglected in engineering practice because (Tarantino and Mountassir, 2013):

- the ground water table is assumed conservatively to be at the ground surface. This latter assumption could result in over-design of engineering structures, while some cost savings are possible if a proper analysis of the unsaturated behaviour (and hydraulic boundary conditions, such as rainfall) are performed;
- in the analyses, i.e. back-analysis of failures, the soil above the water table is considered dry and the pore-pressure is set to zero.

For these reasons, even if it has been recognized that classical (saturated) soil approach is not the best way to analyse a large number of engineering problems and unsaturated soils are present widely throughout the world, unsaturated soil mechanics is still considered a relatively new field and it is rarely applied (Bishop and Blight, 1963; Fredlund and Rahardjo, 1993; Cui and Delage, 1993; Tekinsoy *et al.*, 2004). The main reasons are:

- laboratory tests in unsaturated conditions are time-consuming and sophisticated testing procedures are required;
- a complete understanding of the water retention response and the coupled hydro-mechanical behaviour of soils in unsaturated conditions is relatively difficult to obtain if compared to those under saturated conditions;
- constitutive and numerical modelling in unsaturated conditions are complex, due to the interaction between many physical phenomena such as hydraulic, mechanical, chemical and thermal behaviour, leading the necessity of a large number of parameters.

It is worth to note that in the last decades, significant improvements in the understanding of the behaviour of soils in unsaturated conditions has been achieved in terms of developments of experimental techniques and constitutive modelling, even if, more work should be done.
Among the artificial structures where unsaturated conditions can be found, tailing dams play a central role. Tailing dams are geotechnical systems constituted of an earth fill embankment containing the waste products of mining processes, known as "tailing". Tailings are mixtures of crushed rock materials and fluids resulting from chemical and mechanical mining extraction processes of valuable ores and other minerals such as coal, aluminium, copper, sands, uranium, base metals, gold and silver. The ore-crushing processes of the mining industry produce huge quantities of uneconomic residual metals and chemical process water that, mixed together, have the consistence of slurries. These slurries need to be handled and stored in basins known as "tailing dams" or "tailing storage facilities" which represent some of the more complex geotechnical structures. Due to the extraction processes, the predominant fraction of tailing usually consists in fine material, so its permeability is low and unsaturated phenomena can play a fundamental role in its behaviour. Furthermore, tailing basins have a large surface exposed to many interactions with the atmosphere, causing temporary decreasing or raising of the water head and so variations in the extension of the unsaturated zone within the basin. The position of the phreatic surface within tailing storage facilities has a fundamental role in their stability, so uncontrolled variations of the phreatic level may lead overtopping or severe problems in terms of static liquefaction with, in some cases, breach of the embankment. For these reasons, during design phase it is fundamental to understand the hydro-mechanical unsaturated soil response and if tailings may be prone to liquefy. Indeed, the high rate of collapses of tailing dams demonstrates that static liquefaction phenomena is one of the major cause of collapse.

This research is therefore aimed to extend the knowledge of the hydro-mechanical response in unsaturated conditions of tailing collected after the failure of Stava Basins (Italy) occurred in 1985. The starting point is an available hydro-mechanical laboratory characterization in saturated conditions of the same material, so the present work represents an extension of this characterization to the unsaturated state. The hydro-mechanical unsaturated response of Stava tailing is investigated by means of triaxial tests performed by using a suction controlled triaxial cell at different confinement pressures and suction levels. On the other hand, the hydraulic behavior is studied by means of suction controlled oedometer cell. In order to extend the limited range of matric suction permitted by axis translation technique, the water retention curves obtained by oedometer tests are implemented with data resulting by indirect soil suction measurement and soil suction controlling methods, respectively dew-point technique and vapour equilibrium technique. To account for the heterogeneity of the in-situ tailing material mainly due to the deposition technique, the dependency of the water retention relationship on grain size distribution and on initial density was investigated. The experimental data are aimed both at providing a wider hydro-mechanical characterization and investigate the possible occurrence of the critical state in unsaturated conditions.
Due to the importance and complexity of the static liquefaction phenomena in stability problems of tailing dams, the current study is also aimed at investigate some of the main factors that are supposed to influence the liquefaction response of tailings. A campaign of laboratory tests is performed on Stava silty tailings in unsaturated conditions or close to saturated conditions, by means of conventional triaxial tests. The static liquefaction resistance of the tested material is evaluated in terms of stress-strain behaviour and the B-checks allow to compute the corresponding degree of saturation at each step of the test. A comparison between experimental and theoretical Skempton parameter-degree of saturation relationship is also done for Stava silty tailing, as previously performed in the literature just for sandy soils.

The current research finally shows an innovative technique consisting in irradiation by means of gamma-rays in order to simulate the exposure for long time of tailing at ionizing radiations. This process represents one of the natural phenomena acting on tailings stored within basins or used for industrial purposes. Therefore, in many countries tailing are beginning to be re-used as backfill, landscaping material or feedstock for cement, bricks and concrete. So, if any, long-term physical and chemical modifications could affect the hydraulic and mechanical behaviour of tailing with relevant economic consequences. For these reasons, wet and dry silty samples of Stava tailing are exposed to gamma rays and characterized before and after the treatment. Despite a certain chemical stability, some physical changes were observed, particularly in terms of size particle distribution, inner porosity of the particles and specific surface.

The thesis is organized as follows:

Chapter 2 introduces the motivations of the current research and the main concepts of tailing and tailing dams. A review of tailing's peculiarity is presented together with their deposition techniques inside the storage basins. The main raising techniques adopted for tailing dams are given with some basic design aspects. Failures are then analysed and the case study concerning the collapse of Stava basins is presented.

In Chapter 3 basic concepts regarding the hydro-mechanical behaviour of soils in unsaturated conditions are shown, so the experimental techniques adopted in the current work are presented.

Chapter 4 introduces the basic geotechnical characterization of Stava tailing in saturated conditions. The irradiation treatment of tailing by means of gamma-rays is presented and experimental results of the physical/chemical characterization of Stava silty tailing before and after the gamma-rays treatment are exposed.

Chapter 5 is aimed to describe the experimental results concerning the hydraulical response of Stava tailing in unsaturated conditions. The main features of suction controlled oedometer are presented together with the sample preparation technique. The hydraulical response is presented and interpreted in terms of water retention curves for samples prepared with different initial density and different grain size distribution.

The first section of Chapter 6 is devoted to describe the experimental results obtained from some 1D compression tests in unsaturated conditions, investigating the dependency of preconsolidation stress and stiffness of the soil on suction. The second section of Chapter 6 is aimed to describe the hydro-mechanical response of Stava tailings in unsaturated conditions. Main features of suction controlled triaxial cell are presented together with the sample preparation technique. A review of results obtained on the same material in saturated conditions and the state of the art concerning the critical state in unsaturated conditions are also given in order to be used as a reference for interpreting the following experimental results of the present research.

Chapter 7 describes the static liquefaction response of Stava silty tailing in unsaturated conditions. Some concepts and main factors influencing the static liquefaction resistance from the experimental point of view are given, together with a review of results obtained on the same material in saturated conditions. Main features of the triaxial cell used in the current investigation are presented together with the adopted sample preparation techniques. Finally, the experimental results in terms of dependency of static liquefaction by preparation technique, initial degree of saturation and void ratio are shown together with a comparison of

the experimental and theorical relationships between B-Skempton parameter and degree of saturation.

The conclusions of the overall experimental results in unsaturated conditions, obtained my means both of water retention tests, mono-dimensional compression tests, suction controlled triaxial tests and conventional triaxial tests are presented. Considerations and possible developments are also given about the physical/chemical characterization before and after the gamma-rays treatment. Finally, some suggestions for future works are presented.

Appendix gives details concerning the gamma ray treatment, basic concepts regarding the principles governing physical/chemical characterization test, together with the sample preparation techniques adopted for each test.

REFERENCES

1. Bishop A.W. and Blight G.E. 1963. Some aspects of effective stress in saturated and partly saturated soils. Geotechnique 13 (3), pp. 177–197.

2. Cui, Y.J. and Delage P. 1993. On the elasto-plastic behaviour of an unsaturated silts. ASCE Geotechnical Special Publication 39, pp. 115–126.

3. Fredlund D.G. and Rahardjo H. 1993. Soil Mechanics for Unsaturated Soils. Wiley, New York.

4. Tarantino A. and El Mountassir G. 2013. Making unsaturated soil mechanics accessible for engineers: Preliminary hydraulic–mechanical characterisation & stability assessment. Engineering Geology 165, pp. 89–104

5. Tekinsoy M.A., Kayadelen C., Keskin S. and Söylemez M. 2004. An equation for predicting shear strength envelope with respect to matric suction. Computers and Geotechnics 31 (7), pp. 589–593.

2 Tailing and tailing dams

The first section of this chapter is aimed at provide the main motivations that lead the current research. The importance of considering tailings in unsaturated state is given, together with the relevance of a deep hydro-mechanical characterization of tailings. The importance of investigating the hydro-mechanical behavior by considering the in-situ heterogeneity of tailings is also given. Then, the relevance of investigating the static liquefaction phenomenon for tailing dams' stability is shown. After that, this chapter introduces some of the main geotechnical peculiarities of tailing wastes, together with the construction methods of tailing dams. A review of the causes of tailing dams' failure is given together with some basic design concepts aimed at minimizing risks associated to the occurrence of static liquefaction. The origin of the tested material, history and main features of Stava tailing basins are finally presented, together with some possible explanations of their collapse.

2.1 MOTIVATIONS OF THE CURRENT RESEARCH

2.1.1 Why unsaturated conditions for tailing dams?

Tailing basins are subjected to many external and internal actions affecting their operation, i.e. surface runoff, infiltration, evaporation, consolidation, or capillarity rise, as shown in Fig. 2.1 (Zanardin *et al.*, 2009). When tailings, in form of slurries, are discharged into the basin, water can follow two paths, depending by many factors (i.e. permeability of tailings, degree of saturation and current level of the phreatic surface):

- tailings, after their deposition, start to consolidate, so a fraction of the water infiltrates into the previously deposited tailing wastes;
- the rest of water runoffs toward to the decant pond.

In the first case, water is expelled from the porous material and, due to the ongoing consolidation process, the porosity is reduced. The reduction of porosity leads a decrease of the hydraulic conductivity, which is related to a possible increase of the capillarity rise, leading to variations in the extension of the unsaturated zone above the water table from few centimetres to some meters, depending the type of tailings and weather conditions. Consequently, a wide area of the structure is in unsaturated conditions, and unsaturated phenomena might have a great relevance in the on whole behaviour of such complex structures.

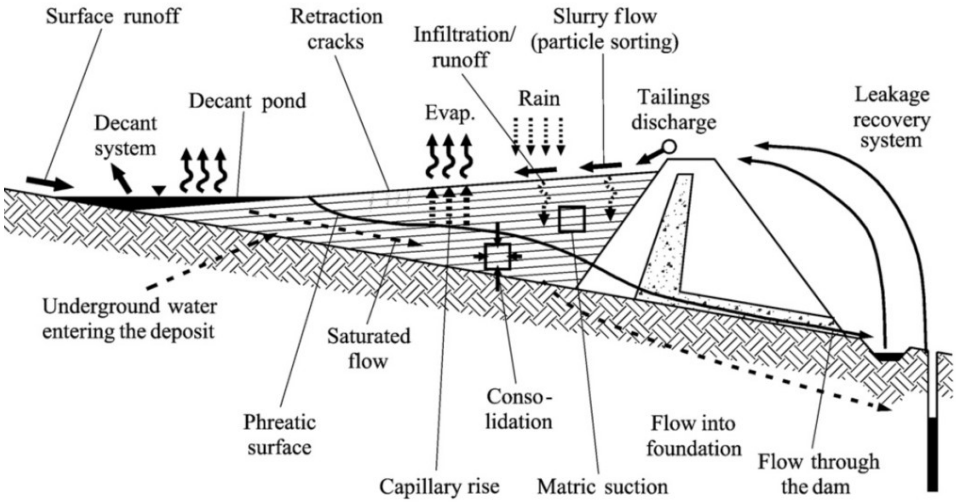

Fig. 2.1 - Interaction of tailing storage facility with atmosphere and location of the phreatic surface (Zanardin *et al*., 2009).

Within the unsaturated zone, capillarity force at the particle contacts can lead to an increase of the shear strength and a decrease of the soil compressibility, but these improvements in mechanical strength could be rapidly lost if the material become saturated, for instance due to a fast increase of the phreatic level. The surface of tailing dams is indeed periodically subjected to drying and wetting phenomena, leading to variations of the phreatic table and so, to changes in the extension of the unsaturated zone above the phreatic level:

- during the dry seasons, evaporation phenomena occur. The rate of drying processes is governed by wind speed, relative humidity of the air, sun radiations, permeability or density of tailings and presence of retraction cracks (Fig. 2.1);
- on the other hand, during rainstorms, water and surface runoff can reach the basin, partially going towards the pond, partially infiltrating into the tailing mass. The rise of phreatic level during a rainfalls can be a fast process while, after its cessation, its draw-down is usually slow. This behaviour can be explained by the presence of capillarity water above the phreatic surface reducing the storage capacity of the tailings pores, and because of the mentioned low hydraulic conductivity of the tailings mass (Zanardin *et al*., 2009).

As shown in Fig. 2.2, different pore water profiles might be assumed for different weather conditions. In all cases, the soil below the phreatic level is saturated (S_P). Above the phreatic surface there is a capillary fringe (*CF*) having a thickness related to the pore size distribution of the soil. The capillary fringe is a saturated zone with negative values of pore water pressure, as given in Fig. 2.2b. Immediately above the saturated capillary fringe there is an unsaturated region (*UN*) having a pore air at atmospheric pressure, negative pore water pressure and a degree of saturation less than 100%. Considering the hydrostatic pore water distribution of Fig. 2.2b as the starting point, during dry weather conditions (Fig. 2.2a), the level of phreatic surface will decrease, moisture from the surface layer of tailings will be lost due to evaporation phenomena and the depth of the unsaturated zone will increase, while the pore water pressure will become more negative. During wet weather conditions (rainstorm or snow melt), the phreatic level will increase, the pore water pressure in the surface tailings layer will increase and the water pressure at the tailing surface can be equal, or higher than

the atmosphere pressure (Fig. 2-2c). The thickness of the unsaturated zone will decrease and this may result in a shallow layer of saturated soil (S_N) having positive or negative pore water pressure above the unsaturated zone. In case of extreme wet conditions, the phreatic surface can rise until reaching the ground surface, leading the disappear of the capillary fringe and unsaturated zone.

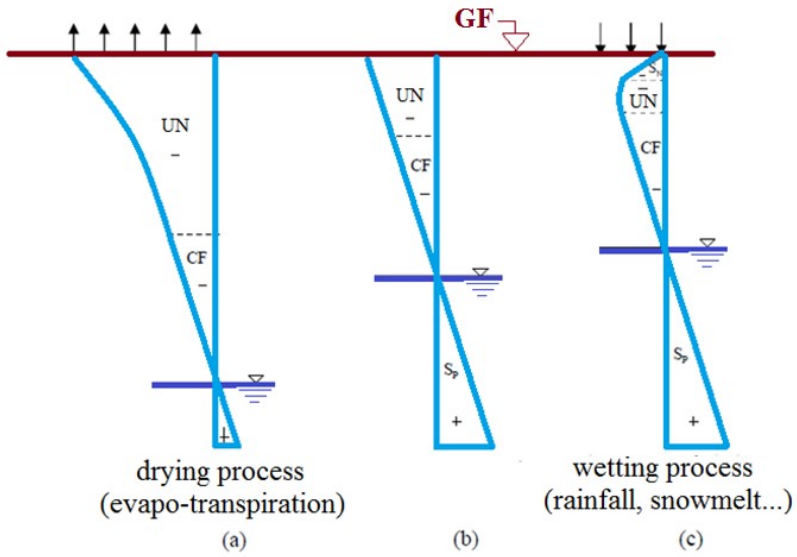

Fig. 2.2 - Pore water pressure profiles in tailing storage facilities.

2.1.2 Why an hydro-mechanical characterization?

Due to the hydro-mechanical coupling in unsaturated soils, the hydraulical response of tailing affects stability problems of tailing dams in terms of resistance properties (i.e. shear strength). Shear strength changes with suction, so an accuracy in predicting the hydraulical behaviour has significant effects on mechanical response with relevant consequences in terms of stability analysis of tailing dams. Indeed, the contribute of matric suction to shear strength of soils, and so taking into account unsaturated conditions, usually results in a increase of bearing capacity and safety factor associated with slope stability calculation (Sheng *et al.*, 2011). In 1997, Rassam and Williams demonstrated that stability of tailing embankment was improved by 30% if suction contribution to shear strength was considered in the stability calculation of the embankment.
In order to investigate the hydro-mechanical behaviour of Stava tailing in unsaturated conditions, both suction-controlled triaxial tests and water retention tests are performed on Stava tailings. This experimental investigation is aimed at extending a previous characterization carried out in saturated conditions of the same material (Carrera, 2008), and also at investigating the occurrence of the critical state in unsaturated conditions.

2.1.3 Why considering tailing as heterogeneous materials?

Because of their relevant spatial extension, long operation-life, raising methods and deposition techniques, tailing storage facilities are made of heterogeneous materials, both in terms of grain size distribution and density. Figure 2.3a gives an example of representative cross sections of an upstream tailing dam. This figure gives an example of the the grain size distribution, and so the variation of the soil properties, of some representative cross sections at different distance from the embankment. Moreover, the heterogeneity of tailing materials inside the basin, and so the deposited profiles, also depend on the grain size of tailing particles and on their mineralogy, as observed in some brazilian iron tailing dams (Esposito *et al*., 2010).

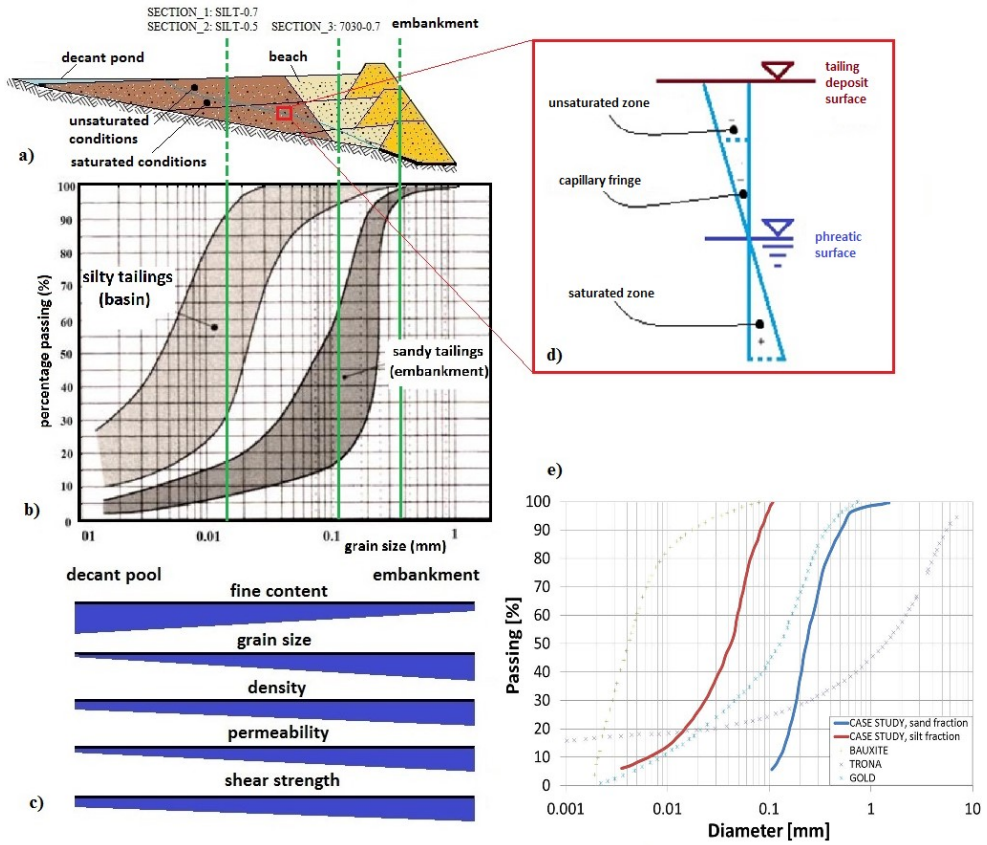

Fig. 2.3 - (a) Example of representative cross sections (1, 2 and 3) at different distances from the embankment. (b) Grain size distribution at different cross sections (modified from ISMES, 1985). (c) Soil properties with respect to deposition location. (d) Pore water pressure profile in tailing basins and (e) typical grain size distributions of tailing wastes (modified from Sarsby, 2013).

The heterogeneity of tailing within the basin is basically related to the deposition technique, usually consisting in hydraulic fills obtained by means of hydro-cyclones. After the construction of a starter dike made of compacted earth or rock, the rest of the embankment is usually raised by using the same tailing materials obtained as results of the extraction processes. According to the classical hydraulic segregation profile, an higher permeability zone made of coarse particles would exist near the embankment/discharge point, a lower

permeability zone (pond) made of fine particles further from this point, and between them there is an intermediate permeability zone (beach) as shown in Fig. 2.3a. It is worth noting the absence of a clear separation between these three zones, so the importance of analysing vertical sections at different distance from the embankment. Additional variability is related to the hydraulic deposition parameters such as spacing between discharge points, concentration of the slurry, discharge height of slurry and flow rate.
Finally, due to the great spatial variations of tailings properties, the knowledge of variability of each geotechnical parameter in field could represent the starting point for the application of a probabilistic method aimed to monitor and design tailing impoundments during their construction stages. According to Esposito (2000) and Esposito *et al*. (2010), a probabilistic method coupled to the classical observational method is able to incorporate the great variability of geotechnical tailing properties in order to make reliable prediction on the behaviour of tailing dams.
In order to consider the in situ heterogeneity of Stava tailings (Fig. 2.3a), in the current research the dependency of the hydraulical behaviour on initial density and grain size distribution is studied by performing water retention tests on tailing samples at different initial void ratio and at different percentages of sand and silt, that can be related to different locations inside the basin.

2.1.4 Why investigating the occurrence of static liquefaction in tailing dams?

As proved by the high rate of collapses due to meteorological events, tailing dams are very susceptible to static liquefaction phenomenon and this because they are usually made of sand or silt soils having low relative density (30-50%) and high degree of saturation (Vick, 1990). If a tailing dam collapses because of static liquefaction, a huge volume of stored tailings will flow as a viscous liquid, travelling large distances with severe consequences such as loss of human lifes, economical damages and environmental pollution.

One of the most relevant example of tailing impoundment failure due to static liquefaction is the collapse of the Merriespruit gold tailing dam. The Harmony Gold Mine was a tailing dam placed 320m up-slope the Merrespruit, a mining village of Virginia in the Free State Goldfields of South Africa. The Merrespruit tailing dam consisted of one basin: a northern compartment dived by means a wall from a southern compartment and an emergency compartment. A vertical decant pipe, connected to an horizontal piped drain placed at the bottom of the facility, was aimed to drain away the excess of water resulting from the consolidation process and runoffs from the central pond. Before the disaster, the division wall between the northern and the southern compartment had breached, resulting in a drainage from southern compartment flowing into northern compartment with an increase of the sizes of its pool that was progressively moved away from the decant pipe, towards the northern wall. In the same time the freeboard was lowered until 500-150mm. At 21:00 on 22 February 1994, after a heavy rainstorm, the 31m high norten dam wall failed with a 150m wide breach: 2.5 million tonnes of liquefied tailings were realized, travelling about 2km, covering about 500000m^2 and ripping the downstream Merrespruit mining village. Seventeen people lost their lives, more than 200 houses were damaged while 8 were swept away. Eyewitness reports, satellite images and laboratory tests were adopted in order to investigate the causes that lead that tragedy. The Harmony tailings were choesionless and fine-graded with more than 60% passing through ASTM n°200 sieve (finer than 74μm). Rain falling in the impoundments (estimated 50000m^3 of water) sudden flowed toward the northern pool that had already previously moved toward the northern wall. The build up of the moisture in the tailings along the wall was considered an ample trigger for static liquefaction. Furthermore the pool of the northern compartment, not having an adequate freeboard and the capacity to contain the additional inflow resulting from the rainstorm, started overtopping at

the lowest point of the wall, eroding the loose tailings. This resulted in a series of retroactive slip failures moving up the slope (about 2H:1V) with a domino effect, leading the 150m wide breach. The collapse of the impoundment caused a massive flowslide consisting in a realising of the liquefied tailings. An appreciable percentage of the specimens obtained from zones close to the failure were like to have been contractant (Fourie *et al*., 2001) during the laboratory triaxial tests carried out after the failure. This example of failure, together with many others (e.g. Wachusett Dam, USA - 1907; Calaveras Dam, USA - 1918; Bafokeng Platinum Tailings Dam, South Africa - 1974; Arcturus Gold Tailings Dam, Zimbawe - 1978; Nerlerk Berm, Canada - 1983; Stava, Italy - 1985; Mount Polley, Canada - 2014) shows the importance of investigating the static liquefaction phenomena and its relationship with the tailings dams stability conditions.

Usually, tailings dams have varying material properties and there could be contractive layers, susceptible to liquefaction, sandwiched within dilative ones. When the liquefaction initiates, the decreasing in shear strength of contractive layers may also decrease the shear strength of dilative layer with a domino effect. Generally, static liquefaction can occur in tailing dams if the tailings exhibit a contractive behaviour if sheared in undrained conditions or if the there is presence of a trigger mechanism:

- change in pore pressure (fast increase of phreatic level due to an excessive rainfall/snowmelt, high pond level or improper drainage/management);
- overloading (excessive raising rate of the embankment);
- quick decrease of confinement within the dam due to erosion phenomena.

Liquefaction phenomenon is usually associated to coarse soils under saturated conditions, but also finer soils, even under unsaturated conditions can be prone to liquefy (Carrera, 2008; Carrera *et. al.*, 2011). Due to the fact that tailing basins surface is exposed to many interactions with the atmosphere, leading temporary changes of the water head or the pond level, the same element of soil can therefore be in saturated or unsaturated conditions (case A or case B shown in Fig. 2.4), depending on the relative position of the phreatic level. Hence the importance of investigating the liquefaction potential of tailing in unsaturated conditions at different degrees of saturation (meaning different levels of the phreatic surface) in order to simulate different scenario and get reliable predictions for dam's stability.
The occurrence of static liquefaction phenomena, and so the long-time stability of tailing dams need to be properly understood by performing laboratories tests in order to evaluate the liquefaction susceptibility of the soil during the design phase, before any engineering works.

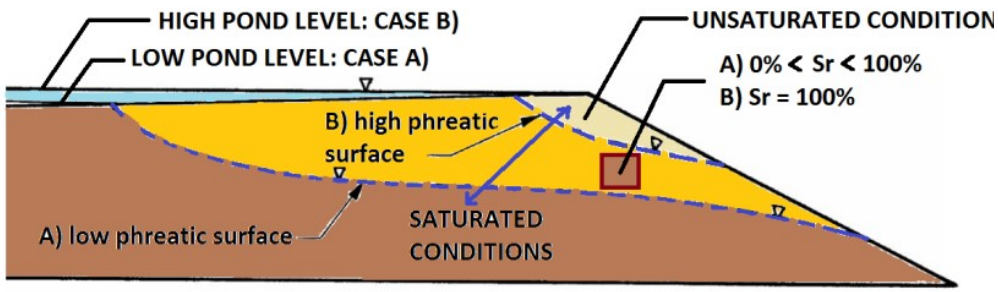

Fig. 2.4 - Schematic view of variations of phreatic surface within a tailing basin and its effects in terms of degree of saturation.

Therfore, the final section of the current research is aimed to study the mechanical behaviour of the fine tailing fraction in order to investigate the static liquefaction resistance of such material in unsaturated conditions, extending a previous characterization (Carrera, 2008) of the same fraction performed under saturated conditions. Due to the importance and complexity of liquefaction phenomena in stability problems of tailing dams, and also the little literature data concerning the static liquefaction on fine tailings in unsaturated conditions, the current research is aimed at investigating some of the main factors that are supposed to influence the liquefaction response of Stava silty tailing, mainly the degree of saturation, the preparation technique of the specimen or the initial density. A campaign of laboratory tests is performed on Stava silty tailing in unsaturated conditions or close to saturated conditions, by means of undrained triaxial tests. A similar hydro-mechanical study under unsaturated conditions on the coarse tailing fraction is left to further studies.

2.2 PECULIARITY OF TAILING WASTES

2.2.1 Grain size distribution

Tailing wastes are mixtures of crushed rocks and processing fluids that results from chemical and mechanical separation processes of mineral extraction. The particle size distribution of tailing wastes covers a wide range of particles (Vick, 1990) and depends on the parent ore as shown in Fig 2.5.

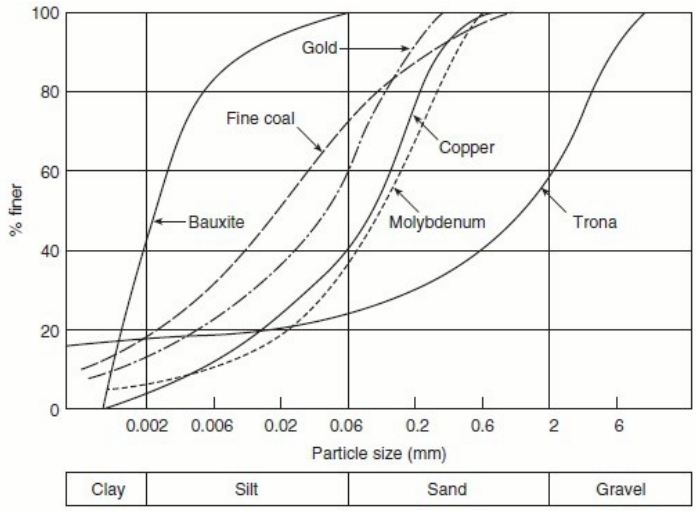

Fig. 2.5 - Example of grading curves for tailing (Sarsby, 2013).

Silt and clay are generated by the crushing work of men, and thus they are likely to be constituted by minerals typical of sands rather than natural silts or clays. This is the reason for which the term clay or silt should be considered only a particle size property rather than a mineralogical or behavioral one. As a consequence, plasticity Index, Activity Index and cohesion show very little values, so , tailing wastes are generally classified as non-plastic.

2.2.2 Friction angle, specific gravity, density / void ratio

Tailing wastes are usually angular and this feature impose them an high friction angle, usually 38°÷41°. In-place dry density is related with three parameters: type of tailing (silt or

sand), clay content and specific gravity, so the dry density of a tailing storage facility shows a wide range of values (Vick, 1990). Typical values of bulk density γ_b (ratio between the total weigh and total volume), dry density γ_d (ratio between weigh of solid particles and total volume) and void ratio e (ratio between volume of voids and volume of solid particles), are given in Tab. 2.1 and Tab.22.

Tab. 2.1 - Range of properties for tailing materials (Vick, 1990).

Ore type	Tailing type	G_s [-]	e [-]	γ_d [kN/m^3]	γ_b [kN/m^3]
Coal	Slimes	1.4÷2.1	0.5÷1.1	0.7÷1.4	0.8÷1.7
Lead	Slimes	2.6÷3.0	0.6÷1.1	1.3÷1.8	1.7÷2.2
Molybdenum	Sands	2.7÷2.8	0.7÷0.9	1.5÷1.6	1.6÷1.8
Copper	Sands	2.6÷2.8	0.6÷0.8	1.5÷1.8	1.8÷1.9
	Slimes	2.6÷2.8	0.9÷1.4	1.1÷1.4	1.5÷1.9
Taconite	Sands	3.0	0.7	1.8	1.9
	Slimes	3.1÷3.3	0.9÷1.2	1.5÷1.7	1.9÷2.2
Bauxite	Slimes	2.8÷3.3	8.0	0.4	1.2
Trona	Sands	2.3÷2.4	0.7	1.5	1.7
	Slimes	2.4÷2.5	1.2	1.1	1.6
Phosphate	Slimes	2.5÷2.8	11.0	0.22	1.1
Gold	Slimes	3.17	1.05	1.5	2.0
Pyrites	Slimes	4.3	0.5÷0.8	2.4÷2.9	2.8÷3.2

Specific gravity of tailing G_s (ratio between mass of soild particles and mass of water occupying the same volume), depends on the mine: for istance, tailings coming from gold extraction exibit high values of G_s, while tailings coming from coal extraction can show low values of specific gravity. A generalized range for tailings is given as 2.6÷3.2. Typical values of specific gravity are summarized in Tab. 2.1.

Tab. 2.2 - Typical values of dry density, void ratio and water content for tailing dam at a certain distance from the discharge point (Bjelkevik and Knutsson, 2005).

Tailing dam	Distance from discharge [m]	γ_d [kN/m^3]	e [-]	w [%]
Kiruna	0	17.0	0.72	22.4
	300	17.7	0.60	20.5
Svappavaara	0	17.6	1.09	22.7
	300	17.4	0.81	24.1
Malmberget	0	21.1	0.61	14.9
	300	19.0	0.70	20.1
Aitik	0	16.4	0.73	23.3
	1500	15.5	0.82	27.5
	3000	12.7	1.21	39.3
Boliden	0	19.7	1.15	16.0
	300	17.5	1.24	12.1
Garpenberg	0	16.1	0.84	25.4
	300	13.1	1.30	36.9
Zinkgruvan	0	15.9	0.75	25.6
	200	14.8	0.90	15.3

2.2.3 Hydraulic conductivity

Hydraulic conductivity *K* (Tab. 2.3) has a significant role on the geomechanical behaviour of tailing wastes. As shown in Tab 2.4, horizontal and vertical permeability range widely from 10^{-4}m/s for coarse sandy tailing to 10^{-9}m/s for slimes, mainly due to layered nature of tailing deposits and their variability in terms of grain size distribution.

Tab. 2.3 - Typical values of hydraulic conductivity for tailing dam at a certain distance from the discharge point (Bjelkevik and Knutsson, 2005).

Tailing dam	**Distance from discharge [m]**	**k [m/s]**
Kiruna	300	$14.70 \cdot 10^{-6}$
Svappavaara	0	$6.08 \cdot 10^{-6}$
	300	$5.67 \cdot 10^{-6}$
Malmberget	0	$16.30 \cdot 10^{-6}$
	300	$18.70 \cdot 10^{-6}$
Aitik	0	$2.54 \cdot 10^{-6}$
	1500	$1.41 \cdot 10^{-6}$
	3000	$1.01 \cdot 10^{-6}$
Boliden	0	$2.58 \cdot 10^{-6}$
	300	$2.78 \cdot 10^{-6}$
Garpenberg	0	$2.68 \cdot 10^{-6}$
	300	$1.70 \cdot 10^{-6}$
Zinkgruvan	0	$18.10 \cdot 10^{-6}$
	200	$5.41 \cdot 10^{-6}$

Tab. 2.4 - Range of permeability values for tailing materials (Sarsby, 2013).

Material	**Source**	$\mathbf{k_v}$ **[x10^{-6}m/s]**	$\mathbf{k_h}$ **[x10^{-6}m/s]**
Sands	Mittal & Morgenstern (1975)	9÷200	-
	Vick (1990)	10÷10000	-
	Genevois & Tecca (1993)	5÷40	-
	Qiu (2001)	25÷100	-
Slimes	Routh (1984)	0.5÷5	-
	Routh (1984)	0.2	20÷50
	Genevois and Tecca (1993)	0.005÷0.01	1
	Blight (1994)	0.001÷0.1	-
	Qiu (2001)	0.2÷11	-

Variations in permeability are also due to other factors, such as plasticity index, depositional technique and depth within the storage (Vick, 1990). For these reasons, the ratio k_h/k_v is commonly assumed as:

- 2÷10, in case of uniform beach sand deposits;

- 100 or more, for transition beach zones between the coarse sand embankment and the central slimes.

Knowing of d_{10} as the 10% tailing's particle grain size, allows a preliminary eximation of the average vertical permeability k_v (eq. 2-1) for loose sand tailing by Hazen's equation (Mittal and Morgenstern, 1975):

$$k_v = 0.015\ d_{10}^2 \tag{2-1}$$

2.2.4 Compressibility

If sand and silt tailing are subjected to one-dimensional consolidation process, the compressibility parameters are close to those of conventional materials, as shown in Tab. 2.5.

Tab. 2.5 - Range of consolidation parameters for tailing materials (Sarsby, 2013).

Source	Sand		Silt	
	C_v [cm^2/s]	C_c [-]	C_v [cm^2/s]	C_c [-]
Mittal and Morgenstern (1975)	-	0.05÷0.11	$9.5\cdot10^{-4}$÷ $9.5\cdot10^{-2}$	0.2÷0.3
Mittal and Morgenstern (1976)	-	-	0.0001	-
Nelson et al. (1977)	101	0.05÷0.13	-	-
Routh (1984)	0.012÷0.045	-	$3.49\cdot10^{-3}$ ÷$1.36\cdot10^{-2}$	-
Volpe (1985)	0.38	0.09	-	-
Volpe (1985)	0.37	-	-	-
Volpe (1985)	-	-	0.15	-
Blight (1988)	-	-	0.0063	-
Vick (1990)	-	0.05÷0.07	$9.5\cdot10^{-5}$÷ $9.5\cdot10^{-3}$	0.19÷0.35
Genevois and Tecca (1993)	-	-	0.019	0.15÷0.37
Chandler and Tosatti (1995)	-	-	$3.01\cdot10^{-2}$	-
Qiu (2001)	0.010÷0.033	0.06÷0.09	$9.5\cdot10^{-5}$÷ $4.4\cdot10^{-3}$	0.08÷0.37

The compression index C_c of tailing usually ranges from 0.20 to 0.30 and from 0.05 to 0.10 for low plasticity slimes and sand tailing, respectively (Vick, 1990). According to Vick (1990), the coefficient of consolidation C_v ranges from about $5\cdot10^{-1}$ to 10^2cm^2/sec for beach

sand deposits, while for slimes tailing, C_v ranges from 10^{-2} to 10^{-4}cm^2/sec. Typical values of coefficient of consolidation and compression index are shown in Tab. 2.5.

2.2.5 Drained / undrained shear strength

Generally, tailing wastes are characterized by absence or low values of cohesion and, as shown in Tab. 2.6 and Tab. 2.7, friction angles 3°÷5° higher than that of natural soils tested at the same density and stress level (Vick, 1990). The friction angles generally fall in a wide range, between 25° and 41° with a little variation between sand and silt tailing. This is due to the fact that, even if silts are the finest tailing's fraction, they result from rock crushing processes and, unlike normal silt/clays, they are generally made of hard and not alterated minerals, so their particles are angular and not flat.

Tailing having a water content close to the liquid limit (w_L) show an undrain shear strength close to 1÷2kPa, while tailing having a water content closed to plastic limit (w_P) exibit an undrained shear strength close to 100kPa or higher. From one limit to an other, an increase/descrease of shear strength of about 100 times is expected when the water content increases.

Tab. 2.6 - Shear strength parameters for tailing materials (Sarasby, 2013).

Fraction	Mineral	c' [kN/m^2]	φ' [°]	S_u/σ'_v [-]	Source
Sand	China clay	0	25÷33	-	Street (1987)
	Copper	0	33.5	-	Mittal and Morgenstern (1975)
		0	33÷37	-	Volpe (1985)
		0	34	-	Qiu (2001)
	Fluorite	0	42.3	-	Genevois and Tecca (1993)
	tungsten	0	28÷38	-	Routh (1984)
Silt	China clay	0	34	-	Wroth and Hugens (1973)
		0	25÷36	-	Routh (1984)
	Coal	10	32	0.24÷0.25	Alonso and Gens (2006)
	Fluorite	0	35÷38	0.15÷0.22	Genevois and Tecca (1993)
	Gold	0	36	-	Jennings (1979)
		0	33	-	Qiu (2001)
	Gypsum	0	31÷32	-	Vick (1990)
	Hydraulic fill	-	-	0.2÷0.4	Charles (1986)
	Minestone	-	-	0.3	Taylor and Cobb (1977)
		-	-	0.16	Taylor and Cobb (1977)
	Oil sands	3	30	-	Qiu (2001)
	Pyrites	0	37÷42	-	Alonso and Gens (2006)
	Tungsten	0	32	-	Routh (1984)

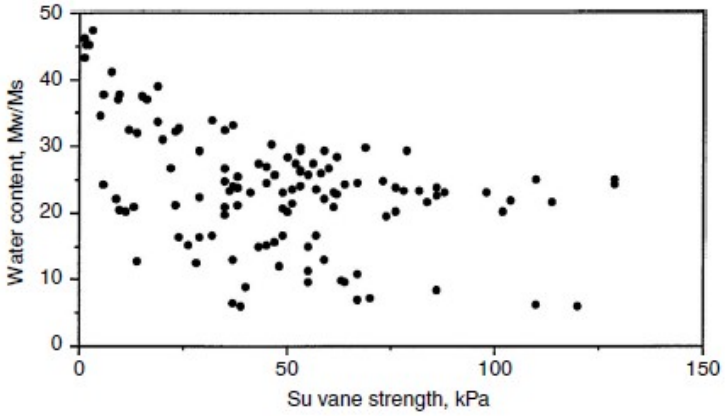

Fig. 2.6 - Vane test shear results on Newman tailings (Fell *et al*., 2015).

Tab. 2.7 - Effective friction angles for tailing materials (modified from Vick, 1990)

Material	φ′ [°]
Copper: sands; slimes	33÷37; 33÷37
Taconite: sands, slimes	34.5÷36.5; 33.5÷35
Lead-zinc silver: sands, slimes	33.5÷35; 30÷36
Gold slimes	28÷40.5
Bauxite slimes	42
Gypsum tailing	32

2.2.6 Characterization from in-situ tests

Geotechnical characterization tests can be done by performing in situ-tests (i.e. cone penetration test CPT, piezocone penetration CPTu, dilatometer test DMT). They can be useful in soils for which sampling is difficult such as sands and tailing material, but most of the correlation between data coming from in situ-tests and geotechnical parameters have an empirical nature and they are calibrated with regards to "ideal" soils, such as pure sand or clay. In intermediate soils as well tailing, these correlations are not so reliable and they are strongly influenced by the unsaturated conditions.

2.2.7 Chemical and mineralogical composition of tailing wastes

Due to their complex nature, chemical composition of tailing wastes is strickly connected with mineralogy of the ore, type of the processing fluids, degree of weathering during storage and efficency of of the extraction process. Depending on the efficency of the extraction process, iron, silica and oxygen are the most common elements and abundant quantities of Ca, Al, K, Mn, Mg, Na, P, S and Ti can be present, together with As, Cu, Zn and Pb. Significant quantities of pyrite, chalcopyrite, sphalerite, galena and pyrrotite can be found in coal tailing wastes, together with Ag, Hg, In, Po, Sb, Se, Sn, and Te.
Finally, in many cases, tailing have accompanying water which contains dissolved salts, heavy metals, contaminants and residual chemicals from the mineralogical processes (Tab. 2.8) that represent a potentially hazard because of their influence on food chains and aquifers if no adequate countermeasures are taken into account.

Tab. 2.8 - Contaminats contained in slurries from mining extraction (modified from Fell *et al*., 2015).

Type of tailing wates	Contaminants
Gold tailing	Cyanide
Coal tailing	High salts content, sulphides
Copper, lead-zinc tailing	Heavy metals, suplhides which oxidise and lead to leaching of heavy metals and yield acid water
Alumina tailing	NaOH
Uranium tailing	Heavy metals, radon

2.3 TYPES OF TAILING DAMS

Tailing wastes are generally in slurry form, so they can be stored into surface retaining structures or into underground cavities. The surface storage consists in deposition of tailing into impoundments such as dykes made of local materials. It is the most economical and common disposal method, while the latter deposition method is named backfilling and represents a good alternative to surface storage. Considering the construction method, two are the most common types of surface retaining structures: retention dams or raised embankments.

2.3.1 Retention dams

Similar to water retention dykes, tailing dams (Fig. 2.7) are build at full height from the beginning of the disposal. Tailing retention dams present *i)* an imprevious low permeability core and *ii)* a filter and an internal drainage system in order to mantain the phreatic surface at a low level, hence decreasing the pore pressures in the embankment body and so reducing the occurrence of static or dynamic liquefaction phenomenon.

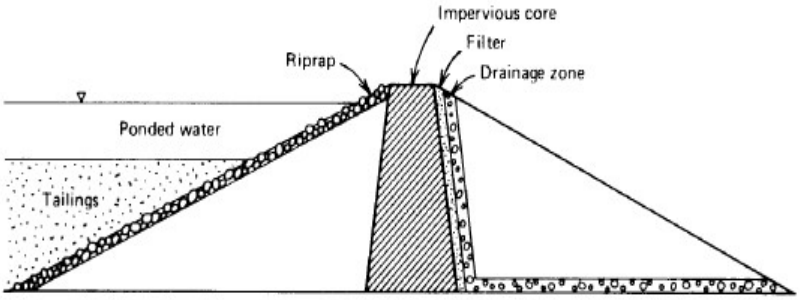

Fig. 2.7 - Water-retention type dam for tailing storage (Vick, 1990).

Suitable for any type of tailing and deposition method, this type of earth structures are similar to water retention embankments with respect to stability considerations, soil properties, surface water and ground water controls.

2.3.2 Raised embankments

Four are the configurations adopted for raised tailing dams (ICOLD 1982, ICOLD 1996; Vick, 1990): upstream, downstream, centreline and modified centerline.The differences in these four configurations consist in the method used to raised the embankment that is driven by topographical, geotechnical and economical considerations.

2.3.2.1 Upstream method

The construction of an upstream tailing dam begins with a pervious starter dyke: tailing are usually discharged from the top of the embankment crest in order to create a beach. This beach will be the foundation for the following embankments raises, each ones constructed as a berm partially on the embankment below, partially on the tailing beach immediatly upstream (Fig. 2.8). Consequently, as suggested by their name, the upstream of this type of dams moves upstream with each stage.

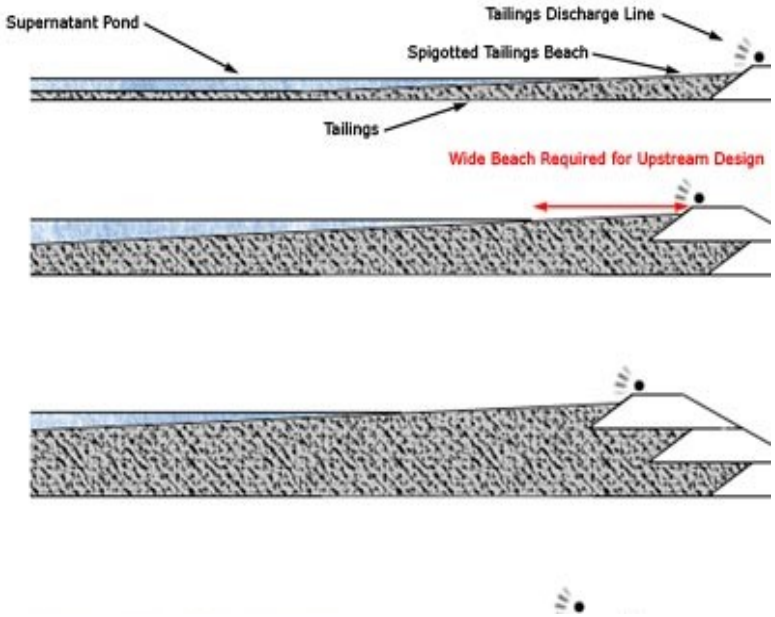

Fig. 2.8 - Upstream tailing dam (Vick, 1990).

Applicable in low risk seismic area, the upstream method is the most common construction technique due to its low costs. Indeed, if compared with other techniques, the upstream method requires the least amount of construction material. Generally this method is realized in areas where the climate is arid and a fast accumulation of water into the impoundment is not so common. Compaction by earthmoving equipment, such as vibratory compaction, is usually adopted in order to increase the degree of safety against static liquefaction hazard of the raising upstream embankments. The denser sand resulting after the compaction treatment will be less prone to liquefaction phenomena that rapresent one of the major failure risk of upstream tailing dam. The medium-coarse beach plays a fundamental role for the stability of upstream tailing facilities: it helps the drainage of water keeping low the phreatic surface and avoiding saturation within the sandy embankment. So, a filter underdrain system coupled

with a wide beach between the crest and the pond is essential to mantain low the level of the phreatic surface, reducing the risk of failure associated at static liquefaction phenomenon. Another aspect to consider is the rate of rising of the upstram embankment. The raising should be slow enough in order to prevent undrained conditions by means an increasing of pore pressure that can reduce the shear strenght of the sandy material.

2.3.2.2 Downstream method

Downstream embankments are realized step-by-step by moving in downstream direction the centerline of the dyke at each phase (Fig. 2.9). A downstream tailing dam is realized beginning with an imprevious starter dyke with internal drains, or an impervious layer on the upstream face. Tailing, at first, are deposited directly behind the starter dike while, subsequently, next enbankments will be raised in downstream direction by using the previous ones as their foundation.
One of the most relevant advantages related to this solution which adopts the installation of imprevious core/layer, is their capability to hold a big volume of water directly against the upstream face, without any risks in terms of static/dinamic liquefaction or stability of the dam due to changes of the level of phreatic surface, so performance of downstream damas are completely indipendent from the geomechanical properties of tailing. Downstream dykes can have unrestricted heights because of the structural indipendence of each raise and the only limit is the advancing toe that can causes problems in case of limited available spaces or enviromental restrictions.
On the other hand, because downstream embankment adopts a large amount of fill material, it is usually the most expansive solution. Subsequently, a wide area around the dam is required, because of the moving out of the toe as more the heigh of embankment is increased.

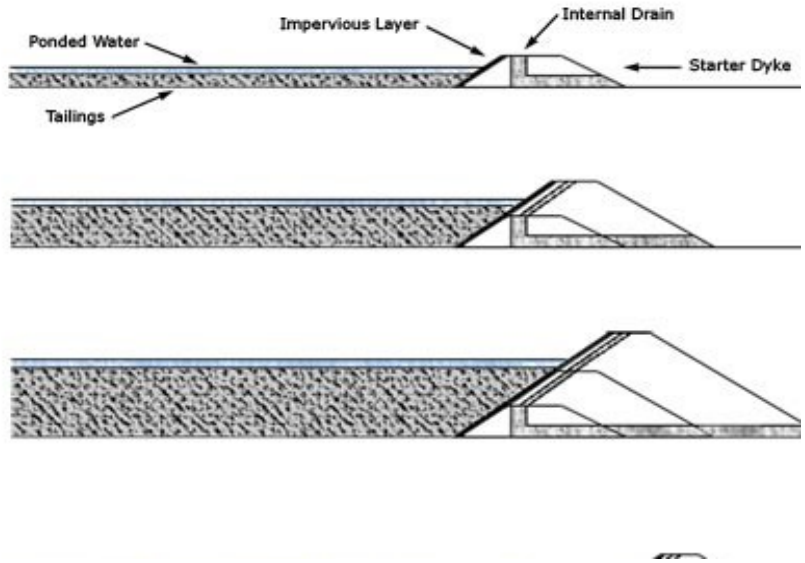

Fig. 2.9 - Downstream tailing dam (Vick, 1990).

2.3.2.3 Centreline method

Centerline embankment crest is raised step-by-step in vertical direction, so the position of the of the centerline of the dyke crest does not change with each stage (Fig. 2.10).

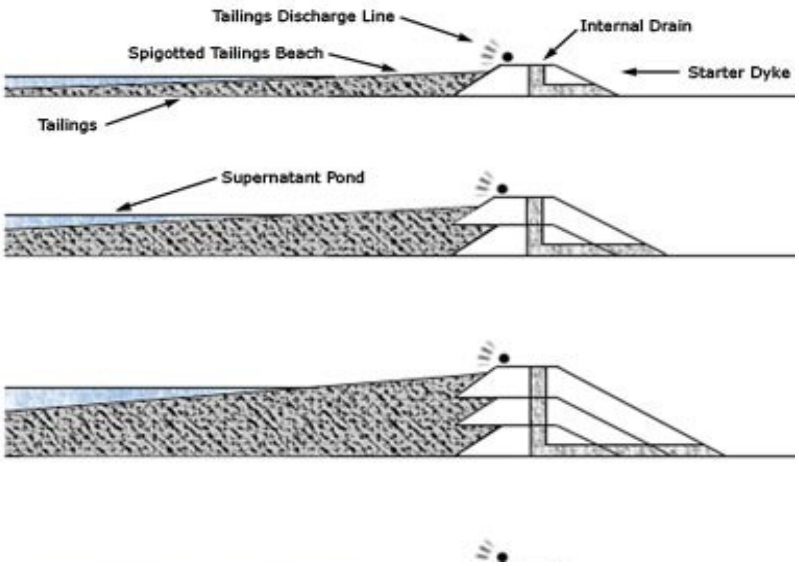

Fig. 2.10 - Centerline tailing dam (Vick, 1990).

The upstream toe of each following dyke is realized slightly over the tailing beach, but the biggest amount of the new embankment is founded on the previous dike. This method is a compromise between higher-cost downstream and higher-risk downstream design. Centerline dams are more stable than upstream ones and do not require as much fill material as for the embankment raised with downstream method. Also centerline design makes use of internal drainage zones in order to avoid risks of failure due the high level of phreatic level within the embankment.

2.3.2.4 Valley and cross impoundments

Sometime, other factors being equal, the use of natural depressions as tailing storage facility, can be economically advantageous because of the reduced dyke sizes. The valley walls can used to contain tailing in one or more sides of the facility, leading to valley impoundment (Fig. 2.11a) or cross impoundment (Fig. 2.11b) configuration.
Valley impoundments can be realized with different shapes single (tailing wastes are placed behind an unique dam), or multiple (a series of connected "stair-step" embankments contain the tailing wastes). Single or multiple configurations are commonly used solutions because they can be easly applied to many topographical depression.
The cross valley design is very similar to the one of conventional water storage reservoir: a dam is constructed connecting the valley, confining tailing wastes into the natural depression.

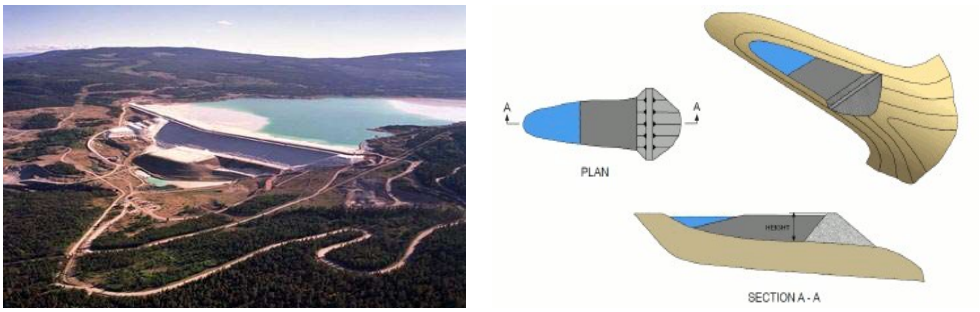

(a)

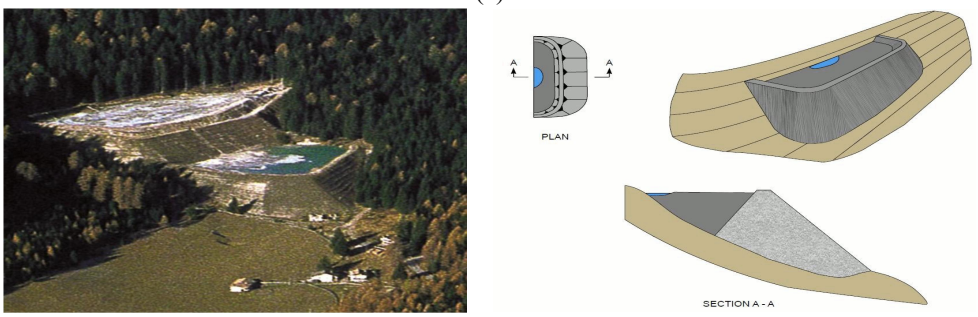

(b)

Fig. 2.11 - (a) Valley impoundment and (b) bottom: cross impoundment (Castiglia, 2015).

The monitoring of inflows across, around, or under the embankment is also a key factor to preserve the structural stability of the valley embankment. An adequate control of waters and an internal drainage system surely helps against static liquefaction, increasing the stability of the embankment due to lower consolidation time and increasing the permeability of tailing. Furthermore, by using the silty fraction of tailing or synthetic materials, the upstream face of the valley embankments is usually designed to create a layer of low permeability in order to lower the phreatic surface through the embankment.

2.3.2.5 Ring-dike impoundments

Where natural depressions are not available or there is a flat topography, the ring-dike configuration is a good solution (Fig. 2.12). This type of impoundment is more flexible for site selection purposes and can usually be placed relatively near to the processing plant (Ritcey, 1989), but it requires large volumes of construction material due to increased wall lengths that contain tailing on all sides.

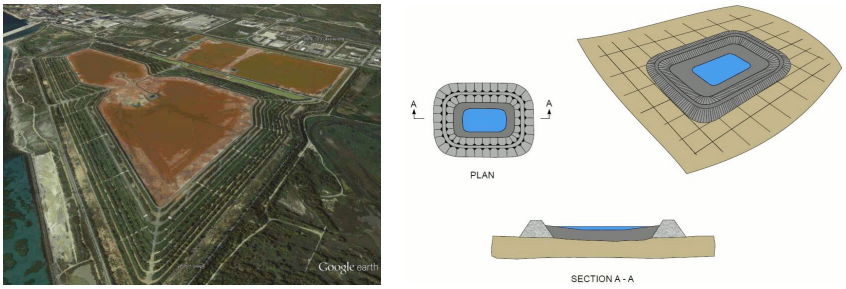

Fig. 2.12 - Ring dike impoundment (Castiglia, 2015).

Modern ring dikes dams have been built by applying the downstream or centerline methods rather than the upstream method, so the storage volume can be organized in single or segmented form and the regular/simple geometry adopted with this configuration makes easy the installation of various kinds of liners (Vick,1990). Since ring dikes have regular shape and relatively low height, the design is often simpler than a high valley dam design. An advantage is that the volume of pond water is limited to that transported with the tailing wastes and from precipitation: there is no runoff other than from outer slopes. The runoff impacts are reduced, less elaborate water control measures are required with a smaller pond area.
A disadvantage of this technique is that, if a ring dyke is raised by using the upstream method, for every raise the storage volume will decrease. The consequence is that the rates of rise will increase in order to obtain the same storage volume after every phase, but an excessive rates leads to increase the pore pressure and subsequently low shear strengths providing the trigger for static liquefaction. Other disadvantages of this technique are the esthetic problems, while in many areas there is no a flat suitable place for ring-dike impoundment.

2.3.3 In pit, subacqueous and river impoundments

In pit, subacqueous and in river impoundments techniques (Fig. 2.13) are less common than sub-aerial disposal methods. Among them, in pit impoundment technique is the most used because there is no need for dyke construction: it simply consists of disposing tailing into open pit surface mines. An advantage of this technique is that embankments are not required: tailing are contained by pit walls, so there are no risks depending from embankment instability. In every case, the stability of pit slopes must be guaranteed, even if the lack of dyke surely reduces the possibility of slope failure. Another advantage of this technique is that, due to its semplicity, a good drainage can be incorporated so many common failure causes are not apply at this kind of technique.


(a)


(b)

(c)

Fig. 2.13 - (a) In pit, (b) subacqueous and (c) river impoundments (Castiglia, 2015).

On the other hand, pit impoundment technique presents some disadvantages. For instance, fast rates of rise of tailing usually occur in the early stages of deposition, but in this phase,

the pit is at its deepest zone and the exposed tailing surface area is the smallest. Consequently, there is a reduction of the drying due to the sun and an increasing of consolidation time with a resulting low strength for a long time. Furthermore the stability of near underground mines or works can be compromised: liquefied tailing may rush into underground voids with catastrophic consequences as happened in Mufulira disaster in 1970.

2.4 DESIGN OF TAILING DAMS AND GOOD PRACTICE RULES

Safety of any tailing dams depends on both good design and management programmes. Generally, design of tailing dams is based on the same principles governing water retention dams, but the presence of saturated/unsaturated tailing materials versus water only, shows unique geotechnical challenges. This section briefly summarizes some considerations and main design rules in order to control the position the phreatic level inside the basin (and so the extension of the unsaturated zone above the water table), minimizing the risk associated to the occurrence of static liquefaction phenomena.

2.4.1 Design for control of phreatic surface

The phreatic surface has a fundamental role in the overall stability of tailing dams, under both static and seismic loading conditions, and hence one of the most important principles in the design phase is that the phreatic surface should not emerge from the dam face and it must be as low as possible, as shown in Fig. 2.14.

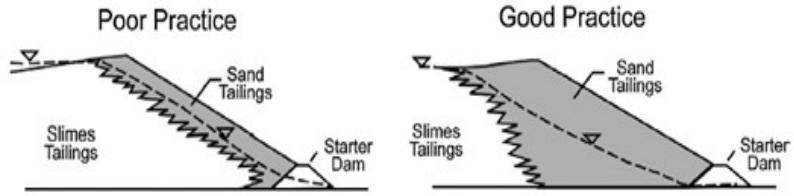

Fig. 2.14 - Phreatic surface through an upstream tailing dam: good and wrong practice (Vick 1990).

The main factors affecting the phreatic level are:

- relative permeability of embankment and storaged tailing (Fig. 2.15 and 2.16). Tailing permeability of internal zones within the storage should increase in the direction of seepage flow, so the embankments should be built with the most pervious available material;
- location of the ponded water with respect to the dam embankment;
- lateral changes of permeability (Fig. 2.17);
- ratio between permeability of tailing and permeability of foundation;
- grain size segregation within the impoundment.

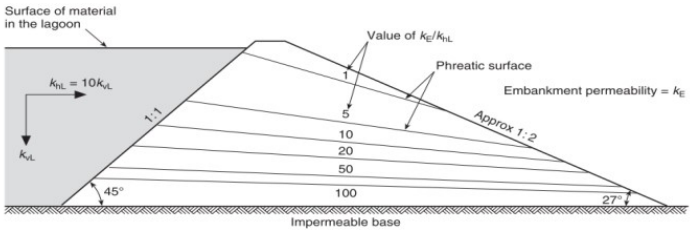

Fig. 2.15 - Infleuence on phreatic surface of relative permeability of embankment and material in the lagoon (Sarsby R. 2013).

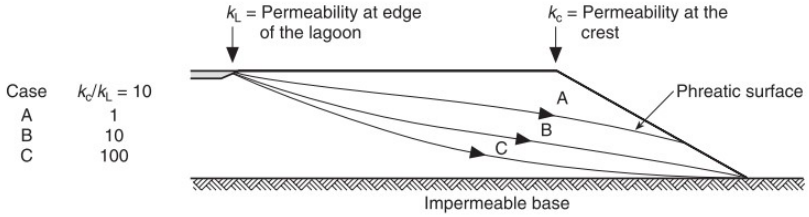

Fig. 2.16 - Influence of permeability variation on the phreatic surface (Vick, 1990).

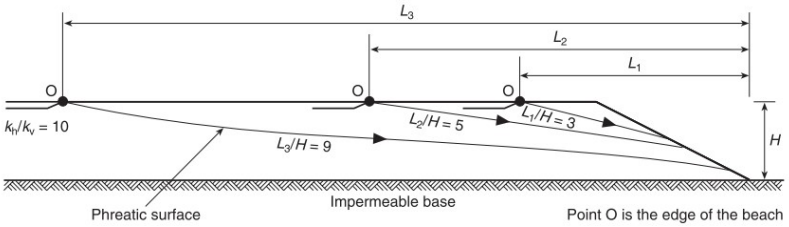

Fig. 2.17 - Influence of the beach width /pond location on the phreatic surface (Vick, 1990).

Other factors affetcting the phreatic surface location are given in Fig. 2.18.

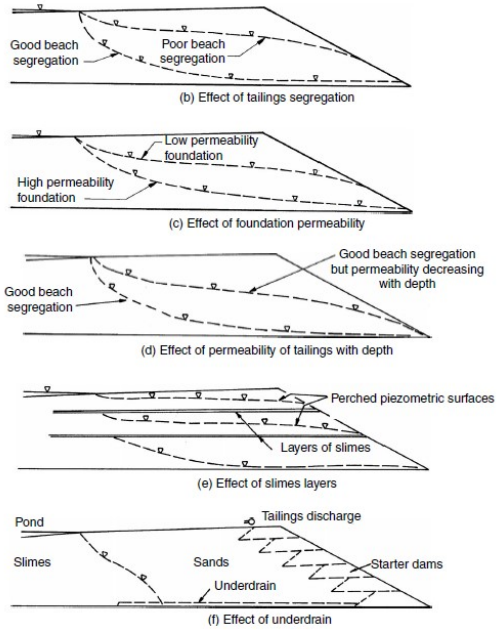

Fig. 2.18 - Factors influencing phreatic level for upstream embankments: (b) Effect of beach grain-size segregation and lateral permeability variation; (c) Effect of foundation permeability; (d) Effect of decreasing tailing permeability with depth; (e) Effect of slimes layers; (f) Effect of under-drains if there are no layers of slimes. (modified from Fell *et al*., 2015).

An example of upstream embankment is given in Fig. 2.19a. Low permeability slimes (k_3) are close the pond and high permeability sands (k_1) are placed at the embankment face. Hence, the phreatic level is fairly lower near the dam face due to coarse material of the embankment. Figure 2.19b shows that a low permeability material at the embankment face (k_1) prevents drainage, resulting in high phreatic level, leading to possible mass instability, piping and erosion. Figure 2.19c shows a downstream embankment where seepage is restricted with an upstream core (k_2) and a pervious downstream previous zone (k_1) to control the phreatic surface.

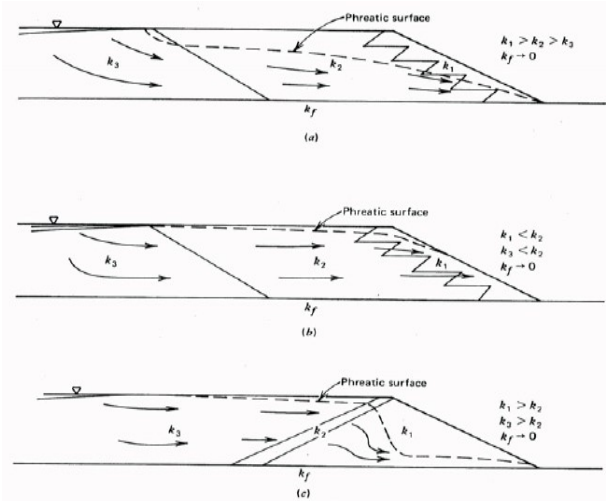

Fig. 2.19 - Effect of internal zoning on phreatic surface. (a) Proper internal permeability configuration for control of phreatic surface, (b) Seepage blocked by low permeability material at embankment face, producing high phreatic surface, (c) Seepage restricted by upstream core and drained by downstream pervious zone to produce good phreatic surface control (Vick, 1990).

2.4.2 Design for drainage zones and for cores

The purpose of drainage systems within a tailing dam is the decrease of pore pressures in the embankment body. According to Vick (1990), the phreatic level can be controlled by internal drainage zones (made of high permeable soils) and/or cores, made of low permeable materials. The chimney drains of internal drainage rise upward within the embankment, either vertically or inclined, depending on the construction method. Fig. 2.20 shows the internal seepage, while Fig. 2.21 gives some possible solutions. As shown in Fig. 2.21a, the phreatic surface level decreases due to the presence of an horizontal blanket drain installed into at the bottom of an upstream tailing dam. It extends upstream from the coarse starter dike that should be more pervious than the tailing wastes in order to avoid the increase in phreatic level at or above the starter dike top. Figure 2.21b shows a downstream embankment with an inclined chimney drain and blanket drain, while Fig. 2.21c gives a centreline embankment with vertical chimney drain. According to Vick (1990), the use of combined chimney-blanket drain arrangements can prevent seepage along the base of structure and saturation of downstream shell. Consequentlly there are no restrictions on permeability of remaining fill zone in the downstream shell that can be realized with any available material that satisfies strength requirements.

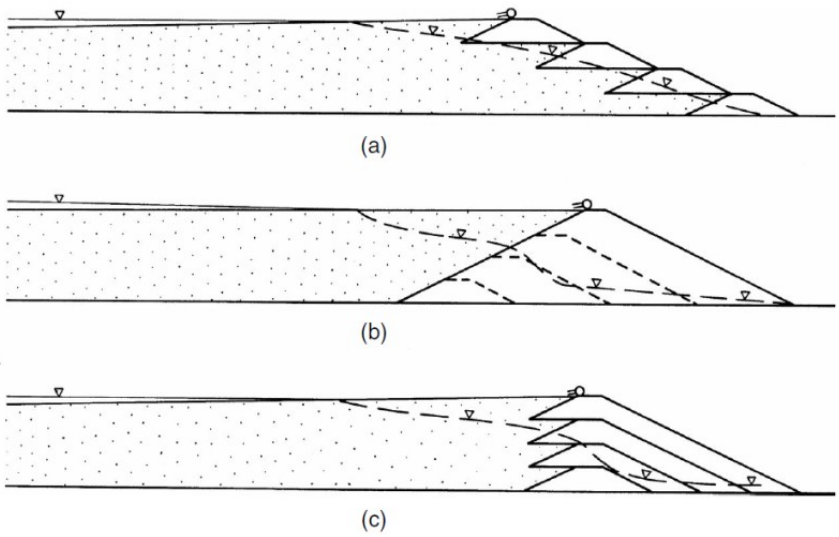

Fig. 2.20 - Internal seepage for (a) upstream tailing dams, (b) downstream tailing dams and (c) centerline tailing dams (Fell *et al*., 2015).

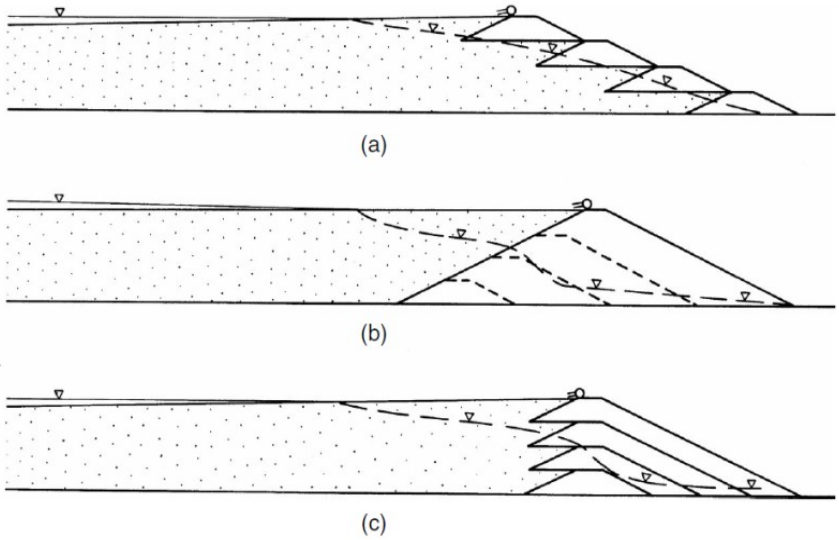

Fig. 2.21 - Internal drains zones for (a) upstream tailing dams, (b) downstream tailing dams and (c) centerline tailing dams (Vick, 1990).

Another fundamental purpose of a under-drainage system is to reduce the seepage into the foundation soil, reduce the head on the liner and attarct the water in order to discharge it into a collector system for recycling it to the process plant (Fig. 2.22) Anyway, the amount of seepage bypassing the drains and their efficacy in reducing pressures on the liner is affected by many factors, for instance the spacing of the drains, the permeability of the liner; and the horizontal and vertical permeability of tailing.

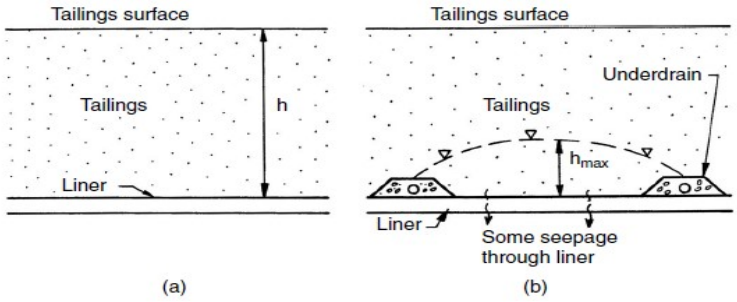

Fig. 2.22 - Head acting on clay liner, (a) without undrain and (b) with undrain (Fell *et al*., 2015).

The core is an impervious/low permeability compacted zone within a tailing' embankment, realized in order to decrease the seeage and keep low the phreatic surface. For these reasons, permeability, shear strength, density, compressibility and erosion resistance are essential in selecting the core material: an high density is desired because it increases the shear strength and erosion resistance, reducing at the same time the permeability of the core. According to Fell *et al*. (2015), the permeability of most compacted earth fill core materials should be less than 10^{-8}m/s or 10^{-9}m/s.
As shown in Fig. 2.23, central cores are suitable for centreline method, while inclined appropriate for downstream dams. According to Vick (1990), if the downstream shell materials are sufficiently pervious with respect to the inner core, the phreatic surface can be controlled by using of vertical or inclined impervious cores.

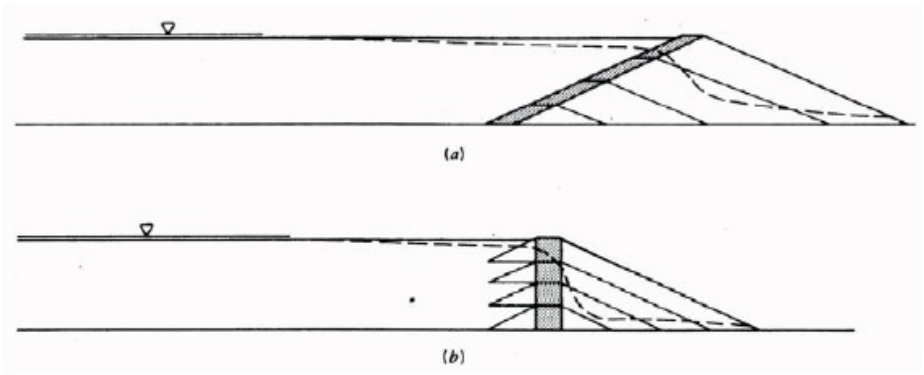

Fig. 2.23 - Cores in raised (a) downstream and (b) centreline tailing dams (Vick, 1990).

If there is a poor availability of local material for drainage zones having high permeable and less permeable for cores, tailing can be used for phreatic level control purposes. The phreatic level decrease when the permeability difference between adjacent zones is two orders of magnitude and this difference is achieved by separating sands and slimes through cycloning Vick (1990).

2.5 DEPOSITION TECHNIQUES

The heterogeneity of deposited tailings has a relevant role in terms of stability of the embankment because it can influence the position of the phreatic level within the basin, as shown in Fig. 2.15, Fig. 2.16, Fig. 2.17 and Fig. 2.18.
After extraction of the valuable ore by means of chemical and mechanical separation processes, tailing slurries are transported from the mill to the impoundment by using

pipelines. Once the tailing reach the storage facility site, many deposition techniques are available. Three deposition methods are usually adopted: single point discharge, spigotting or cycloning.
The single point technique (Fig. 2.24a) allows to discharge tailing from the open end of a pipeline placed above the embankment. It is not appropriate when the pond must be kept away from the embankment. This method requires that the discharge point must be periodically moved to another section of the dam in order to avoid unequal raising of the dam sections.

(a)
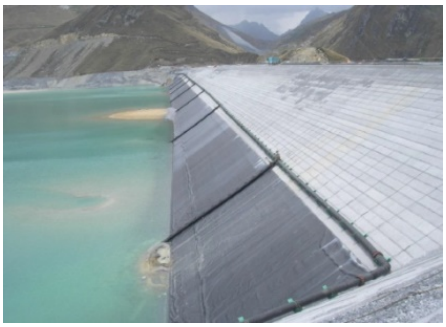
(b)

Fig. 2.24 - (a) Single point discharge and (b): multiple point discharge (Castiglia, 2015).

The spigotting technique (Fig. 2.24b) is a sequentially discharge of tailing through small pipes (spigots), from multiple points placed at regular intervals along the dike, achieving a uniform flow of tailing. Spiggotting technique also forms a sloping beach: the coarsest fraction settles closed the discharge point while the finer fraction is deposited farther from the spigot. As a result of this procedure, geomechnaical parameters such as density, shear strength, and permeability decrease with increasing distance from the discharge point.
Hydrocyclones (Fig. 2.25) are mechanical devices moving on rails and adopted to separate the larger tailing sand sized particles from the finer silt by using centrifugal action. When the slurry enters the cyclone, fine particles (overflow) and water move to the top outlet, while coarse particles (underflow) spiral downward and exit from the bottom part. While the underflow is used to create the tailing embankments, the overflow is discharged into the impoundment by using pipeline. It is worth noting that two cyclones can be use in series: this technique is called two-stage cycloning, and it is often used to obtain a sand fraction that contains less fines than single-stage cycloning. Both underflow and overflow must be checked in order to measure densities, gradation, inlet pressures aimed to impose the correct adjustments of the cyclones. For instance, tailing containing less than 60% of particles passing ASTM sieve n°200, have an adeguate sand quantity to be cycloned.

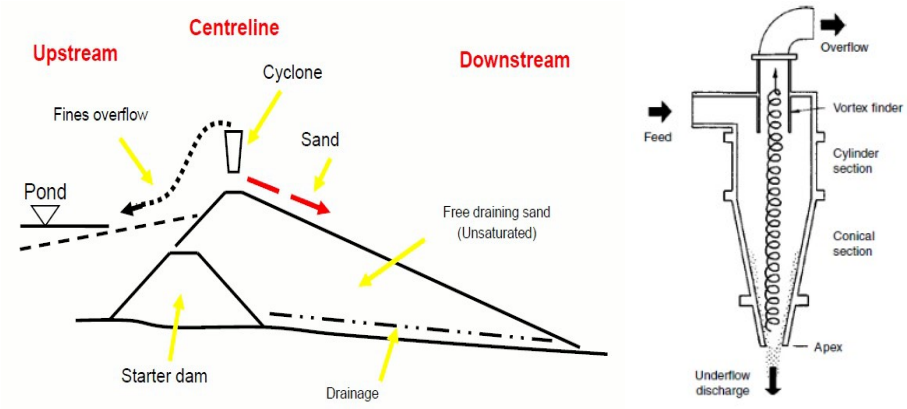

Fig. 2.25 - Cycloning technique (Fell *et al*., 2015).

Two are the cycloning methods commonly used for raising tailing dykes and segregating particles: central cycloning or on-dam cycloning. The first method consists in a single permanent high capacity cyclone at a strategic position. The underflow is moved by earthmoving equipments from the stockpile to the dam where it is used in embankment construction and then compacted, while the fine particles are discharged into the center of the impoundment. The second method consists of many cyclone units placed on towers, trucks, scaffolds or suspended from cranes along the dam crest. The resulting sand is deposited directly on the embankment face while the fine particles are discharged into the impoundment. The high pulp density of the coarse fraction (70÷75% solids) results in the deposition of sand having a slope of 3:1 to 4:1 on the face of the dyke under construction. Relative densities between 45% and 50% can be achieved, but values below 30% are not uncommon. As a consequence, these low relative densities don't permit the use of this method if the tailing storage facility is placed in high seismic area. If the coarse fraction is used for embankment raising, the coarse-medium fraction will form a beach against the dyke, while the resulting water and the finest fraction are deposited in the centre of the facility, creating the so-called "pond".
According to hydraulic segregation profile, on-dam cycloning allows to have an higher permeability zone made of coarse particles near the embankment/discharge point, a lower permeability zone (pond) made of fine particles further from this point, and an intermediate permeability zone (beach) between them. It is worth noting the absence of a clear separation between these three zones, so the importance of analysing vertical sections at different distance from the embankment.

2.6 WATER RECOVERY METHODS

The huge amount of water deposited with tailing wastes into the disposal is usually partially removed from the pond mainly by two recovery methods (Fig. 2.26). In the first case (Fig. 2.26a), water is removed by a pump mounted on a floating barge. In the second case (Fig. 2.26b) water is intercepted by a decant tower connected with decant pipe (placed at the bottom of the facility) and discharged out of the basin. At each raising of the tailing level, the lower decant tower is closed and the upper one is open. There is no preferred method: the first system is usually more flexible than the second one and requires less stringent control of tailing deposition to maintain the decant pond near the decant tower. Furthermore, it avoids the potential weakness, from of having a conduit through the embankment that can leads problems and possible failures connected to internal erosion, piping phenomena and static liquefaction phenomena.

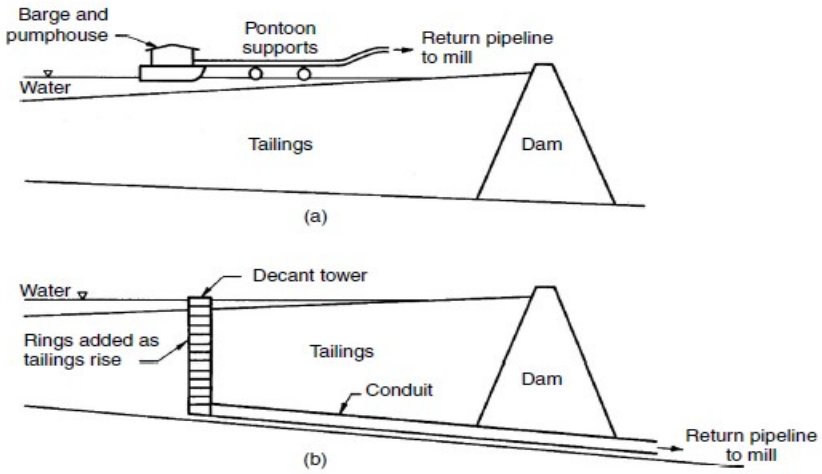

Fig. 2.26 - Water recovery methods for tailing storage facilities (Fell *et al*., 2015).

These operations, aimed to remove as much water as possible, have a fundamental relevance in the stability of tailing dams because they allow to keep the pond as far as possible from the dam, so decreasing the phreatic surface within the basin and the consolidation times. It is worth remembering that the phreatic surface must be as low as possible, even after rainstorm, in order to not emerge from the dam face and so reducing the occurrence of static liquefaction of the medium-coarse embankment.

2.7 REHABILITATION OF TAILING DAMS

After mining activities, tailing storages facilities must be designed to contain the tailing indefinitely and, at the same time, minimise long term impact on the environment. Again, factors affecting the long term behaviour of tailing storage facilities are mainly the effects on groundwater/surface water associated to the stability of the embankment.

When mining operations cease, measures should be taken in order to limit water infiltrations due to rainfall, leading to an increase of phreatic surface, expecially if the deposited tailing waste contains contaminants trapped in the water when mining operations cease. One of the countermeasure consists in planting vegetation on the tailing in order to encourage transpiration. The alternative is covering the surface deposit, but it is not possible to consider that just a ‘clay cover’ can provide a ‘seal’ of the tailing. In the first place, because the clay, even if well compacted, has a finite permeability and then because its permeability can be easly increased by cracking due to drying processes, settlement and penetration by aminals and roots. In any case, long term seepage and control of phreatic surface must be considered during design phase. Some possibilities for covering tailings surface are shown in Fig. 2.27.

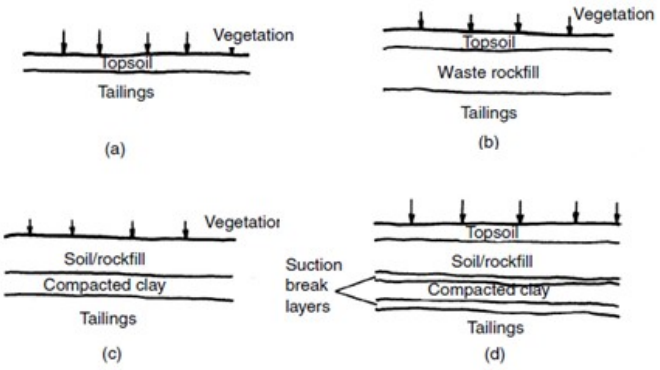

Fig. 2.27 - Some examples for covering tailing facilities in increasing degree of sophistication and cost from (a) to (d) (Fell *et al.,* 2015).

Each layer shown in Fig. 2.27 has a specific purpose:

- vegetation promotes evapotranspiration, controls erosion and enhances the appearance of the area.
- topsoil is placed to promote the vegetation above it;
- soil rockfill is aimed to control erosion and protect the underlying compacted clay from dring processes, as shown in Fig. 2.27d;
- filter layers can be used to avoid migration of fines into the drainage layer;
- compacted clay cover is aimed to reduce infiltrations;
- suction break layers are made of sand in order to control desiccation and the compacted clay layer. Furthermore, suction break layer can prevent the transfer of contaminants up through the compacted clay from the deposited tailing wastes.

2.8 TAILING DAMS FAILURES

Tailing impoundments should last forever, but many old and recent failures (i.e. Bento Rodrigues dam disaster, occourred in Brazil, november 2015) pose a serious environmental threat when the mine closes or is still active. There is a great number of peculiarities that makes tailing impoundments more vulnerable than other type of retention dams such as water-retention dykes:

- tailing dams are embankments made by locally collected material such as tailing, soil, coarse waste from mining activities;
- tailing dams are dykes raised often step by step;
- tailing impoundments require high cost of maintenance during life cycle and after closure of mining activities;
- sometimes tailing dams are affected by lack of specific design criteria and regulations with lack in stability requirements concerning continuous monitoring activities during every phase of the mine.

Even if a large amount of databases concerning tailing dam failures are not accessible or incomplete, statistics are good tools for understanding possible relationships between failure, causes, construction method, temporal and spatial distribution. Figure 2.28 gives a qualitative comparison of sizes, capacity and tailing realised from some failed tailing dams and the active Zelazny Most tailing dam.

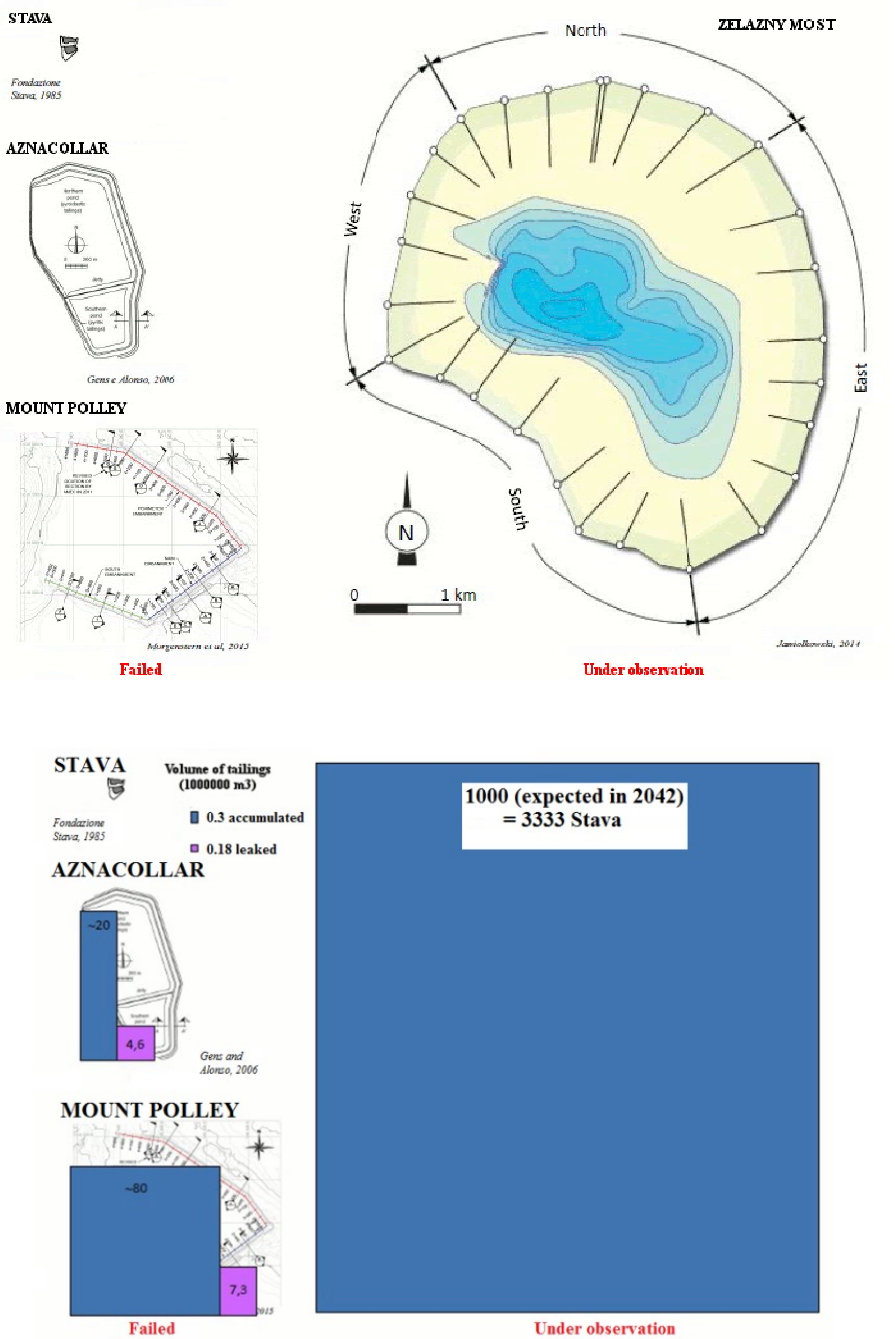

Fig. 2.28 - Comparison between dimensions, capacity and tailing leaked of some collapsed tailing dams: Stava (1985, Italy), Aznacollar (1998, Spain), Mount Polley (2014, Canada), and the active Zelazny Most tailing dam, Poland (Jamiolkowski, 2013 and Simeoni, 2015).

There are many common failures modes to which tailing dams may be vulnerable, each one can cause partial or complete embankment failure. ICOLD 1996 bullettin n°106, Tab. 2.9 gives a summary of the main failure modes, together with the causes and possible remedies.

Tab. 2.9 - Failures modes, causes and remediation (ICOLD 1996).

Failure mode	Causes	Remedies
Overtopping	Inadequate hydrological or hydraulic design Loss of freeboard due to crest settlement	Gabions, mine pit waste or surrounding borrow material may be quickly imported to aid the strength of the embankment Opening of emergency pumps and spillways
Slope instability	Overstressing of foundation soil or dam fill Inadequate control of pore pressure	Soil reinforcement and strengthening measures Installing a drainage trench at the toe of downstream face and/or horizontal bore drains. Filters can prevent the entry of fill material into the drain.
Internal erosion	Inadequate control of seepage Bad filter and drain design Poor design or construction control resulting in cracks or leakage through conduits	Raising downstream embankments with drainage blanket Installation of horizontal bores to relieve pressure Installation of deep trenches towards downstream face
External erosion	Inadequate slope and toe protection	Vegetation of the downstream face Placing crushed mine waste on the downstream embankment face Construction of berms on downstream face Placing rock fill such as mine pit waste adjacent to the toe
Earthquake action	Steep slopes Liquefaction of embankment and foundation soil	Filling of cracks with a suitable material
Damage to decant system	Excessive settlement Chemical attack on concrete and steel	Opening of emergency pumps or spillways

According to Davies *et al*. (2000) and Rico *et al.* (2010), a distribution of tailing dams failures by causes is given in Fig 2.29.

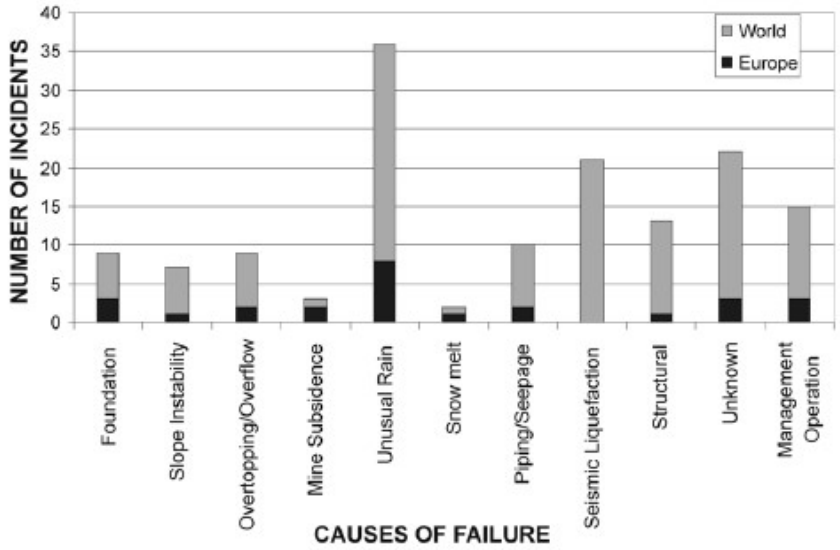

Fig. 2.29 - Number of incidents versus cause of failure, World and Europe (Shaid and Qiren, 2010).

It can be noticed that:

- about 25% of worldwide and 35% of european failure are due to meteorological causes: intense rainfall, hurricanes, rapid snowmelt, or ice accumulation in the tailing dam. It is worth noting that meteorological causes are usually associated to static liquefaction phenomena. Except the collapse of Stava tailing dams that will be presented at the end of the current chapter, another relevant example of failure due to static liquefaction with severe consequences is represented by Sullivan Mine collapse, occurred in Canada in 1991. The increase in pore pressures during construction phases (incremental raisings), led to static liquefaction in the foundation of tailings consisting in fine-grained silty sand to sandy silt;
- the second most significant cause is due to poor management: inappropriate dam procedures such as rapid dam growth, poor beach management or faulty maintenance of the drainage structures. Deficient management practice causes for 10% of worldwide incidents and 12% of European failures;
- the third cause of dams failure (world 6% and Europe 12%) is related to wrong design choices: failures of the dam foundations, poor choice of dam placement; poor choice of dam construction;
- other common causes are seepage/piping, overtopping and mine subsidence. Finally, dinamic liquefaction represent 14% of worldwide cases, while in Europe this cause is completely absent.

2.9 THE CASE STUDY: STAVA TAILING DAMS

One of the most relevant case of tailing dam's failure is the collapse of Stava basins, whose material's hydromechanical behaviour is studied in the current research. The disaster occurred in the municipality of Tesero (Trento, Italy) in the summer of 1985 and it was caused by the failure of two tailing dams located just upstream from the village of Stava, a small town located in an holiday resort region of the Dolomite Mountains in Northern Italy (Fig. 2.30).

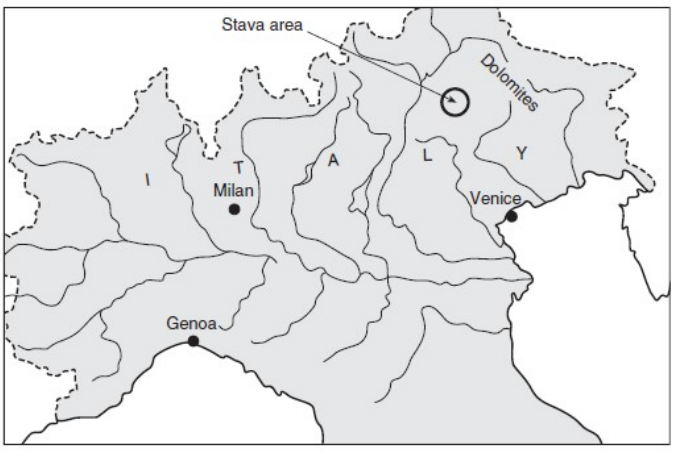

Fig. 2.30 - Localization of the Stava basins (Sarsby, 2013).

The whole structure consisted in two storage facilities (Fig. 2.31), the first one started in 1961 and the second one was built in 1969, in order to store the huge amount of slurry tailing coming from the separation floatation process of the Prestavel fluorite mine.

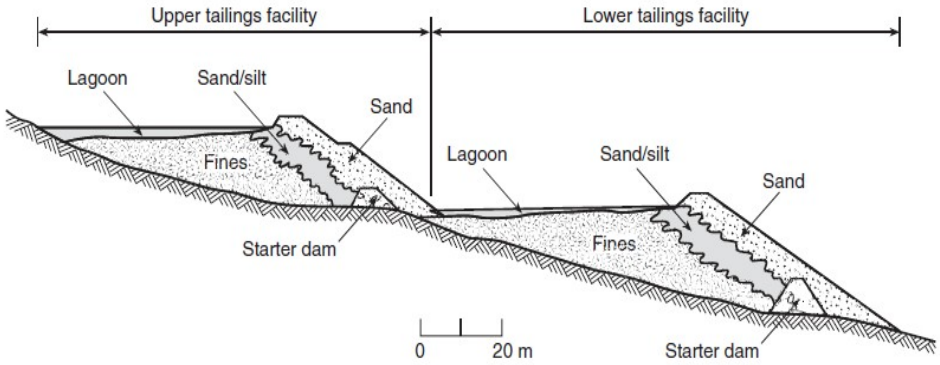

Fig. 2.31 - Schematic section of the two Stava tailing dams (Sarsby, 2013).

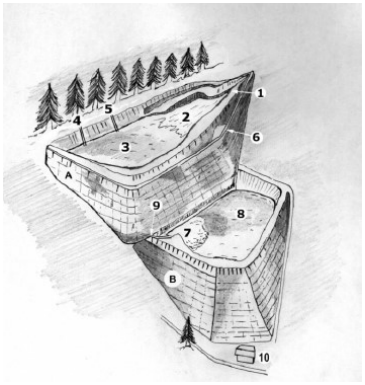

Fig. 2.32 - Graphical representation of the two Stava tailing dams: (A) upper basin, (B) lower basin, (1) cyclone, (2) sandy deposit, (3) silty deposit, (4) drainage service, (5) emergency drainage, (6) service road, (7) sand cone (8) silty deposit, (9) drainage from the upper basin, (10) caretaker's house (Luino *et al*., 2012).

The two impoundments were arranged in step form, so the upper facility decanted into the lower one. The downstream sides of the basins were contained by steep earth embankments, while upstream sides rested directly on the natural slope (Fig. 2.32 and Fig. 2.33). Both upper and lower dams were made principally of medium-fine sand and thin or fairly uniform layers of saturated clayey silt.
The elevation of the lower and upper basins were 1350.80m and 1378.83m, respectively. In 1985, at the time of the disaster, the maximum dam crest over the ground level was of 22÷23 m for the lower basin and 28m for the upper impoundment. The total height from the base of the lower embankment to the crest of the upper dam was about 50m. The surface area of the lower impoundment was about 6500m^2 with a storage capacity about 100000m^3, while the upper storage facility, placed behind and upstream from the lower one, had a surface area of 9800m^2 with storage capacity of 150000m^3.

2.9.1 Raising dam method

Two systems of tailing slurry disposal were adopted: central cycloning and on-dam cycloning. The on-dam cycloning is shown in Fig. 2.33a and Fig. 2.33b. At least within the upper dam, a fixed cyclone at the northern edge of the upper impoundment was used in the last three years of activity. The hydrocycloned sands, after densification process, went for the construction of the dam raise near the cyclone, while the remaining part of the embankment was built by mechanically transporting the sand from the point of deposit. The upper embankment was raised using the upstream method, which relied on the support of the silt deposits in the lower basin for subsequent raising.

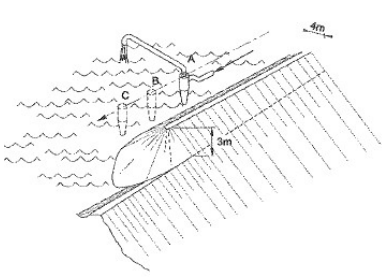

(a)

(b)

Fig. 2.33 - (a) Schematic drawing of the technique adopted for raising the Stava embankments, (b) one of the hydrocyclone adopted (Ricceri, 2001).

These silty materials consisted of thin, poorly densified layers, with some being composed of "loose" saturated sediments and others partially cohesive. So, the downstream foot of the upper dam came to rest on the unconsolidated sediments of the lower facility.

2.9.2 Decant pipes

After passing into the hydrociclone, coarse particles were separated from finer ones. The first fraction was used to rise the embankment, while the slimes were pumped into the basin. Upon into the basin, consolidation process began, so water flowed slowly down where it was collected by decant pipe and discharged out of the basin. At each raising of the bottom, the lower decant tower was closes and the upper one was open, as shown in Fig. 2.34a.
Two decant pipes were realized as shown in Fig. 2.34a,b,c. They were 200mm diameter, set below the existing ground level in a concrete surround and discharge points were located at provided intervals and sealed progressively as the tailing wastes level was raised.

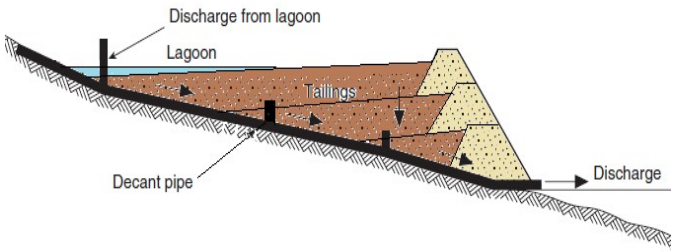

(a)

(b)

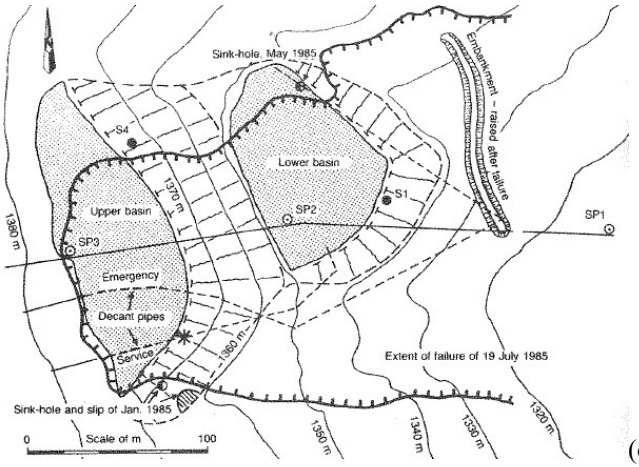

(c)

Fig. 2.34 - (a) Schematc representation (left) of the system adopted for drawing off water from the slimes pond, (b): schematc representation of the system adopted for drawing off water from the slimes pond and decant pipe (right) showing overflow holes after the failure and (c) plan of Stava storage facilities on 1983 (modified form Sarsby, 2013; Chandler and Tosatti, 1995).

2.9.3 Summary of the Stava basins operations

The first document concerning the Mount Prestavel mining activity dates back to 1528 concerning the extraction process of argentiferous galena until 1934 when mining was redirected to the extraction of fluorite (30 tons per day).

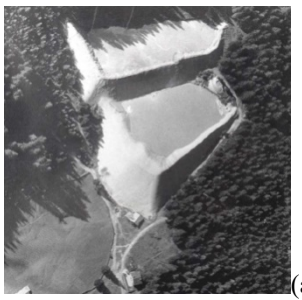

(a)

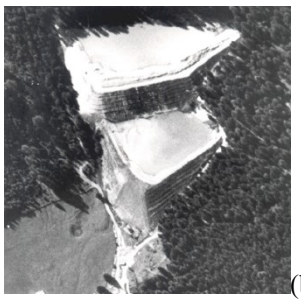

(b)

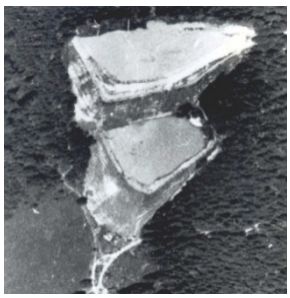

(c)

Fig. 2.35 - Aerial pictures of Stava impoundments a) In 1973, two years after the construction of the top dam, the upper embankment is raising from the orographic left side. b) In 1978 the geometry of the upper dam is different from the previous picture. Upstream method is in progress c) In 1983 the upper basin is 13m higher than in 1973. It can be observed the delta deposit close to the cyclone, at the orographic left side of the top dam. From 1971 until the failure of 19 July 1985, the height of the upper impoundment embankment was increased by 28m (Luino *et al*., 2012).

The first processing technique for refining the extracted fluorite was the gravimetric method (Fig. 2.36). The gravimetric system did not require any water, the waste products consisted in rocks and inherts and the obtained fluorite having purity 75÷85% was suitable for the steel industry.

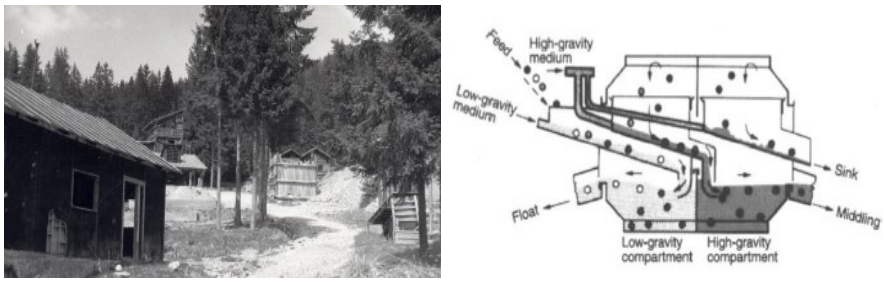

Fig. 2.36 - Gravimetric plant adopted in Stava Valley until 1960 (Lucchi, 2015).

In 1961, the company changed processing method, by using a flotation system in order to produce a fluorite at the 97-98% purity, required for the booming chemical industry (Fig. 2.37).

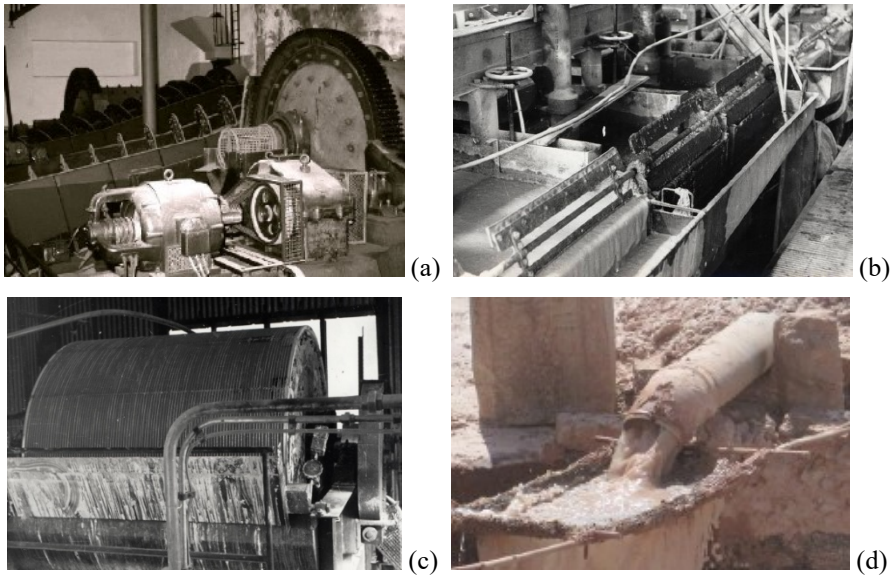

Fig. 2.37 - Flotation plant adopted in Stava Valley until 1985. a) Rock was crushed until sand having diameter less than 0.5mm was obtained. A quanty of $10m^3$ of water per ton of rock was added. b) Air is suffled and, by adding chemical reagents, fluorite ore is water-repellent. c) Fluorite join to air bubbles and moves to the surface and it is densified. d) Waste products are tailing consisting in slurries stored in the basins by using pipes. (Lucchi, 2015).

A flotation plant would require a huge quantity of water and a place suitable for decanting and storaging the wet tailing sludge leftover from the flotation process. The flotation plant was realized on the mountainside, together with a chair lift for transporting workers, an aqueduct and a cable car to transport the extracted material from the mine and a chair lift for transporting workers.
Two events occurred in 1985, some months before the failure, which highlighted problems with the decant pipes in both basins and which throw light on the possible reason for the failure. In January 1985 a small slip occurred on the right side of the upper embankment which was followed by the development of a sink-hole in the outer side of the basin, just upstream of the slip. It was concluded that both the slip and sink-hole resulted from leakage

from the decant pipe after this had become blocked by freezing at its outfall (Chandler and Tosatti, 1995). Seepage close to the slip continued into March 1985. Later, in May 1985, another sink-hole developed, this time in the lower embankment, resulting from a flow of decant water and slimes into the decant pipe which ran beneath the lower basin. Repairs were done, but these two events, occurred in January and March 1985, shown the poor quality of the drainage system.

2.9.4 Climate and geological settings

The two tailing storage facilites were at altitudes between 1340÷1375m on a mountain slope inclined between 12° and 16°. The mean annual precipitation, recorded at Cavalese (at an altitude of 990m, 4km South-West of Stava) was 820mm during the period between 1921-1987 (Fig. 2.38). During the first six months of 1985 when the disaster occourred, the precipitation was 465 mm, compared with the general mean value of 365mm, while in June 1985 the rainfall was 115mm, compared to a mean value of 98mm.

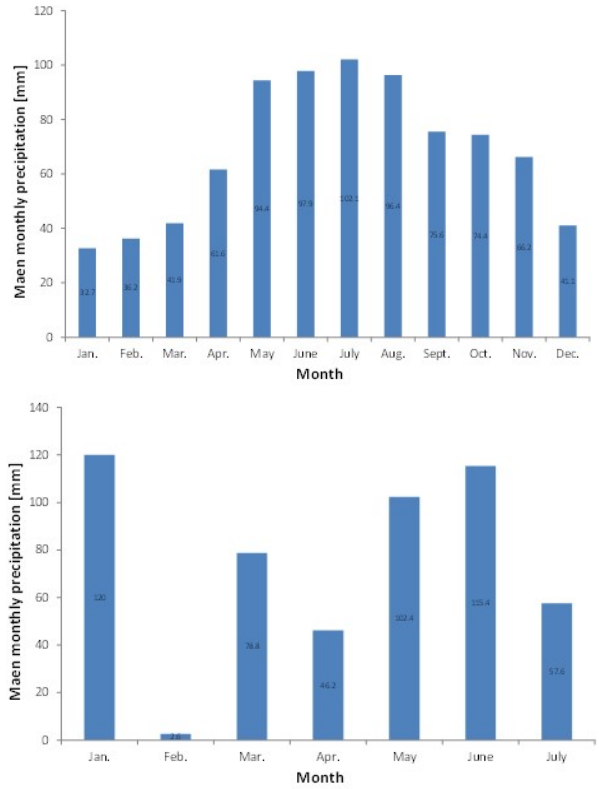

Fig. 2.38 - (a) Mean rainfall during 1921-1987 and (b) precipitation during 1985 (modified from Chandler and Tosatti, 1995).

The Stava tailing dams which lied on Pleistocene glacio-fluvial and moraine deposits of Wurn age. The slope deposits of the area, talus, landslide debris and alluvial fans, are more recent, while Holocene fluvial deposits are found along the main watercourses. The glacial deposits often directly underlie the more recent deposits (Chandler and Tosatti, 1995). According to Colombo and Colleselli (2003) and Berti *et al.* (1987), borings and geophysical investigation carried out in the area of the tailing storage facilities, show that tailing

embankment were constructed on glacio-fluvial deposits which are heterogeneous, with boulders, cobbles and gravel set in a finer matrix and have a thickness of 60÷70m.

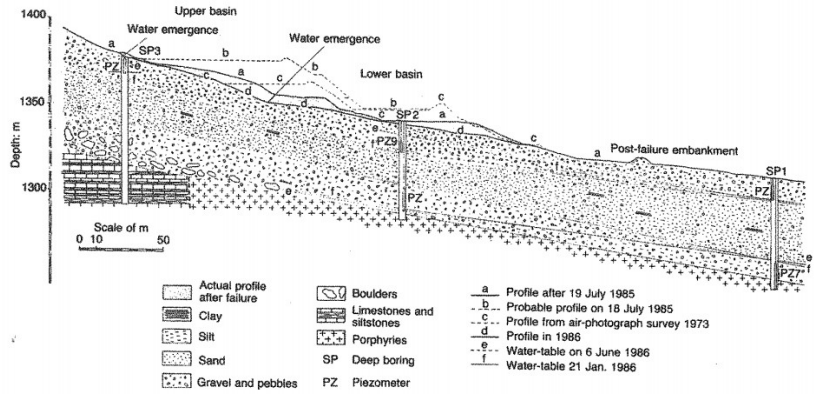

Fig. 2.39 - Geological section through Stava tailing dams (Chandler and Tosatti, 1995).

2.9.5 The event

At 12:22:55 on 19 July 1985 the front of the upper embankment collapsed accompanied by a "hollow rumble" that some eyewitnesses said sounded like a "strong blast of explosives being detonated" (Lucchi, 2002). The mudflow poured from the upper tailing dam into the lower basin which, in turn, collapsed triggering a flowslide consisting in more than 200000m^3. The mixture of water debris and sediments travelled down the Stava valley to speeds of 90km/h obliterating everything in its path for a stretch of 4.2km, until it reached municipality of Tesero and then it flowed into the Avisio river, as shown in Fig. 2.40.

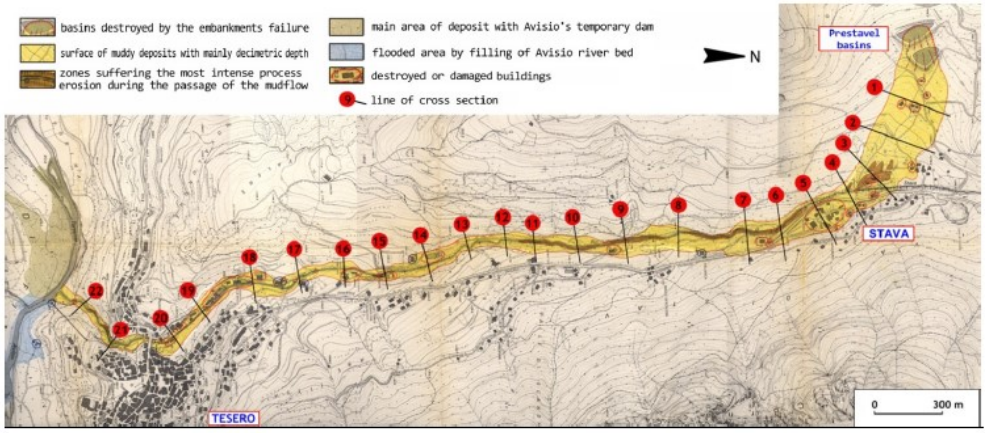

Fig. 2.40 - The mudflow paths along the Stava valley (modified from Govi and Luino, 2003).

This catastrophic mudflow killed 268 people, 100 people were injured while only 8 people rescued alive (Lucchi, 2002). It also caused damage valued at 133 milions euros (Lucchi, 2011): three hotels, fifty-three homes, eight bridges and six industrial buildings were destroyed, while nine more buildings were damaged. A layer of mud of 200÷400mm in thickness covered an overall surface of 4350000m^2. The time intervals during which the tailing dams collapsed were extimated from a seismogram recorded at the nearby Cavalese

station located 4.1km from the Prestavel storage facilities. The seismogram was used by Takahashi (1991) to estimate the velocity of the mudflow at different sections. In the same time, physical measurements of the velocity of the mudflow passage were carried out at certain points along the track by measuring the mudflow height on the external bank versus the internal bank at Stava where the mudflow entered a wide curve. The velocity ranged from 20m/s to 27m/s. There is a good agreement between these results and those calculated by Takahashi.

2.9.6 Causes of failure

According to Chandler and Tosatti (1995), many circumstances contributed to the failure of the Stava tailing dams. To explain the static liquefaction of the upper basin, many enquires have been performed. Results shown that tailing dams were raised in such a manner as to be only marginally stable due to the natural ground slope (about 15°) and the high slope of the basins between 34° and 39° (Colombo and Colosselli, 2003). In 1975, two stabilty analysis were performed by using Fellenius approach and considering the peak fricition angles extimated from triaxial tests carried on sandy fraction of the dams (assuming $\Phi = 35°$) and silty fraction of the basins (assuming $\Phi = 30°$). Even if at that time there was not any italian regulation aimed to give a minimum safety factor, the stability analysis were performed by refering to the guidelines published in the First International Tailing Symposium in 1972. A minimum safety factor equal to 1.5 was recommended for stability analysis concerning earth embankments. Stability analysis carried in 1975 (Fig. 2.41), shown only two sliding circles, 1 and 2 that involved the the upstream slime tailing (1) and the two dams (2).

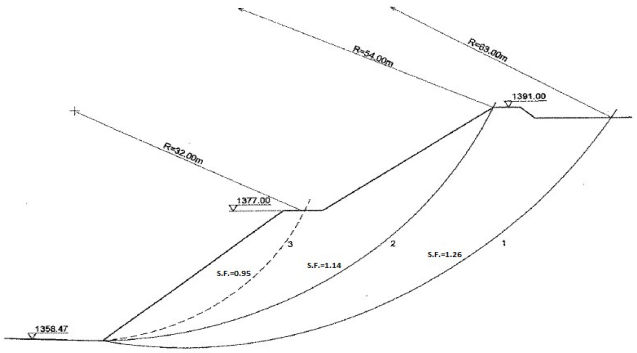

Fig. 2.41 - Stability analysis performed in 1975 (Ricceri, 2001).

Their safety factor were equal to 1.26 and 1.14, respectively, well below than 1.5. An other sliding circle (3) was obtained after the failure, in 1985, by appling the same geometry and geotechnical parameters. It would cross the lower basin with a safety factor equal to 0.95, showing an unstable slope already before the raising of the upper basin.
The fact that such an instable structure did not collapse before 1985 can be only due to stabilizing phenomena such as cementation, three dimensional effects or random causes not taken into account during the stability analysis (Colombo and Colosselli, 2003).
Observations after the disaster show a possible mechanism that is consistent with the events prior the failure and which can explain the failure itself. During the investigations it was noticed that at one place the decant pipe of the upper basin had a vertical section founded directly on the original ground surface. Enquires shown that, even if the original decant pipe had been laid below the ground surface, at an early stage of the filling of the upper basin, this pipe had become blocked. So a section of the pipe was replaced, using a length of steel pipe

laid on the surface of the tailing that had already been deposited, connected to a short vertical section that in turn was connected to the original decant pipe, as shown in Fig. 2.42.

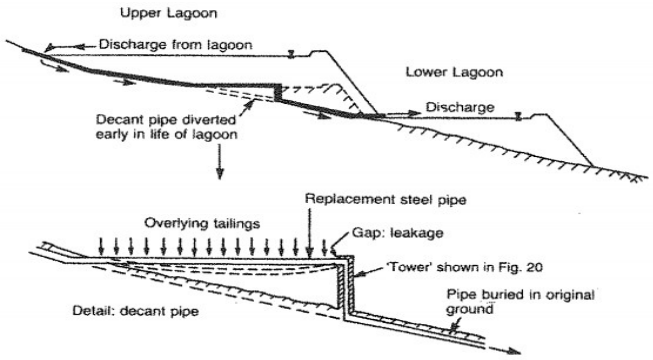

Fig. 2.42 - Hypotesys of events leading to decant pipe failure (Chandler and Tosatti, 1995).

The continuous deposition of tailing on the length of steel pipe would have caused it to sag because it was unsupported by the highly compressible tailing on which the pipe had been placed. As it sagged, it could have pulled out from one or both of the two ends of the concrete pipe to which it was attached, leaving a gap from which water could escape. Consequently, water escaped from the two ends of the pipe or, if the decant pipe was to become blocked towards its lower end when the pipe outfall froze, as happened in January 1985, water would back up in the pipe and would discharge from any cracks or gaps in the pipe. The low state of stability of the dam was such that it could not withstand the rise in water-levels generated by the leaking pipe, and probablly failed as a consequence. Summarizing, the main factors that keep high the level of phreatic surface leading to static liquefaction of the sand in the central part of the Upper dam which then involved the retained water and the stored silty tailing (Colombo and Colosselli, 2003), were supposed to be:

- rainfall during the six months before the disaster in 1985 was 465mm, compared to a mean value of 365 mm for the same six months from 1921-1987. In June 1985 the rainfall was 155mm, compared to the mean value of 98mm from 1921-1987;
- tailing dams were placed on sloping, soft and poorly drained ground with surface water and springs and so the mistaken assumption that the tailing deposited in the impoundments would consolidate fairly quickly;
- the hight pond levels resulted from surface run-off from the neighbouring hill slopes;
- the upstream construction lacked any form of underdrainage;
- the upper embankment was constructed partially over not-consoildated tailing deposited into the lower basin.

The final trigger that caused the sudden static liquefaction of the upper embankment (Carrera, 2008) and so the disaster, was supposed to be a consequence of the poor construction details of the upper decant pipe. It resulted in a repeated leak developed where the pipe was excessively deformed by the weight of the overlying tailing. The leak was certainly responsable for the minor failure occurred in January 1985 (Chandler and Tosatti, 1995). Thus, a repetition of the blockage of the decant pipe due to further leakages provides a good explanation for the static liquefaction of the upper dam and so the final failure.

REFERENCES

1. Alonso E.E. and Gens A. 2006. Aznalcollar dam failure. Part1: Field observations and material properties. Geotechnique **56**(3), pp. 165–183.

2. Berti G., Brauns J., Dovera D., Genevois R. and Villa F. 1987. Il crollo dei bacini di Stava nel Trentino: esame delle cause e proposte metodologiche di prevenzione. "Terra", n. 4, Pàtron Editore, Bologna, pp. 5-9.

3. Bjelkevik A. and Knutsson S. 2005. Swedish tailing comparison of mechanical properties between tailing and natural geological materials. Proceedings securing the future, International Conference on Mining and the Environment Metals and Energy Recovery, pp. 117.

4. Blight G.E. 1988. Some less familiar aspects of hydraulic fill structures, in Hydraulic Fill Structures, edited by D.J.A. Van Zyl and S.G. Vick, ASCE Geotech. Special Pub. No. **21**, pp. 1000–1064.

5. Blight G.E. 1994. The master profile for hydraulic fill tailing beaches. Proceedings of the ICE – Geotechnical Engineering **107**, pp. 27–40.

6. Carrera A. 2008. Mechanical behaviour of Stava tailing. Ph.D. thesis, Politecnico di Torino.

7. Carrera A., Coop M. and Lancellotta R. 2011. Influence of grading on the mechanical behaviour of Stava tailings. Géotechnique Vol. **61**(11), pp. 935–946.

8. Castiglia C. 2015. Aspetti costruttivi e gestione degli impianti. Proceedings of "La sicurezza dei riempimenti di terra: bacini di decantazione, colmate e discariche", 15-19 of July, Stava, Italy.

9. Chandler R.J. and Tosatti G. 1995. The Stava tailing dams failure, Italy, July 1985. Proceedings of the ICE – Geotechnical Engineering **113**, pp. 67–79.

10. Charles J.A. 1986. Hydraulic fills, colliery discard lagoons – review paper. Proceedings of the ICE Conference on Building on Marginal and Derelict Land. Thomas Telford, London, pp. 95–109.

11. Colombo P. and Colleselli F. 2003. The Collapse of the Stava Tailing basins. A review of scientific contributions on the Satva Valley disaster, ITALY. Pitagora editrice Bologna, pp. 335-358.

12. Davies M., Martin T. and Lighthall P. 2000. Mine Tailing Dams: When Things Go Wrong. Tailing Dams 2000. Association of State Dam Safety Officials, U.S. Committee on Large Dams, Las Vegas, Nevada, pp. 261–273.

13. Esposito T.J. 2000. Metodologia probabilística e observacional aplicada a barragens de rejeito construída por aterro hidráulico. Ph.D. thesis Universidade de Brasília.

14. Esposito, T., Assis, A. and Giovannini, M. 2010. Influence of the variability of geotechnical parameters on the liquefaction potential of tailing dams, International Journal of Surface Mining, Reclamation and Environment, **16**:4, 304-316.

15. Fell R., Mac Gregor P., Stapledon D., Bell G., Foster M. 2015. Geotechnical Engineering of Dams. CRC Press, Taylor and Francis Group Publishing, 1138 pp.

16. Fourie A.B., Blight G.E., Papageorgiou G. 2015. Static liquefaction as a possible explanation for the Merriespruit tailings dam failure. Ca. Geotech. J. **38**: 707-719

17. Genevois R. and Tecca P.R. 1993. The tailing dams of Stava (North Italy): an analysis of the disaster. In Environmental Management, Geo-water and Engineering Aspects (Choudhury P and Sivakumar A (eds)). Balkema, Rotterdam, pp. 23–36.

18. Govi M. and Luino F. 2003. La colata di fango di Stava (Trentino) del 19 luglio 1985, in: A review of scientific contributions on the Stava Valley disaster (Eastern Italian Alps), 19 July 1985, edited by: Tosatti, G., Pitagora Editrice Bologna, ISBN 88-371-1405-2, pp. 359–397.

19. ICOLD. 1982. Manual on Tailing Dams and Dumps, Bulletin 45.

20. ICOLD. 1996. A Guide to Tailing Dams and Impoundments - Design, construction, use and rehabilitation, Bulletin 106.

21. ISMES. 1985. Indagini geotecniche di laboratorio su materiali provenienti dai bacini Prestavel in località Stava - Tesero (TN), Final report.

22. Jamiolkowski M. 2013. Soil Mechanics and the observational method: Challenges at the Zelazny Most copper tailing disposal facility. Geotechnique, 64(8), pp.590-619.

23. Jennings J.E. 1979. The failure of a slimes dam at Bafokeng. Die Siviele Ingenieur in Suid-Afrika **21**(6): pp. 135–141.

24. Lucchi G. 2002. Stava perchè, 2nd Edition, edited by: Curcu & Genovese, Trento, 254 pp.

25. Lucchi G. 2011. L'attività mineraria in Val di Stava, in: Stava-Tesero la ricostruzione e La memoria, 1985–2010, Litotipografia Alcione, pp. 23–50.

26. Lucchi G. 2015. Genesi, cause e responsabilità della catastrofe del 19 luglio 1985 in val di Stava. Proceedings of "La sicurezza dei riempimenti di terra: bacini di decantazione, colmate e discariche", 15-19 of July, Stava, Italy.

27. Luino F. and De Graff J. V. 2012. The Stava mudflow of 19 July 1985 (Northern Italy): a disaster that effective regulation might have prevented. Nat. Hazards Earth Syst. Sci., **12**, pp. 1029–1044.

28. Martin T.E., McRoberts E.C. 1999. Some considerations in the stability analysis of upstream tailing dams. In proceedings of sixth International Conference on Tailing and Mine Waste '99, Fort Collins, Colorado, 24-27 January 1999. A.A Balkema Rotterdam, pp. 1- 17.

29. Mittal H.K. and N.R. Morgenstern. 1975. Parameters for the Design of Tailing Dams. Canadian Geotechnical Journal, Vol. **13**, pp. 277-293.

30. Mittal H.K. and N.R. Morgenstern. 1976. Seepage Control in Tailing Dams. Canadian Geotechnical Journal, Vol. **12**, pp. 235-261.

31. Monaco P. 2014. Overconsolidation and Stiffness of Venice Lagoon Sands and Silts from SDMT and CPTU. Journal of geotechnical and geoenvironmental engineering **140**(1): pp. 215–27.

32. Nelson J., Shepherd T. and Charlie W. 1977. Parameters affecting the stability of tailing dams. Proceedings of a Conference on Geotechnical Practice for Disposal of Solid Waste Materials, University of Michigan. American Society of Civil Engineers, New York, pp. 444–460.

33. Qiu Y. 2001. Laboratory properties of mine tailing. Canadian Geotechnical Journal **38**(1): pp. 183–190.

34. Rassam D.W. and William D.J. 1997. Shear Strength of Unsaturated gold tailings. In: Proceedings of the eigth Astralia-New Zeland conference on geotechnics, vol **1**. Hobart, pp. 329-335.

35. Ricceri G. 2001. Il crollo dei bacini di Stava. Istituto Universitario di Architettura di Venezia, Crolli e affidabilità delle strutture civili, **11** pp., 6-7, Venezia.

36. Rico M., Benito G., Salgueiro A.R., Díez-Herrero A. and Pereirac H.G. 2010. Reported tailing dam failures: A review of the European incidents in the worldwide context. Journal of Hazardous Materials. Volume **152**, Issue 2, pp. 846–852.

37. Ritcey, G.M. 1989. Tailing management. Elsevier.

38. Robertson P.K. and Campanella R.G. 1983. Interpretation of cone penetration test, Part 2, Clay. Canadian Geotech. J., Vol. **20**, No. 4, pp. 734–745.

39. Routh CD .1984. Civil engineering aspects of China clay and tungsten tailing. Conference on Materials for Dams, Monte Carlo, pp. 1–24.

40. Sarsby R. 2013. Environmental Geotechnics, ICE Publishing.

41. Shahid A. and Qiren L. 2010. Tailing Dam Failures: A Review of the Last One Hundred Years. Geotechnical News, pp. 50-53.

42. Sheng D., Zhou A. and Fredlund D.G. 2011. Shear Strength Criteria for Unsaturated Soils. Geotech Geol Eng, **29**, pp. 145-159.

43. Simeoni L. 2015. Piani di gestione e controlli: monitoraggio e controllo dei riempimenti di terra. Proceedings of "La sicurezza dei riempimenti di terra: bacini di decantazione, colmate e discariche", 15-19 of July, Stava, Italy.

44. Street A. 1987. The Portworthy china clay tailing disposal scheme. Proceedings of the ICE, Part 1 82: pp. 551–566.

45. Taylor R.K. and Cobb A.E. 1977. Mineralogical and geotechnical controls on the storage and use of British coal-mining wastes. Proceedings of the 9th ICSMFE, Tokyo, pp. 373–388.

46. Takahashi T. 1991. Debris flows, IAHR Monograph, Balkema, Rotterdam, pp. 92–99.

47. Vick S.G. 1990. Planning, Design and Analysis of Tailing Dams. BiTech Publishers Ltd.

48. Volpe R. and W.E. Kelly. 1985. Seepage and Leakage from Dams and Impoundments. American Society of Civil Engineers.

49. Wroth C.P. and Hughs J.M.O. 1973. An instrument for the in-situ measurement of the properties of soft clays. Proceedings of the 8th ICSMFE, Moscow, vol. **1**, pp. 487–494.

50. Zanardin M.T., Oldecop L.A., Rodriguez R. and Zabala F. 2009. The role of capillary water in the stability of tailing dams, Engineering Geology, **105**, pp.108-118.

3 Unsaturated soil response

3.1 OVERVIEW OF THE ROLE OF SUCTION ON THE HYDRAULIC BEHAVIOUR AND SHEAR STRENGTH OF SOILS IN UNSATURATED CONDITIONS

This section describes the main concepts regarding the hydro-mechanical behaviour of soil in unsaturated conditions.

3.1.1 The role of capillarity

If the water within a soil mass is subjected only to gravity force, the soil above the phreatic level would be in dry conditions, while it is saturated until a certain height and then, above that level, it is in unsaturated state. This is due to capillarity phenomena. Capillarity phenomena can be described with respect to a tube of small diameter: if this is placed into a box containing water (Fig. 3.1), one can observe a curved air-water meniscus and water rising into the tube until a certain height (h_c) that depends on the radius of the tube. The capillarity height can be expressed as (eq. 3-1):

$$h_c = \frac{2 \cdot T}{r \cdot \gamma_w} \cos\alpha \tag{3-1}$$

where T is the surface tension, r is the radius of the tube, α is the contact angle between meniscus and the vertical wall of the tube, γ_w is the unit weight of water. The ability of a fluid to raise a narrow tube against gravity is known as capillarity.

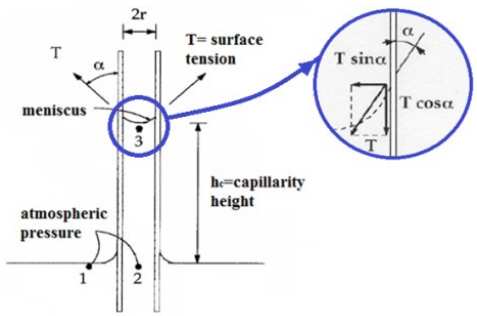

Fig. 3.1 - Capillarity rise into a glass tube.

Water pressure at point 1 and 2 (Fig. 3.1) is equal to the atmospheric pressure. Within the tube, it assumes negative values and at point 3 it is equal to the product $-h_c \cdot \gamma_w$. The concave shape of meniscus is due to air pressure (u_a), higher than water pressure (u_w).

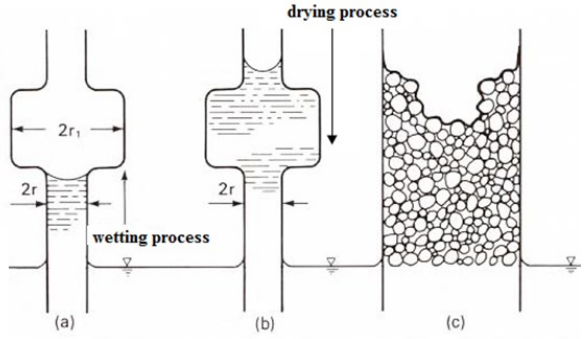

Fig. 3.2 - Capillarity height in different conditions (modified from Taylor, 1948).

The vertical component of the surface tension ($T \cdot cos\alpha$) leads a compression state of stress, while the horizontal component ($T \cdot sen\alpha$) leads a radial state of stress. The capillarity height cannot be reached if the height of tube is lower than h_c. Furthermore, if the radius of the tube is not constant, the capillarity height changes, depending on drying or wetting process. For instance, a tube having $r_1 > r$ limits the capillarity rise during wetting process (Fig. 3.2a), while the drying process is not lead by the bulb radius r_1, but by tube radius r (Fig. 3.2b).
If a mass of soil/tailings is considered instead a single narrow tube, the same phenomena will occur. Soils are random aggregates of particles and voids are complex systems of meandering channels with a large number of pore sizes. Therefore, many capillarity heights can be expected. Inside pores, water can rise from the phreatic level, reaching different heights so the soil will be saturated until a certain height and immediately above which it will be in unsaturated conditions. The degree of saturation decreases with height, depending on the distribution of pore size, which influences the capillarity height (Tab. 3.1) and so the thickness of the unsaturated zone.

Tab. 3.1 - Capillarity heights (modified from Lancellotta, 2004).

Soil	d_{10} [mm]	h_c [m]
Gravel	0.82	0.05
coarse sand	0.11	0.80
medium sand	0.03	1.60
fine sand	0.02	2.40
Silt	0.006	3.60
Clay	0.001	>10.00

3.1.2 Concept of suction

Soils above the phreatic surface have an affinity for water that, partially or fully, fill the voids within the pores. The affinity of soils for water is known as total suction (Ψ). The concept of suction was introduced from the early 1900s, but a general definition of soil suction and its components was given by Aitchison only in 1965. Defining p_p as the partial pressure of water vapour and p_s as the saturated water vapour pressure, the ratio (p_p/p_s) is the

relative humidity *RH* of the air in equilibrium with the pore water. The total suction Ψ can be defined as the total free energy of the soil water per unit volume. It is related to the relative humidity (*RH*) by Kelvin's law (eq. 3-2):

$$\Psi = -\frac{RT}{V_{mol}} ln\left(\frac{p_p}{p_s}\right) \tag{3-2}$$

where *R* is the universal gas constant (8.314J/mol·K), *T* is the absolute temperature (295K for laboratory conditions), V_{mol} is the molecular volume of water vapour (assumed constant and equal to $18m^3/mol$).
The total suction is the sum of two components (eq. 3-3), the matric suction (*s*) and the osmotic suction (π):

$$\Psi = \pi + s \tag{3-3}$$

Matric suction is usually assumed to be the main component of total suction in non-plastic and cohesionless soils with a pure pore fluid, while osmotic suction is appreciable in high plastic clays or in cases where the pore fluid contains dissolved salts (Blatz *et al.,* 2008).

Osmotic suction is a function of the difference in the salt concentration within the pore water from that of pure water, which presence gives raise to additional affinity for water of the soil. According to Van't Hoff (1887), the osmotic suction can be derived from (eq. 3-4):

$$\pi = iRTc \tag{3-4}$$

where *i* is the number of atoms which constitute the salt molecule (e.g. 2 for NaCl, 3 for $CaCl_2$) and *c* is the salt molar concentration.
The soil water above the phreatic surface, as previously described, is usually under a negative pore water pressure. Matric suction, which can arise thanks to the existence of surface tension at the water-air interface, (eq. 3-5) is defined as the excess of pore air pressure (u_a) over pore water pressure (u_w) and it becomes the negative pore water pressure - u_w at an atmospheric air pressure (u_a =0):

$$s = u_a - u_w \tag{3-5}$$

Matric suction is caused by two physical phenomena, the surface adsorption and the capillarity.
Surface adsorption is relevant for clay minerals because it occurs as a result of the attraction between the strong electrical forces around clay particles and water molecules. For instance, montmorillonite clay minerals can retain a relevant amount of water around their particles and remains saturated even at high suction levels, 10÷20MPa. Capillarity is related to the surface tension. The capillarity force, and thus the matric suction, are proportional to the curvature of the air-water meniscus. In unsaturated conditions, voids within soil are partially filled with water and air: this is possible due the presence of air-water interfaces (meniscus) made of water molecules. In field conditions, pore air pressure is usually equal to atmospheric pressure (u_a = 0) because the air voids are interconnected and connected to the atmosphere at ground level. So, the pore water pressure in unsaturated conditions, if compared to atmospheric pressure, is negative, giving the concave shape at the air-water meniscus.
The smaller the pore size of soil, the greater the curvature and the higher the water will rise within the soil channels above the phreatic surface channel (eq. 3-1). Considering the equilibrium of the forces acting on a infinitesimally element of air-water interface (Fig. 3.3),

according to Fisher (1926), eq. 3-6 gives the relation between matric suction (s), surface tension (T_s) and principal radii of curvature (r_1 and r_2) assumed positive if they are measured on the air side:

$$s = T_s\left(\frac{1}{r_1} + \frac{1}{r_2}\right) \tag{3-6}$$

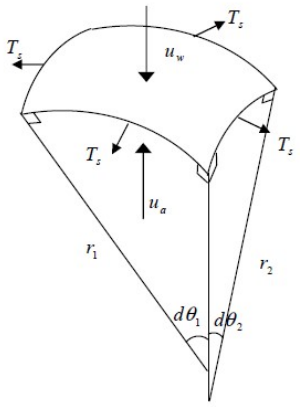

Fig. 3.3 - Forces acting on the air-water infinitesimally meniscus (Fredlund and Rahardjo, 1993).

Tab. 3.2 - Surface tension at different temperatures (modified from Fredlund and Rahardjo, 1993).

Temperature, T [°C]	Surface tension, Ts [mN/m]
0	75.70
10	74.20
15	73.50
20	72.75
25	72.00
30	71.20
40	69.60
50	67.90
60	66.20
70	64.40
80	62.60
100	58.80

3.1.3 The hydraulic behaviour of soils: general features

As stated before, soils are complex systems made of grains and voids creating of meandering channels with a large number of pore sizes. These channels having different dimensions can

be compared to capillarity tubes having different diameters, so many capillarity heights can be expected in the unsaturated zone above the phreatic level. In this zone, because of the different capillarity heights, the degree of saturation ranges between 0% and 100% depending on the suction level.
The hydraulic behaviour of unsaturated soil is usually expressed as the variation of the amount of water retained within the pore soil and suction. This relationship is named water retention curve as shown in Fig. 3.4. The water retention curve represents therefore a constitutive relationship between either degree of saturation S_r (or water content w, or volumetric water content θ) and suction s expressed in logarithmic scale.

$$\omega = \frac{W_w}{W_s}; \qquad S_r = \frac{V_w}{V_v}; \qquad \theta = \frac{\omega G_s}{1+e} = \frac{S_r e}{1+e} \tag{3-7}$$

where W_w, W_s, V_w, V_v, G_s and e represent the weight of water, weight of soil particles, volume of water, volume of voids, specific gravity of soil particles and void ratio, respectively. The amount of water retained within a soil at a given suction mainly depends on various factors, including grain size distribution, shape of pores, mineralogy of solid particles and others. If a soil volume at initial fully saturated condition undergoes an increase of suction, it will follow a drying process (A→C), so the water retention behaviour follows a unique curve (main drying curve) of variation of degree of saturation with suction. As supported also by thermodynamic considerations, if the suction is increased to about 10^6kPa, degree of saturation will become zero, independently from the soil type, pore size distribution or initial void ratio.

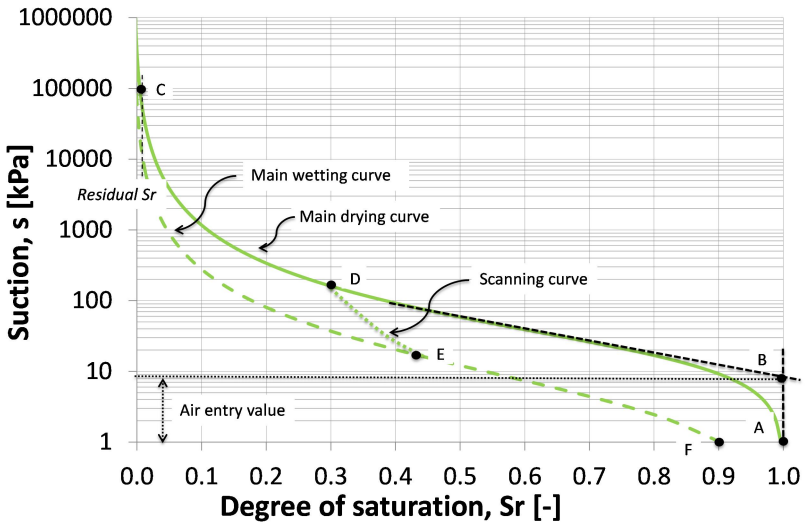

Fig. 3.4 - Water retention curve.

If the previous soil sample, from a dry state, undergoes a decrease of suction, it will follow a wetting process (C→E) by tracing another unique curve, known as main wetting curve.
If a soil sample is following a main drying or main wetting path and the suction variation is inverted, the water retention behaviour will traces the so-called scanning curve (D→E or E→D). The presence of different scanning curves during drying and wetting is known as hydraulic hysteresis. It is worth noting that infinite scanning curves can be obtained by starting at any specific saturation if the suction is increased or decreased, respectively and re-joining the main boundary curves. As shown in Fig. 3.4, the two main branches of the water retention curve have a shape similar to a sigmoidal function, an inflection point, a specific

value of suction known as air entry value (AEV) and a specific value of degree of saturation, named residual degree of saturation (Sr^{res}).
The AEV is the pressure required for air to fill the biggest soil pores during the drying process. The transition of suction from lower to higher values than the AEV means the transition of the soil from the saturated state to unsaturated conditions. Finally, the residual degree of saturation is defined as the minimum degree of saturation for the soil of concern.

3.1.3.1 Hydraulic models including main drying and main wetting curves

Many formulations have been proposed to model the hydraulic behaviour in terms of main wetting and main drying curves. Most of them have an empirical nature (i.e. Brooks & Corey 1964), while other models are based on the pore size distribution function and capillarity theory (i.e. Van Genuchten, 1980; Fredlund and Xing, 1994).
The model proposed by Brooks and Corey (1964) represents one of the simplest formulations because it requires the calibration only of the parameter *b* (eq. 3-8):

$$\begin{aligned} S_r &= 1 && \text{if } s < a \\ S_r &= \left(\frac{s}{a}\right)^{-b} && \text{if } s \geq a \end{aligned} \tag{3-8}$$

where *a* is the AEV of the soil. On the other hand, this model is not much flexible as others formulations and the discontinuity of the equation during the transition from suction values lower than AEV to suction values higher than AEV, gives rise to numerical instability if this formulation is implemented in some finite element code.
The model proposed by Van Genuchten (1980) allows to describe the entire range of suction by using a single expression (eq. 3-9):

$$S_r = \frac{1}{(1 + (\alpha s)^n)^m} \tag{3-9}$$

where *α*, *m* and *n* are parameters associated to the AEV of the soil, asymmetric shape of the water retention curve and rate of variation slope of the curve. Taking into account the residual degree of saturation, the effective degree of saturation S_e can be obtained:

$$S_e = \frac{S_r - Sr^{res}}{1 - Sr^{res}} \tag{3-10}$$

A modified version of Van Genuchten model relates the *m* parameter with *n* parameter (eq. 3-11):

$$m = 1 - \frac{1}{n} \tag{3-11}$$

In the current research work, the water retention curves will be modelled by using the simplified version of Van Genuchten equation. The advantages of this formulation are a good capability to fit the experimental data, an high flexibility and the absence of the discontinuity if compared to Brooks & Corey's model (Fig. 3-5). On the other hand, Van Genuchten formulation requires the calibration of three parameters instead of one.
Similarity to Van Genuchten, the model proposed by Fredlund and Xing (1994) requires the calibration of three parameters *a*, *m* and *n* (eq. 3-12), where *e* is the base of natural logarithms:

$$S_r = \frac{1}{\left(\ln\left(e + \left(\frac{s}{a}\right)^n\right)\right)^m} \tag{3-12}$$

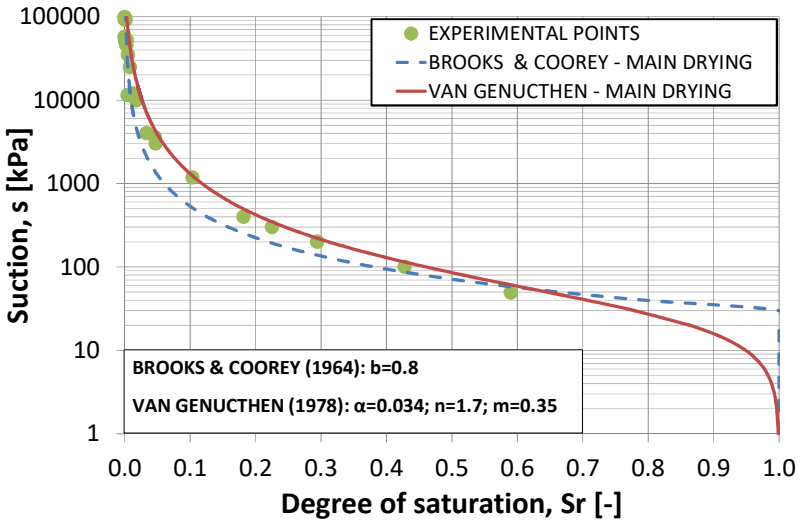

Fig. 3.5 - Comparison of water retention curves obtained by using Brooks & Corey equation or Van Genuchten equation on Stava silty specimen in water retention test.

3.1.3.2 Hydraulic model including variation in void ratio

The water retention behaviour of unsaturated soils is affected by mechanical behaviour so many Authors proposed additional formulations in order to incorporate mechanical parameters such as void ratio. Gallipoli *et al.* (2003a) proposed a modified version of the Van Genuchten equation, aimed to include the influence of the variation of the void ratio e on the hydraulic behaviour, so the soil constant α is replaced as follow (eq. 3-13):

$$\alpha = \Phi(v-1)^{\psi} \tag{3-13}$$

where Φ and Ψ are soil parameters and v is the specific volume $v = 1+e$. If eq. 3-12 is moved into eq. 3-9, Gallipoli formulation is given (eq. 3-14):

$$S_r = \frac{1}{(1 + [\Phi(v-1)^{\psi} s]^n)^m} \tag{3-14}$$

3.1.4 Stress variables for description of the mechanical behaviour of unsaturated soils

In describing the constitutive behaviour of unsaturated soils, the choice of appropriate stress-strain variables has a fundamental role. A possible combination of stress variables is given by the matric suction (s) and the net stress (p_{net}) assumed as the difference between the total stress and pore air pressure:

$$(s,\ p_{net})$$

Another possible pair of stress variables is given by the matric suction (s) and the effective stress (p'):

$$(s,\ p')$$

The consequence of variation in additional inter-particle normal force with suction is the increase of stability at contacts and many experimental evidences (e.g. Fredlund *et al.*, 1978) proved that, under the same confining/net stress, shear strength of unsaturated soil is higher than saturated soil. Different formulations for strength criteria can be found in the literature to predict the shear strength in unsaturated conditions. Some of these formulations are embodied on experimental data from triaxial or direct shear tests (Vanapalli *et al.*, 1996) and they generally contain material parameters because they are related to the water retention curve. These equations are usually based on two different hypothesis related to the role of suction and net stress: strength criteria based on Bishop stress variables and strength criteria based on independent stress variables.

3.1.4.1 Shear strength criteria based on Bishop approach

The shear strength formulation based on the Bishop approach was assumed to be governed by a single effective stress. Bishop and Blight (1963) suggested the following extension of the effective stress equation to unsaturated soils:

$$p' = p_{net} + \chi s = (\sigma - u_a) + \chi(u_a - u_w) \tag{3-15}$$

where σ is the total stress, p_{net} is the net stress assumed as the difference between the total stress and pore air pressure, while χ is a parameter related to the degree of saturation, to the soil structure and the way the actual degree of saturation has been reached (Lancellotta, 2008). For saturated conditions, this parameter is equal to 1 and eq. 3-15 reduces to effective stress proposed by Terzaghi. As for saturated conditions, the total stress can be obtained:

$$\sigma = \frac{\sigma_a + 2\sigma_r}{3} \tag{3-16}$$

where σ_a and σ_r are the axial and radial stresses, respectively. The group of shear strength formulations based on the Bishop approach are an extension of Terzaghi's effective stress equation for saturated soils:

$$\tau = c' + (\sigma - u_a)\tan\Phi' + \chi(u_a - u_w)\tan\Phi' \tag{3-17}$$

Many formulations were proposed for the evaluation of χ parameter, e.g. Jennings & Burland (1962) stated that χ parameter can be assumed as a function of the degree of saturation. Bishop (1959) suggested that the value of χ depends on the degree of saturation, on the soil structure and the cycle of wetting and drying. Very often the χ parameter has been assumed equal to degree of saturation:

$$\chi = Sr \tag{3-18}$$

Basing on their experimental shear strength data, Khalili and Khabbaz (1998) proposed an alternative evaluation of χ parameter:

$$\chi = 1 \qquad \text{if } (u_a - u_w) \leq (u_a - u_w)_b \tag{3-19a}$$

$$\chi = \left[\frac{(u_a - u_w)}{(u_a - u_w)_b}\right]^{-0.55} \qquad \text{if } (u_a - u_w) > (u_a - u_w)_b \qquad (3\text{-}19b)$$

where the term $(u_a\text{-}u_w)_b$ is the matric suction of the soil at which air begins to fill the pore voids of the soil (air entry value).
Defining the macropores as soil pores where capillary effects are the dominant phenomenon (Romero *et al*., 1999), Tarantino and Tombolato (2005) and Tarantino (2007) stated that the shear strength of an unsaturated soil can be related to the degree of saturation of the macropores Sr_M:

$$\chi = Sr_M = \frac{e_w - e_{wm}}{e - e_{wm}} \qquad (3\text{-}20)$$

where e is the void ratio, e_w is the water ratio (defined as the product between the void ratio and the degree of saturation) and the additional parameter e_{wm} is the microstructural water ratio that is related with the adsorbed water in the saturated aggregates:

$$e_{wm} = Sr^{res} e \qquad (3\text{-}21)$$

3.1.4.2 Shear strength criteria based on Fredlund approach

In 1978, Fredlund *et al.* suggested that the shear strength (τ) of soil under unsaturated conditions can be computed by using two independent stress variables, the matric suction s and the net stress p_{net} (eq. 3-22):

$$\tau = c' + (\sigma - u_a)\tan\Phi' + (u_a - u_w)\tan\Phi^b \qquad (3\text{-}22)$$

where c' is the effective cohesion intercept, Φ' is the friction angle associated with changes in net stress, while Φ^b is the friction angle associated with changes in suction. If plotted in the space τ, p_{net}, s the relationship expressed in eq. 3-22 has the shape shown in Fig. 3.6 and 3.7.
The friction angle associated with changes in suction is not a constant value because, when suction assumes high values the soil cannot physically have infinitive shear strength. Consequently the shear strength relationship with suction is not linear, so the friction angle Φ^b is assumed to change with suction and it could even become negative at high values of suction, also leading a decrease in the shear strength. Before suction reaches the air entry value (saturated conditions), the friction angle Φ^b is equal to Φ' but, when suction is higher than the air entry value (unsaturated conditions), the value of Φ^b would decrease to a value lower than of Φ' as the increasing of suction (Fig. 3.8). The reduction of Φ^b is also related to dilation of the soil sample during the shearing phase, as stated by Gan and Fredlund (1996). According to the strength criteria as proposed by Fredlund *et al.* (1978), soil volumes showing dilative behaviour, for instance those sheared at low net stress, show a greater reduction of Φ^b with suction than those having lower dilation, such as those sheared at high net stress (Fig. 3.8).

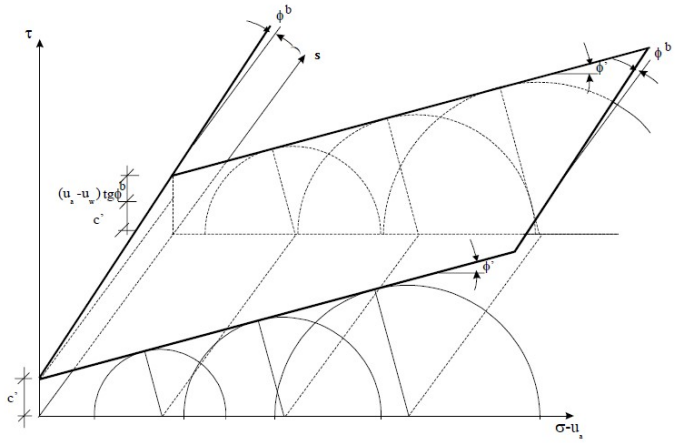

Fig. 3.6 - Extended Mohr-Coulomb criteria for low suction values in p_{net},s,τ plane (Fredlund *et al.*, 1978).

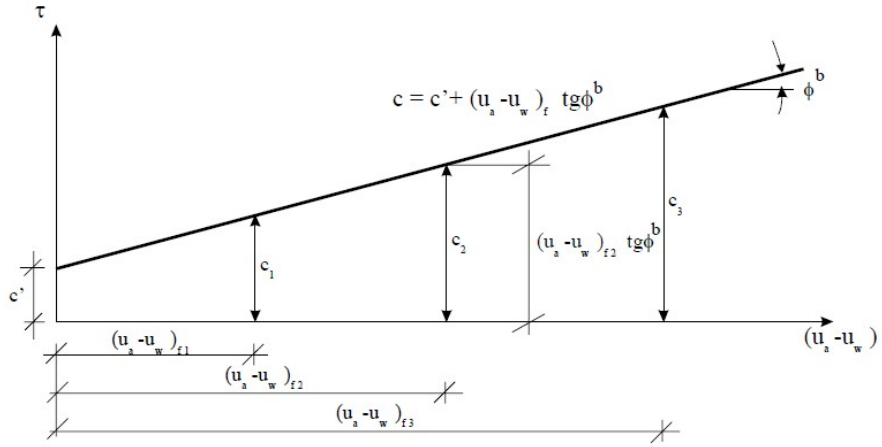

Fig. 3.7 - Extended Mohr-Coulomb criteria for low suction values in s,τ plane (modified from Fredlund *et al.*, 1978).

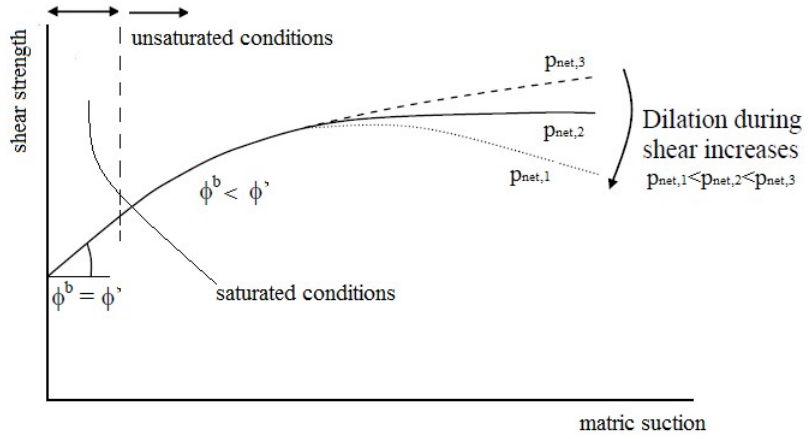

Fig. 3.8 - Shear strength versus matric suction (modified from Gan and Fredlund, 1996).

3.1.5 Coupling between mechanical and hydraulic behaviour: influence of void ratio on water retention curve

The hydraulic behaviour of a soil is usually influenced by its mechanical behaviour leading a coupling between hydraulic and mechanical behaviour, especially in terms of influence of void ratio (mechanical behaviour) on water retention curve (hydraulic behaviour). The main drying and wetting curves are strictly influenced by changes of void ratio. A variation of void ratio means a change in pore size distribution and this influences the hydraulic behaviour in terms of water retention curve. If the main drying curve is considered, an increase of void ratio, and so an increase of pores' size, will shift the water retention curve to lower suction range, so a lower suction is required to empty the pores is requested (Fig. 3.9).

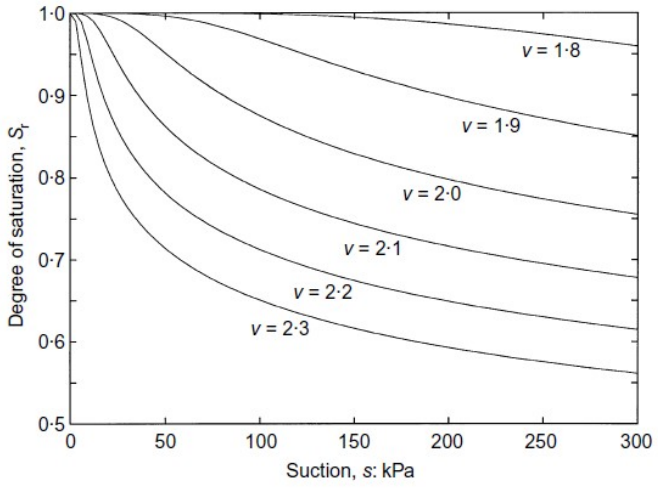

(a)

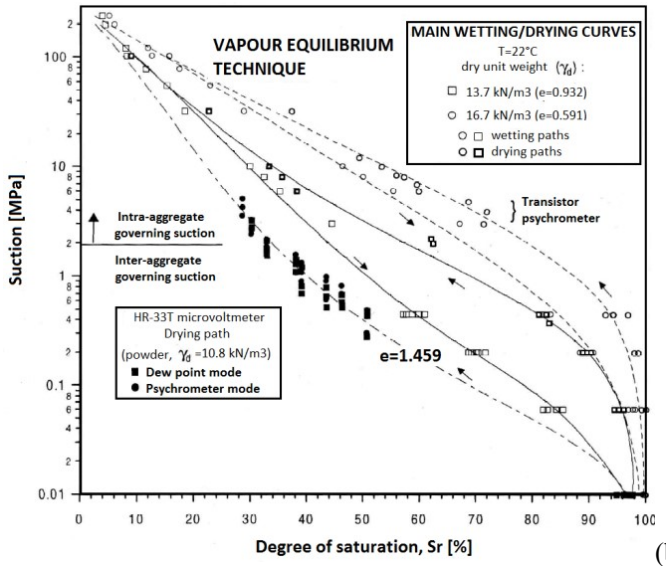

(b)

Fig. 3.9 - (a) Shifting of main wetting curves for different values of ν on compacted Speswhite Kaolin (Gallipoli *et al*., 2003) and (b) on kaolinitic-illitic compacted soil at different void ratio (modified from Romero, 1999).

3.2 EXPERIMENTAL TECHNIQUES ADOPTED IN THE PRESENT RESEARCH TO IMPOSE OR MEASURE SUCTION

This section describes the principles governing the experimental techniques adopted for the unsaturated hydro-mechanical characterization of Stava tailings performed in this research.

3.2.1 The axis translation technique

Developed and adopted for the first time by Hilff (1956), the axis translation technique is one of the most common method in experimental study of unsaturated soils because it allows an easy control and measurement of suction. The working principle of the axis translation technique can be represented using the model of a capillary pore as shown in Fig. 3.10 where a pore is subjected to atmospheric air pressure u_a (i.e. zero pressure) with the water climbing the capillary tube with negative water pressure u_w, less than atmospheric. If the capillary tube is closed and subjected to a large, positive air pressure u_a higher than atmospheric pressure, the system will respond as shown in Fig. 3.11 under the hypothesis (Olson and Langfelder, 1965) that the solid and water boundaries are sufficiently incompressible, so the curvature of the meniscus is not modified.

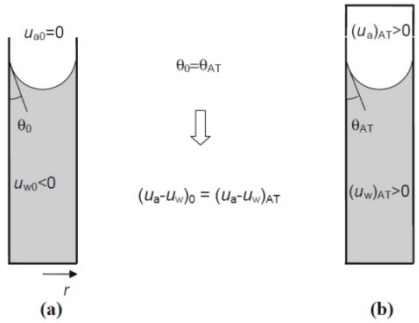

Fig. 3.10 - Principle of axis translation technique (Marinho *et al.*, 2008).

Under these assumptions, the water pressure within the capillary tube has now risen to measurable positive pressure, so the initial and final suction $u_a - u_w$ remains unchanged (Fig. 3.11). This technique is known as ‘‘axis translation technique’’ because water pressure has been shifted upwards with the air pressure origin, in order to prevent cavitation in water drainage systems.

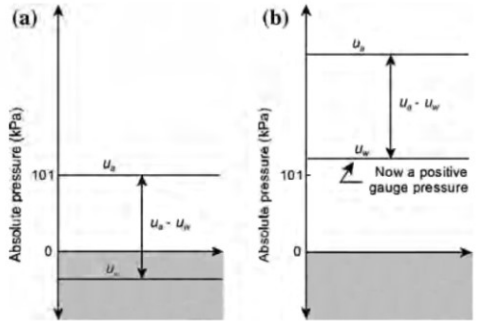

Fig. 3.11 - The axis translation technique: (a) atmospheric conditions and (b) axis translation (modified from Marinho *et al.*, 2008).

The same concept, valid for a capillary tube, is extended to pores of an unsaturated soil, where the total stress, pore water and air pressures are controlled independently. The total stress and the pore air pressure increase of the same amount, so the net stress remains constant, while the target suction is imposed by controlling the difference between pore air pressure and pore water pressure. In the current research, the different suction steps were imposed by controlling the pore water pressure, while the pore air pressure is kept constant and well above the atmospheric pressure. The water inside the sample and the water inside the measurement system are connected by using an high air entry value porous stone (HAEV). The high air entry value porous stone consists in a ceramic disc having an air entry value higher than the maximum applied matric suction in order to avoid the passage of air from the sample into the water drainages. Consequently the maximum air entry value and the maximum value of cell pressure limits the suction that can be imposed. A proper selection of the HAEV porous stone is also fundamental to minimize the time for equalization of the water pressure, because the lower the entry value, the higher the pressure ability and permeability of the ceramic disc. An example of the time required, for equalization of the water content *w,* obtained from a water retention test performed in the oedometer device, is given in Fig. 3.12. In this example two suction increment steps, by using axis translation technique, are shown.

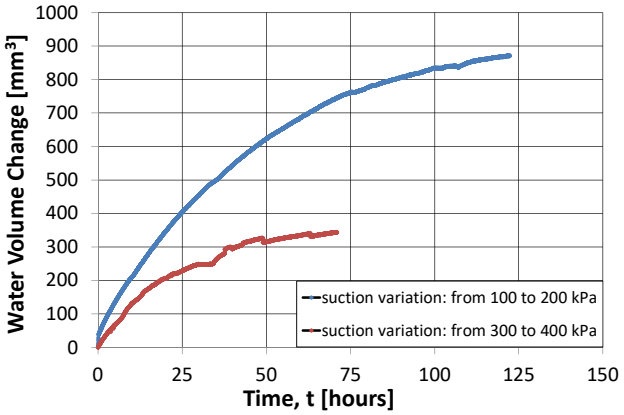

Fig. 3.12 - Example of time required for the equalization of water content within the soil specimen by using the axis translation technique in water retention test.

Ceramic discs having HAEV between 0.1MPa and 1.5MPa are usually used in oedometer and triaxial apparatuses. In the current study, the axis translation technique is used in suction control triaxial and oedometer cells in order to impose values of matric suction ranging between 10kPa and 400kPa even if, according to Romero (1999) and Sivakumar (1993) it can be used for suction from zero suction to values greater than 1.5MPa, depending on the adopted ceramic disc.

3.2.2 The vapour equilibrium technique

First used by Esteban and Saex (1988), the vapour equilibrium technique is a widespread method for controlling relative humidity (*RH*) and total suction in experimental studies of unsaturated soils. This method have been adapted for use with many laboratory tests including oedometer, direct shear and triaxial tests. In the current research the vapour equilibrium technique was used during the suction equalization phase with the suction controlled triaxial cell and to obtain water retention data at high suction levels.

In the vapour equilibrium technique the relative humidity of the air phase surrounding the specimen is imposed by controlling the composition of saturated salt or acid solution. These solutions, under isothermal conditions, have a defined chemical potential which imposes the equilibrium of the air with which they come in contact. The chemical potential is than "transmitted" by the air to the specimen, and is either measured in terms of relative humidity or suction. Figure 3.13a and Figure 3.13b show a sealed glass container with a porous support above the chemical solution, which suspends the unsaturated soil specimen in the chamber at controlled relative humidity.

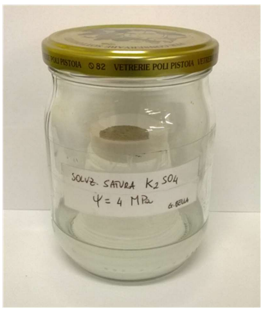

(a)

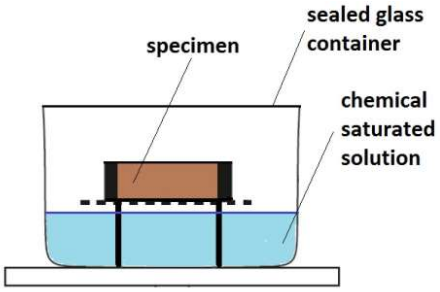

(b)

Fig. 3.13 - (a) Equipment used for vapour equilibrium technique and (b) schematic drawing.

The total suction within the unsaturated specimen is associated to a net water exchange between the liquid phase within the soil specimen and vapour phase in the headspace of a box, until vapour equilibrium between the two phases is achieved. During the transient phase, the soil sample can be extracted from the sealed chamber and weighted at regular intervals. An equilibrium condition is reached when the weight of the unsaturated sample remains constant, that means no further changes in suction and water content will occur. The relative humidity of the air, and in turn the corresponding total suction, depend on the molarity and concentration of the chemical solution. It is worth nothing that even small variations of *RH* (or temperature) can lead big errors in the imposed total suction, because of the non-linearity relationship between them.

In the current research, the relative humidity of air was controlled by using saturated salt solutions of K_2SO_4, KNO_3, $Ca(NO3)_24H_2O$, $NaNO_2$ in order to impose total suctions of 4MPa, 11MPa, 92MPa and 57MPa within the tailing specimens under relative humidity *RH* of 97%, 92%, 51% and 66%, respectively (Romero, 2001).

The vapour equilibrium technique is based on the relationship between total suction and relative humidity that can be represented by the psychrometric law (Fredlund and Raharadjo, 1993) given in eq. 3-23:

$$\psi = -\frac{\rho_w RT}{M_w} \ln\left(\frac{RH\%}{100}\right) \tag{3-23}$$

where ψ is the total suction, R is the universal gas constant (8.314K/mol·K), T is the laboratory absolute temperature (295K), RH is the relative humidity of air, ρ_w is the unit weight of water (1000kg/m^3) and M_w is the molecular weight of water (18.016kg/kmol).

The time required for equilibrium of specimen was more than one month, during which the weight of the tailing sample was constantly measured. An example of the equilibrium time need to achieve an equilibrium condition is given in Fig. 3.14.

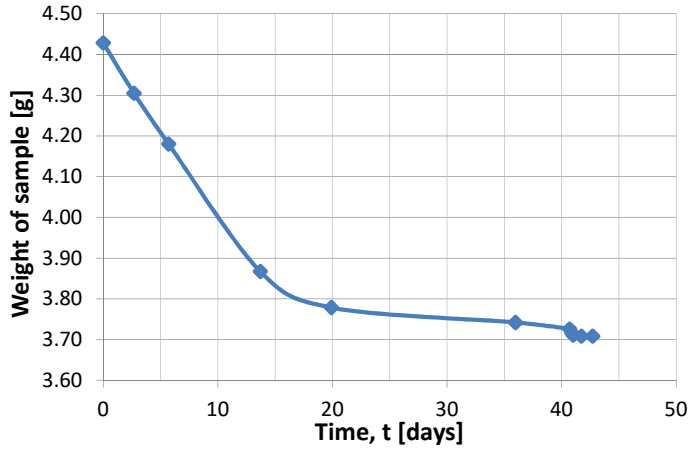

Fig. 3.14 - Water volume exchange with time.

3.2.3 The dew-point technique

The dew point technique allows measuring the relative humidity of a small specimen. In the current research the dew-point technique was adopted, together with the vapour equilibrium technique to obtain the water content-suction relationship in the high suction range. Measurement of total suction with the dew-point technique consists on equilibrating the liquid phase of the water within the unsaturated soil sample with the vapour phase of the water in the air space above the sample in a closed chamber, by measuring the relative humidity (Fig. 3.15). At equilibrium conditions, the relative humidity of the air in the chamber is the same as the relative humidity of the soil. The total soil suction ψ is measured from the partial vapour pressure (u_v) in equilibrium with the soil water, relative to the saturated vapour pressure (u_{v0}) at the same temperature in equilibrium with pure water. This latter two pressures u_v and u_{v0} are related to the relative humidity ($RH = u_v/u_{v0}$) by applying the psychrometric law.

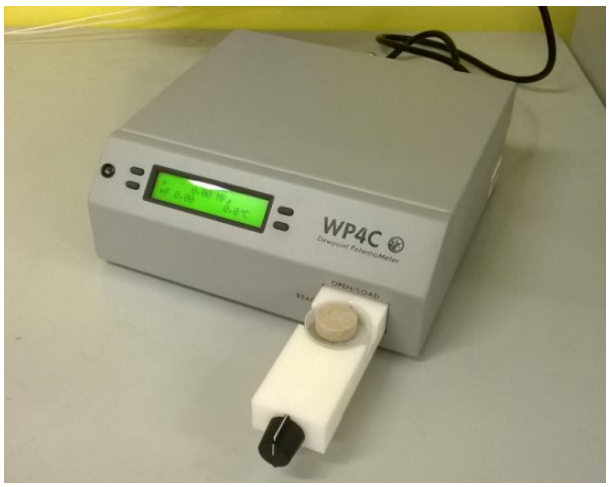

(a)

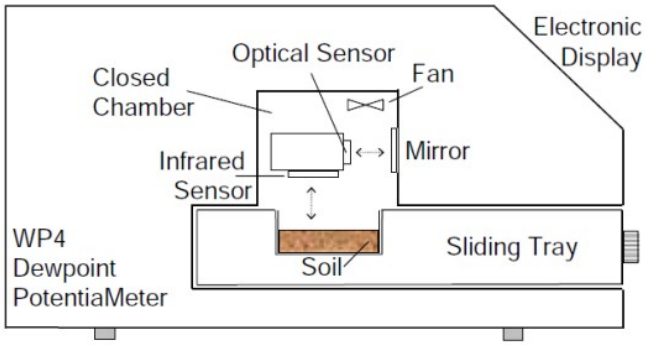

(b)

Fig. 3.15 - (a) The WP4C Dew Point Potentiameter and (b) its schematic drawing (Bulut *et al.*, 2002).

A cooling system is used to cool a mirror until dew forms. An optical sensor is used to detect the dew formed on the mirror, while a thermocouple attached to the mirror measures the dew point temperature. In the meantime, the temperature of the unsaturated specimen is measured with an infrared thermometer. A fan is also used to circulate the air in the sensing chamber and speed up vapour equilibrium. Both the soil sample temperature and the dew point are employed to obtain the relative humidity above the soil sample and so its total suction by applying the psychrometric law (eq. 3-37).
The chilled-mirror psychrometer used in this research is known as WP4C Dew Point Potentiameter and the investigated suction levels range from 1MPa to 150MPa, with an equilibrium time equal to 15-30 minutes. For each step, the weight of the soil sample after the suction reading was measured in order to associate the current suction value to its corresponding water content and degree of saturation.

REFERENCES

1. Bishop A.W., Blight G.E. 1963. Some aspects of effective stress in saturated and partly saturated soils. Geotechnique 13: pp. 177–197.

2. Blatz J.A., Cui Y.J. and Oldecop L. 2008. Vapour Equilibrium and Osmotic Tecnnique for Suction Control. Geotechnical and Geological Engineering Vol. 26(6), pp. 661-673.

3. Brooks R.H. and Corey A.T. 1964. Hydraulic properties of porous media. Hydrology Paper No.3, Colorado State Univ., Fort Collins.

4. Bulut R, Hineidi S.M. and Bailey B. 2002 Suction measurements - filter paper and chilled mirror psychrometer, Proceedings of the Texas Section American Society of Civil Engineers, Fall Meeting, Waco, 2-5 October.

5. Esteban V. and Saez J. 1988. A device to measure the swelling characteristics of rock samples with control of the suction up to very high values. Proc. ISRM Symposium on Rock Mechanics and Power Plants, Madrid, Vol. 2.

6. Fisher R.A. 1926. On the capillary forces in an ideal soil: correction of formulae given by W. B. Haines. J. Agric. Sc. Vol. 16(3), pp. 492–505.

7. Fredlund D.G., Morgenstern N.R. and Widger R.A. 1978. The shear strength of unsaturated soils. Canadian Geotechnical Journal, Vol.15, pp. 316-321.

8. Fredlund D.G. and Rahardjo H. 1993. An Overview of Unsaturated Soil Behaviour, Proceedings of ASCE Specialty Series on Unsaturated Soil Properties, Dallas, TX, pp. 1-31.

9. Fredlund D.G and Xing A.Q. 1994. Equations for the soil–water characteristic curve. Canadian Geotech. Journal, Vol. 31(4), pp. 521–532.

10. Gallipoli D., Wheeler S.J., Karstunen M. 2003. Modelling the variation of degree of saturation in a deformable unsaturated soil. Geotechnique, 53, 1: pp. 105–112.

11. Gan J. K.M. and Fredlund D.G. 1996. Shear strength characteristics of two saprolitic soils. Can. Geot. J. 33, pp. 595-609.

12. Hilf J.W. 1956. An investigation of pore-water pressure in compacted cohesive soils", Ph.D. Dissertation, Technical Memorandum No. 654, United State Department of the Interior Bureau of Reclamation, Design and Construction Division, Denver, Colorado, USA.

13. Khalili N., Khabbaz M.H. 1998. A unique relationship for the determination of the shear strength of unsaturated soils. Geotechnique 48(5): pp. 681–687.

14. Lancellotta R. 2008. Geotechnical Engineering. Taylor & Francis Group.

15. Lancellotta R. 2004. Geotecnica. Bologna, Zanichelli.

16. Marinho F.A.M., Take W.A. and Tarantino A. 2008. Geotechnical and Geological Engineering, Volume 26, No. 6, 615–631.

17. Olson R.E. and Langfelder L.J. 1965. Pore-water pressure in saturated soils. ASCE J Soil Mech Found Div SM4: 127–150.

18. Romero E. 1999. Characterisation and thermo-hydromechanial behavior of unsaturated Boom clay: an experimental study. Ph.D. thesis, Universitat Politecnica de Catalunya.

19. Romero E., Gens A and Lloret A. 1999. Water permeability, water retention and microstructure of unsaturated compacted Boom clay. Engng Geol. 54, No. 1-2, pp. 117-127.

20. Romero E. 2001. Controlled-suction techniques. 4° Simposio Brasileiro de Solo Nao Saturados. W.Y.Y. Gehling & F. Schnaid (eds.). Porto Alegre, Brasil: 535-542.

21. Sivakumar V. 1993. A critical state framework for unsaturated soils. PhD Thesis, University of Shffield.

22. Tarantino A., Tombolato S. 2005. Coupling of hydraulic and mechanical behaviour in unsaturated compacted clay. Geotechnique, 55, 4: pp. 307–317.

23. Tarantino A. 2007. A possible critical state framework for unsaturated compacted soils. Technical Note, Geotechnique, Vol. 57(4), pp. 385-389.

24. Taylor D.W. 1948. Fundamentals of soil mechanics. New York, J. Wiley, 1948.

25. Vanapalli S.K., Fredlund D.G., Pufahl D.E. and Clifton A.W. 1996. Model for the prediction of shear strength with respect to soil suction. Canadian Geotechnical Journal, Vol. 33, pp. 379–392.

26. Van Genuchten M.T. 1980. A closed-form equation for predicting the hydraulic conductivity of unsaturated soil. Soil Sci. Soc. Am. J. Vol. 44, pp. 892–898.

27. Van't Hoff J.H. 1887. Die Rolle des osmotischen Druckes in der Analogie zwischen Losungen und Gasen. Zeitschr. physikal. Chem. Vol.1, pp. 481-508.

4 Material characterization and gamma ray treatment

4.1 GEOTECHNICAL CHARACTERIZATION OF STAVA TAILINGS

The starting point of the present study is an available hydro-mechanical characterization performed by Carrera (2008). The soils investigated in the current research are the same studied by Carrera in saturated conditions. Soil samples proceed from the lower portion of the upper Stava tailing dam. Geotechnical index properties of tailings used to raise the embankments and stored inside the basin are given in Tab. 4.1 in terms of d_{50}, d_{10}, d_{90} and specific weight *Gs*.

Tab. 4.1 - Geotechnical index properties of silty and sandy fraction (ISMES, 1986 and Carrera, 2008).

Material	d_{50} [mm]	d_{10} [mm]	d_{90} [mm]	Gs [-]
Sandy fraction	0.200	0.080	0.350	2.721
Silty fraction	0.025	0.003	0.070	2.828

Figure 4.1 (a) gives the grain size distribution of Stava tailings performed by ISMES in 1985, showing a good separation between the fraction of tailings that seemed to be part of the embankment and finer ones that seemed to be deposited inside the storage facility. Figure 4.1(c) shows the grain size distribution of Stava tailings performed by Carrera in 2008 of the same material. The coarse fraction (sandy tailings), not passing through the 0.074mm sieve, was analysed by sieving technique, while the grain size distribution of the finest fraction (silty tailings with 8% in weight of clay) was obtained through sedimentation, according to ASTM D422. The mineralogy is also influenced by the anthropic and recent origin of the Stava tailings. All particles are made of hardly breakable minerals typical of sands rather than of clay because the natural rock crushing and alteration processes leading creation of mineral typical of clay had no time to develop. The fine particles are (e.g. clay and silty fraction) are generated by the anthropic crushing processes, so they are constituted by minerals typical of sands and for these reason, the term clay should be used as a grain size property rather than behavioural (Carrera, 2008).

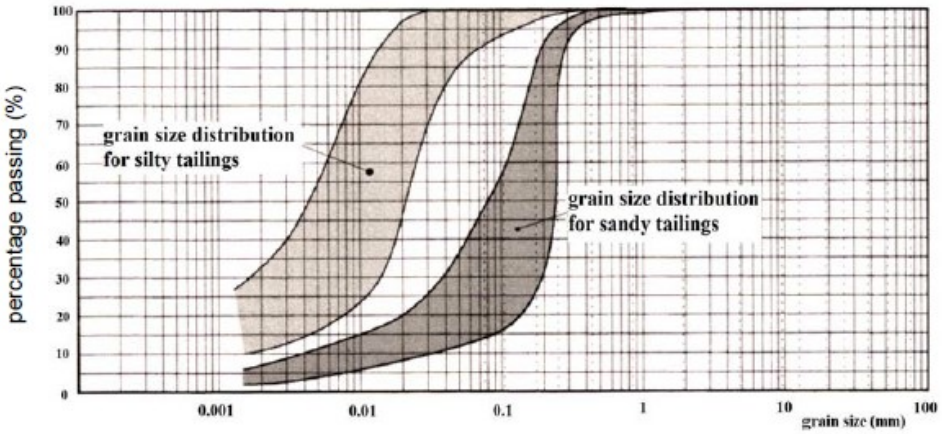

(a)

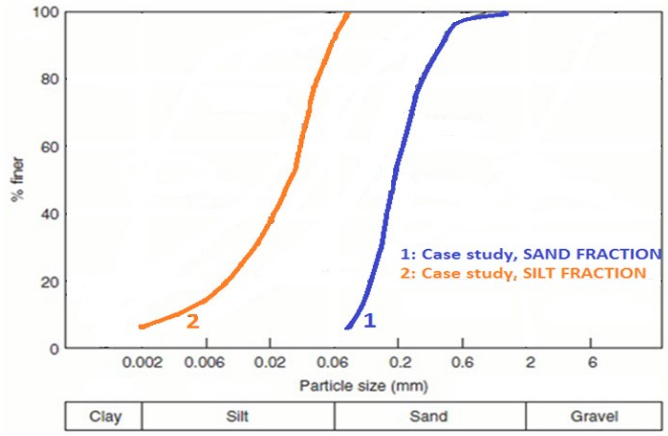

(b)

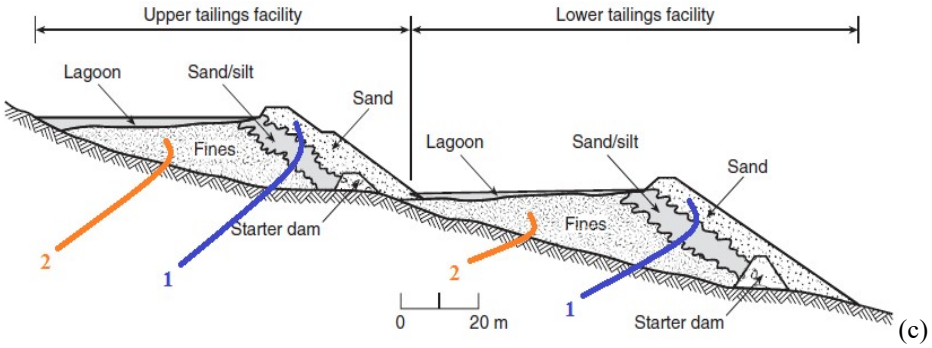

(c)

Fig. 4.1 - (a) Grain size distributions of Stava tailings by ISMES (1985). (b) Grain size distributions obtained by Carrera (2008) compared with grain size distributions of other tailings having different mineralogical compositions. (c) Location of tailing fraction investigate din the current research (modified from Sarsby, 2013; Luino and De Graff, 2012).

Liquid and plastic limits of the silty fraction (Tab. 4.2) obtained by ISMES (1985) and Carrera (2008) show that it can be defined as an inorganic clay with medium-low plasticity and compressibility (Fig. 4.2). The maximum void ratio (e_{max}) and the minimum void ratio (e_{min}) of the sandy fraction were determined by Carrera (2008) measured using the ASTM D425 and ASTM D4254 procedures.

Tab. 4.2 - Geotechnical index properties of silty and sandy fraction (ISMES, 1985 and Carrera, 2008).

Material	w_L [%]	w_P [%]	PI [%]	Gs [-]	e_{min} [-]	e_{max} [-]
Sandy fraction	-	-	-	2.721	1.068	0.615
Silty fraction	27.4	18.0	9.4	2.828	-	-

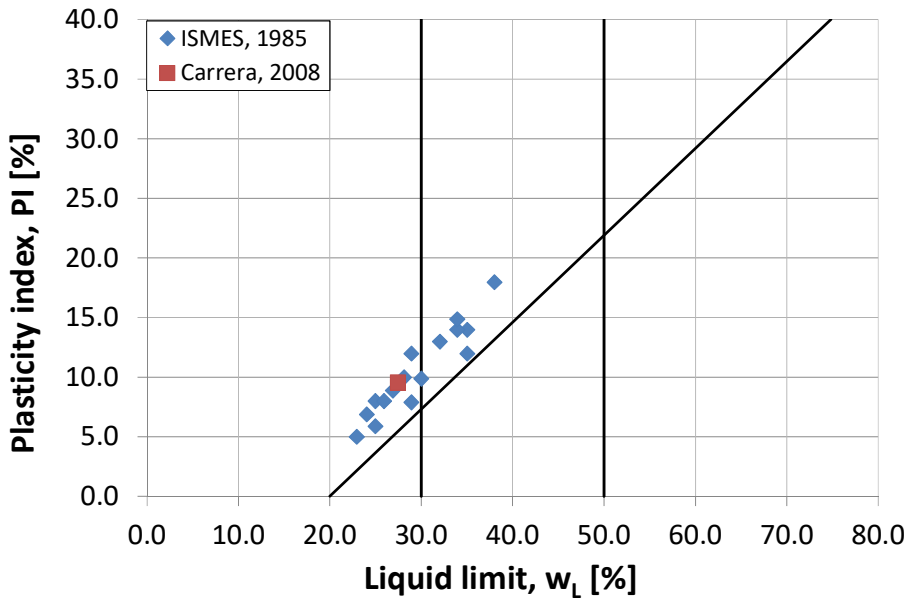

Fig. 4.2 - Comparison between plasticity evaluated by ISMES (1985) and Carrera (2008).

An X-ray diffraction analysis on sandy and silty fractions was carried out in 1985 by ISMES. Principles of this technique are recalled in Appendix. Both fractions were predominantly made of quartz, with significant amount of calcite and fluorite. As expected, because of the same source, the mineral composition for the two grading is the same even if with percentages little bit different. The silty fraction contain much kaolinite than the sandy fraction that shows more quartz, calcite and feldspar.

A second X-ray diffraction analysis with the "powder method" on Stava tailings was carried out in 2015 at Politecnico di Torino (Tab. 4.3).

Tab. 4.3 - Percentages of minerals in silty and sandy fractions.

Mineral/Sample	Silt	Sand
magnetite	-	11%
quartz	36.4%	70%
feldspars K	Traces	Traces
feldspars Na	-	Traces
calcite	11.9%	6%
fluorite	47.8%	2%

Figure 4.3 shows the corresponding spectra on silty and sandy fraction obtained in 2015.

Comparing X-ray analysis carried out in 1985 by ISMES (1985) and X-ray analysis carried out in the current work in 2015, can be observed that Stava tailings show a certain chemical stability. Except for quartz concentration, no appreciable variations in calcite and fluorite concentration can be appreciated from sandy specimen. Except for quartz concentration, same considerations can be made for silty specimens. These little differences could only be due to heterogeneity of the Stava tailings within the basin, and so a little chemical heterogeneity of the tested specimens.

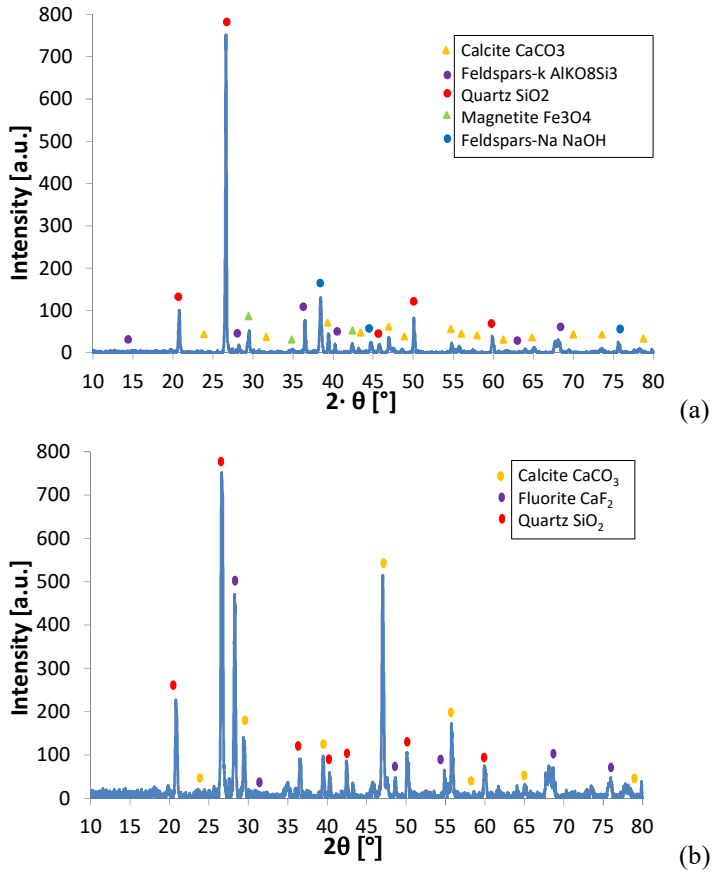

Fig. 4.3 - X-ray diffraction spectra from sandy (a) and silty (b) fraction.

4.2 GAMMA RAY TREATMENT AND PHYSICAL/CHEMICAL CHARACTERIZATION OF STAVA TAILINGS

After describing the main long-term processes acting on tailing materials, this chapter introduces another long term process affecting tailing materials: it consists in the natural ionizing radiation from radioactive isotopes of the soils, cosmic rays and ultraviolet rays from the sun. So, a gamma ray treatment is proposed in order to simulate the ionizing radiations on the surface of tailing deposits, or in the tailing brick faces used for buildings or other economical purposes. Finally, the results of physical-chemical characterization tests carried out at Centro de Desenvolvimento da Tecnologia Nuclear in Belo Horizonte (Brazil) before and after the gamma ray treatment are presented and discussed in order to study the influence of ionizing radiations on the chemical/physical properties of tailings.

4.2.1 Long term processes acting on tailings: literature review

After their deposition, mineral wastes can experience aging processes with chemical and physical variations depending on the interactions between source mineralogy and local conditions. These aging processes can lead oxidation processes. Furthermore, in many countries, tailings are beginning to be re-used as backfill, landscaping material or feedstock for cement, bricks, aggregate in road construction or feedstock for cement and concrete pavings, especially in Brazil, USA, Canada, China, India and Australia, as shown in Fig. 4.4 (Esposito *et al*., 2014). Long-term physical, chemical and geotechnical properties of tailings need to be understood in detail in order to approach engineering problems related to this man-made materials, i.e. stability analyses of tailing embankments or re-usage of tailings for economical purposes.

(a) (b)

Fig. 4.4 - Example of re-usage of tailings: a brick (a) and a civil structure (b) made of iron tailings (Esposito *et al*., 2014).

Few studies concerning simulation of long-term processes on tailings can be found in the literature, sometimes with contrasting results (Tarazona, 2015). Troncoso *et al*. (1988) investigated the cyclic resistance on aged copper tailing samples by means of cyclic triaxial tests. They found that cementation between particles can increase the cyclic liquefaction resistance of tailings much than 250% over 30 years.

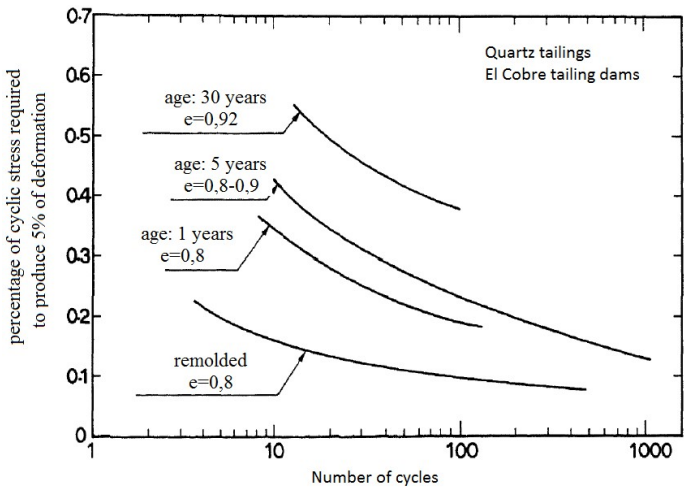

(a)

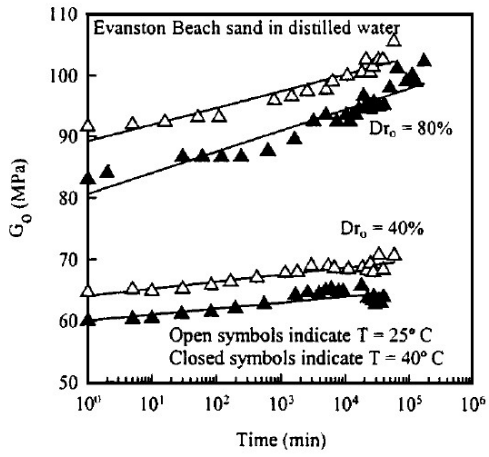

(b)

Fig. 4.5 - (a) Cyclic triaxial tests show an increasing of liquefaction resistance (modified from Troncoso *et al.*, 1988) and (b) changes of shear modulus at small strains with time. Tested material was the Evanston Beach sand in distilled water at two relative densities and temperatures (Baxter and Mitchell, 2004).

The results of cyclic triaxial tests on the 30,5 and 1 years old quartz tailing samples are shown in Fig. 4.5a in terms of cyclic stress ratio (ratio of amplitude of cyclic axial stress to twice the initial confining stress) required to obtain 5% double amplitude axial strain. In 2014, Larrahondo and Burns performed some triaxial tests in order to simulate the increased interlocking of particles in order to evaluate the shear strength of sandy tailing wastes. They have shown that cementation of particles leads to an increasing of the friction angle at critical state. Craw *et al.* (1999) and Devasahayam (2007) carried out chemical tests on tailings samples after drying, wetting and oxidation processes for 4 years, obtaining some chemical and mineralogical variations. Other experimental investigations on sandy soils show improvements with time due to aging process (Mitchell and Solymar, 1984; Schmertmann, 1987; Mesri *et al.*, 1990, Baxter and Mitchell, 2004) by showing increase of shear modulus G (Daramola, 1980, Schmertmann, 1991, Pender et al., 1992), also at small strains, G_0 (Afifi and Woods, 1971; Anderson and Stokoe, 1978; Baxter and Mitchell, 2004 as shown in Fig. 4.5b), penetration resistance (Joshi *et al.*, 1995 as reported in Fig. 4.6) and liquefaction resistance (Seed, 1979; Ishihara, 1985).

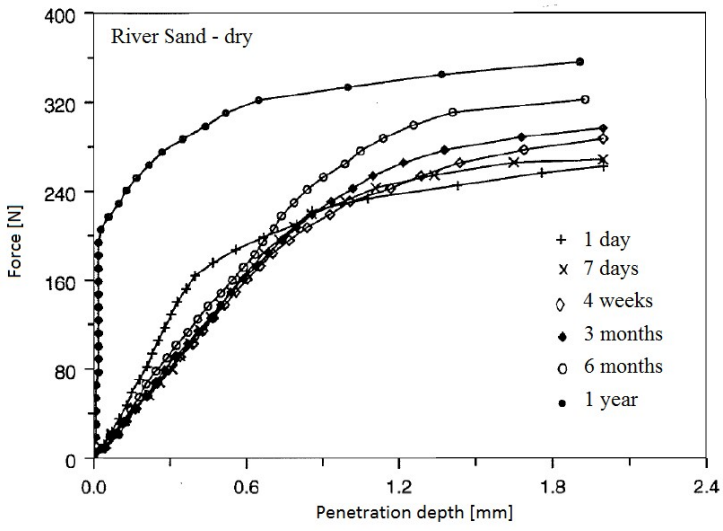

(a)

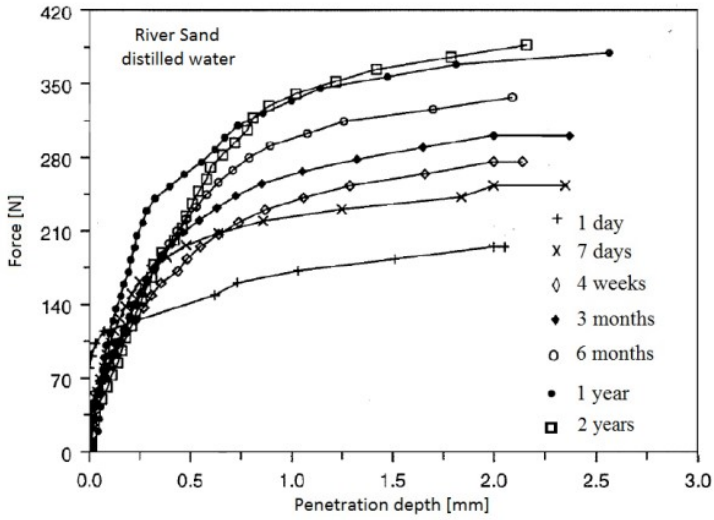

(b)

Fig. 4.6 - Aged River Sand in (a) dry and (b) wet conditions. It is evident an increasing penetration resistance with time (modified from Joshi *et al.*, 1995).

Despite an increasing number of researches showing properties improvements, there are other field studies (Baxter, 1999; Jefferies *et al*. 1988; Charlie *et al*. 1992; Jefferies and Rogers, 1993) and laboratory tests i.e. Human (1992), Miller (1994), Baxter and Mitchell (2004, Fig. 4.7) in which no significant aging effects were shown.

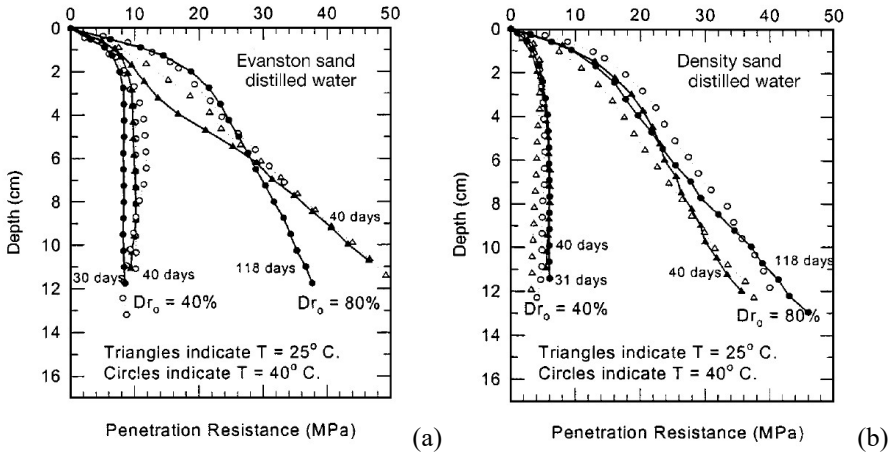

Fig. 4.7 - Results of minicone penetration tests for (a) Evanston and (b) Density sand samples. No appreciable increase of penetration resistance with time is shown (Baxter and Mitchell, 2004).

4.2.2 Gamma ray treatment

4.2.2.1 Why a gamma ray treatment?

Among the long-term processes, the natural ionizing radiation from radioactive isotopes of the soils, cosmic rays and also ultraviolet rays from the sun, can be considered, as proposed in the current research. Several minerals contain potassium in their composition, which is composed of 0.01% of ^{40}K, a natural occurring isotope that emits beta rays and gamma rays. On the surface of tailings deposits or in the tailings bricks faces used for constructions, the minerals are exposed to cosmic rays and ultraviolet rays. The energy of these radiations are absorbed by the minerals by displacing electrons from their original positions in the crystal structure of minerals. In the long-term these radiations may trigger alterations of the materials due to its ionizing character. Aimed to study the effects of natural ionizing radiation and so its influence on physical and chemical properties especially on tailings containing potassium, Stava silty tailings were exposed to gamma ray treatment, here proposed as an innovative technique to accelerate the natural ionizing radiation. The gamma ray treatment was performed at Centro de Desenvolvimento da Tecnologia Nuclear (CDTN), in Belo Horizonte (Brazil) between January and April 2016. Dry and wet Stava samples were exposed to gamma rays from a ^{60}Co source up to a dose of 1000kGy in order to simulate the natural long term ionizing process in two extreme cases: dry conditions if tailings are used for bricks, wet conditions for tailings deposited within the storage facility. Finally, before and after the gamma ray treatment, Stava silty tailings were characterized by means of chemical and physical test in order study the influence of ionizing radiations on their chemical/physical properties.

4.2.2.2 Gamma irradiation facility

The source of gamma ray used in the current study is the radionuclide Cobalt-60, also referred to Co-60 or $^{60}_{27}Co$. It represents the most widspread source of gamma ray radiation, both for medical and industrial purposes. Cobalt-60 is produced starting from natural pure cobalt that is a rare transition metal element with 100% abundance of the stable isotope, Cobalt-59, also named Co-59 or $^{59}_{27}Co$. Small cylinders made up of pure cobalt are welded in

Zircaloy capsules and put into a nuclear power reactor for 18÷24 months (Gilmore, 2008), in order to obtain unstable radionuclide Cobalt-60 atom by absorbing a neutron *n*:

$$^{59}_{27}Co + n \rightarrow {}^{60}_{27}Co \quad (4\text{-}1)$$

$$^{60}_{27}Co \rightarrow {}^{60}_{28}Ni + e^{-} + \gamma \quad (4\text{-}2)$$

After irradiation into nuclear power reactor, the capsules containing the $^{60}_{27}Co$ cylinders are encapsulated in corrosion resistant stainless steel to produce the source pencils which represents the building blocks of a radiation rack and then placed into a gamma irradiation facility. Unstable Cobalt-60 then transforms to a stable nuclide of Nickel-60, by decaying according to Fig. 4.8a and nuclear equation:

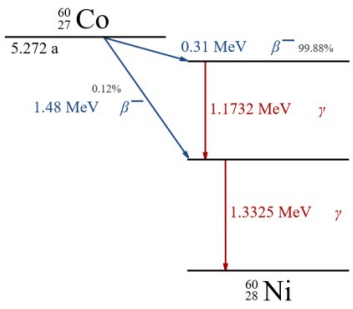

(a)

(b)

Fig. 4.8 - (a) Decay scheme of Cobalt-60 (Gilmore, 2008) and Shielded room inside the irradiation facility at CDTN Institute.

First, a neutron decays to a proton with the emission of electrons (β^{-}rays). An amount of 99.88% of β^{-} rays has an energy of 0.31MeV, while 0.12% has an energy of 1.48MeV. Two gamma-rays are immediately emitted: one with 1.1732MeV and the other one with 1,3325MeV in order to reach the stable state of non-radioactive isotope $^{60}_{28}Ni$. So, Stava samples have been irradiated with 50% of gamma-rays with 1.1732MeV and 50% of gamma-rays with 1.3325MeV.

The main components of every irradiation facility, as well for CDTN's facility, are:

- irradiation room;
- shielded storage room;
- source hoist mechanism;
- control room;
- radiation shield surrounding the irradiation room;
- control and safety interlock system;
- control room.

The irradiation room is the place where the material is irradiated and represents the focal point of the facility. It is surrounded by concrete wall 2m thick in order to attenuate the radiation emanating from the source. When the facility is not working, it is placed into an underground pool 6m depth. Water has some good characteristics as a shielding material: it is an easily available transparent fluid and it is convenient to circulate for heat transfer. For dry stationary irradiator as CDTN facility, the radiation source is moved from an underground chamber after the product containers have been placed there for the treatment.

The irradiations, in a panoramic multipurpose gamma irradiator, category II, from MDS Nordion, model IR-214 BG-127, was equipped with a ^{60}Co gamma source, dry storage, with maximum activity of 2200TBq or 60000Ci. Samples were attached on the wall of the cylindrical gamma source as shown in Fig. 4.8b. Finally, Tab. 4.4 summarizes the irradiation conditions.

Tab. 4.4 - Gamma irradiation conditions.

Irradiation time	7 days
Exposure dose	1000kGy
Distance to the gamma source	0cm
Gamma source	^{60}Co
Photon energy	1.17 ÷ 1.33MeV
Frequency of gamma photon	$2.83\times10^{20} \div 3.22\times10^{20}$Hz
Temperature	Irradiation chamber temperature (about 60°C)

4.2.2.3 Computation of sun-exposure time

The correspondence between sun-exposure time and gamma ray-exposure time adopted in the current research is now given. Frequency υ_γ of gamma-rays may be calculated from Plank equation:

$$E_\gamma = h\nu_\gamma \tag{4-3}$$

where E_γ is the photon energy and h is the Planck constant ($4.136\cdot10^{-15}$eV·s):

$$E_\gamma = 1.3325\ \text{MeV} \rightarrow \nu_\gamma = 3.222\cdot10^{20}\text{Hz} \tag{4-4a}$$
$$E_\gamma = 1.1732\ \text{MeV} \rightarrow \nu_\gamma = 2.837\cdot10^{20}\text{Hz} \tag{4-4b}$$

The intensity (I_{sun}^{UV}) of ultraviolet radiation from the sun on earth surface is (Steinhilber *et al.*, 2012):

$$I_{sun}^{UV} = 250\cdot10^{-6}\frac{\text{W}}{\text{cm}^2} \tag{4-5}$$

The power P_γ emitted by the gamma-rays source is given by:

$$P_\gamma = A_\gamma E_\gamma \tag{4-6}$$

where A_γ is the activity of gamma-rays source and E_γ is the photon energy. Gamma-rays activity of Cobalt-60 source is A_γ = 30000Ci, (1Ci corresponds to $3.7\cdot10^{10}$ disintegrations of Cobalt-60 nuclei per second), while in the current study the average photon energy E_γ was 1.3MeV. Gamma-rays power P_γ was so obtained:

$$P_\gamma = A_\gamma E_\gamma = 30000\times3.7\times10^{10}s^{-1}1.2\times10^{6}\text{eV} = 13.2\times10^{20}\text{eVs}^{-1} \tag{4-7}$$

By considering the following equivalence:

$$1\ \text{eV} = 1.60 \cdot 10^{-19}\text{J} \tag{4-8}$$

gamma-rays power P_γ can be rewritten as:

$$P_\gamma = 2.13 \times 10^2\text{W} \tag{4-9}$$

The energy intensity I_γ of gamma source can be computed as the ratio between gamma-rays power the area of the cylindrical source:

$$I_\gamma = \frac{P_\gamma}{\pi \Phi h} \tag{4-10}$$

Gamma-rays source used at CDTN was a cylinder having diameter $\boldsymbol{\Phi}$ = 20cm and height h = 100cm, so:

$$I_\gamma = \frac{2.13 \cdot 10^2}{\pi \cdot 20 \cdot 100} = 3.39 \cdot 10^{-2}\,\frac{\text{W}}{\text{cm}^2}$$

By comparison between gamma-rays intensity and ultraviolet intensity:

$$I_\gamma \cong 136 \cdot I_{sun}^{UV} \tag{4-11}$$

the energy density ρ_γ can be computed from gamma-rays exposition time t_γ (hours) as follow:

$$\rho_\gamma = I_\gamma t_\gamma \tag{4-12}$$

Stava sample was exposed 7 days to gamma irradiation, so the energy density was:

$$\rho_\gamma = 3.39 \cdot 10^{-2} \cdot 7 \cdot 24 = 5.7\,\frac{\text{Wh}}{\text{cm}^2} \tag{4-13}$$

Similarity to eq. 4-13, for UV-sun exposure can be applied:

$$\rho_{sun}^{UV} = I_{sun}^{UV} t_{sun}^{UV} \tag{4-14}$$

An equivalent energy density $\rho_{sun}^{UV} = \rho_\gamma$ needs UV-sun esposition time t_{sun}^{UV} (hours):

$$t_{sun}^{UV} = \frac{\rho_{sun}^{UV}}{I_{sun}^{UV}} = \frac{5.7}{250 \cdot 10^{-6}} = 22400\text{h} \cong 2.6\text{years} \tag{4-15}$$

Now we have to consider the interactions of ionizing radiation with matter. As previously shown, gamma rays interact with matter in three ways: photoelectric effect, Compton scattering, and pair production. On the other side, UV-rays interact with matter mainly by the photoelectric effect. The ionizing activity of gamma radiation in matter is equal to 50÷500ions/cm. A value of about 50ions/cm is considered since, due to photoelectric effect, electrons with even 1.2÷1.3MeV energy are emitted and interact with matter by ionization or Bremsstrahlung. The specific ionization for UV-rays, is about 1÷2ions/cm. In order to obtain a good estimation $t_{sun,est}^{UV}$ of the corresponding UV-ray exposure time, we have to multiply t_{sun}^{UV} by at least 25, giving:

$$t_{sun,est}^{UV} = t_{sun}^{UV} \cdot 25 \cong 70 \text{ years} \quad (4\text{-}16)$$

This latter quantity $t_{sun,est}^{UV}$ is the real sun-exposition time and it is equivalent to the gamma-ray exposition t_γ imposed during the irradiation test at CDTN. Summarizing, use of gamma ray allows to simulate and, of course accelerate, the long term process consisting in the interaction of UV ray with matter. In one week, gamma radiation allows to simulate what usually happen during 70 years of exposure to UV-rays, with a frequency ν_{sun}^{UV} about 10^{16}Hz.

4.2.3 Physical and chemical characterization before and after the gamma ray treatment

Physical and chemical modifications of the Stava silty specimen were investigated by means of several characterization analysis performed before and after the gamma ray treatment.
In the current research the silty fraction of the Stava tailings passing through sieve ASTM n°200 was tested. A sample of 1kg of silt, labelled "not irradiated", was oven dried at 120°C for 24 hours and then characterized, as shown in Tab. 4.5. From not irradiated sample, a second sample, 500g weigh (labelled "dry irradiated" sample), was obtained and then treated by means gamma irradiation in the form of loose, dry material and then characterized (Tab. 4.5). A third sample, 500g weight (named "wet irradiated" sample), was obtained from not irradiated sample and irradiated and then characterized as (Tab. 4.5) in wet conditions by means of adding a quantity of deionized water corresponding to the liquid limit in order to obtain a slurry.

Tab. 4.5 - Characterizations performed on the tailing samples.

Property	Technique	Equipment
Grain size distribution	Laser diffraction	Cilas, model 1190
Electronic microscopy	SEM	Carl Zeiss, model VP
Energy dispersive X-ray spectroscopy	EDS	Bruker, model XFlash 4.0
Particle morphology	Image analysis	Quantikov*
Particle density	Helium pycnometry	Quantachrome, model Ultrapycnometer
Specific surface and pore diameter	N_2 adsorption	Quantachrome, model NOVA 2000
Chemical analysis	Infrared spectroscopy	ABB Bomem, model MB102
	X-ray fluorescence	
Mineral composition	X-ray diffractometry	Rigaku, model D\MAX\ULIMA**

* Software developed by Pinto (1996).
** XRD spectra were collected with Cu-Kα radiation and data collected with 2θ in the range of 20°-80°.

Due to the fact that, in many countries tailings are beginning to be re-used as backfill, landscaping material or feedstock for cement and concrete, the long-term chemical and physical properties need to be understood in order to approach engineering problems related to this man-made materials, i.e. their re-usage for economical purposes. If any, the long-term physical and chemical modifications could affect the hydro-mechanical behaviour of the tailings with relevant economic consequences.
Physical characterization analysis performed in the current research before and after the gamma-ray treatment, consist in the determination of: grain size distribution by laser technique, particle morphology by means of image analysis, particle density by means of helium pycnometry test, specific surface by N_2 adsorption test. If any, modifications in grain

size distribution, particle morphology or specific surface could modify the hydro-mechanical behaviour of the studied tailings in terms of permeability or shear strength.
Any chemical and mineralogical modifications before and after the gamma ray treatment were investigated by means of chemical characterization tests. The mineral composition was studied by X-ray diffraction test, while the chemical composition was investigated by means of X-ray fluorescence tests, infrared spectroscopy tests and electronic microscopy.

4.2.3.1 Particle size distribution by laser diffraction

Results in terms of grain size distribution are shown in Fig. 4.9, Fig. 4.10 and Fig. 4.11 for all samples, before and after gamma-ray irradiation. As shown in Fig. 4.9 and Fig. 4.10, a variation in grain size distribution of silt fraction can be observed on the same sample, before and after dry or wet gamma-ray irradiation. Before and after the gamma ray treatment, it is possible to note four modal distributions. In both cases, after irradiation test, grain size distribution is shifted to the left and this means an increasing amount of smallest particles. This increase after irradiation process, corresponds to an equal decrease of the biggest particles. In both dry and wet irradiated samples, it is evident a decrease of peak corresponding to particles having 35μm diameter, counterbalanced by an uplift of peak corresponding to particles having 16μm and 4μm diameter. These results can lead to argue that one of the effects of gamma-ray irradiation, and so of ageing in terms of sun-exposure, consist into a breaking of some particles. In Fig. 4.11, a comparison in terms of grain size distribution after gamma-ray irradiation of dry and wet samples, is shown. As can be noted, the two lines are completely overlapped and this means the same effects are documented for both dry and wet conditions.
The volume of each fraction can be computed as the area below the plot and above the horizontal axis, in a certain grain size of interest (Fig. 4.12, Fig. 4.13, Fig. 4.14). Considering situation before and after irradiation of dry silt sample, Fig. 4.9 shows a 3.2% volume decrease of particles having size comprised between 19μm and 100μm. The same amount is related to an increase of particles comprise between 0.5μm and 10μm. Taking into account size before and after irradiation of wet sample, Fig. 4.14 shows a 3.0% volume decrease of silt particles having size comprise between 19μm and 100μm. The same amount is related to an increase of particles comprises between 0.4μm and 10μm. These little variations in grain size distribution, both for dry irradiated samples and for wet irradiated samples, are no relevant from a geotechnical point of view since are well below the expected heterogeneity of the deposit. Furthermore, variations ranging between 3%÷4% would not significantly influence the water retention curve, hence they have no appreciable effects on the hydraulic and mechanical behaviour of the soil. It is worth to note that “not irradiated samples” consist in tailings collected in 2005 and tested in 2016, while the Stava failure occurred in 1985. So the “not irradiated samples” have been exposed for about twenty years to natural solar radiations before being stored and tested 11 years later. Hence, it is not possible to predict the entity of physical/chemical variations of dry/wet irradiated samples if the tested material would be the original silty fraction before its first natural exposure. Indeed, possible variations could have been developed from 1985 to 2005 under the natural solar irradiation, already making the soil more stable from a chemical-physical point of view.

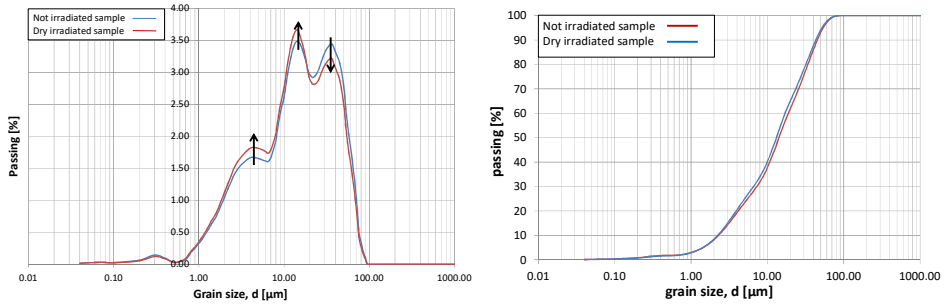

(a) (b)

Fig. 4.9 - (a) not cumulative and (b) cumulative grain size distribution: not irradiated Vs dry irradiated sample.

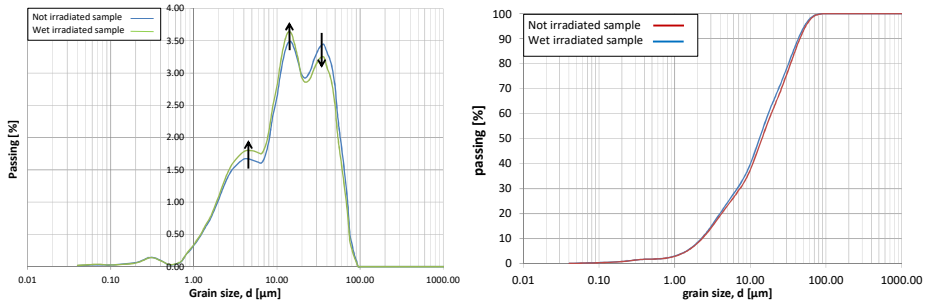

(a) (b)

Fig. 4.10 - (a) not cumulative and (b) cumulative grain size distribution: not irradiated Vs wet irradiated sample.

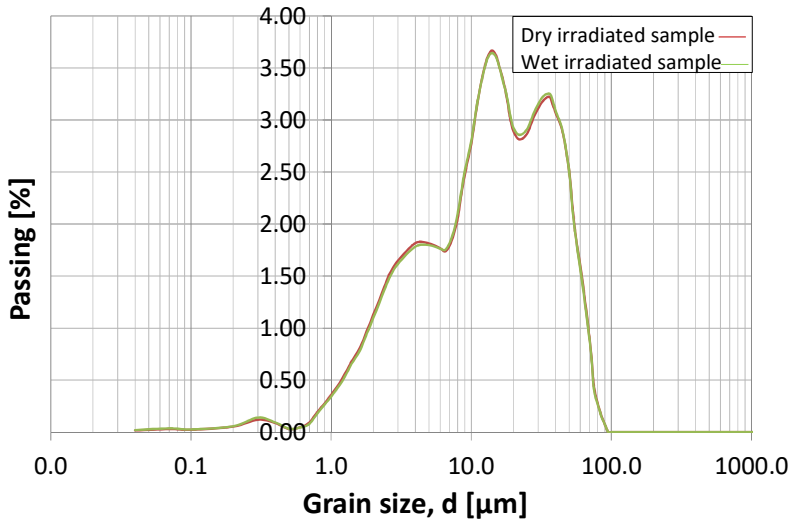

Fig. 4.11 - Grain size distribution: dry irradiated Vs wet irradiated sample.

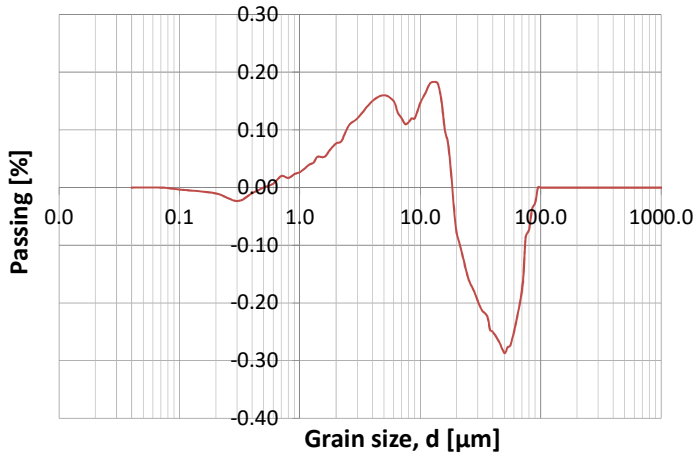

Fig. 4.12 - Difference between not irradiated and dry irradiated grain size distribution.

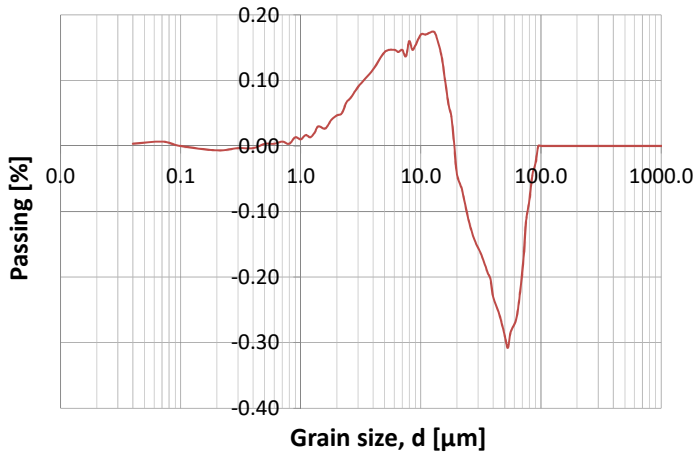

Fig. 4.13 - Difference between not irradiated and wet irradiated grain size distribution.

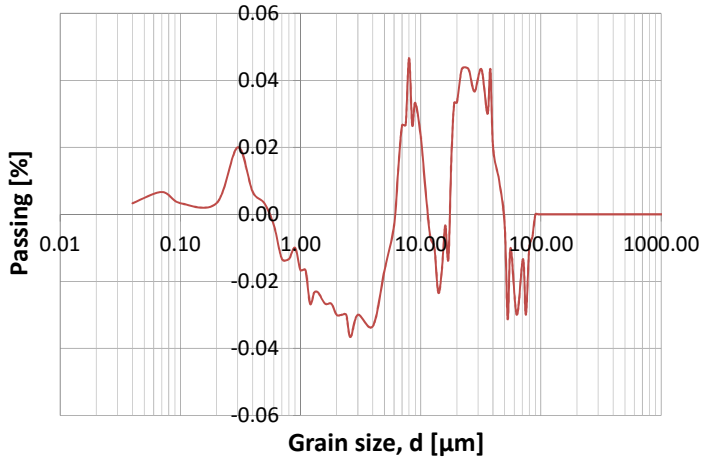

Fig. 4.14 - Difference between dry irradiated and wet irradiated grain size distribution.

4.2.3.2 X-ray Fluorescence (WD-XRF, ED-ERF) and Energy X-ray Spectrometry (EDS)

Table 4.6 shows the elemental composition of silt samples obtained by XRF test. The semi-quantitative analysis gives the elemental concentration levels expressed in percentage before and after gamma irradiation test carried out on dry and wet samples.
All the analysis exhibit negligible changes or same levels of metal concentration before and after treatments. These results show that no modifications occur due to gamma-ray irradiation treatment in terms of metal composition. According to results of further X-ray diffraction analyses, Tab. 3.7 shows a high concentration of fluorine, calcium and silicon ranging to 25.8%÷26.7%, 34.0%÷34.8% and 26.8%÷27.0%, respectively.
All these elements represent constituents of chemical compounds that were obtained from X-ray diffraction analyses and they confirm, in qualitative terms, the results of previous SEM analysis.

Tab. 4.6 - Metal concentration levels from semi-quantitative XRF analysis.

Metal (%)	Not irradiated	Wet irradiated	Dry irradiated
F	26.700	26.600	25.800
Na	0.100	0.100	0.080
Mg	0.400	0.400	0.400
Al	6.200	6.200	6.200
Si	27.000	26.800	26.900
P	0.070	0.070	0.070
S	0.180	0.240	0.180
Cl	0.015	0.015	0.010
K	2.900	2.900	2.900
Ca	34.000	34.100	34.800
Ti	0.180	0.270	0.270
Cr	0.007	0.008	0.007
Mn	0.090	0.090	0.090
Fe	1.300	1.430	1.400
Cu	0.007	0.009	0.009
Zn	0.500	0.500	0.500
Rb	0.014	0.014	0.014
Sr	0.008	0.009	0.009
Y	0.009	0.009	0.011
Zr	0.011	0.011	0.011
Pb	0.300	0.300	0.300
Ba	0.040	0.030	0.030

4.2.3.3 Scanning electron microscope analysis (EDS)

SEM spectra before and after irradiation process are shown in Fig. 4.15, Fig. 4.16 and Fig. 4.17.

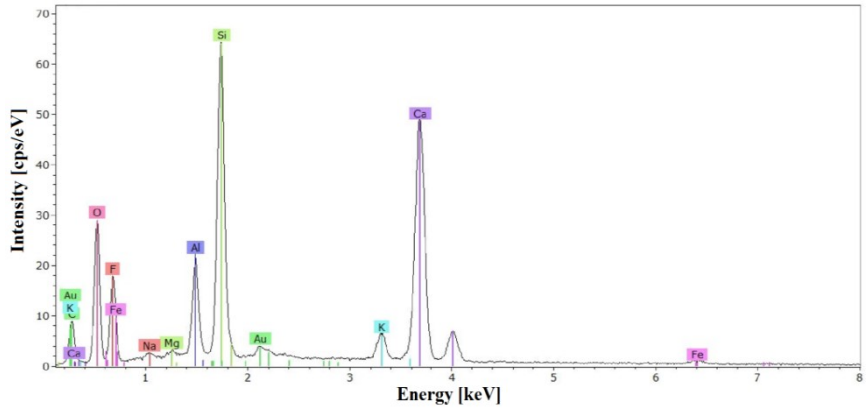

Fig. 4.15 - Not irradiated sample: EDS spectrum.

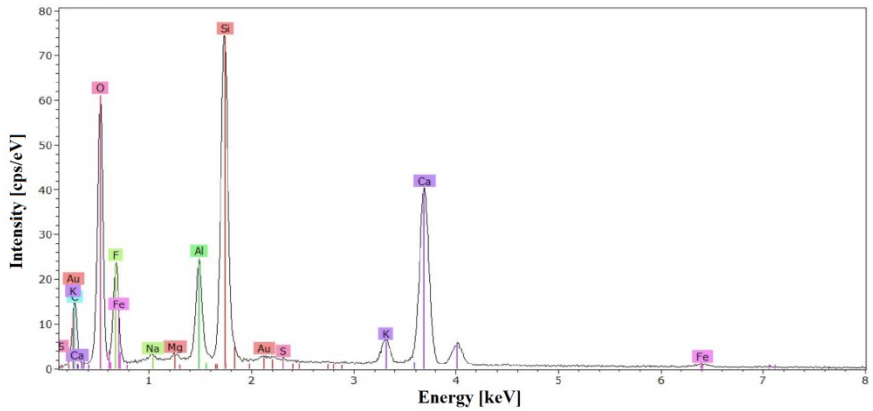

Fig. 4.16 - Dry irradiated sample: EDS spectrum.

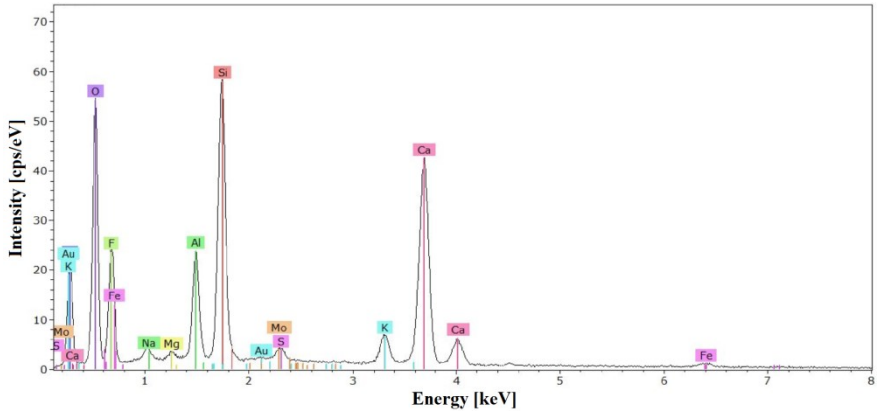

Fig. 4.17 - Wet irradiated sample: EDS spectrum.

SEM Spectra (Fig. 4.15, Fig. 4.16 and Fig. 4.17) are given in terms of X-rays emitted radiation intensity (cps/eV) plotted on y-axis and energy level of ejected electrons (keV)

plotted on x-axes. The main elements, according to XRF and XRD analysis performed at Politecnico di Torino (2015) and CDTN (2016), show no relevant changes in concentration before and after irradiation process. As in case of XRD and XRF analyses, in this case a qualitative indication about elemental concentration is given by the height of peaks. Finally, presence of peaks typical of gold in terms of emitted energy, is only due to the metallization treatment during sample preparation.

4.2.3.4 Quantikov image analyzer

An image analyzer (Quantikov) was used to investigate the particle morphology in terms of values of area, diameter and roundness of Stava silty particles passing through the 0.074mm sieve before and after the gamma ray treatment.
It is worth to note that the diameter is computed as the one of an ideal spherical particle having the same surface of the real grain's area. On the other hand, the roundness is a non-dimensional parameter related to the sharpness of the edges and corners of a particle. According to Wadell (1932), the roundness ranges between zero (very angular grain) and one (well-rounded grain) and is defines as:

$$R = \frac{\sum_{i=1}^{i=n} r_i}{R_i \cdot n} \tag{4-17}$$

where r_i is the radius of curvature of the corners of a soil grain, n is the number of corners and R_i is the radius of the largest inscribed circle, as shown in Fig. 4.18.

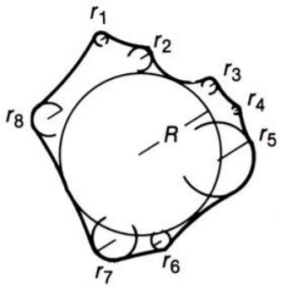

Fig. 4.18 - The concept of roundness (Wadell, 1932).

Diameter of particles is related to their grain size distribution, while roundness how 'smooth" a grain is, so if any, variations in diameter and roundness of particles before and after the gamma ray treatment, could affect the hydro-mechanical behaviour of the studied tailings. Results obtained on Stava silty particles from Quantikov image analyzer are shown in Tab. 4.7.

Table 4.7 - Area, diameter and roundness of Stava silty tailings.

	Not irradiated	**Dry irradiated**	**Wet irradiated**
Area [μm^2]	245.77	198.74	199.42
Diameter [μm]	15.64	14.86	14.35
Roundness [-]	0.72	0.71	0.68

As can be observed in Tab. 4.7, all the particles have the same roundness parameter close to 0.7 and this value means a well-rounded grain. In terms of surface, tailing grains before irradiation process are bigger than ones after the treatment, while there are no meaningful

differences if gamma ray treatment is carried out on dry or wet tailing sample. Same considerations can be made for diameter: irradiated tailings particles show a lower diameter, about 14.5µm**,** than not irradiated ones, about 15.6µm. Such results in terms of surface mean value and diameter mean value provide a good support to data obtained by laser particle analyzer. There is in fact a physical agreement between the reduction in diameter obtained by Quantikov image analyzer and the decrease in volume of biggest silty grains as suggested by changes in particle size distribution obtained from laser diffraction technique.

4.2.3.5 Density determination

Density determination is a physical characterization test aimed to obtain the density of solid samples by means of an ultra-gas pycnometer apparatus (details in Appendix). According to British Standard Institution (BSI), the true density (also named "true particle density") is defined as the mass of a particle m_p divided by the true volume V_S. According to BSI, the true volume is the volume of grains excluding open pores and closed pores (Fig. 4.19).

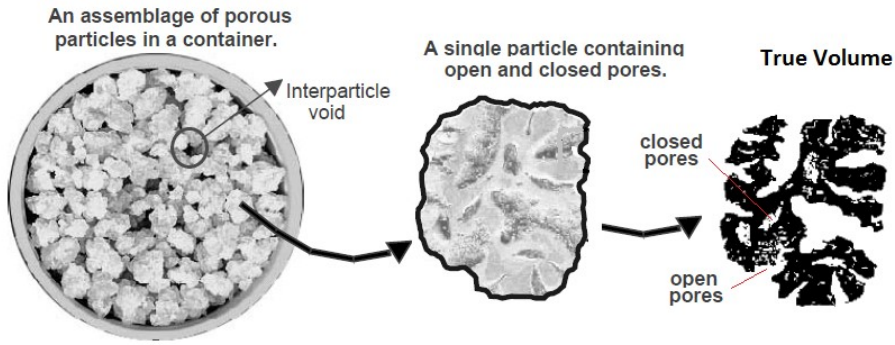

Fig. 4.19 - The concept of open, closed pores within a single particle (modified from Webb, 2001).

If any, variations in true density may be associated at variations in elemental composition, e.g. a relevant increase of true density should be related to an increase of concentration of heavy chemical element such as fluorine.

Table 4.8 shows the mean values of true density (ρ_T) and true volume (V_S) before the gamma ray treatment. Results of density determination on gamma-rays irradiated dry and wet specimens are shown in Tab. 4.9 and Tab. 4.10, respectively.

Tab. 4.8 - Values of particle density and solid volume before irradiation.

m_P [g]	V_S [cm^3]	ρ_T [g/cm^3]	st. dev, V [%]
23.4590	8.0956	2.8978	0.0004

Tab. 4.9 - Values of true density and solid volume after irradiation, dry sample.

m_P [g]	V_S [cm^3]	ρ_T [g/cm^3]	st. dev, V [%]
21.7395	7.4786	2.9069	0.0007

Tab. 4.10 - Values of true density and solid volume after irradiation, wet sample.

m_P [g]	V_S [cm^3]	ρ_T [g/cm^3]	st. dev, V [%]
24.9214	8.4654	2.9439	0.0037

As shown in Tab. 4.8, Tab. 4.9 and Tab. 4.10, true density does not change significantly before and after gamma-ray irradiation process. It maintains a constant value of approximately 2.916g/cm^3. For this reason, from a geotechnical point of view, no relevant variations in concentration of chemical element can be assumed because of the gamma ray treatment.
The mean value of 2.916g/cm^3, even if considered more precise due the use of gas technique, is relatively high because of the presence of heavy minerals such as fluorite. It is worth to note the current value is very close to specific gravity measured for silt fraction (ASTM D 854) by Carrera (2008) and equal to 2.828g/cm^3.

4.2.3.6 Surface area determination

Surface area determination is a physical characterization test aimed to obtain the surface specific area of powder material by means of the gas adsorption technique (details in Appendix). Since Kozeny-Carman equation allows to estimate the hydraulic conductivity of a saturated soil by knowledge of its surface area and density, variations (if any) in surface area may be associated at variations in hydraulical conductivity, affecting the hydro-mechanical behaviour of the studied tailings. Results in terms of specific surface, total inner pore volume, true volume and inner porosity are summarized in Tab. 4.11. The inner porosity n_i has been computed as the ratio between the inner pore volume V_p (volume of open and closed pores inside the grain) and the sum of the true volume V_s and the inner pore volume V_p:

$$n_i = \frac{V_p}{V_s + V_p} \tag{4-18}$$

Tab. 4.11 - Results of gas adsorption test: surface specific area S, total inner pore volume V_p, solid volume V_s f and inner porosity n_i on samples tested.

	S [m^2/g]	V_p [cm^3/g]	V_S [cm^3]	n_i [%]
Not irradiated	5.35	0.01376	8.09560	3.83
Dry irradiated	5.65	0.01554	7.47860	4.32
Wet irradiated	5.92	0.01576	8.46540	4.43

As shown in Tab. 4.11 , it is possible to observe a moderate increase of the specific surface area for the Stava silty fraction analysed. The specific area of dry irradiated tailings is 5.6% higher than not irradiated ones, while the specific area of wet irradiated specimen is about 10% higher than not irradiated. It is also possible to observe a moderate increase of inner porosity n_i. Intragrain porosity of dry irradiated tailings is 12.8% higher than not irradiated ones, while inner porosity of wet irradiated specimen is about 15.7% higher than not irradiated.

4.2.3.7 Mineralogical analysis

The mineral composition of the Stava silty specimens, before and after the gamma ray treatment, was investigated by means of the X-ray diffraction technique (XRD): details and principles of this technique are given in Appendix. Figures 4.20, Fig. 4.21 and Fig. 4.22 show the XRD spectra for not irradiated and irradiated tailing specimens.

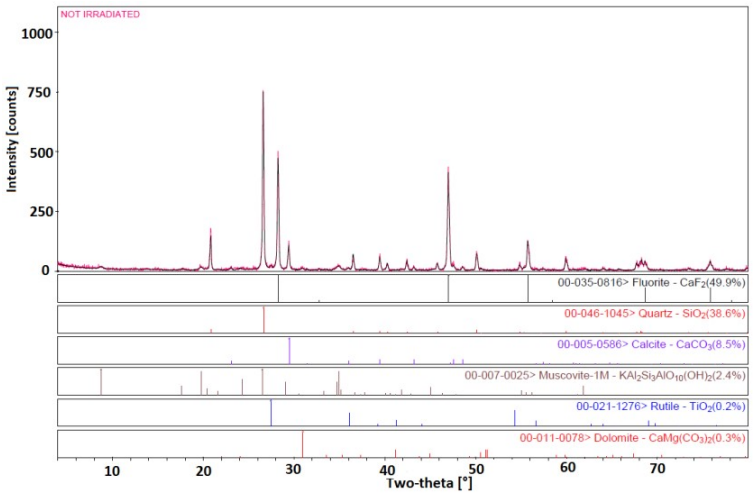

Fig. 4.20 - Not irradiated specimen: XRD spectrum.

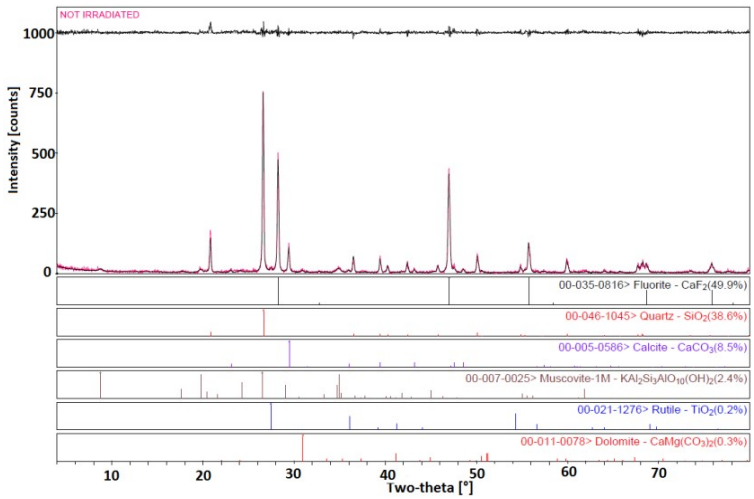

Fig. 4.21 - Dry irradiated specimen: XRD spectrum.

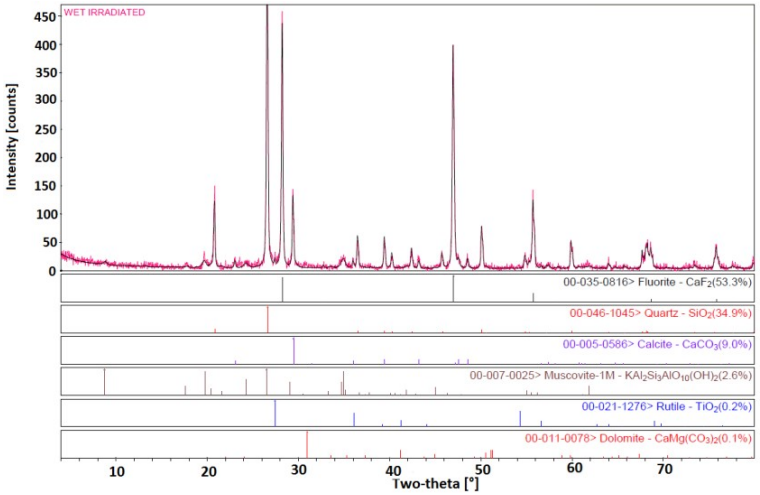

Fig. 4.22 - Wet irradiated specimen: XRD spectrum.

Figure 4.23 summarizes the previous three figures, showing the superposition of the three spectra.

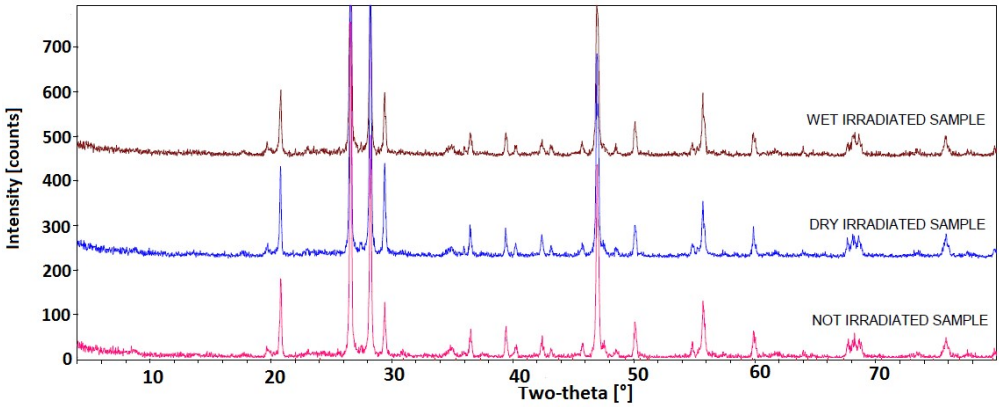

Fig. 4.23 - Superposition: not irradiated, dry irradiated and wet irradiated specimen, XRD spectrum.

Tab. 4.12 - Mass concentration of minerals found in specimens.

Mineral		Not irradiated	Dry irradiated	Wet irradiated
		[%]	[%]	[%]
Fluorite	CaF_2	49.9	49.8	53.3
Quartz	SiO_2	38.6	35.2	34.8
Calcite	$CaCO_3$	8.5	9.2	9.0
Muscovite	$KAl_2Si_3AlO_{10}$	2.4	4.3	2.6
Rutile	TiO_2	0.2	0.4	0.2
Dolomite	$CaMg(CO_3)_2$	0.3	1.1	-

As shown in Fig. 4.23, XRD spectra in the three cases can be easily overlapped: it is possible to observe that peaks are practically equal. This means the presence of the same minerals in angular position and intensity. These results are also confirmed by values of mass concentration obtained by quantitative analysis, reported in Tab. 4.12. In all three cases the higher mass concentration belongs to fluorite (about 50%), followed by quartz (about 35%) and calcite (about 9%), with traces of muscovite, rutile and dolomite. These values obtained at CDTN in 2016 are in good agreement with the results obtained at Politecnico di Torino in 2015 on not irradiated Stava silty tailings, as shown in Tab. 4.3 and Fig. 4.3.

4.2.3.8 Fourier Transform Infrared Spectroscopy (FTIR)

Fourier transform infrared spectroscopy (FTIR) technique is a powerful tool for qualitative and quantitative identification either organic or inorganic chemicals, impurities and percent crystallinity by using infrared radiation (IR) through a solid, liquid or gaseous samples (details in Appendix). Figures 4.24, Fig. 4.25 and Fig. 4.26 show the FTIR spectra for not irradiated and irradiated Stava silty specimens.

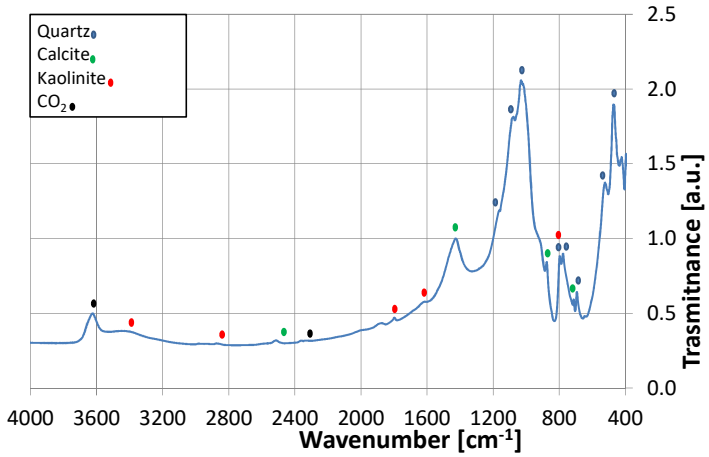

Fig. 4.24 - FTIR spectrum: not irradiated specimen.

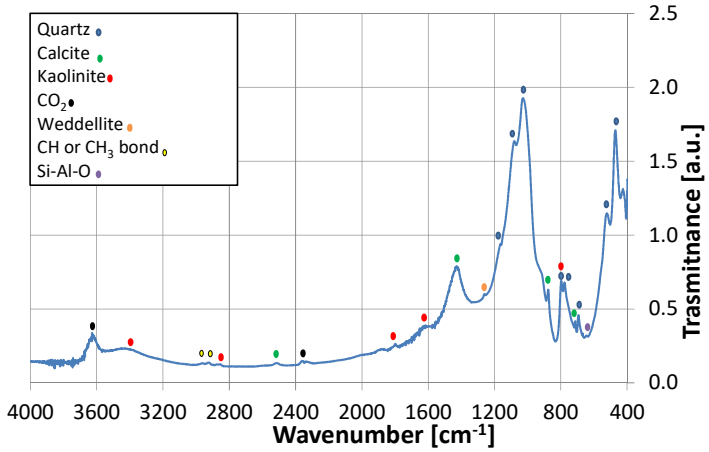

Fig. 4.25 - FTIR spectrum: dry irradiated specimen.

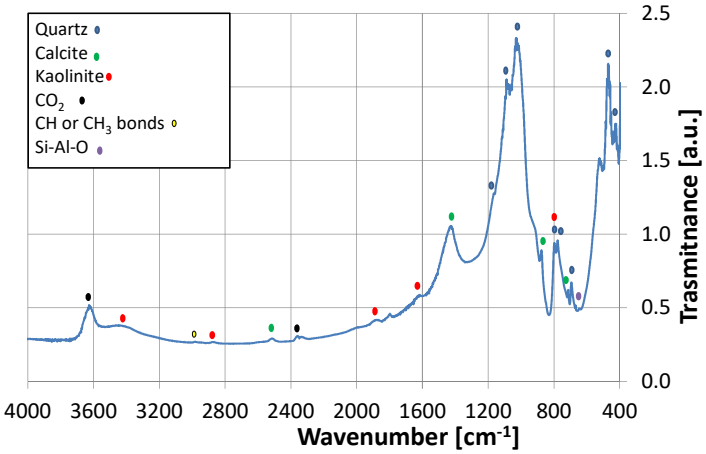

Fig. 4.26 - FTIR spectrum: wet irradiated specimen.

As shown in Fig. 4.24, Fig. 4.25 and Fig. 4.26 the main elements identified with the FTIR technique are quartz, calcite and kaolinite, in good agreement with results coming from mineral identification carried out by X-ray diffraction from elemental composition obtained by X-ray fluorescence. It is worth to note the absence of peaks concerning fluorite, just because this mineral cannot be detected by using FTIR technique. Some noise and peaks of CO_2 due to instrumentation and presence of operators in the same room, respectively. If FTIR spectra obtained from not irradiated and dry irradiated specimen are compared, it is possible to observe new peaks. These peaks are probably related to the presence of a new mineral known as weddellite. In the same time, other new peaks can be observed: some are due the creation of new chemical bonds (C-H or C-H_3), while some others are related to the creation of Si-Al-O bond. Comparing results from not irradiated and wet irradiated specimen, it is possible to observe the presence of new peaks related to C-H or C-H_3 bonds and some others are due to the creation of Si-Al-O bonds.

4.2.4 Summary and final considerations

Gamma radiations bombardment were carried out on silty specimens of Stava tailing storage facility, in order to simulate one of the long terms process acting on tailing: the natural ionizing radiation from radioactive isotopes of the soils. Tailings were treated and characterized both in dry and wet conditions in order to study the influence of UV radiations on the physical and chemical properties of tailings on the surface of tailings deposits or in the tailings bricks faces used for buildings or other economic purposes. Seventy years of UV-rays exposition were properly simulated by seven days of gamma-rays exposition. Grain size distribution was obtained by laser technique. True density determination, X-ray fluorescence, X-ray diffraction, energy X-ray spectroscopy, digital images analysis, surface determination and infrared spectroscopy technique tests were performed before and after the ionizing treatment.

From the physical point of view, little changes were observed. A very small increase of silty fractions was observed, both after dry irradiation and after wet irradiation. A decrease of about 3.0% in volume concerning particles having size comprise between 19µm and 100µm was observed. A corresponding increase of particles comprise between 0.5µm and 10µm was shown. Anyway these variations are so small that they are not expected to cause any significant effect from the geotechnical point of view, leading no modifications on mechanical or hydraulic behaviour after the treatment. Image analysis shown that tailing particles before irradiation had a bigger surface and average diameter than ones after the

ionizing treatment. No differences seemed to be evident if gamma ray treatment was carried out on dry or wet tailing specimen. These results provided a good support to data obtained by laser particle analyzer. There was a physical concordance between reduction in mean diameter obtained by Quantikov image analyzer and the decrease in volume of biggest silt grains as suggested by changes in particle size distribution obtained from laser diffraction technique.

Also from the chemical point of view, it has been demonstrated that Stava tailings exhibit a certain stability. From adsorption tests, it was possible to observe that the specific surface area of dry irradiated specimen is 5.6% higher than those of not irradiated specimen. Furthermore, the specific surface area of wet irradiated specimen is 10% higher than those of not irradiated specimen. It was also possible to observe an increase of inner porosity n_i for dry irradiated tailings and for wet irradiated ones, while in terms of true density it was possible to state that the value is constant in all three cases. X-ray fluorescence analysis exhibit little changes of metal concentration before and after treatments. In terms of metal composition, no modifications occur due to gamma-ray irradiation ageing test. According to results from XRD analysis, XRF gives an high concentration of fluorine, calcium and silicon. These elements are the constituents of chemical compounds obtained from XRD analyses and they are confirmed, also in quantitative terms, by SEM analysis. The main elements identified by Fourier transform infrared technique were quartz, calcite and kaolinite, confirming the results coming from by X-ray diffraction and X-ray fluorescence. If not irradiated sample's FTIR spectra and dry irradiated sample's spectra were compared, it was possible to observe the presence of new little peaks. They were probably connected to the presence of weddellite and some new chemical bonds such as C-H (or $C\text{-}H_3$), and Si-Al-O.

These very small chemical changes are also expected not to have any relevant effect on the hydro-mechanical behaviour of the studied tailings. The entity of variations experienced in grain size distributions and specific surface cannot influence the water retention curve, hence they have no consequences on the hydraulic and mechanical behaviour. Tested tailing before gamma irradiation was exposed to natural solar radiations for twenty years before being collected in 2005. Hence it could have been subjected at chemical/physical modifications prior its storage in 2005 and its testing in 2016. These possible initial modifications due to natural exposure at solar radiation could make the soil grains more stable, providing a suitable justification about little chemical-physical variations before and after the induced gamma ray bombardment.

This study intends furthermore to give a starting point for a characterization procedure applicable to a wide range of natural or wastes materials that can be re-used after their deposition. Results such as relevant changing in grain size distribution, specific surface and chemical composition due to ageing process, could influence the re-usage of these materials. It is worth to note the wet irradiation was carried out in pure water, while the real environment is more complex. In the site, tailings are mixed with water which contains dissolved salts, heavy metals, contaminants and residual chemicals from the mineralogical processes. This choice was adopted to simplify the experimental program. Hence, in order to improve the affinity with the real environment, further wet irradiations tests could be carried out by using processing water. Additionally, other tests can also be performed by increasing the photon energy emitted by gamma rays, in order to simulate a greater ionizing exposure period both on dry and wet specimens, and mixtures made of sandy and silty tailings in different percentages have to be tested in order to take into account the heterogeneity of in situ tailings.

REFERENCES

1. Afifi S.S. and Woods R.D. 1971. Long-term pressure effects on shear modulus of soils, J. Soil Mech. Found. Div., 97: 1445-1460.

2. Anderson D.G. and Stokoe K.H. 1978. Shear modulus, a time-dependent soil property, Dynamic Geotechnical Testing, ASTM STP, **654**: 66–90.

3. ASTM. 1997. Annual book of ASTM standards.

4. Baxter C.D.P. 1999. An experimental study on the aging of sands, PhD Thesis Virginia Polytechnic Institute and State University, Blacksburg, Virginia.

5. Baxter C.D.P. Mitchell J.K. 2004. Experimental study on the aging of sands, Journal of Geotechnical and Geoenvironmental Engineering, **130**: 1051-1062.

6. British Standard BS 2955. 1991. Glossary of Terms Relating to Particle Technology, British Standards Institution, London.

7. Carrera A. 2008. Mechanical behaviour of Stava tailings. Ph.D. thesis, Politecnico di Torino.

8. Charlie W.A., Rwebyogo, M.F.J., and Doehring D.O. 1992. Timedependent cone penetration resistance due to blasting," J. Geotech. Eng., **118**: 1200-1215.

9. CrawD., Chappel D., Nelson M. and Walrond M. 1999. Consolidation and incipient oxidation of alkaline arsenopyrite-bearing mine tailings, Macraes Mine, New Zealand, Applied Geochemistry, **14**: 485-498.

10. Devasahayam S. 2007. Application of particle size distribution analysis in evaluating the weathering in coal mine rejects and tailings," Fuel Processing Technology, **88**: 295-301.

11. Daramola O. 1980. Effect of Consolidation Age on Stiffness of Sand, Geotechnique, **30**: 213-216.

12. Espósito T., Mantilla J.N.R., Carrasco E.V.M., Moreira L.E., 2014. Utilização de rejeito de minério para a fabricação de Tijolos de Rejeito-Cimento – TRC., Proc. XVII Congresso Brasileiro de Mecânica dos Solos e Engenharia Geotécnica, Goiânia (Brazil).

13. Gilmore G. 2008. Practical Gamma-Ray Spectrometry, 2nd edition, John Wiley & Sons, Ltd.

14. Human C.A. 1992. Time dependent property changes of freshly deposited or densified Sands, PhD Thesis, University of California at Berkeley, Berkeley.

15. Ishihara K. 1985. Stability of natural deposits during earthquakes, Proc., 11th Int. Conf. on Soil Mechanics and Foundation Engineering, San Francisco, 321-376.

16. ISMES (1985). Indagini geotecniche di laboratorio su materiali provenienti dai bacini Prestavel in località Stava – Tesero (TN). Final report.

17. Jefferies M.G. and Rogers B.T. 1993. Discussion of 'Timedependent cone penetration resistance due to blasting', by W. A. Charlie, M. F. J. Rwebyogo, and D. O. Doehring, J. Geotech. Eng., **119**: 2008-2012.

18. Joshi R.C., Achari G., Kaniraj S.R. and Wijiweera H. 1995. Effect of aging on the penetration resistance of sands, Canadian Geotechnical Journal, **32**: 767-782.

19. Kozeny J. 1927. Ueber kapillare leitung des wassers imboden. Sitzungsberichte Weiner Akademie, 136, n. 2a, pp. 271-306.

20. Larrahondo J.M. and Burns S.E. 2014. Laboratory-prepared iron oxide coatings on sands: surface characterization and strength parameters, Journal of Geotechnical and Geoenvironmental Engineering, **140**: 1-9.

21. Luino F. and De Graff J. V. 2012. The Stava mudflow of 19 July 1985 (Northern Italy): a disaster that effective regulation might have prevented. Nat. Hazards Earth Syst. Sci., 12, pp. 1029–1044.

22. Mesri G., Feng T.W.E. and Benak J.M. 1990. Postdensification penetration resistance of clean sands, Journal of Geotechnical Engineering - ASCE, **116**: 1095-1115.

23. Miller H.J. 1994. Development of instrumentation to study the effects of aging on the small strain behavior of sands, PhD Thesis, Univ. of New Hampshire, Durham, N.H.

24. Mitchell J. and Solymar Z. 1984. Time-Dependent strength gain in freshly deposited or densified sand, Journal of Geotechnical Engineering - ASCE, **110**: 1559-1576.

25. Oberg A., Sallfors G. 1997. Determination of shear strength parameters of unsaturated silts and sands based on the water retention curve. Geotech. Test J GTJODJ 20(1): pp. 40–48.

26. Pender M.J., Peploe R.J. and Duske G.C. 1992. Simple shear compaction of basecourse aggregates, Geotechnical Risk- Identification, Evaluation, and Solutions, Proc., 6th Australia–New Zealand Conf. on Geomechanics, Christchurch, New Zealand, 370-374.

27. Pinto L.C.M. 1996. Quantikov: Um Analisador Microestrutural Para o Ambiente Windows, PhD Thesis, Instituto de Pesquisas Energéticas e Nucleares (IPEN), São Paulo.

28. Sarsby R. 2013. Environmental Geotechnics, ICE Publishing.

29. Seed H.B. 1979. Soil liquefaction and cyclic mobility evaluation for level ground during earthquakes, J. Geotech. Eng. Div., Am. Soc. Civ. Eng., **105**: 201–255.

30. Schmertmann J.H. 1987. Discussion of Time-dependent strength gain in freshly deposited or densified sand, by J. Mitchell and Z. V. Solymar, Journal of Geotechnical Engineering - ASCE, **113**: 173-175.

31. Schmartmann J.H. 1991. The mechanical aging of soils, Journal of Geotechnical Engineering, American Society of Civil Engineers, **117**: 1288-1330.

32. Steinhilber F., Abreu J.A., Beera J., Brunnera I., Christl M., Fischer H., Heikkilä U., Kubikb P.W., Manna M., McCracken K.G., Miller H., Miyahara H., Oerter H. and Wilhelmsf F. 2012. 9,400 years of cosmic radiation and solar activity from ice cores and tree rings, Proceedings of the National Academy of Sciences, 109: 5967-5971.

33. Tarazona C.F. 2015. Estudo da alteracao em laboratorio de rejetos de mineracao de ferro para analise em longo prazo, PhD Thesis, Universidade Federal do Rio de Janeiro.

34. Troncoso J.H., Ishinara K., Verdigo R. 1988. Aging Effects on Cyclic Shear Strength of Tailings Materials. Proceedings of ninth world conference on earthquake engineering. Tokyo-Kyoto, Japan. p. 121-126.

35. Wadell H. 1932. Volume, shape, and roundness of rock particles. Journal of Geology 40, PP. 443–451.

36. Webb P.A. 2001. Volume and Density Determinations for Particle Technologists. Micromeritics Instrument Corp. 2/16/01.

5 Hydraulic behaviour of Stava tailings in unsaturated conditions

In this chapter, the water retention behaviour of Stava tailings, as obtained for unsaturated conditions, is described. The dependency of the water retention curve (WRC) on the soil initial density and grain size distribution is studied by testing samples prepared at different initial void ratio and different percentages of sand and silt fractions. Furthermore, due to the coupling between hydraulic and mechanical behaviour, the water retention behaviour is an essential element to investigate the mechanical response detailed in Chapter 6.

5.1 DESCRIPTION OF THE EXPERIMENTAL EQUIPMENT USED IN THE INVESTIGATION

5.1.1 Suction controlled oedometer

The hydraulical behavior of Stava tailing was studied by performing water retention tests, by means of a controlled oedometer apparatus, into which the axis translation technique was adopted for most of the experimental investigation. To minimize the equalization times and the effects of side friction, the oedometer sample having 20mm height and 50mm diameter were used. A picture of the apparatus and a schematic view are given in Fig. 5.1a and Fig. 5.1b. An axial stress (maximum allowed 1.6MPa) is applied by pressurized air acting on the loading plate. The water pressure is applied to the sample from the bottom of the oedometer, where a high air entry value (*AEV*) porous stone is placed. The air pressure is applied to the sample from the top.
The axial displacements of the specimens are measured by using a linear variable differential transducer (*LVDT*) connected to the top plate. An air trap is installed in the air drainage system to protect the pressure regulator from water condensation. The maximum and minimum values of matric suction imposed during the tests were s=400kPa and s=10kPa, respectively. A water volume-meter (capacity 50cm^3, accuracy ±40mm^3) was connected to the bottom *AEV* porous stone and allows to quantify the water volume exchange with the soil sample during drying and wetting processes. Finally, an additional water channel connected to the water chamber is used to remove any air bubbles accumulated in the water chamber due to air diffusion phenomena.

(a)

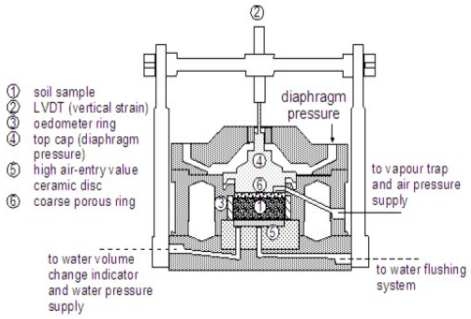

(b)

Fig. 5.1 - (a) Suction controlled oedometer apparatus used in the current research and (b) its schematic view (Romero and Jommi, 2008).

5.1.2 Sample preparation

Water retention tests were done on both statically compacted samples and reconstituted samples having a high initial void ratio. Static compaction was induced by hand-mixing dry soil powder with a certain amount of demineralized, de-aired water. The mixture was put inside a cylindrical mould and it was statically compacted by gradually applying an axial force. A controlled-axial displacement Wykeham Farrance loading frame (Fig. 5.2b) was used to increment the axial load until the desired volume was reached under controlled water content.

(a)

(b)

Fig. 5.2 - (a) Hermetic mould for suction controlled and (b) Wykeham Farrance loading frame.

Samples were then extracted from their mould and tested, keeping them inside the metallic ring. Table 5.1 gives the list of the water retention tests with their initial state in terms of percentage of silt and sand, void ratio (e_0) , dry weight (γ_d) and water content (w_0).

Tab. 5.1 - List of water retention tests.

Sample	Technique	Sand fraction [%]	Silt fraction [%]	e_0 [-]	w_0 [%]	γ_d [kN/m^3]	Comments
OED_SILT_0.5	Axis translation	0	100	0.5	15.9	18.9	Compacted sample
OED_SILT_0.6	Axis translation	0	100	0.6	15.0	17.6	Compacted sample
OED_SILT_0.7	Axis translation	0	100	0.7	17.3	16.6	Compacted sample
OED_SILT_0.8	Axis translation	0	100	0.8	27.4	15.9	Reconstituted sample
OED_3070_0.6	Axis translation	30	70	0.6	17.2	17.4	Compacted sample
OED_7030_0.7	Axis translation	70	30	0.7	17.8	16.2	Compacted sample

Reconstituted sample OED_SILT_0.8 was prepared by means of a water content equal to the limit liquid and an initial void ratio e_0 = 0.8. The sample hence had the consistence of a slurry, so it was not performed a static compaction before putting it inside the cell, as it had been done for all the other samples.

5.1.3 Water retention testing phases and required variables for the water retention curve determination

The specimen is placed inside the oedometer cell, so an initial vertical load and air pressure are applied. Then, the desired suction is imposed by changing the imposed value of pore water pressure, while the pore air pressure is usually kept constant, until reaching the equilibrium in terms of water volume exchanged between the soil sample and volumemeter (Fig. 5.3). Because of the oedometric conditions, net stress is defined as:

$$\sigma_{net} = (\sigma_a - u_a) \tag{5-1}$$

where σ_a and u_a are the applied axial stress and air pressure, respectively.

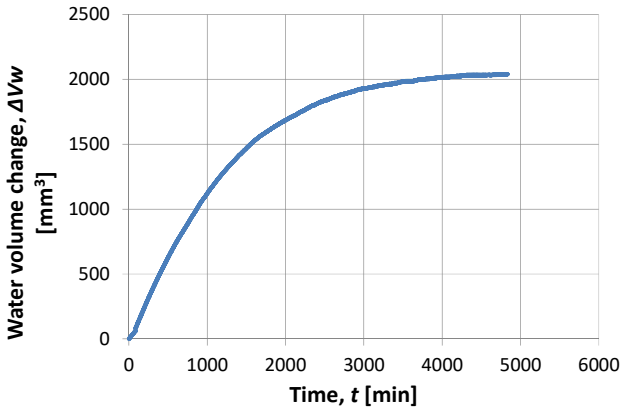

Fig. 5.3 - Water volume changed for suction s=200kPa (drying phase), sample: OED_SILT_0.7.

When the water content of the sample reaches a constant value, suction level is increased or decreased by changing again the water pressure, leading a drying or wetting process.
The axial strain ε_a is the only deformation allowed and it can be computed from the initial height h_0 and the axial displacement Δh obtained from the LVDT, assuming positive values of ε_a for compressive deformation:

$$\varepsilon_a = \frac{\Delta h}{h_0} \tag{5-2}$$

Because of null radial strain ε_r, the volumetric strain ε_v is equal to the axial strain ($\varepsilon_V = \varepsilon_a$). The current total volume V can be computed from the initial total volume V_0:

$$V = V_0 - \varepsilon_v V_0 \tag{5-3}$$

The current volume of void V_v is computed from the current total volume V and the volume of solid V_s :

$$V_v = V - V_s \tag{5-4}$$

The current void e is obtained:

$$e = \frac{V_v}{V_s} \tag{5-5}$$

The gravimetric water content can also be computed by knowledge of the mass of water M_w and the mass of solid M_s:

$$w = \frac{M_w}{M_s} \tag{5-6}$$

Finally, knowledge of the solid specific gravity G_s allows to compute the degree of saturation S_r and the water ratio e_w:

$$S_r = \frac{wG_s}{e} \tag{5-7}$$

$$e_w = e \cdot S_r \tag{5-8}$$

Plotting the imposed matric suction s, at each step, versus the degree of saturation (water content or water ratio), allows to obtain the water retention curve.

5.2 SUCTION MEASUREMENT BY DEW POINT TECHNIQUE

The dew-point technique is used to measure the total suction by means of a psychrometer aimed to extend the characterization of the water retention curve at suction levels higher than those permitted by the axis translation technique adopted with the suction controlled oedometer. Also in this case, the dependency of the water retention curve on initial density and grain size distribution is studied by testing samples prepared at different initial void ratio, water content and different percentages of sand and silt.

5.2.1 Testing procedure

A cylindrical sample (20mm diameter and 10mm height) was extruded from the oedometer samples, whose preparation was described previously, and allowed to dry by exposing it to laboratory air. Every two-three hours the total suction was measured by means of a psychrometer. After that, the net mass *M* of the sample was measured in order to associate the current suction value at its corresponding water content (Fig. 5.4).

Fig. 5.4 - Weighing of sample WP4C_1.

In a few days the weight of the sample reached a constant value, meaning no further water exchanges. Table 5.2 gives a list of the drying tests with their initial state in terms of percentage of silt and sand, void ratio (e_0) , dry weight (γ_d) and water content (w_0).

Tab. 5.2 - List of drying tests.

Sample	Suction measurement technique	Sand fraction [%]	Silt fraction [%]	e_0 [-]	w_0 [%]	γ_d [kN/m^3]	Comments
WP4C_1	Dew-point	30	70	0.7	8.0	16.4	Compacted sample
WP4C_2	Dew-point	0	100	0.7	17.3	16.6	Compacted sample
WP4C_3	Dew-point	0	100	0.7	6.0	16.6	Compacted sample
WP4C_4	Dew-point	0	100	0.7	8.0	16.6	Compacted sample
WP4C_5	Dew-point	0	100	0.8	27.4	15.9	Reconstituted sample

The drying process took 24÷36 hours and the measures of suction and weight were taken about every two hours.

5.2.2 Required variables

After the net weight did not exhibit any change, the drying process was assumed to be ended, so the sample was oven dried for 24 hours at 105°C and then the dry mass *Ms* of solid was measured. At each step, the mass of water M_w was obtained by subtracting the dry mass (M_S) to total mass (M):

$$M_w = M - M_s \tag{5-9}$$

The water content w was obtained:

$$w = \frac{M_w}{M_s} \tag{5-10}$$

Assuming no variations of void ratio e during the drying process, the degree of saturation S_r can be computed by equation (5-7), while the water ratio was computed with the equation (5-8).

5.3 VAPOUR EQUILIBRIUM TECHNIQUE

5.3.1 Purposes

The vapour equilibrium technique is used to impose a certain total suction in order to extend the experimental characterization of the water retention curve at suction levels higher than those permitted by the axis translation technique, and to complement those obtained with psychrometer (Tab. 5.2). The dependency of the water retention curve on initial density is studied by testing samples prepared at different initial void ratios.

5.3.2 Testing procedure

Cylindrical samples (20mm diameter and 10mm height) were extruded from the oedometer samples, whose preparation was described previously, and put inside sealed chambers containing saturated salt solutions corresponding to different total suctions. Every day the sample was extracted from the sealed chamber, weighted and the total suction also measured by means of the psychrometer. This procedure was repeated until the weight of the sample reached a constant value, meaning that total suction was in equilibrium with the one imposed by the salt solution. After that, the sample was extracted from the sealed chamber and exposed to dry to laboratory air, following the same procedure described in section 5.2.2.
Table 5.3 gives a list of the tests performed by following this procedure with initial state of the specimens in terms of percentage of silt and sand, void ratio (e_0) , dry weight (γ_d), water content (w_0) and saturated salt solutions.

Tab. 5.3 - List of tests with suction imposed by mean vapour equilibrium technique.

Silty sample	Technique	e_0 [-]	w_0 [%]	γ_d [kN/m^3]	Comments
VET_1	Vapour equilibrium	0.7	17.3	16.6	Sample compacted K_2SO_4 saturated solution (ψ = 4MPa)
VET_2	Vapour equilibrium	0.7	17.3	16.6	Sample compacted KNO_3 saturated solution (ψ = 11MPa)
VET_3	Vapour equilibrium	0.6	15.0	17.7	Sample compacted $Ca(NO3)_24H_2O$ saturated solution (ψ = 70MPa)
VET_4	Vapour equilibrium	0.6	15.0	17.7	Sample compacted $NaNO_2$ saturated solution (ψ = 57MPa)

5.4 WATER RETENTION BEHAVIOUR OF STAVA TAILINGS

This section is aimed to describe the hydraulic behaviour in unsaturated conditions of specimens of Stava tailings. A detailed description of the results obtained from suction controlled will be given for OED_SILT_0.7, while main results will be shown for other tests. Finally, an overall comparison and interpretation will be proposed.

5.4.1 Water retention behaviour of the silt specimen with initial void ratio e_0=0.7

The results obtained on the silt sample prepared at an initial void ratio e_0 = 0.7 (OED_SILT_0.7, Tab. 4.1) are here exposed. The water volume change at each step of the water retention test is shown in Fig. 5.5. Figure 4.3 therefore represents a detail of Fig. 5.5. A positive water volume change means that samples is losing water (drying phase), while a negative water volume change means that water is filling the soil pores (wetting phase). The drying phase needed about 25 days to be completed, increasing the suction from an initial value of 50kPa to the maximum value (400kPa). The same time was required to complete the wetting phase, decreasing the suction from 400kPa until the minimum value equal to 10kPa. Any increase/decrease of suction was imposed only when the water volume change of the previous step approached an asymptotic value, meaning no further variations of water content within the sample. It is also possible to see that water volume change during the first steps of drying phase are bigger than those of the last steps and vice-versa for the wetting phase. During last two steps of wetting phase (suction 20kPa and 10kPa was difficult to reach) a constant water volume change. Finally it is worth to note that, the initial suction of the sample was unknown, but it can be roughly estimated. Indeed, because of the loss of water from the beginning of the test, it is possible to state that the initial suction, corresponding to the initial degree of saturation imposed during the preparation of the sample (equal to 70%), the initial suction was certainly less than 50kPa.

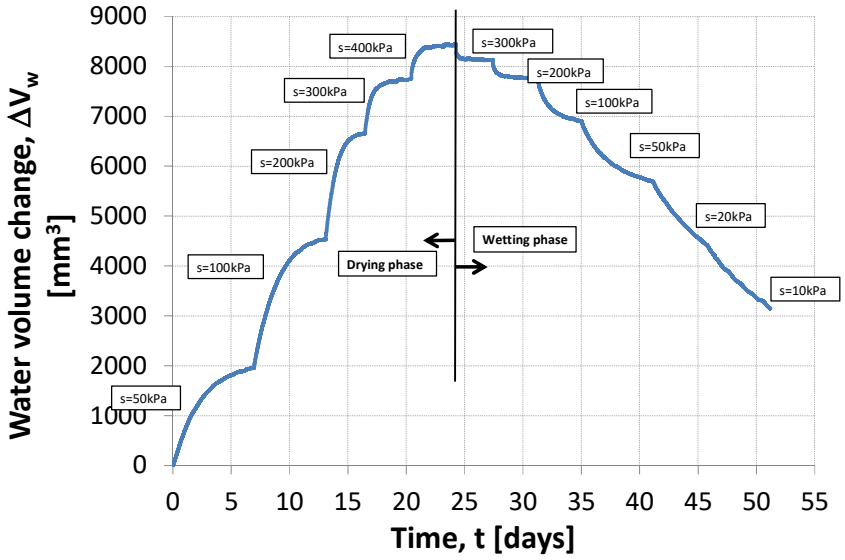

Fig. 5.5 - OED_SILT_0.7: water volume change with time.

Axial stress, water pressure and air pressure values imposed during the test are shown in Fig. 5.6. It is worth to note that at the end of the drying step at suction s = 300kPa, the air pressure u_a was increased of 50kPa and the water pressure u_w was decreased of 50kPa in order to obtain 400kPa of suction. Consequently, the axial stress σ_a was increased of 50kPa in order to maintain a constant net stress equal to 100kPa. The current test represents the only case where air and axial stress were changed. In the other water retention tests, after reaching σ_a = 520kPa and u_a = 420kPa, axial and air pressure were maintained unchanged.

Variations of degree of saturation associated to variations of suction along time are shown in Fig. 5.7.

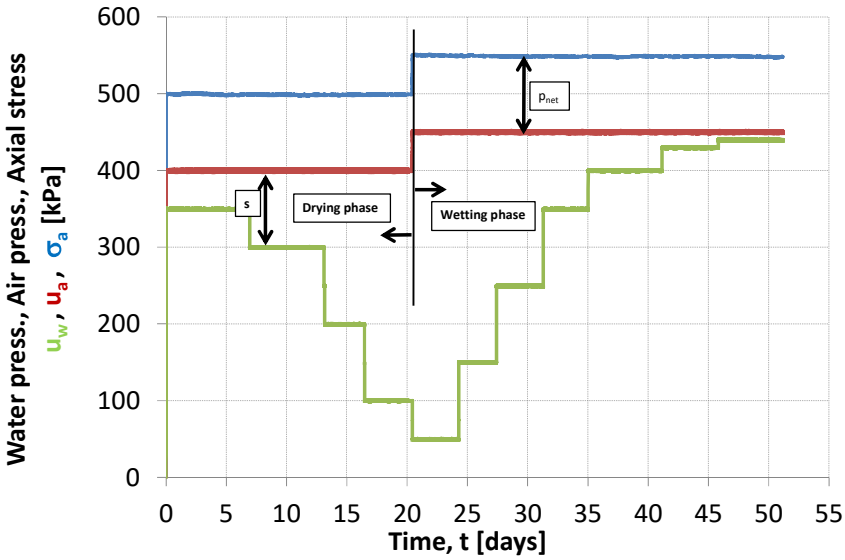

Fig. 5.6 - OED_SILT_0.7: axial stress, air and water pressure during the time.

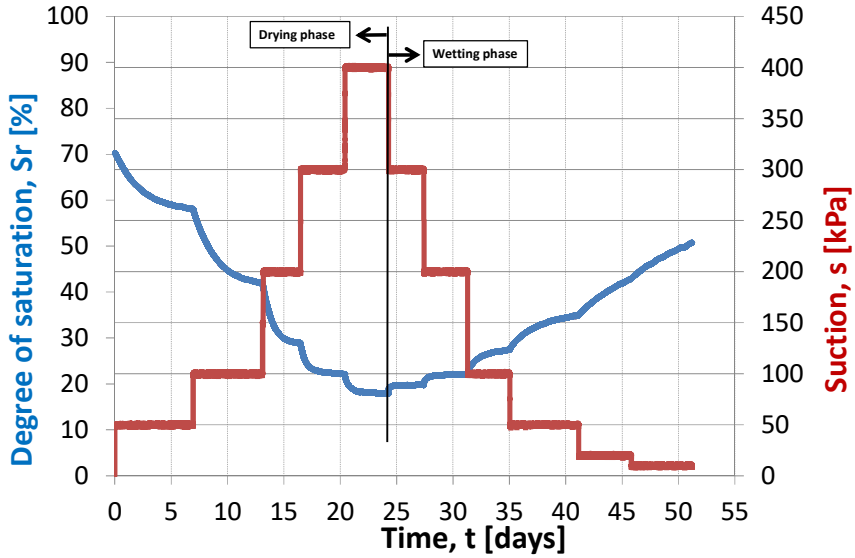

Fig. 5.7 - OED_SILT_0.7: degree of saturation and suction during the time.

Variations of void ratio and axial strain experienced by the sample during the test are shown in Fig. 5.8. During the entire oedometric test no relevant axial strains were detected. After the initial increase up to 0.30% due to the application of the axial stress, the axial strain remained practically constant. Consequently, no relevant variations of void ratio were appreciated: it remained stable at 0.7 during the entire test.

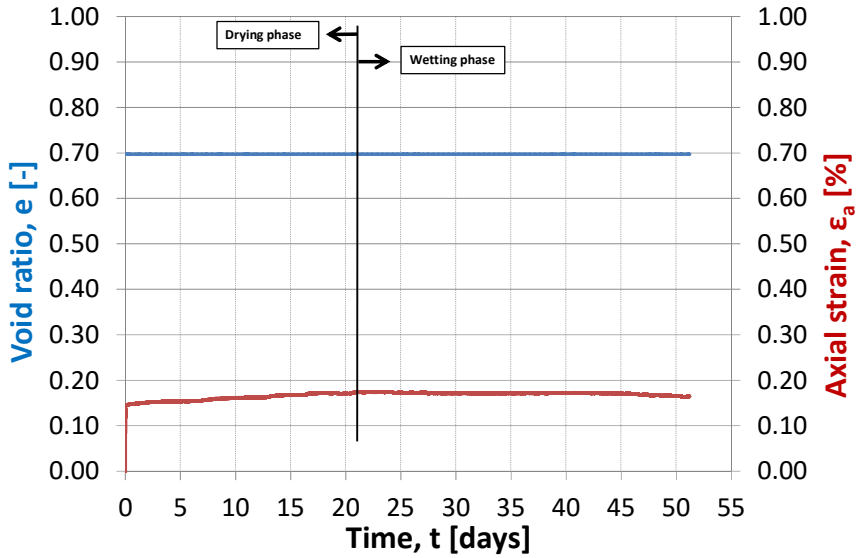

Fig. 5.8 - OED_SILT_0.7: void ratio and axial strain during the time.

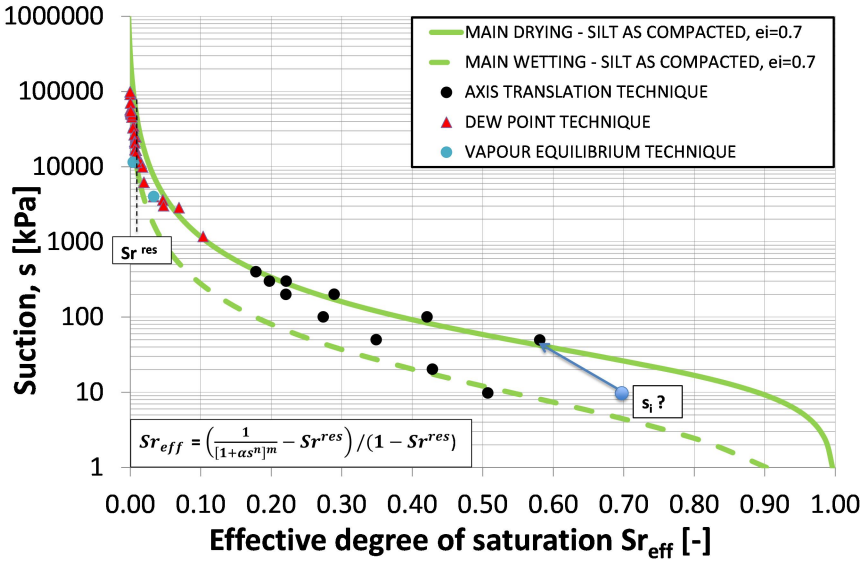

Fig. 5.9 - OED_SILT_0.7: water retention curve (s-Sr_{eff}): experimental points (circles, triangles, diamonds) and fitting curves (Van Genuchten model) for the three applied techniques.

The water retention curve in terms of suction and effective degree of saturation is shown in Fig. 5.9. Experimental points, the adopted experimental techniques and fitting curves are also given in the same figure. Black circles are obtained by means of the axis translation technique with the suction controlled oedometer. Red triangles are obtained from the drying tests measuring the suction by means of the psychrometer (dew-point technique), while the two blue points at suction 4MPa and 11MPa are obtained by applying the vapour equilibrium technique. Equalization time for axis translation technique ranged between 3 and 14 days depending on the imposed suction level. The vapour technique requires an equalization time of about 25÷30 days, while measure of the suction by means of dew-point technique required 10-30 minutes for each point. Experimental points are then fitted by the simplified Van Genuchten model in order to obtain the main drying (solid green line) and main wetting branch (dot green line). Since drying in the suction controlled oedometer was limited to s = 400kPa, and wetting was imposed on the same specimen, the following points having suction 300kPa, 200kPa and 100kPa do not belong to the main wetting branch. They are supposed to belong to scanning curve, due to hysteresis phenomena typical of hydraulical behavior in unsaturated conditions. The blue point marked as "s_i?" represents the possible initial state in terms of degree of saturation and suction. The initial degree of saturation is imposed (70%), but the initial value of suction is unknown but, because of the drying response at imposed suction 50kPa, the initial suction will be less than 50kPa, as mentioned above. Because of the location of the main drying and wetting curves that defines a domain, the initial suction ranges between 4kPa and 30kPa. The blue arrow gives the hydraulic path followed by the sample from its initial state to the first step of drying phase (s = 50kPa). During the entire main drying curve it is therefore possible to observe a decrease of the effective degree of saturation and an increase of suction, while the wetting curve is characterized by an increase of degree of saturation and a decrease of suction. The residual degree of saturation is 0.5%, while the air entry value is about 18kPa.

Similar considerations can be done with respect to the water retention curve expressed in terms of suction s and water ratio e_w (Fig. 5.10). Also in this case, experimental points are fitted by the simplified model proposed by Van Genuchten.

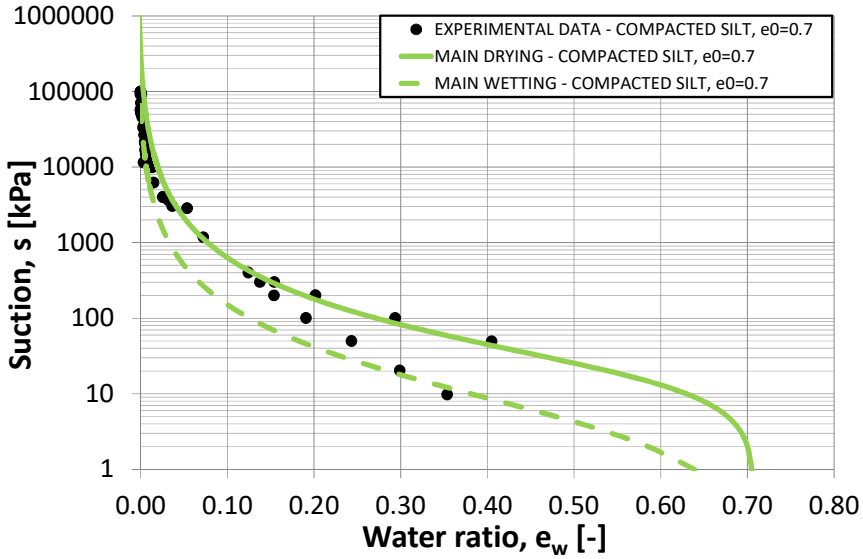

Fig. 5.10 - OED_SILT_0.7: water retention curve (s-e_w): experimental points (black circles) and fitting curves, Van Genuchten model.

5.4.2 Results: other tests

The water retention curve in terms of suction and effective degree of saturation for the compacted silt samples prepared at an initial void ratio e_0 = 0.5 (OED_SILT_0.5) is shown in Fig. 5.11.

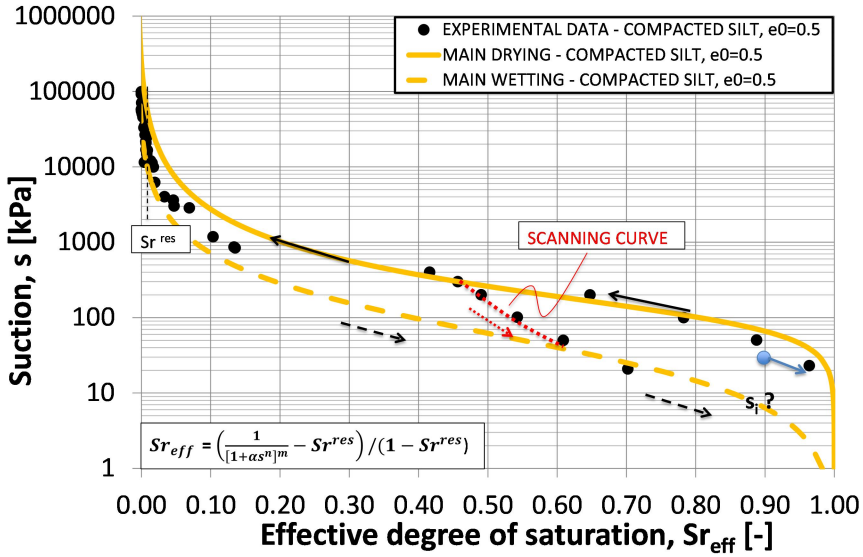

Fig. 5.11 - OED_SILT_0.5: water retention curve (s-Sr_{eff}): experimental points (black circles), fitting curves, Van Genuchten model.

Experimental points are fitted by the simplified Van Genuchten model in order to obtain the

main drying (solid yellow line) and main wetting branch (dotted yellow line). Also in this case, since drying in the suction controlled oedometer was limited to s = 400kPa, and wetting was imposed on the same specimen, the following points having suction 300kPa, 200kPa and 100kPa do not belong to the main wetting branch. They are supposed to belong to scanning curve (dotted red line). The blue point marked as "s_i?" represents the possible initial state in terms of degree of saturation and suction. The initial degree of saturation is imposed (90%), but the initial value of suction is unknown and, because of a little wetting response at imposed suction 20kPa, the initial suction will be higher than 20kPa. Because of the location of the main drying and wetting curves that defines a domain, the initial suction ranges between 6kPa and 70kPa. The blue arrow gives the hydraulic path followed by the sample from its initial state to the first step reaching the imposed suction of 20kPa. The residual degree of saturation is 0.5%, similar to those of OED_SILT_0.5.

The water retention curve (suction, effective degree of saturation) for the compacted silt sample prepared at an initial void ratio e_0 = 0.6 (OED_SILT_0.6) is shown in Fig. 5.12. The Van Genuchten model was used to fit the experimental points, so the main drying (solid brown line) and main wetting branch (dot brown line) are obtained. It in this case, the sample in the suction controlled oedometer was dried until suction 400kPa, then it was extracted. A second compacted silt sample was prepared at the same initial state and allowed to dry at laboratory air (ψ = 1.2MPa). Then it was put inside the suction control oedometer cell and a wetting process was commenced by imposing an initial suction equal to 400kPa until a final value of 20kPa. Because of this procedure the wetting phase started with a sample (the second one) completely dry, so all points obtained by decreasing the suction from 400kPa until 20kPa belong to the main wetting curve and not to a scanning curve. Also in this case, the blue point marked as "s_i?" represent the initial state. The initial degree of saturation is imposed (70%), while the initial value of suction is unknown but, again because a little wetting when the imposed suction was imposed 20kPa at the first step, the initial suction will be higher than 20kPa. Due to the location of the main drying and wetting curves, the initial suction is supposed to range between 20kPa and 60kPa. The residual degree of saturation is 0.5%, similar to those of OED_SILT_0.5 and OED_SILT_0.7.

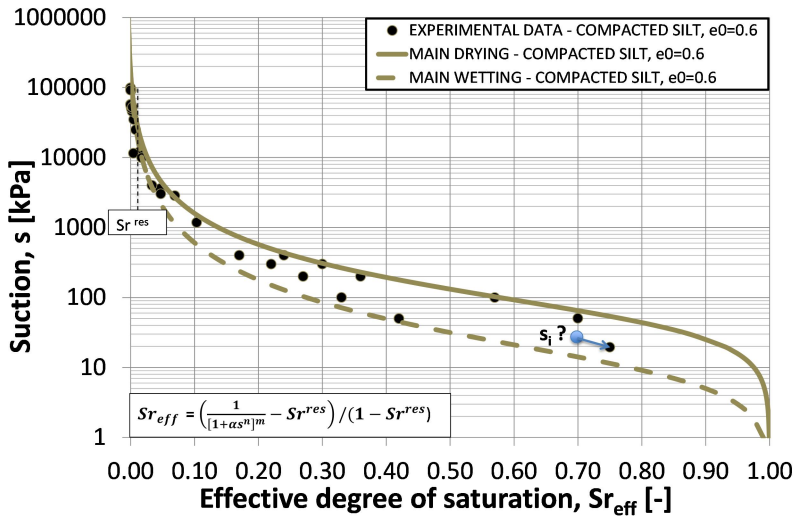

Fig. 5.12 - OED_SILT_0.6: water retention curve (s-Sr_{eff}): experimental points (black circles), fitting curves, Van Genuchten model Nocera (2017).

The water retention (s-Sr_{eff}) for the reconstituted silt sample, prepared at initial void ratio e_0 = 0.8 (OED_SILT_0.8) is shown in Fig. 5.13. Main drying (solid purple line) and main wetting (solid purple line) curves are obtained by fitting the experimental points using the simplified Van Genuchten model. Since drying in the suction controlled oedometer was limited to s = 400kPa, and wetting was imposed on the same specimen, the following points having suction 300kPa, 200kPa and 100kPa do not belong to the main wetting branch. They are supposed to belong to scanning curve.
The blue point marked as "s_i?", representing the initial state in terms of degree of saturation and suction, lies on horizontal axis because the sample was prepared by using a water content corresponding to its liquid limit, so it was completely saturated (zero suction). The sample hence had the consistence of a slurry, so it was not performed a static compaction before putting it inside the cell, as it had been done for all the other samples. The blue arrow gives the hydraulic path followed by the sample from its initial state (s = 0kPa, Sr = 100kPa) to the first step reaching the imposed suction of 20kPa. The residual degree of saturation is 0.5%, similar to those of OED_SILT_0.5, OED_SILT_0.6 and OED_SILT_0.7.

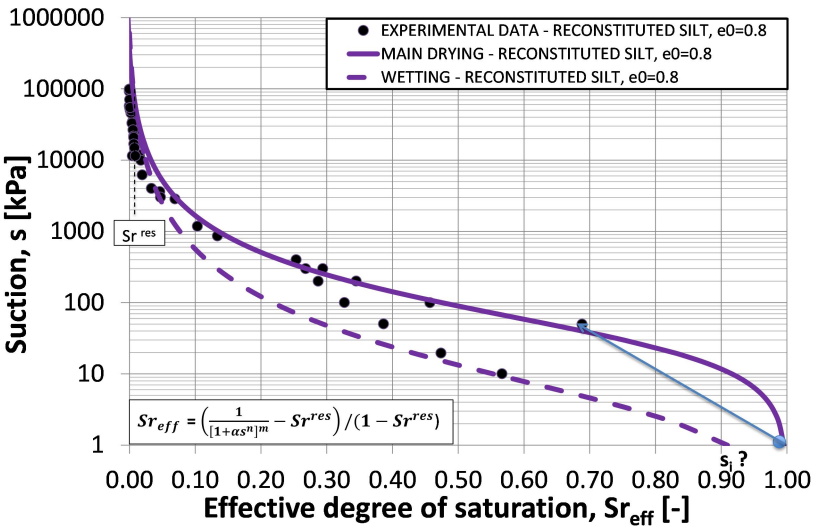

Fig. 5.13 - OED_SILT_0.8: water retention curve (s-Sr_{eff}): experimental points (black circles), fitting curves, Van Genuchten model.

Figure 5.14 shows the water retention curve (degree of saturation-suction) for a sample consisting in a mixture made of 30% of sand and 70% of silt, compacted at an initial void ratio e_0 = 0.6 (OED_3070_0.6). Both main drying (solid red line) and main wetting (solid red line) curves are obtained by fitting the experimental data using simplified Van Genuchten model. Again, since drying in the suction controlled oedometer was limited to s = 400kPa, and wetting was imposed on the same specimen, the following points having suction 300kPa, 200kPa and 100kPa do not belong to the main wetting branch. They are supposed to belong to scanning curve. An initial degree of saturation Sr = 80% was imposed, while the initial value of suction is unknown but, because of a little wetting occurred when imposing the first step suction (s = 20kPa), the initial suction will be higher than 20kPa. Because of the location of the main drying and wetting curves, the initial suction ranges between 20kPa and 40kPa. The blue arrow gives the hydraulic path followed by the sample from its initial state to the first step reaching the imposed suction of 20kPa. The residual degree of saturation is 0.5%, similar to those of silty samples.

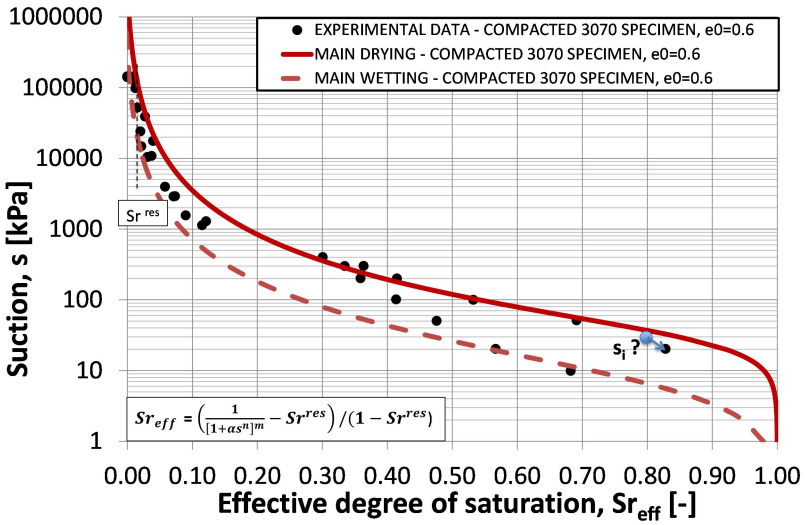

Fig. 5.14 - OED_3070_0.6: water retention curve (s-Sr_{eff}): experimental points (black circles), fitting curves, Van Genuchten model.

Finally, Fig. 5.15 gives the water retention curve (s-Sr_{eff}) for the mixture 7030 consisting in 70% of sand and 30% of silt, compacted at initial void ratio e_0 = 0.7 (OED_7030_0.7). The main drying (solid green line) and the main wetting (solid green line) branches are obtained by fitting the experimental data using the simplified model of Van Genuchten. The initial degree of saturation Sr = 70%: because of the drying process occurring when the first suction step was imposed (s = 50kPa) at the first step, the initial suction will be lower than 50kPa. Because of the location and the shape of the main branches, the initial suction must be lower than 8kPa. The blue arrow gives the hydraulic path followed by the sample from its initial state to the first step reaching the imposed suction of 50kPa. The residual degree of saturation is 0.5%.

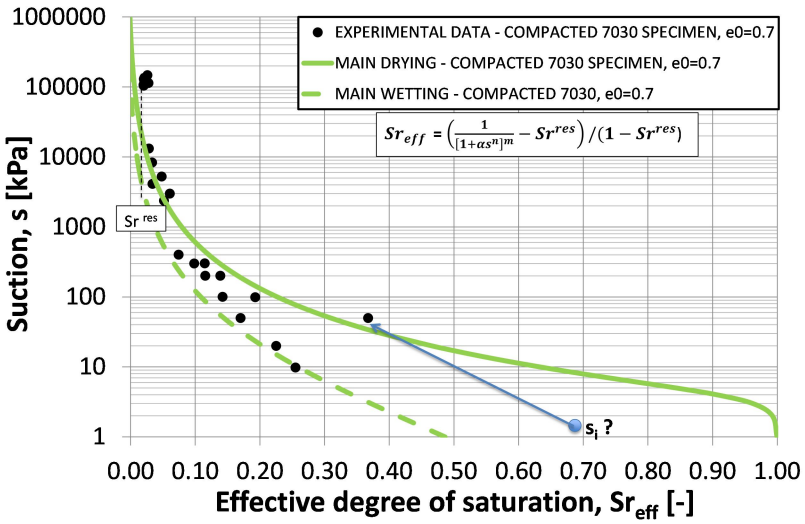

Fig. 5.15 - OED_7030_0.7: water retention curve (s-Sr_{eff}): experimental points (black circles), fitting curves, Van Genuchten model.

Calibrated parameters of water retention curves obtained with Van Genuchten model are given in Tab. 5.4.

Tab 5.4 - Calibrated Van Genuchten parameters (*α, m, n*) for each sample.

Sample	Main drying branch			Main wetting branch		
	α [kPa^{-1}]	n [-]	m [-]	α [kPa^{-1}]	n [-]	m [-]
OED_SILT_0.5	0.010	2.20	0.31	0.02	1.00	0.80
OED_SILT_0.6	0.019	1.66	0.40	0.01	1.55	0.36
OED_SILT_0.7	0.055	1.55	0.35	0.20	1.00	0.56
OED_SILT_0.8	0.031	1.30	0.44	0.30	1.10	0.40
OED_3070_0.6	0.036	2.22	0.21	0.14	1.40	0.35
OED_7030_0.7	0.280	4.40	0.10	0.60	0.40	1.20

Void ratio, air entry value and residual degree of saturation for each specimen are given in Tab. 5.5. The air entry value of the tested tailing samples can also be obtained as the reverse of α parameter (Tab 5.4).

Tab 5.5 - Void ratio (e_0), air entry value (*AEV*) and residual degree of saturation (Sr^{res}).

Sample	e_0 [-]	AEV [kPa]	Sr^{res} [%]
OED_SILT_0.5	0.5	100.0	0.5
OED_SILT_0.6	0.6	52.0	0.5
OED_SILT_0.7	0.7	18.0	0.5
OED_SILT_0.8	0.8	32.3	0.5
OED_3070_0.6	0.6	27.8	0.5
OED_7030_0.7	0.7	3.6	0.5

The air entry value with the void ratio is plotted in Fig. 5.16. It worth to note that the AEV of denser silt specimen (OED_SILT_0.5) is higher than to of looser silt specimen (OED_SILT_0.7). An increase of void ratio means the size of the pores increase, so a lower suction (AEV) to empty the pores is requested.

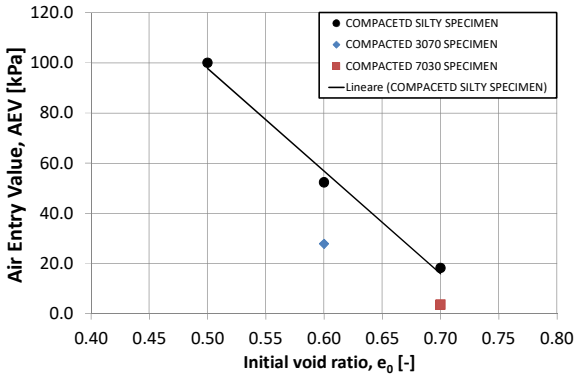

Fig. 5.16 - Initial void ratio with air entry value.

5.4.3 Influence of initial void ratio on the water retention curve

Figure 5.17 shows the influence of void ratio on water retention curve for the silt samples having the same grain size distribution, but different initial void ratio, respectively e_0 = 0.5 (OED_SILT_0.5), e_0 = 0.6 (OED_SILT_0.6), e_0 = 0.7 (OED_SILT_0.7) and e_0 = 0.8 (OED_SILT_0.8).

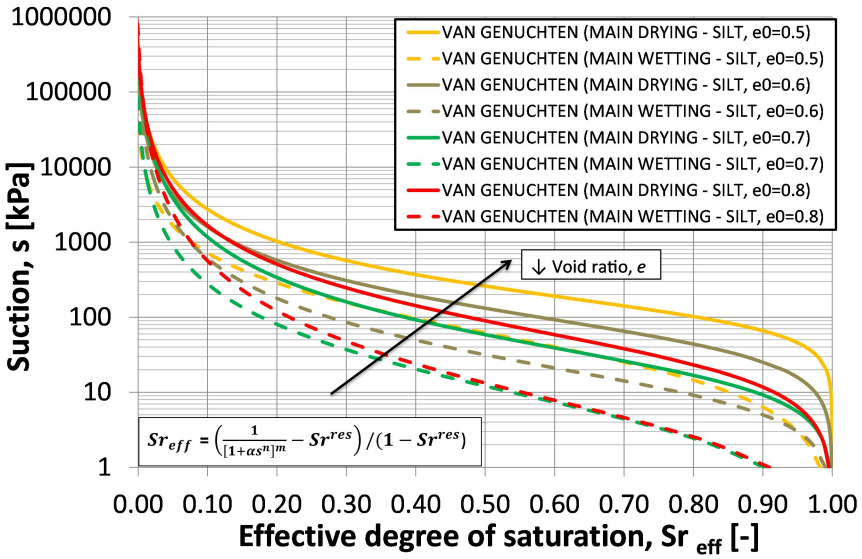

Fig. 5.17 - The influence of initial void ratio on the water retention curve (s-Sr_{eff}), Van Genuchten model.

It is possible to note that both the main drying and main wetting branches are strongly influenced by variations of void ratio. Change of void ratio is related to variations in pore size distribution and this influences the hydraulical behaviour in terms of water retention curve. A decrease of void ratio will shift the water retention curve to higher suction range because the size of the pores decreases, so a high suction to fill or empty the pores is requested. For these reasons, for all the silt samples, the water retention curve of sample OED_SILT_0.5 is shifted up than those of OED_SILT_0.6, OED_SILT_0.7, OED_SILT_0.8. For instance, during the drying process (from s=0kPa to s=100kPa) sample OED_SILT_0.5 keeps a bigger amount of water than sample OED_SILT_0.7, so its corresponding degree of saturation remains higher than those of OED_SILT_0.7. Usually, the higher is the AEV, the lower is the void ratio as confirmed in the current results (Tab. 5.4). The air entry value of sample OED_SILT_0.7 is estimating being 18kPa, very lower than those of sample OED_SILT_0.5 and OED_SILT_0.6, estimated as 100kPa and 52kPa, respectively. Indeed, the lower void ratio sample has small pores, so higher AEV is requested to desaturate them. It is worth noting that while OED_SILT_0.5, OED_SILT_0.6 and OED_SILT_0.7 are prepared by means of a static compaction and so results from these sample are easy to compare, while sample OED_SILT_0.8 was not compacted because of its consistency, so it is not easy a comparison with the other silt samples in terms of effect of void ratio on the water retention behaviour. Similar results can be observed by considering the water retention curve in terms of suction-water ratio, as shown in Fig. 5.18.

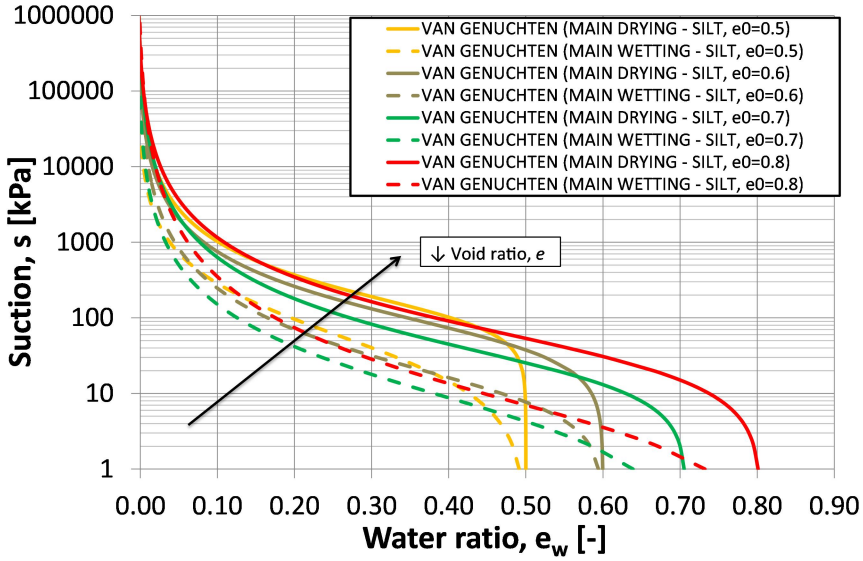

Fig. 5.18 - The influence of initial density on the water retention curve (s-e_w), Van Genuchten model.

5.4.4 Influence of grain size distribution on the water retention curve

Figure 5.19 shows the influence of fine content *"fc"* on the water retention curve for samples having different fine content:

- sample OED_SILT_0.7 (pure silt, $e_0 = 0.7$);
- sample OED_3070_0.6 (30% sand and 70% silt, $e_0 = 0.6$);
- sample OED_7030_0.7 (70% sand and 30% silt, $e_0 = 0.7$).

Also in this case, it is possible to note that both the main drying and wetting branches are affected by the changes of the grain size distribution. The increase of the fine content increases the water retention capability of the soil, an effect similar to reducing void ratio. Increasing fine content shifts the water retention curve to higher suctions because the larger pores between the particles having the size of sand are now filled with smaller particles of the size of silt. These considerations are confirmed by the AEV estimated from the water retention curve: air entry value of sample OED_7030_0.7 is equal to 3.6kPa, lower than those of sample OED_SILT_0.7, equal to 18kPa. This means that, even if void ratio is the same, the silt specimen (OED_SILT_0.7) has and higher water retention capability because its pores between the particles having the size of sand are filled with smaller particles of the size of silt.
Both main wetting and main drying curves of sample, OED_3070_0.6 (red lines) are significantly shifted to higher suctions than those of sample OED_7030_0.7 (blue lines). The water retention curve suggests which is the main contribute of the two opposite factors (density and grain size distributions) observed by comparing sample OED_3070_0.6 and sample OED_SILT_0.7. Because both main drying and main wetting curves of sample OED_3070_0.6 are placed at higher suction than those of sample OED_SILT_0.7, the effect of initial density seems to be predominant respect to the effect of grain size distribution. Similar results can be observed by considering the water retention curve in terms of suction-water ratio, as shown in Fig. 5.20.

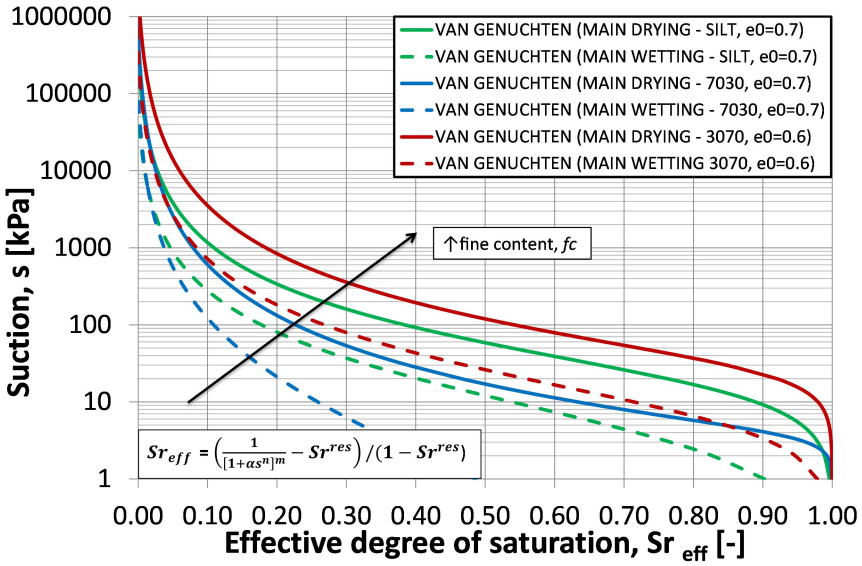

Fig. 5.19 - The influence of grain size distribution on the water retention curve (s-Sr_{eff}), Van Genuchten model.

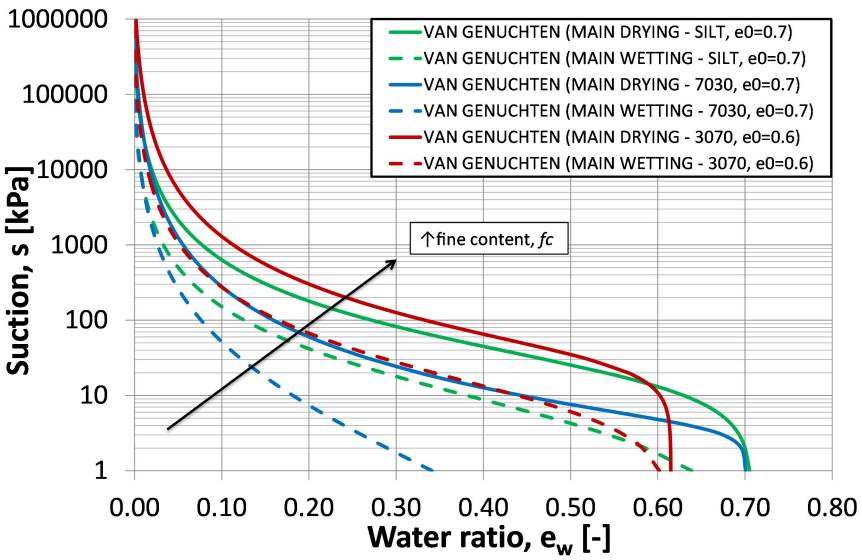

Fig. 5.20 - The influence of grain size distribution on the water retention curve (s-e_w), Van Genuchten model.

5.4.5 *Influence of density and grain size distribution on the pore size distribution*

The pore size distribution (PSD) has been evaluated from Laplace equation, assuming cylindrical pores having radius r, contact angle α between water and pore's wall equal to 0° and water surface tension T_s equal to 72mN/m at a temperature of 20°C (Ethington, 1990):

$$r = \frac{2T_s \cos\alpha}{s} \tag{5-11}$$

where s is the suction. Knowledge of radius r, effective degree of saturation Sr_{eff} and specific weight Gs allows to obtain the pore size distribution:

$$PSD = \frac{\Delta\left[\frac{e(1-Sr_{eff})}{Gs}\right]}{\Delta\log(r)} \tag{5-12}$$

The effect of initial density on the pore size distributions of Stava silty samples are given in Fig. 5.21a, while the effect of the grain size distribution on the pore size distributions of Stava silt-sand mixtures are shown in Fig. 5.21b. As mentioned above, it is worth to note that the pore size distributions showed in Fig. 5.21 were not by mercury intrusion porosimetry tests, but they are obtained from the theoretical water retention curves.

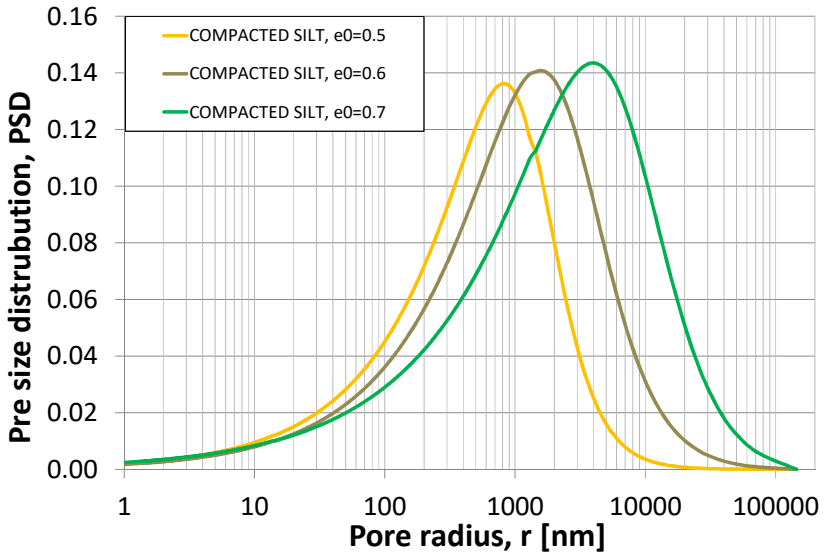

(a)

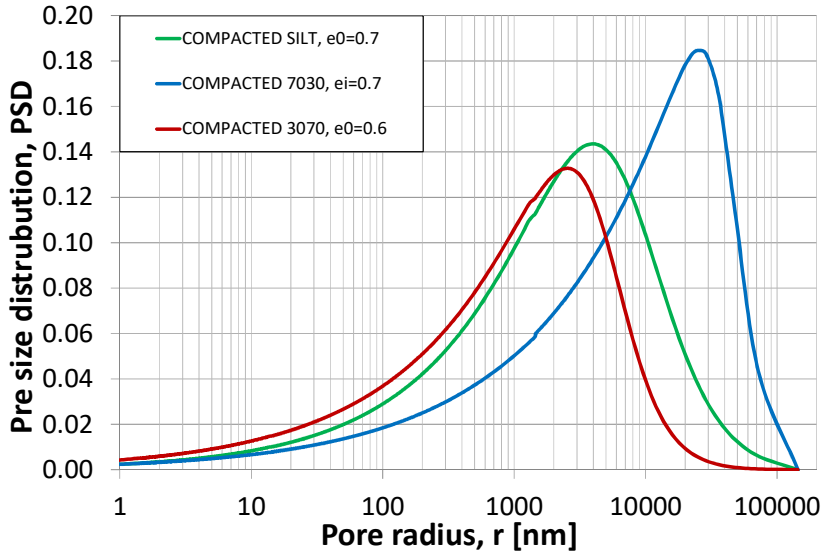

(b)

Fig. 5.21 - (a) Pore size distributions of Stava silt samples OED_SILT_0.5, OED_SILT_0.6, OED_SILT_0.7 and (b) Stava mixtures OED_SILT_0.7, OED_7030_0.7, OED_3070_0.6.

The effect of void ratio on the pore size distribution can be observed by comparing the PSD of silt samples with different initial density, i.e. sample OED_SILT_0.7 (green line), sample OED_SILT_0.6 (brown line) and sample OED_SILT_0.5 (yellow line) shown in Fig. 4.21a. It can be observed from Fig. 5.21a that the peak of the sample OED_SILT_0.7 occurs at a larger radius than the one of OED_SILT_0.6 and OED_SILT_0.5. This is consistent with their estimated air entry values given in Tab 5.5. The pore size distribution of sample OED_SILT_0.7 is wider than the pore size distribution of sample OED_SILT_0.6 and OED_SILT_0.5. This means that sample OED_SILT_0.7 has a larger range of pores size than sample OED_SILT_0.6 and OED_SILT_0.5, so sample OED_SILT_0.7 has a lower water retention capability than sample OED_SILT_0.6 and OED_SILT_0.5. This is confirmed by plot shown in Fig. 5.23, representing the cumulative value of the pore size distribution with the pore radius. In other terms, the cumulative value of the pore size distribution is the area below the PSD shown in Fig. 5.22. Sample OED_SILT_0.7 has indeed a bigger cumulative curve than sample OED_SILT_0.5. This means that OED_SILT_0.7 has a higher number of large size pores that can be firstly intruded by water. Same considerations can be made for sample OED_SILT_0.6 and sample OED_SILT_0.8.

The expected effect of grain size distribution on the pore size distribution can be observed by comparison samples with same initial density and different sand-silt percentages, i.e. sample OED_SILT_0.7 (green line) and sample OED_7030_0.7 (blue line) as shown in Fig. 5.21b . The two samples has the same void ratio, but different grain size distributions. Because of the higher fraction of sand in sample OED_7030_0.7 than in sample OED_SILT_0.7, it is expected that sample OED_7030_0.7 is more permeable than sample OED_SILT_0.7. The air entry value of sample OED_7030_0.7 is lower than those of sample OED_SILT_0.7 (Tab 5.4). This is consistent, because lower is the air entry value (AEV), higher is the permeability or void ratio. An expected high permeable sample such as OED_7030_0.7 has many pores, also having big sizes, so lower pressures (AEV) are required to fill them. As can be observed in Fig. 5.21b the peak of the sample OED_7030_0.7 occurs at a higher radius than those of sample OED_SILT_0.7 and this is consistent with their AEV.

The pore size distribution of OED_7030_0.7 seems to be wider than those of sample OED_SILT_0.7. This means that sample OED_7030_0.7 has a larger range of pores size than sample OED_SILT_0.7. This is confirmed by the plot of the cumulative value of pore size distribution with the pore radius (Fig. 5.22) where sample OED_7030_0.7 has a bigger cumulative curve than sample OED_SILT_0.7. Even if sample OED_SILT_0.7 and OED_7030_0.7 have the same initial cumulative value of the PSD (at r = 1nm) due to their same initial void ratio (e_0 = 0.7), cumulative PSD of sample OED_7030_0.7 is bigger than those of OED_SILT_0.7. This means that the mixture OED_7030_0.7 has a higher number of large size pores that can be firstly filled by water.

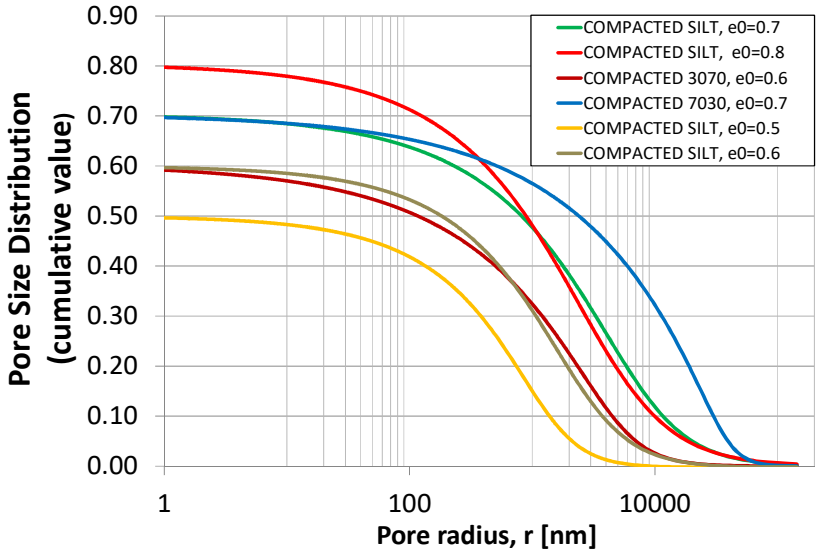

Fig. 5.22 - Intruded void ratio of Stava tailing samples.

5.4.6 Influence of void ratio on the water retention curve

The influence of void ration e on hydraulic response was also investigated by using the model proposed by Gallipoli *et al.* (2003) for the estimation of the water retention curve. As state in chapter 3.2.3.2, Gallipoli *et al.* (2003) proposed a model aimed to include the influence of the variation of the void ratio on the hydraulic behaviour. The soil constant α introduced by Van Genuchten (1980) is then replaced as follow:

$$\alpha = \Phi(v-1)^{\Psi} = \Phi e^{\Psi} \tag{5-13}$$

where Φ, Ψ are soil parameters, while and v is the specific volume. Hence the Gallipoli formulation is given (eq. 5-14):

$$S_r = \frac{1}{(1+[\Phi e^{\Psi} s]^n)^m} \tag{5-14}$$

This model requires the calibration of four parameters (ψ, Φ, n, m) instead of three (α, n, m) as required by Van Genuchten model. Despite the higher number of required parameter, Gallipoli's model allows to describe the water retention curves at different void ratio by

using a constant set of ψ, Φ, n, m parameters, only changing the void ratio e. In the current research Gallipoli formulation is adopted to model both main drying and main wetting curves of the three as compacted silty samples OED_SILT_0.5, OED_SILT_0.6 and OED_SILT_0.7. Sample OED_SILT_0.8 was not taken into account for the calibration process because its preparation technique didn't involve a static compaction as did for the other silty sample.

It is also expected that the air entry value of the soil depend on the void ratio, as follows:

$$AEV = \frac{1}{\Phi e^{\psi}} \tag{5-15}$$

According to Gallipoli *et al*., (2003), knowledge of normal compression line in *s*-*Sr*-*e* space would allow a three-dimensional least-squares fit of eq. 5-14 in order to calibrate ψ, Φ, n, m parameters. In the current research the same parameters were obtained by following a different procedure. The AEV of each samples is plotted with void ratio and the points are then fitted by means of a potential law, according to eq. 5-15:

$$AEV = ax^{b} \tag{5-16}$$

Values of Φ and ψ can be obtained:

$$\Phi = a^{-1} \tag{5-17a}$$
$$\psi = -b \tag{5-17b}$$

Calibration of n and m is finally required, hence Gallipoli formulation can be implemented just changing the void ratio and keeping constant Φ, ψ, n, m parameters. The same procedure is repeated also for the main wetting curve. The parameters n, m, Φ, ψ for this path are given in Tab. 5.6. The values of air entry values estimated by means Gallipoli relationship at different void ratio are shown in Tab. 5.7.

Tab 5.6 - Calibrated parameters (n, m, Φ, ψ) for water retention curve estimated by means Gallipoli model based on OED_SILT_0.5, OED_SILT_0.6, OED_SILT_0.7.

Main drying branch				**Main wetting branch**			
n	**m**	**Φ**	**Ψ**	**n**	**m**	**Φ**	**Ψ**
[-]	**[-]**	**[-]**	**[-]**	**[-]**	**[-]**	**[-]**	**[-]**
1.38	0.43	0.299	5.01	1.00	0.62	2.38	6.58

Tab 5.7 - Estimated air entry values (AEV), dry branch, for Stava silty tailing at different void ratio.

e [-]	0.5	0.6	0.7	0.8
AEV [kPa]	108.0	43.5	20.1	10.3

Figure 5.23a, b, c shows the experimental points and the theoretical relationship proposed by Gallipoli for sample OED_SILT_0.5, OED_SILT_0.6, OED_SILT_0.7.

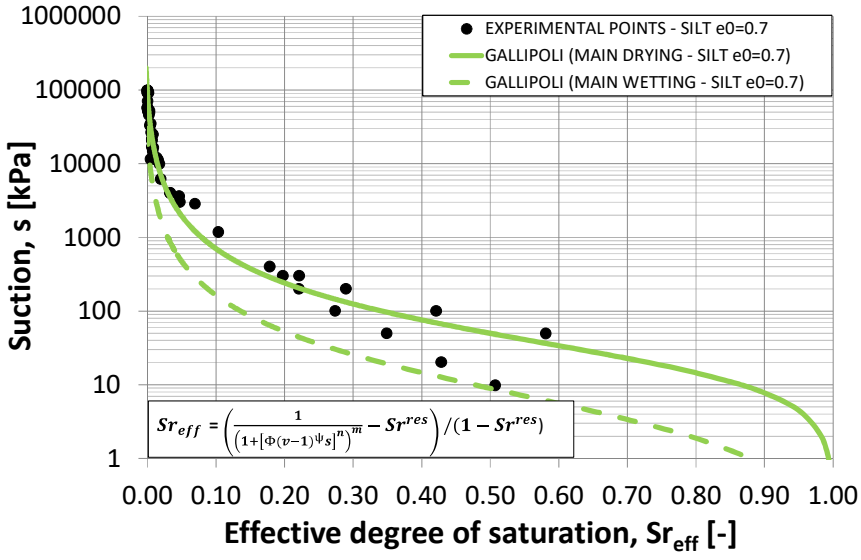
EXPERIMENTAL POINTS - SILT e0=0.7
GALLIPOLI (MAIN DRYING - SILT e0=0.7)
GALLIPOLI (MAIN WETTING - SILT e0=0.7)
Suction, s [kPa]
1000000
100000
10000
1000
100
10
1
0.00 0.10 0.20 0.30 0.40 0.50 0.60 0.70 0.80 0.90 1.00
Effective degree of saturation, Sr eff [-]
$Sr_{eff} = \left(\frac{1}{\left(1+[\Phi(v-1)\psi s]^n\right)^m} - Sr^{res}\right)/(1 - Sr^{res})$

(a)

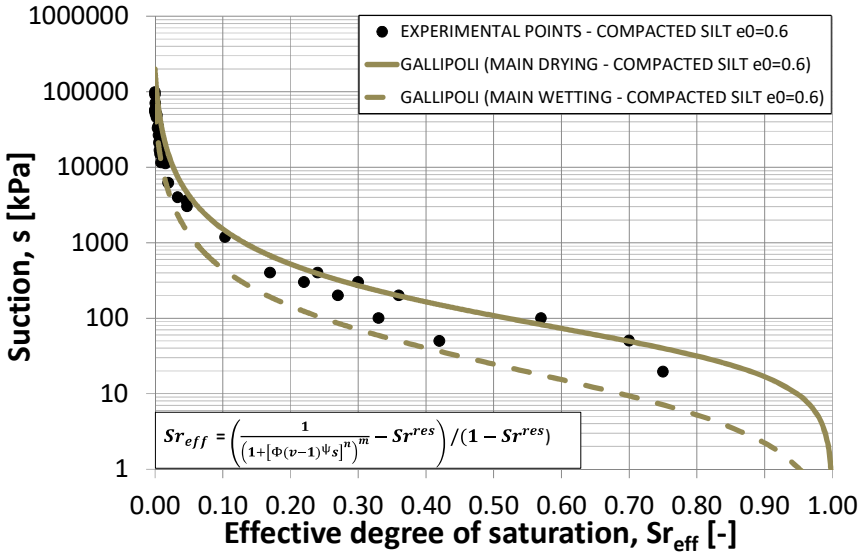
EXPERIMENTAL POINTS - COMPACTED SILT e0=0.6
GALLIPOLI (MAIN DRYING - COMPACTED SILT e0=0.6)
GALLIPOLI (MAIN WETTING - COMPACTED SILT e0=0.6)
Suction, s [kPa]
1000000
100000
10000
1000
100
10
1
0.00 0.10 0.20 0.30 0.40 0.50 0.60 0.70 0.80 0.90 1.00
Effective degree of saturation, Sr eff [-]
$Sr_{eff} = \left(\frac{1}{\left(1+[\Phi(v-1)\psi s]^n\right)^m} - Sr^{res}\right)/(1 - Sr^{res})$

(b)

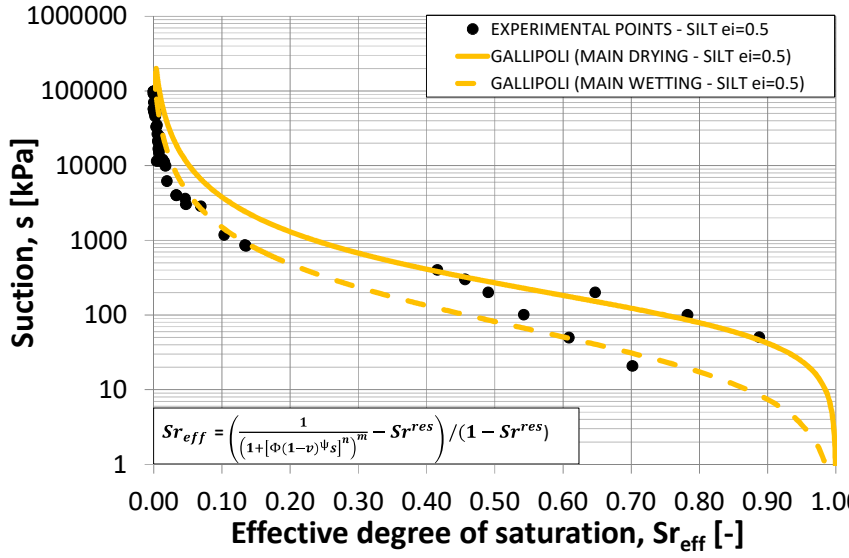

(c)

Fig. 5.23 - Experimental points and water retention curve (s-Sr_{eff}) according to Gallipoli model for (a) sample OED_SILT_0.7, (b) sample OED_SILT_0.6, (c) sample OED_SILT_0.5.

In the three cases represented in Fig 5.23 there is a quite good accordance between the theoretical fitting curve proposed by Gallipoli and the experimental points, especially for main drying curves. For these reasons, Gallipoli model will be used in the following chapter to include the hydro-mechanical stress path resulting from triaxial tests inside a three-dimensional water retention domain. Figure 5.24a,b and Fig, 5.25a,b show the water retention curve in s-Sr_{eff} and s-e_w planes respectively, corresponding to the void ratios of the compacted silt samples tested in the current study ($e_0 = 0.5$, $e_0 = 0.6$, $e_0 = 0.7$), together with the estimated water retention curve at higher ($e_0 = 0.8$) or lower void ratio ($e_0 = 0.4$).

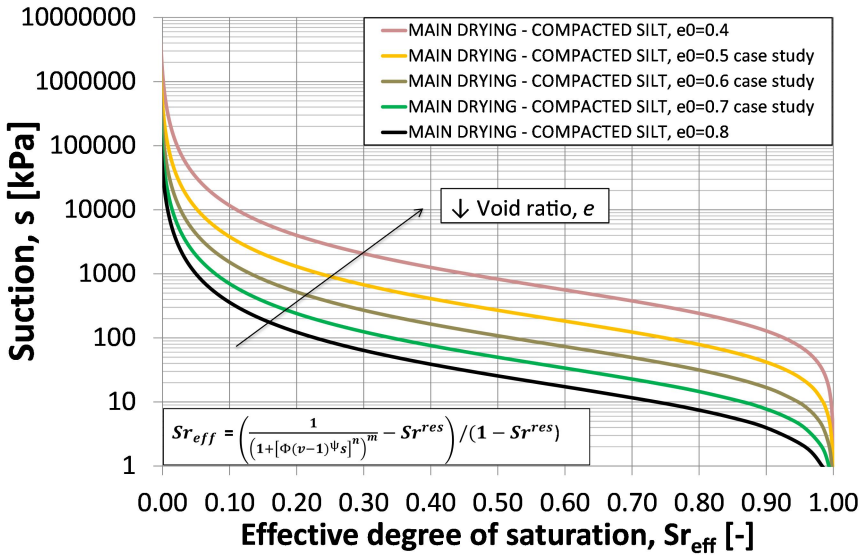

(a)

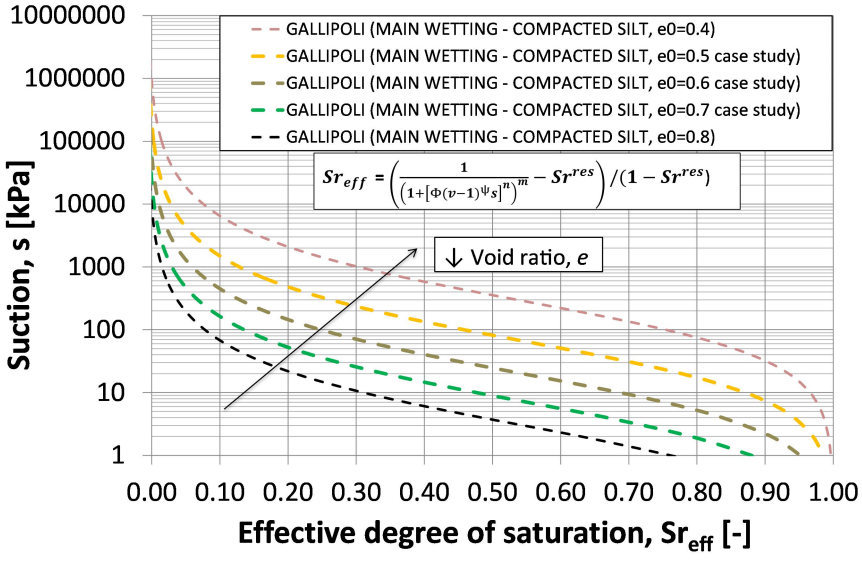

(b)

Fig. 5.24 - Main drying curves (a) and main wetting curves (b) of Stava silty tailing at different void ratio, water retention curve estimated by means Gallipoli model (s-Sr_{eff}).

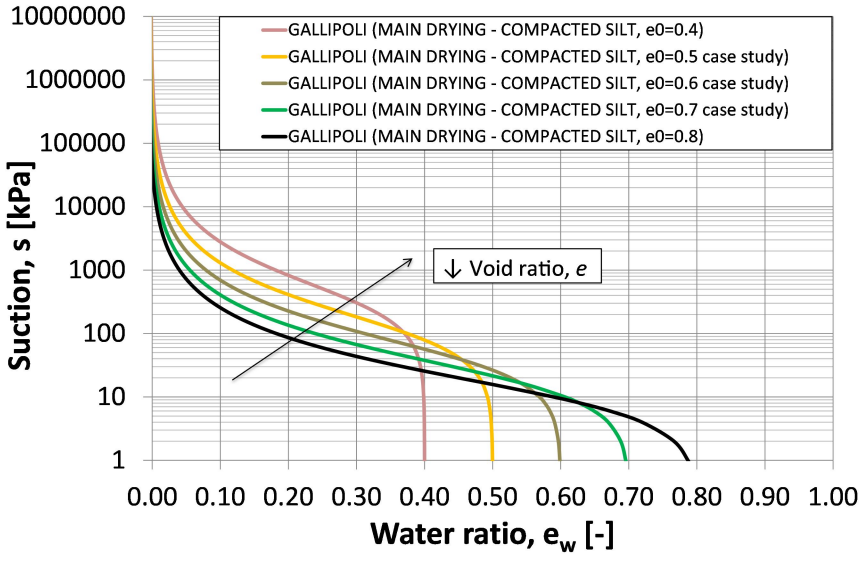

(a)

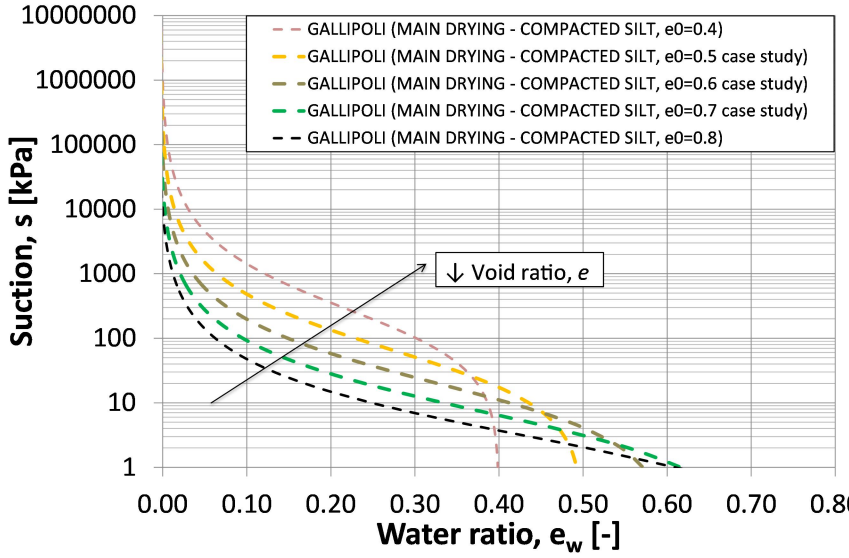

(b)

Fig. 5.25 - Main wetting curves (a) and main drying curves (b) of Stava silty tailing at different void ratio, water retention curve estimated by means Gallipoli model (s-e_w).

Finally, some literature data showing the main drying branches of WRC for different type of soils (tailings and more standard materials) under different compaction states are given in Fig. 5.26 in order to highlight similarities and differences with results of the current research.

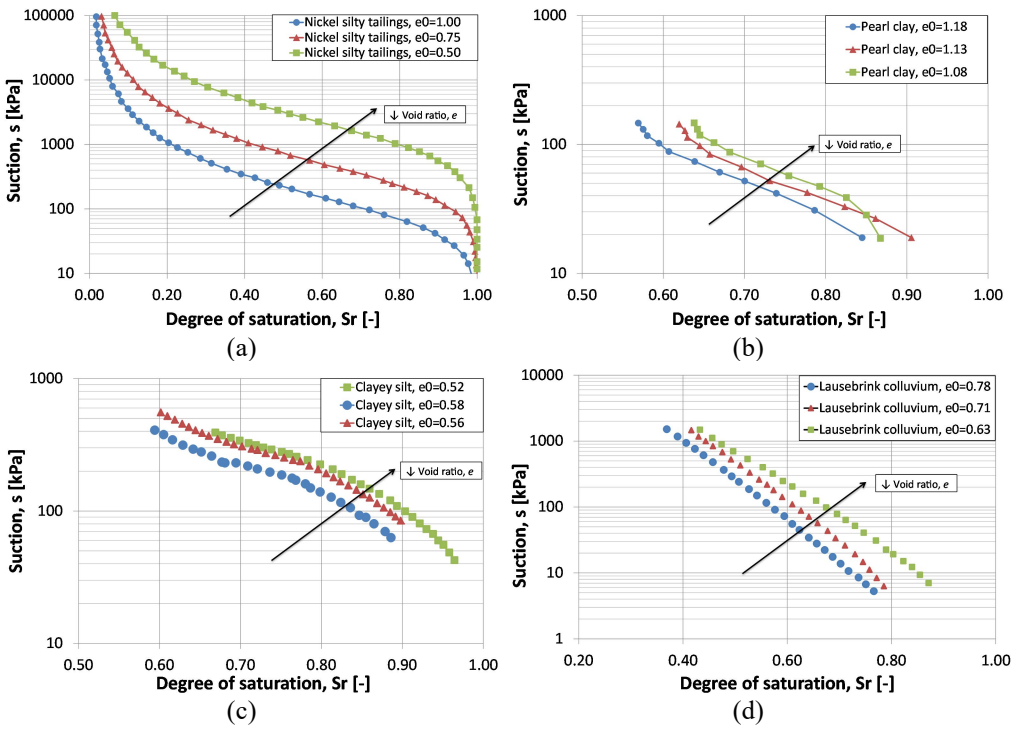

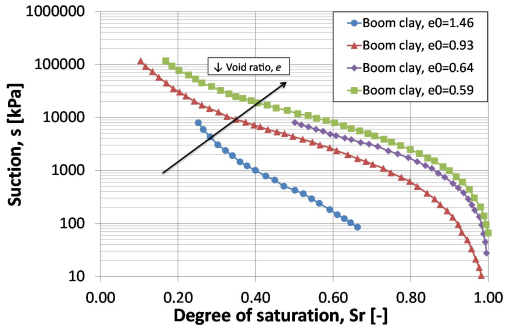

(e)

Fig. 5.26 - Water retention curves for different type of soils:
(a) Nickel tailings (modified from Zanardin *et al*., 2009);
(b) Pearl clay (Sun *et al*., 2007);
(c) Clayey silt (modified from Vanapalli *et al*., 1999);
(d) Lausebrink colluvium (modified from Sugii *et al*., 2002);
(e) Boom clay (modified from Romero, 1999).

Figure 5.26a shows the best fitting water retention curves obtained from nickel tailing samples, coming from the Pedro Sotto Alba tailings impoundment located in the southeast of Cuba, for different compaction states (e_0 = 1.00, e_0 = 0.75, e_0 = 0.50). Figure 5.26b gives the WRC for different initial void ratios (e_0 = 1.18, e_0 = 1.13, e_0 = 1.08) on Pearly clay specimens for a suction range between 10 and 200kPa. Figure 5.26c shows the WRC obtained from a compacted clayey silt for three different initial void ratios (e_0 = 1.00, e_0 = 0.75, e_0 = 0.50), while Fig. 5.26d gives the WRC for a loam (e_0 = 0.78, e_0 = 0.71, e_0 = 0.63). Finally, Fig. 5.26e gives the main drying water retention curves at different compaction states (e_0 = 1.46, e_0 = 0.93, e_0 = 0.64, e_0 = 0.59) for Boom clay specimens. These literature data, both for tailing materials (Fig. 5.26a) and more standard soils (Fig. 5.26b - Fig. 5.26e) show good agreement with results of the water retention tests obtained in the current research on Stava tailings at different compaction state (Fig. 5.17 and Fig. 5.24). Indeed, in both cases and within the suction range investigated, the water retention curves are shifted upward with decreasing initial void ratio of the compacted soil. Finally, as shown from the current research and literature data on standard soils, except for very loose Boom clay specimen e_0 = 1.46 (Fig. 5.26e), the void ratio changes seems not alter the shape of the WRC.

5.5 SUMMARY AND FINAL CONSIDERATIONS

A deep knowledge of the water retention curve is essential to assess stability problems in terms of shear strength. Indeed, many formulations have been proposed to predict the shear strength in unsaturated conditions by knowledge of some parameters of the water retention curve, (e.g. through suction acting at failure). For these purposes, the hydraulic behavior of unsaturated tailings mixtures was studied in terms of water retention tests. Opposite effects of fine contents and void ratio on Stava tailing are also investigated in terms of water retention curve and expected pore size distribution. Results in terms of water retention curve obtained from a limited number of sample at different void ratio are extended, by means of the Gallipoli model in order to extend the hydraulic characterization to a larger domain of void ratio and to allow implementation in modelling. Changes in void ratio and grain size distribution were confirmed to strictly affect main drying and wetting curves and so the hydraulical behavior of soils in terms of water retention curve. Because of the in situ heterogeneity of tailing materials within the basin, results obtained from water retention tests representing different vertical cross sections and depths can be used in numerical modelling of tailing basins to better approach stability problems, allowing reliable predictions. These results will be used and integrated in the next chapter with an hydro-mechanical characterization tests by means of unsaturated triaxial tests.

REFERENCES

1. Ethington E.F. 1990. Interfacial contact angle measurements of water, mercury, and 20 organic liquids on quartz, calcite, biotite, and Ca-montmorillonite substrates. Rep., USGS, 90-409, 1–18.

2. Gallipoli D., Wheeler S.J., Karstunen M. 2003. Modelling the variation of degree of saturation in a deformable unsaturated soil. Geotechnique, **53**, 1: pp. 105–112.

3. Nocera E. 2017. Studio sperimentale del comportamento idromeccanico in condizioni non sature del limo di Stava. MSc. thesis, Politecnico di Torino.

4. Romero E. 1999. Characterisation and thermo-mechanical behaviour of unsaturated Boom clay: An experimental study. Ph.D. thesis, UPC Barcelona.

5. Romero E. and Jommi C. 2008. An insight into the role of hydraulic history on the volume changes of anisotropic clayey soils, Water Resources Research, 44.

6. Sugii T., Yamada K. and Kondou T. 2002. Relationship between soil-water characteristic curve and void ratio. In UNSAT 2002, Proc. 3rd Unsaturated Soils Conference, Recife, eds. Juca, de Campos and Marinho, pp. 209-214.

7. Sun D., Sheng D. and Xu Y. 2007. Collapse behaviour of unsaturated compacted soil with different initial densities. Can. Geotech. J. **44**, pp. 673-686.

8. Van Genuchten M.T. 1980. A closed-form equation for predicting the hydraulic conductivity of unsaturated soil. Soil Sci. Soc. Am. J. Vol. **44**, pp. 892–898.

9. Vanapalli S.K., Fredlund D. and Pufahl D.E. 1999. The influence of soil structure and stress history on the soil-water characteristics of a compacted till. Geotechnique, 49(2), pp.143-59.

10. Zanardin M.T., Oldecop L.A., Rodriguez R. and Zabala F. 2009. The role of capillary water in the stability of tailing dams, Engineering Geology, 105, pp. 108-118.

6 Hydro-mechanical behaviour of Stava tailings in unsaturated conditions

This chapter is devoted to the description and analysis of the experimental work on the hydro-mechanical behaviour of unsaturated specimens of Stava silt under shearing paths, with special reference to the behaviour at critical state conditions. Different specimens, having different degree of saturation, imposed suction and initial void ratio, are tested at different confining levels. In the first part, this chapter gives a framework about the critical state models in unsaturated soil mechanics, summarizing the different approaches proposed by several authors, based on experimental or theorical considerations. After that, the concept of state boundary surfaces is presented. The preliminary characterization involved oedometer tests performed under constant degree of saturation in order to estimate the preconsolidation stress and its dependency on suction. The suction-controlled triaxial cell used for the unsaturated hydro-mechanical characterization of Stava silt tailings is described, together with the sample preparation techniques and the different test phases. A detailed description of the experimental results obtained from suction controlled triaxial tests is given for one test, together with the main results of the whole experimental campaign. Finally, an overall comparison and interpretation of the experimental results is proposed.

6.1 CRITICAL STATE CONDITIONS IN UNSATURATED SOIL MECHANICS

6.1.1 Critical state condition for saturated soils

The concept of critical state is a fundamental one for the description of the mechanical behaviour of saturated soils. The critical state is defined as an ultimate condition, attained at large deviator strains. In this state, as deformation proceed with shearing, a saturated volume of soil tends toward an ultimate state in which shearing strains can continue without further variations of volume or mean effective stresses:

$$\frac{\delta \varepsilon_v}{\delta \varepsilon_s} = \frac{\delta q}{\delta \varepsilon_s} = \frac{\delta p'}{\delta \varepsilon_s} = 0 \tag{6-1}$$

where ε_v is the volumetric strain, ε_s is the deviatoric strain, q is the deviator stress and p' is the mean effective stress. If the collection of critical state conditions attained at different confining pressures are plotted in (q-p') plane as shown in Fig. 6.1a, the critical state condition projects a line known as Critical State Line (*CSL*) having a constant slope M:

$$M = \frac{q_{cs}}{p'_{cs}} = \frac{6\sin(\Phi_{cv})}{3 - \sin(\Phi_{cv})} \tag{6-2}$$

where Φ_{cv} is the friction angle at critical state. If the same data are plotted in the compression plane (v,p'), as shown in Fig. 6.1b, the Critical State Line has a constant slope λ

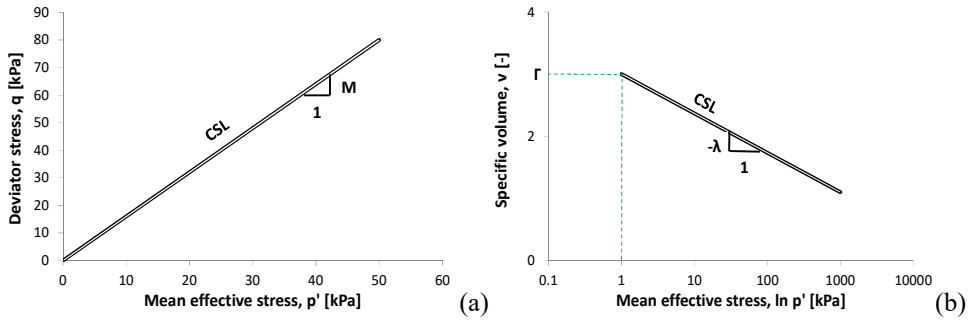

Fig. 6.1 - Critical State Lines in (q-p') and (v-p') planes.

The approach to model the critical state for saturated soils involves three variables (p', q, v) and two critical state equations aimed to predict the deviator stress (q) and specific volume (v), according to eq. 6-3a and 6-3b:

$$q = Mp' \tag{6-3a}$$
$$v = \Gamma - \lambda \ln(p') \tag{6-3b}$$

where M, Γ and λ are the critical state parameters for saturated conditions. Description of Critical State for soils in unsaturated conditions requires further variables to be taken into account. These variables are those inherently associated to the more general description of state and behaviour of unsaturated soils. Different approaches have been proposed for the definition of a critical state locus. According to Tarantino (2007), the extension to model the possible critical state of soils in unsaturated conditions involves five variables (p, s, q, e , e_w) and three critical state equations in order to predict the deviator stress, the degree of saturation and the void ratio, when p and s are given, according to eq. 6-2a, 6-2c:

$$f_1(p, s, q, e, e_w) = 0 \tag{6-4a}$$
$$f_2(p, s, q, e, e_w) = 0 \tag{6-4b}$$
$$f_3(p, s, q, e, e_w) = 0 \tag{6-4c}$$

Triaxial tests performed on gravel and sandy clay, let Toll (1990) and Toll and Ong (2003) estimate the deviatoric stress at critical state as:

$$q = M_a(S_r)p_{net} + M_b(S_r)s \tag{6-5}$$

where the two slopes M_a and M_b depend on the degree of saturation.
In 1996, Vanapalli *et al*. proposed an approach based on the concept of effective degree of saturation:

$$q = M(p_{net} + sSr^k) \tag{6-6}$$

The Authors suggested that when there is no any clay fraction or of it can be neglected, and little or no aggregates are expected, experimental data can be fitted by imposing e_{wm}=0 and

the exponent *k* can be set equal 1 emphasizing the concept that e_{wm} is correlated with the clay fraction.

Basing on results of triaxial tests of Speswhite kaolin, Wheeler and Sivakumar (1995, 2000), proposed estimating the ultimate deviatoric stress as follow (eq. 6-7):

$$q = M(s)p_{net} + \mu(s) \tag{6-7}$$

where the two functions *M(s)* and *μ(s)* can be assumed as fitting parameters that depend on suction level.

Rampino *et al*. (2000), presented triaxial data for silty sand and suggested modelling the ultimate deviatoric stress (eq. 6-8):

$$q = Mp_{net} + \mu(s) \tag{6-8}$$

where *M* is the saturated critical state parameter and *μ(s)* is a function of suction level. It is worth to note that the model proposed by Rampino *et al*. (2000) is simpler than those proposed by Wheeler and Sivakumar (1995, 2000) because in the first case the stress ratio is a constant value, while in the latter case the stress ratio depend from the suction level.

Tarantino and Tombolato (2005) proposed to model the shear strength q in terms of degree of saturation the macro-pores Sr_M:

$$q = M(p_{net} + sS_{rM}) \tag{6-9}$$

where *M* is the slope of the saturated critical state line (*CSL*) in the (*p'*,*q*) plane, e_w is the water ratio at critical state. The degree of saturation of the macro-pores Sr_M is defined as:

$$S_{rM} = \frac{e_w - e_{wm}}{e - e_{wm}} \tag{6-10}$$

where e_{wm} is an additional parameter known as microstructural water ratio that is related with the adsorbed water in the saturated aggregates (Tarantino and Mountassir, 2013). This parameter, according to Romero and Vaunat (2000), separates the region of inter-aggregate porosity from the region of intra-aggregate porosity. The idea of this approach based on the concept of microstructural water ratio is that only capillarity water filling the macro-pores (water in the pores between aggregates) has an effect on the shear strength.
Even if no significant differences in terms of accuracy can be observed between the approach proposed by Tarantino and Tombolato (2005) and Wheeler-Sivakumar (1995, 2000), the first one is simpler because only one parameter (e_{wm}) is required, instead of two, *M(s)* and *μ(s)*.
As reported in Tarantino and Mountassir (2013), the models proposed by Tarantino and Tombolato, 2005 (eq. 6-9) and Vanapalli *et al*., 1996 (eq. 6-6) are validated, resulting that in both cases, the experimental data of different types of soils are fitted well, in a similar way.

6.1.2 Degree of saturation and void ratio at critical state

A formulation in order to estimate the void ratio at critical state in unsaturated conditions was proposed by Gallipoli *et al.* (2003):

$$e_{uns} = [\Gamma - \lambda \ln(p + sS_{rM})]\{1 - a[1 - \exp(b\xi)]\} \quad (6\text{-}11)$$

where Γ and λ are the critical state parameters in saturated conditions, a and b represent two other parameters that can be obtained from isotropic compression test. In the current research a and b are obtained as fitting parameters from the e/e_{sat} - ξ graph. It worth noting that e is the experimental void ratio at critical state in unsaturated conditions, while the void ratio at critical state in saturated conditions e_{sat} can be obtained by knowledge of Γ, λ:

$$e_{sat} = \Gamma - \lambda \ln(p') \quad (6\text{-}12)$$

where p' is the mean Bishop stress:

$$p' = p_{net} + \chi s = (\sigma - u_a) + Sr(u_a - u_w) \quad (6\text{-}13)$$

The parameter ξ is the bonding variable, defined as:

$$\xi = f(s) \cdot (1 - S_r) \quad (6\text{-}14)$$

The variable ξ takes into account the magnitude of the inter-particle bonding due to water menisci and it can be considered resulting of two contributions (Gallipoli *et al.,* 2003). The first is represented by the number of water menisci per unit volume of the solid fraction. In eq. 6-14 this contribution is related to the degree of saturation of air (1-*Sr*). The second is the normal force exerted at the inter-particle contact by a single water meniscus *f(s)*, which depends on suction and it can be obtained from the analytic solution of Fisher (1926).
If the degree of saturation is given by:

$$S_r = \frac{e_w}{e} \quad (6\text{-}15)$$

Equation 6-11 can be rewritten as:

$$e_{uns} = \left[\Gamma - \lambda \ln\left(p + s\frac{e_w}{e}\right)\right] \cdot \left\{1 - a\left[1 - \exp\left(b \cdot f(s) \cdot \left(1 - \frac{e_w}{e}\right)\right)\right]\right\} \quad (6\text{-}16)$$

It is worth noting that eq. 6-11 (or eq. 6-16) are expressed in term of total degree of saturation, but the degree of saturation of the macro-pores (S_{rM}) can be more appropriate (Tarantino, 2007).

6.1.3 State boundary surfaces

An approach to the critical state theory of soil mechanics was given in 1950s-1960s at Cambridge University by introducing two state boundary surfaces, Roscoe Surface and Hvorslev Surface, respectively. This approach is aimed to explain, in q/p'_e - p'/p'_e space, the difference in shear response between normally consolidated and over-consolidated saturated soils. Under saturated conditions, a soil that is drier or denser than the critical state will show a dilative behaviour to reach the critical state (drained conditions), or a decrease in pore water pressure (undrained conditions). On the other hand, a soil that is wetter or looser

than the critical state will exhibit a contractive behaviour to reach the critical state (drained conditions), or an increase in pore water pressure can be measured (undrained conditions). In saturated conditions. All drained and undrained stress paths performed on normally consolidated soils lie on a three-dimensions surface bounded by the critical state line at the top and the normal consolidation line at the bottom. This 3D surface is defined as the Roscoe Surface, as given in Fig. 6.2. On the other hand, the Hvorslev Surface links up with the Roscoe surface at the critical state line. It is a straight line in the normalized space of q/p'_e - p'/p'_e and it cannot extent to the q/p'_e axis because of the no tension line, as shown in Fig. 6.2.

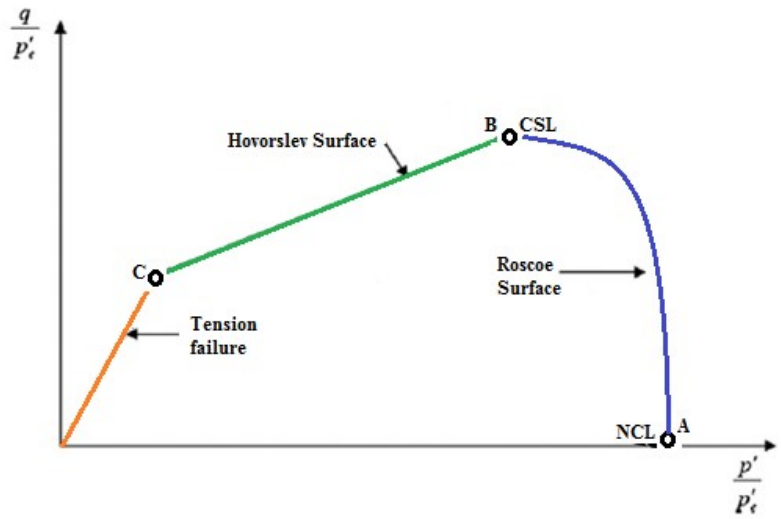

Fig 6.2 - Saturated conditions: state boundary surfaces.

The equivalent pressure p'_e is defined as:

$$p'_e = e^{\left[\frac{N(0)-v}{\lambda(0)}\right]} \tag{6-17}$$

where $N(0)$ and $\lambda(0)$ are the intercept (p' = 1kPa) and slope of the saturated virgin line, respectively. Under saturated conditions, the Hvorslev surface in the q/p'_e - p'/p'_e plane has equation:

$$\frac{q}{p'_e} = g + h\left(\frac{p'}{p'_e}\right) \tag{6-18}$$

where g and h are the intercept and slope of Hvorslev surface, respectively. The complete state boundary surface (for drained and undrained tests on normally consolidated and over-consolidated samples in saturated conditions) is given by both Roscoe Surface and Hvorslev surface. The latter one was detected by several authors with compression and extension tests (e.g. Houlsby *et al.* 1982).

Some authors have attempted to extend this framework to unsaturated soils (Toll, 1990; Wheeler and Sivakumar, 1995; Maâtouk *et al*., 1995; Wang *et al.,*2002; Loret and Khalili, 2002; Toll and Ong, 2003; Khalili *et al.*, 2004; Tarantino, 2007; Estabragh and Javadi, 2008; Jotisankasa *et al.*, 2009), but the experimental data are still scarce because of the complex

and time-consuming nature associated with the testing of unsaturated soils. Under unsaturated conditions, the Hvorslev surface in the q/p'_e - p'/p'_e can be defined as:

$$\frac{q}{p'_e} = g(s) + h(s) \cdot \left(\frac{p_{net}}{p'_e}\right) \tag{6-19}$$

where $g(s)$ and $h(s)$ are the intercept and slope of Hvorslev surface at a certain suction s, while p_{net} is the net stress. According to Estabragh and Javadi (2014), in unsaturated conditions normally consolidated samples (or with low *OCR* ranging between 1.37 and 2.75) approach the critical state from the Roscoe surface, as for saturated soils. On the other hand, over-consolidated samples (i.e. *OCR* ranging between 5.5 and 11) approach the critical state condition from the Hvorslev surface.
Estabragh and Javadi (2014) show results of a mechanical characterization carried out on unsaturated compacted silt specimens (inorganic silt, very fine sand) prepared with moist tamping technique. The Roscoe and Hvorslev state boundary surfaces for the unsaturated soil were studied by means drained triaxial shearing tests on the unsaturated samples with different *OCR*. Stress path at different suction and *OCR* are shown in Fig. 6.3. Samples with high *OCR* (*OCR* = 11 and σ_3 = 50kPa; *OCR* = 5.5 and σ_3 = 100kPa) approach the critical state condition from the Hvorslev surface. Samples with low *OCR* (*OCR* = 2.75 and σ_3 = 200kPa; *OCR* = 1.37 and σ_3 = 400kPa) approach the critical state condition from the Roscoe surface.

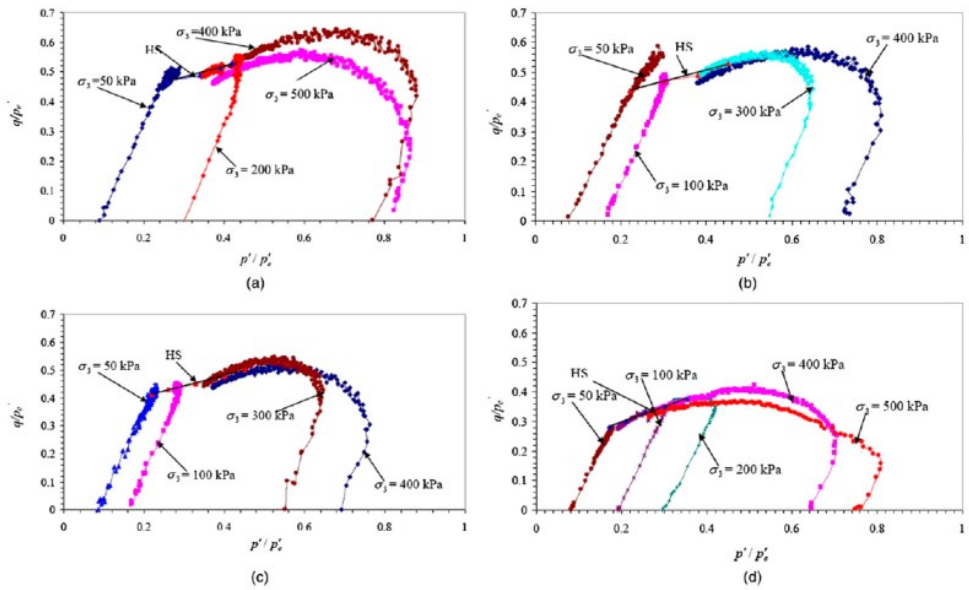

Fig. 6.3 - Stress paths for samples sheared at different suction levels (a: s = 300kPa; b: s = 200kPa; c: s = 100kPa; d: s = 0kPa) and different *OCR* (Estabragh and Javadi, 2014).

The Authors observed that (Fig. 6.3), during suction-controlled triaxial shearing, Roscoe surface expands by increasing the suction, Hvorslev surface remains planar, parallel, moving up by increasing the suction, and finally the term h remains constant by increasing the suction while $g(s)$ increases by increasing the suction.

6.2 OVERVIEW OF SOME CONSTITUTIVE MODELS FOR UNSATURATED SOILS

The Barcelona Basic Model (BBM), proposed by Alonso *et al*. (1990), is one of the most widely adopted elasto-plastic critical state constitutive model for soils in unsaturated conditions. Representing an extension of the Modified Cam Clay Model (Roscoe and Burland, 1968) for saturated soils, the BBM is intended to model low-moderate plasticity fine-grained soils and it is able to account for aspects of the mechanical behaviour of soils in unsaturated conditions (i.e. volume change and shear strength behaviour) in the three-dimensional stress space (*p, q, s*) by using two independent stress variables: matric suction and net stress. Within the frame of BBM, the compressibility of the soil is a function of suction. The Author assumed that the compression index (λ) decreases with suction, so the predicted collapse potential increases with the mean stress *p* (Fig. 6.4a). The model proposed by Wheeler and Sivakumar (1995) is similar to BBM, but fewer simplifications are introduced in order to have a more flexible model. Unlike the Barcelona Basic Model, in Wheeler's model the normal compression lines are fitted by means of experimental data at different suction. Furthermore, in Wheeler's model the compressibility index was assumed to increase with suction because it was observed that the compressibility of the soil increased since large pores formed during drying process. Consequently, the collapse potential predicted by this model decreases with the means stress, as shown in Fig. 6.4b. Within the model proposed by Jommi (2000), the behaviour of unsaturated soil is interpreted by using the average soil skeleton stress (difference between the total stress and the mean value of the fluid pressures weighted with the degree of saturation) as an effective stress. In the net mean stress-specific volume plane (Fig. 6.4c), the NCL for unsaturated soil is no more linear. In this model, the unsaturated compression index decreases with suction, but increases with net stress. It is worth to point out that it always remains smaller than saturated compression index.

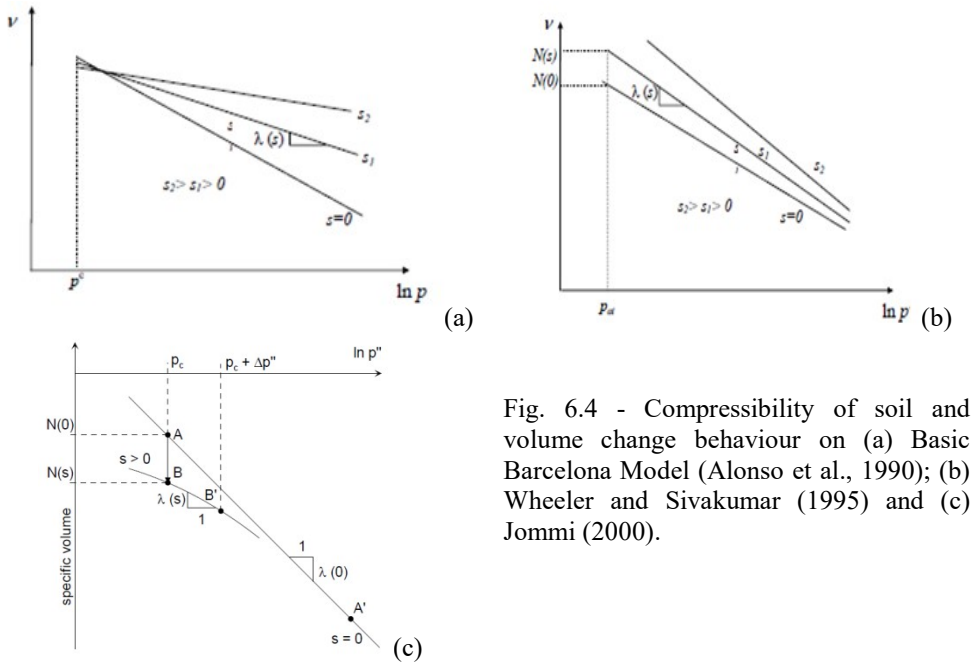

Fig. 6.4 - Compressibility of soil and volume change behaviour on (a) Basic Barcelona Model (Alonso et al., 1990); (b) Wheeler and Sivakumar (1995) and (c) Jommi (2000).

6.3 INFLUENCE OF COMPACTION AND DEGREE OF SATURATION ON THE COMPRESSIBILITY AND PRE-SHEARING STATE OF STAVA SILT

6.3.1 Purposes

Since the initial (pre-shearing) state of the soil has an important effect on the behaviour shown during shearing before reaching the critical state conditions as briefly introduced in previous sections, few 1D compression tests were aimed at characterizing the influence of initial void ratio and degree of saturation on the oedometer curves of Stava silt compacted specimens. Five oedometer tests were performed on unsaturated silt specimens in order to obtain the preconsolidation stress at different initial void ratios and degree of saturation. The tests were performed in conventional oedometers, where no water was placed in the reservoirs and porous stones. A quick loading sequence was applied (load increment each 12 hours). Mass based analysis performed at the end of the test show that the degree of saturation remained about constant during the tests (as a compensation of water lost because of evaporation and preferential compression/expulsion of air during the tests).
Results of these tests obtained in the current research will be compared with results in saturated conditions obtained by Carrera (2008) in order to investigate the dependency of preconsolidation stress and the stifness from suction.

6.3.2 Oedometer apparatus

Specimens had 50mm diameter and 20mm initial height. The maximum vertical strain that can be measured is 2.5mm with an accuracy equal to ±2μm. Every 12 hours, a steel load was added (loading process) or removed (unloading process), as summarized in Tab. 6.1a and Tab. 6.1b (samples oed_0.70-60 and oed_0.80-90), and Tab. 6.1c and Tab. 6.2c (samples edo_0.60-100, edo_0.60-70 and edo_0.60-50).

Tab 6.1a - Loading process (samples oed_0.70-60 and oed_0.80-90).

σ_v [kPa]	12.3	24.5	49.0	98.1	196.1	392.3	784.5	1569.1	3138.1

Tab 6.1b - Unloading process (samples oed_0.70-60 and oed_0.80-90).

σ_v [kPa]	784.5	196.1	49.0	12.3

Tab 6.1c - Loading process (samples edo_0.60-100, edo_0.60-70 and edo_0.60-50).

σ_v [kPa]	25	50	99.9	199.8	399.7	799.4	1598.8	3197.61	6395.1

Tab 6.1d - Unloading process (samples edo_0.60-100, edo_0.60-70 and edo_0.60-50).

σ_v [kPa]	3197.61	1598.8	799.4	199.8	50	12.5

6.3.3 Sample preparation

Oedometer tests were carried on both "statically compacted" Stava silt specimen (oed_0.70-60, oed_0.60-70, oed_0.60-50) and Stava "hand compacted" silt specimen (oed_0.80-90, oed_0.60-100).
The statically compacted specimen oed_0.70-60 was prepared at initial void ratio e_0 = 0.7 and initial degree of saturation Sr = 60%, while the statically compacted specimens oed_0.60-70 and oed_0.60-50 were prepared at initial void ratio e_0 = 0.6 and initial degree of saturation Sr = 70% and Sr = 50%, respectively. The hand compacted specimen oed_0.80-90 was prepared at initial void ratio e_0=0.8 and initial degree of saturation Sr = 90%, while the sample oed_0.60-100 was prepared at initial void ratio e_0 = 0.6 and initial degree of saturation Sr = 100%.
In the first case, statical compaction was induced by hand-mixing dry soil powder with a certain amount of demineralized, de-aired water. The mixture was put inside a cylindrical mould and it was statically compacted by gradually applying an axial force. A controlled-axial displacement Wykeham Farrance loading frame was used to increment the axial load until the desired volume was reached under controlled water content. The specimen was then extracted from the mould, by keeping it inside the metallic ring and then placed inside the oedometer cell in order to be tested.
In the second case, the specimen was remolded outside the cell at a consistence of a slurry, so it was not performed a static compaction before putting it inside the cell, as it had been done for all the other samples. It was instead compacted by a normal procedure within the oedometer ring to obtain the desired initial state (void ratio and saturation). A similar procedure was adopted, only for saturated samlples edo_028 (e_0 = 0.772), edo_020 (e_0 = 0.885), edo_17 (0.930), edo_019 (0.925), by Carrera (2008). The slurry was carefully poured inside the ring and then placed inside the oedometer cell in order to be tested.

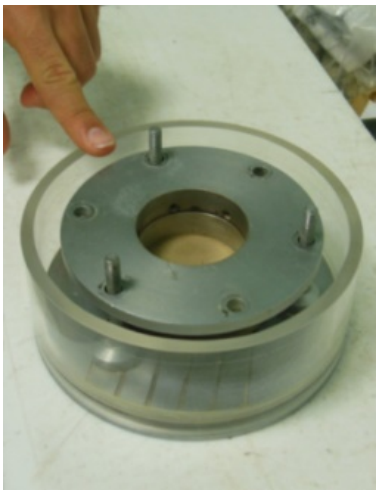

Fig. 6.5 - Plexiglass cell for conventional oedometer apparatus.

Table 6.2 gives the initial state of silt specimens tested by using the conventional oedometer in terms of initial void ratio (e_0), dry weight (γ_d) and degree of saturation (Sr_0).

Tab. 6.2 - List of the tests and initial state.

Sample	e_0 [-]	Sr_0 [%]	γ_d [kN/m^3]	Comments
oed_0.70-60	0.7	60.0	16.6	Statically compacted sample (Current research)
oed_0.80-90	0.8	90.0	15.7	Hand compacted sample (Current research)
oed_0.60-100	0.6	100.0	17.6	Hand compacted sample (Nocera, 2017)
oed_0.60-70	0.6	70.0	17.6	Statically compacted sample (Nocera, 2017)
oed_0.60-50	0.6	50.0	17.6	Statically compacted sample (Nocera, 2017)

6.3.4 Oedometer testing results

Basing on the water retention curve estimated by Gallipoli model, knowledge of degree of saturation allowed to estimate the corresponding suction on the main wetting branch (loading phase) or on the main drying branch (unloading phase). Under such an hypothesis, for each test (during loading and unloading phase) the suction intervals are obtained (Tab. 6.3). As expected, by considering samples prepared at the same initial void ratio (oed_0.60-100, oed_0.60-70, oed_0.60-50), an higher value of suction can be associated to specimens with a lower degree of saturation and vice-versa.

Tab. 6.3 - List of suction intervals.

Sample	Loading phase s [kPa]	Unloading phase s [kPa]
oed_0.70-60	5 ÷ 15	50 ÷ 60
oed_0.80-90	0.5 ÷ 1	9 ÷ 10
oed_0.60-100	~ 0	~ 0
oed_0.60-70	9 ÷ 30	80 ÷ 100
oed_0.60-50	30 ÷ 100	200 ÷ 300

Figure 6.6a shows the oedometric curves, the Normal Compression Line *1D-NCL* (soild black line) and the Critical State Line *CSL* (dotted red line) obtained by Carrera (2008) from Stava silt samples (edo_028, edo_020, edo_17, edo_019) in saturated conditions in the (*e-p'*) plane. Basing on the vertical stress σ_v applied during the loading/unloading phase of the oedometer test, the radial stress σ_r was computed by means of the Jacky formula (eq. 6-20), allowing to obtain the mean effective stress p' (eq. 6-21).

$$\sigma_r = (1 - \text{sen}\Phi)\sigma_v \tag{6-20}$$

$$p' = \frac{\sigma'_v + 2\sigma'_r}{3} \tag{6-21}$$

Figure 6.6b shows the oedometric curves obtained by Carrera (2008) in saturated conditions (edo_028, edo_020, edo_17, edo_019), the oedometric curves obtained in the current research in unsaturated conditions (oed _0.70-60, oed _0.80-90), and the oedometric curves resulting from Nocera (2017) in saturated and unsaturated samples (oed _0.60-100, oed _0.60-70, 0.60-50).
Figure 6.6c shows the *1D*-Normal Compression Line (solid black line) obtained by Carrera (2008) in saturated conditions for samples edo_028, edo_020, edo_17, edo_019. The slopes of oedometric curves obtained by Nocera (2017) in saturated and unsaturated conditions for samples oed _0.60-100, oed _0.60-70, 0.60-50 are represented by the solid blue, pink and green lines respectively.

As a preliminary effort, the preconsolidation stress of saturated specimens (Carrera, 2008) was estimated equal to 840kPa. Data obtained by Nocera (2017) allowed the estimation of the preconsolidation stress of unsaturated specimen oed_0.60-100 (σ'_p = 820kPa), oed_0.60-70 (σ'_p = 900kPa), and specimen oed_0.60-50 (σ'_p = 950kPa). As expected, specimens oed_0.60-70 and oed_0.60-50, due to their low degree of saturation, were stiffer than specimen oed_0.60-100. For this reason, the preconsolidation stress σ'_p of samples oed_0.60-70 and oed_0.60-50 were higher than those of sample oed_0.60-100. It is worth to note that the preconsolidation stress of saturated specimen (Carrera, 2008) was very close to the preconsolidation stress of specimen oed_0.60-100. This is consistent because both samples can be assumed fully saturated or very close to saturated conditions.

Tab. 6.4 - Preconsolidation stress and estimated suction.

Sample	s [kPa]	σ_p [kPa]
oed_0.60-100	~ 0	820
oed_0.60-70	50	900
oed_0.60-50	200	950

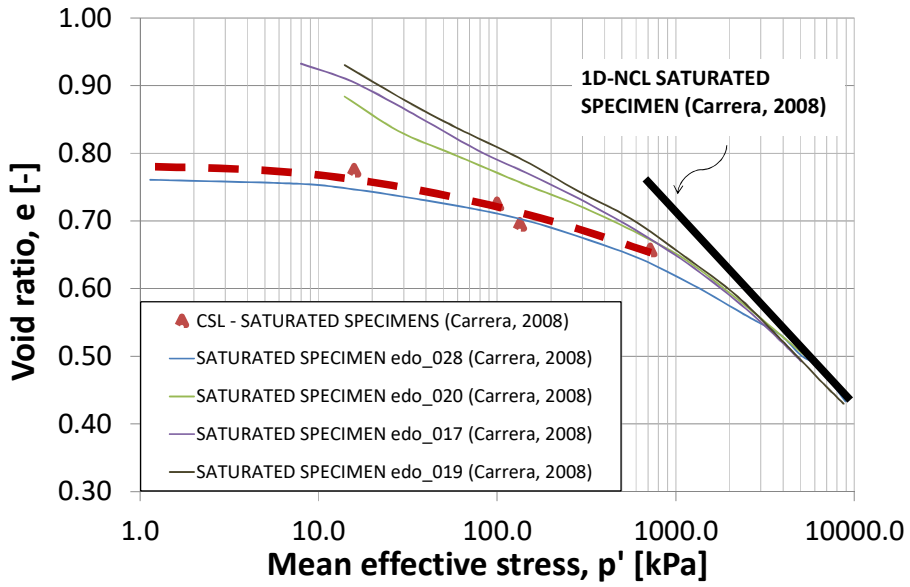

(a)

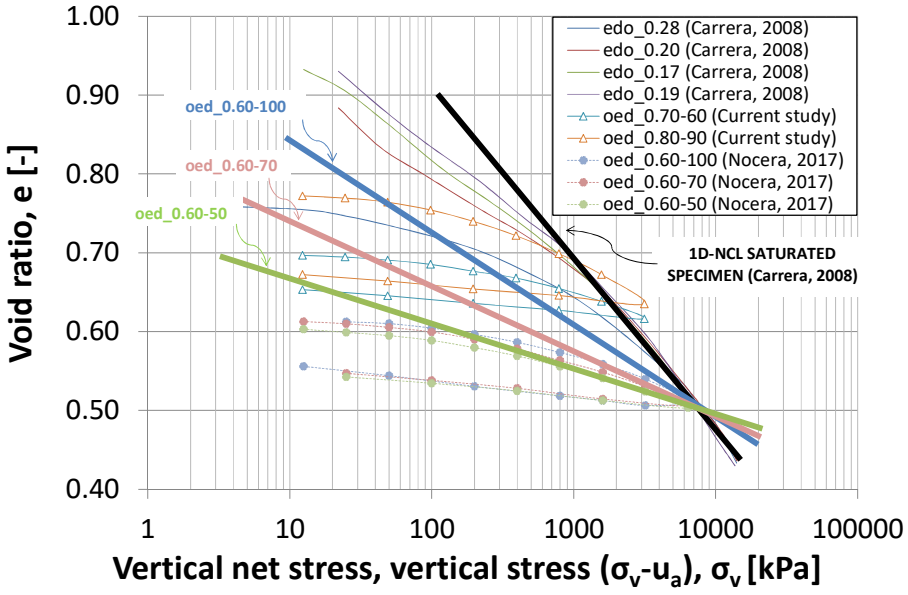

(b)

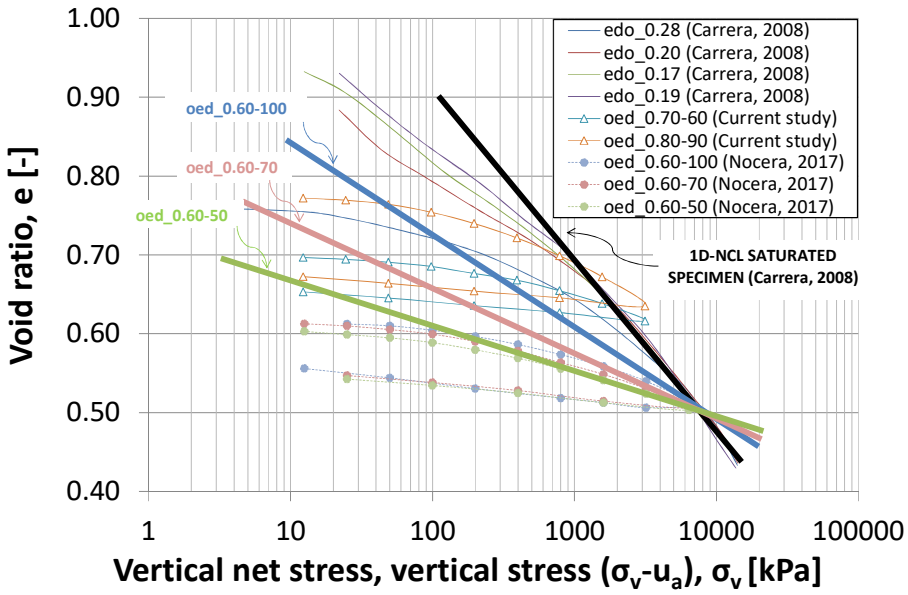

(c)

Fig. 6.6 - (a) Oedometric curves, *1D-NCL* and *CSL* for saturated silt samples. (b) Oedometric curves for saturated specimens and unsaturated specimens. (c) Normal compression lines for saturated and unsaturated specimens.

As given by Fig. 6.6, the slope of the oedometric curves of unsaturated specimens (oed_0.60-100, oed_0.60-70, oed_0.60-50) is lower than those of saturated specimen obtained by Carrera (2008). The unsaturated condition of specimens tested in the current research results in their higher values of suction than those of saturated specimen tested by Carrera (2008). Furthermore, the lower slope of the oedometric curves of unsaturated specimens is related to their higher stiffness, if compared with those of saturated specimen. Consequentlly, by

analysing Fig. 6.6, it is possible to state that, within the suction range investigated, an increase of stiffness of the specimen is related to an increase of suction, according with the model proposed by Alonso *et al*. (1990).

It is worth to note that the preconsolidation stress was not computed for unsaturated samples oed_0.60-70 and oed_0.80-90. It is supposed that a sufficiently high value of vertical stress was not reached during the test. Indeed there is not a clear evidence of the compression curve (Fig. 6.5b), not allowing any estimation of the preconsolidation stress σ_p.

6.4 SUCTION CONTROLLED TRIAXIAL CELL

6.4.1 Purposes

A suction controlled triaxial cell was used to investigate the hydro-mechanical behavior of tailing samples in unsaturated conditions. Experimental results provide additional information on the behaviour of silt tailings in unsaturated conditions investigating the occurrence of the critical state and extending a previous characterization of the same material in saturated conditions performed by Carrera (2008).

6.4.2 Suction controlled triaxial apparatus

The mechanical behavior of Stava tailing was studied by performing triaxial tests under shearing at constant water content (undrained conditions) or constant suction (drained conditions) applying mainly the axis translation technique. The triaxial apparatus used in this research allows to monitor the sample volume changes and to control the suction, due to the independent control of water and air pressure. It also allows performing extension or compression tests, under stress or strain controlled conditions. The cylindrical specimen is placed inside 15mm thick wall cell enclosed by a stainless cylinder, as shown in Fig. 6.7a and Fig. 6.7b.

(a)

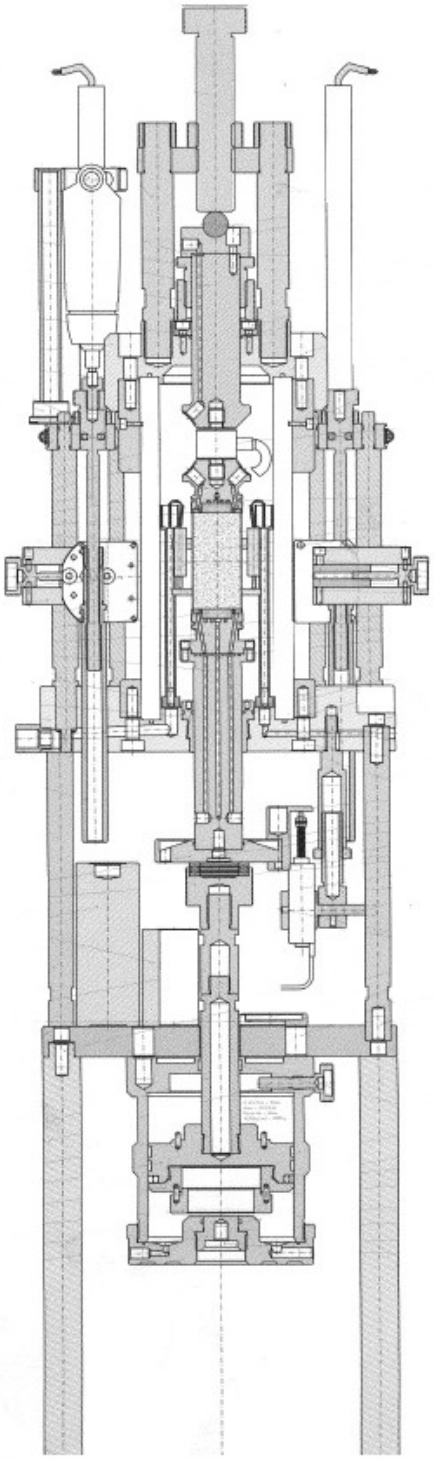

(b)

Fig. 6.7 - (a) Suction controlled triaxial apparatus used in the current research and (b) its schematic view.

Inside a loading chamber, placed at the bottom of the triaxial cell and filled with de-aired water, there is a piston. The control of the pressure inside that chamber allows to push the piston upwards, transferring the pressure to the bottom of the sample as an axial load. A metallic cap is placed and fixed at the top of the sample and it is connected to an adjustable rod aligned with the sample and the piston inside the cell. The rod passes through the top and can be adjusted in vertical direction allowing to pull or to push the sample against the fixed top cap. A loading cell, aimed to measure the axial force, is placed between the rod and the top cap. Top and bottom caps are equipped each with two porous stones. Top and bottom porous stones are made of two concentric parts, an external coarse steel porous stone and an internal *AEV* ceramic porous stone. This assemblage allows minimizing the suction equalization times because the drainage path is halved with respect to the one existing with a *AEV* porous stone placed on one side and a porous stone placed on the other side. The ceramic *AEV* is used to avoid free passage of air into water drainages with occurrence of cavitation phenomena. The outer porous stone is connected to the air drainage lines, while the inner porous stone is connected to the water drainage lines. In the current research 100kPa and 1.5MPa *AEV* porous stones were used.

6.4.3 Burette for water volume change measurement and its calibration

The water exchange, in or out of the triaxial sample, was measured by using a glass burette (Fig. 6.8b) filled with two fluids, kerosene and de-aired water. The two fluids are immiscible and the de-aired water drainage is connected to a separation cell on one side (Fig. 6.8c).

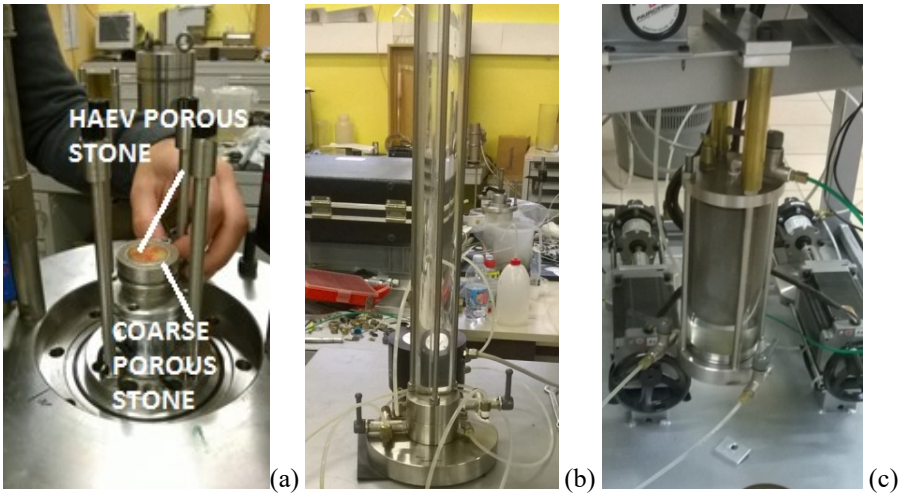

Fig. 6.8 - (a) Bottom porous stone, (b) glass burette and (c) separation cell.

The separation cell is a system aimed to convert the pneumatic pressure to water pressure. On the other side, the de-aired water inside the burette is connected to the upper and lower water drainages of the sample. The interface of kerosene and water inside the glass burette changes in height because of variations of water volume inside the sample. A differential diaphragm pressure transducer, connected to the burette, is aimed to record the water volume variations (maximum 7cm^3) because of the different hydraulic head when the water-kerosene interface changes its position. If a drying process occurs into the sample, the volume of water inside the burette will increase and vice-versa. Finally, if the water volume change is close to the limit value, it is also possible connect the water outside or inside of burette to the sample by means of two lateral valves, in order to reverse the direction of water flow during the test.

As reported by Azizi (2016), the calibration of the burette was done by weighting the amount of water expelled from the burette and also monitoring changes of the interface kerosene deaired water. Figure 6.9 gives the calibration data for the two methods and the offset error.

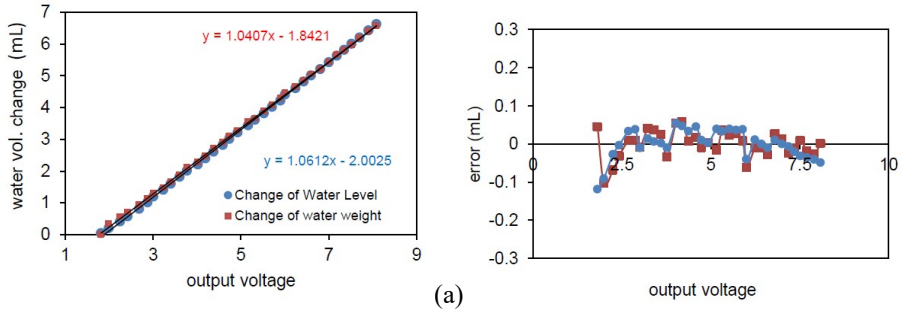

(a) (b)

Fig. 6.9 - (a) Calibration of water volume change by monitoring the variation of water level or variation of water weight and (b) offset error (Azizi, 2016).

6.4.4 Phenomena affecting the water volume change

Even if the HAEV disk is adopted to avoid passage of air into water lines, some air bubbles could appear in water drainages due to diffusion of air through the water in the porous stone. For these reason a flushing operation is suggested by means an air trap placed in the drainage of water lines. If any, diffused air can be accumulated into grooves below the porous stone, leading incorrect measurement of water pressure or water volume change, especially for long time triaxial tests. The rate of air diffusion dV_d/dt can be computed using equation 6-22 (Fredlund and Rahardjo equation, 1993), assuming the concentration of dissolved air is the main mechanism:

$$\frac{dV_d}{dt} = \frac{nADh(u_a - u_w)}{(u_w + u_{atm})t_c} \tag{6-22}$$

where A and t_c are the cross section area and the thickness of the porous stone respectively, h is the solubility of the air in water, n represents the porosity, u_a is the air pressure, u_w is the water pressure, D is the diffusion coefficient, while u_{atm} is the absolute atmospheric pressure.
Another phenomena that could affect the measures of water volume change is the evaporative flux of water from the sample to the surrounding air because vapour pressure in the air drainages of the triaxial cell is not the same of vapour pressure at the surface of the sample.
These two phenomena have two opposite effects on the water volume change: air diffusion increase the amount of water volume change, while water evaporation decrease the amount of water volume. For these reasons the water volume change readings should be corrected by evaluating the influence of air diffusion and water evaporation. In the current research, many suction controlled triaxial tests shown a drying process during the suction equalization phase, so the water content of the sample decreased. At equilibrium, due to combination of air diffusion and water evaporation effects, the water volume change does not approach an horizontal asymptote but a linear one, with predominance either of evaporation or air diffusion effects (Fig. 6.10).

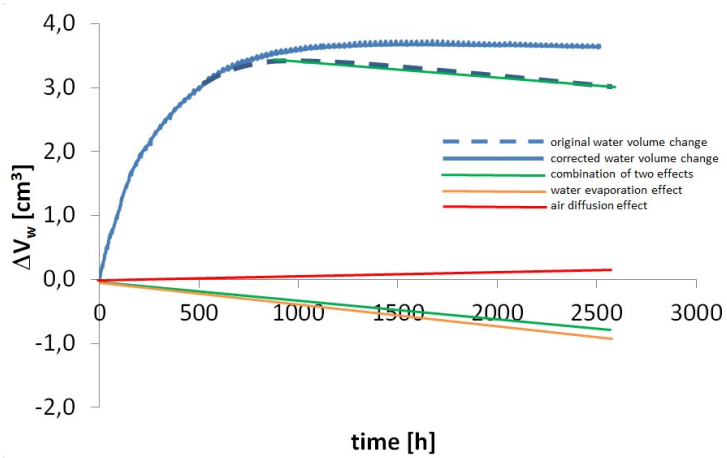

Fig. 6.10 - Example of the correction applied to water volume change for test TX_0.70-60-200.

These two combined effects can be represented by the green line having the same slope of the measured water volume change (blue dot line), meaning the rate of air diffusion is constant as those of water evaporation. The correct water volume change was obtained by subtracting the measured water volume change from the sum of water evaporation and air diffusion. A quantification of the two separate effects (rate of air diffusion and water evaporation) can also be performed: the rate of air diffusion is given from eq. 6-23, so the rate of water evaporation is obtained by subtracting the rate of air diffusion from the slope of the green dotted line.

6.4.5 Axial, radial deformation measurement devices and calibration

In the current research an external LVDT was used to measure the axial displacement of the sample (Fig. 6.11). This LVDT was calibrated by monitoring the changing of voltage related to the applied axial displacement (Fig. 6.12a and Fig. 6.12b).

Fig. 6.11 - External LVDT for axial displacement measurement.

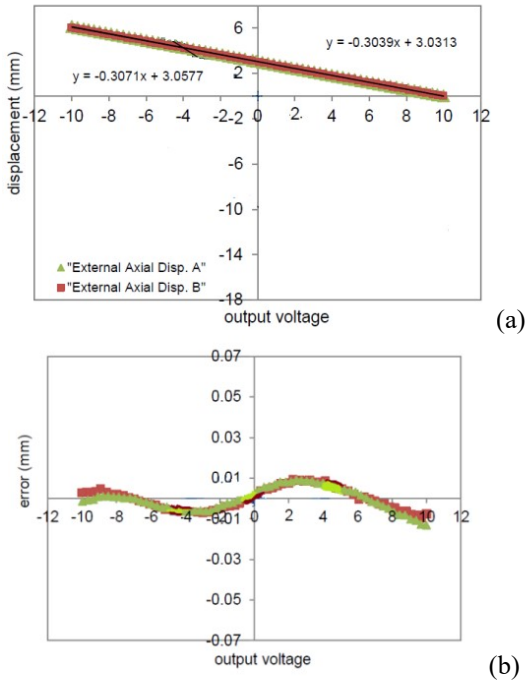

Fig. 6.12 - (a) Calibration curve of the external LVDT and (b) offset error (modified from Azizi, 2016).

A electro-optical laser sensors placed at opposite sides of the sample were used to measure the radial deformation, as shown in Fig. 6-13a and Fig. 6-13b. Furthermore, they are placed outside the wall cell so they are not effected by changing in temperature or pressure inside the cell or by deformation of the sample during the test. The two laser sensors are allowed to move in vertical direction by means of electric motors, so the entire profile of the sample can be obtained during the test. The vertical displacements of laser sensors is measured by means two LVDT and the required time for a complete scanning profile in less than one minute, so the loading is not affected by the laser scanning. The laser system makes use of the optical trianglulation as explained into detail by Romero (1999). The sensor head contains a laser light source and a detector. The laser beam hits the target represented by the sample and it is reflected onto a detector. When the sample moves, the laser beam path proportionally changes and the new signal on the detector is used to compute the distance between target and source. For this reason, the sample surface needs to be covered by a membrane. The two opposite sides of the latex membrane which contains the specimen are painted along the entire height of the sample in order to have two vertical white bars that are laser scanned. The use of the white paintings also avoids any possible errors due to change in colour of the latex membrane, especially for test that require a long time. The positioning of the membrane is shown in Fig. 6.13b. The lasers are placed at a distance of 45mm from the surface of the sample (5mm because of the distance between external wall and sensor front face, 15mm due to the thickness of the Perspex wall and 25mm is the distance between the internal face of the Perspex wall and the lateral surface of the sample). After the assemblage of the cell, the position of the lasers is adjusted at middle of the sample height. Adopting this configuration, the measurement range of the laser sensors is -15mm +15mm. The resolution is 2µm and the response time is 60ms.

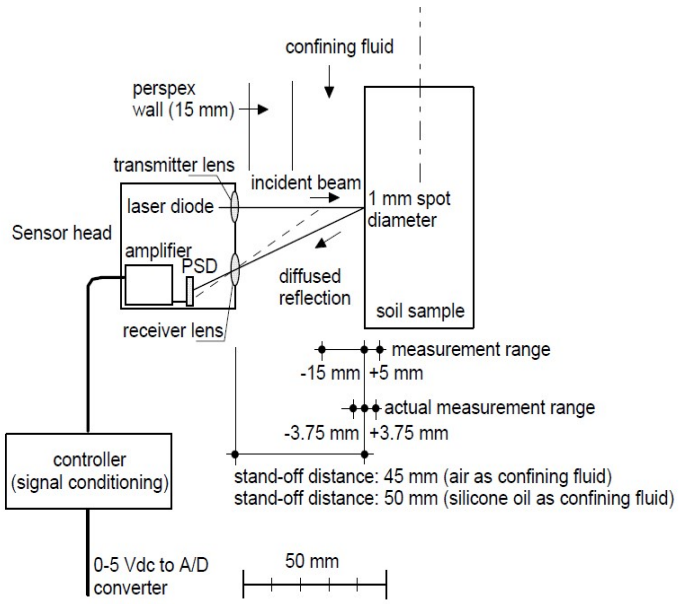

(a)

(b)

Fig. 6.13 - (a) Schematic view Laser device (Romero, 1999) and (b) picture of the laser set-up with specimen.

The calibration of the laser system is explained in detail in Azizi (2016). A metallic sample was covered by the latex painted membrane and the triaxial cell was assembled. The lasers were then moved backward and forward in order to simulate the radial displacement of the stainless sample. The output voltages were monitored, the displacements of lasers were measured by using micrometers. These calibration procedure was repeated for two constant cell pressures, equal to 22kPa and 800kPa (Fig. 6.14a and Fig. 6.14b).
In the current research, a laser scanning was done before the suction equalization phase and before the consolidation phase. During the shearing phase, the profile of the sample was scanned every one-two hours (Fig. 6.15).

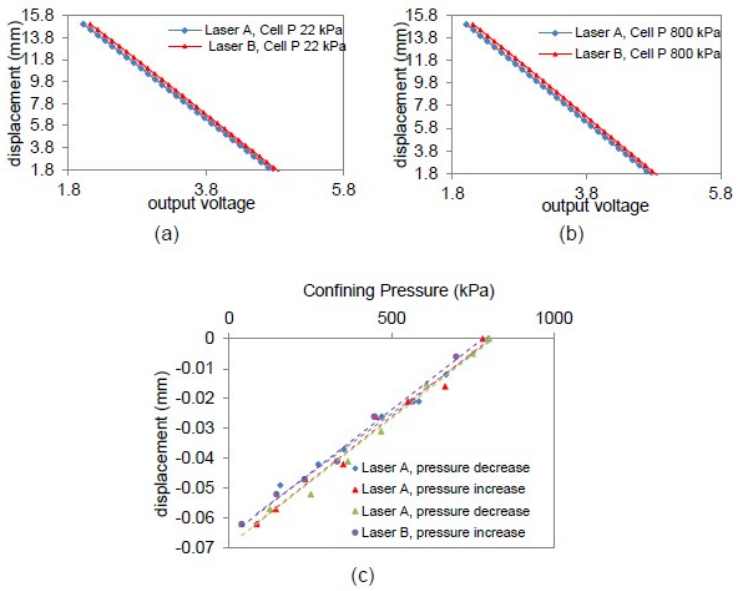

Fig. 6.14 - Calibration of laser system at constant cell pressure of (a) 22kPa , (b) 800kPa and (c) at fixed position of lasers (Azizi, 2016).

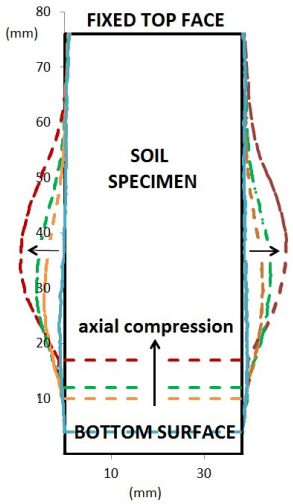

Fig. 6.15 - Vertical profiles of silt sample TX_0.70-60-400 during shearing phase, not in scale (black q = 0kPa, ε_a = 0%; blue q = 630kPa, ε_a = 2.1%; orange q = 770kPa, ε_a = 10.5%; green q = 750kPa, ε_a = 14 %; red q = 730kPa, ε_a = 20%).

A second calibration procedure was performed by keeping fixed the position of lasers and changing the cell pressure from 0kPa to 800kPa and vice-versa. In latter case, the radial displacement Δr measured by each sensor is affected by changes of cell pressure $\Delta\sigma_3$:

$$\Delta r = \alpha_1(\Delta V + \alpha_2 \Delta\sigma_3) \tag{6-23}$$

where ΔV is the total volume change of the sample and the parameters α_1 and α_2 are given by the slopes of output-displacement and cell pressure-displacements graphs, respectively.

6.4.6 Axial force measurement and calibration of load cell

The axial force is measured by means of a load cell placed the rod and the top cap, having a maximum capacity of 5kN. It was calibrated by using a certified load cell with high accuracy and a stainless sample (Fig. 6.16a).

(a)

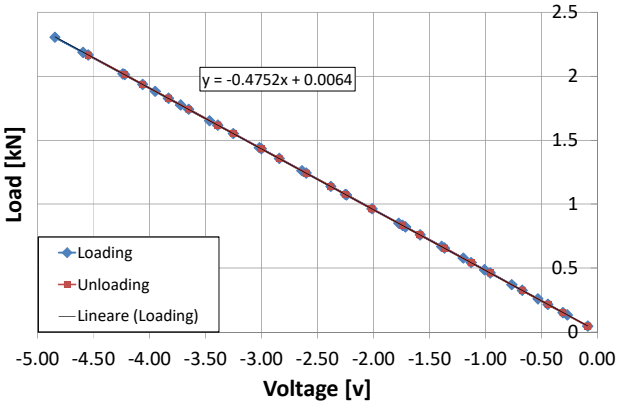

(b)

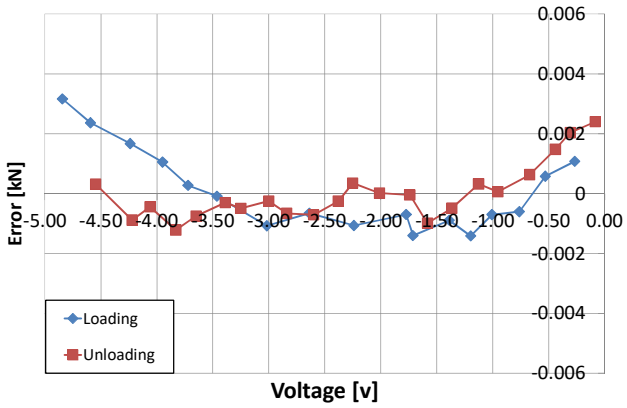

(c)

Fig. 6.16 - (a) High accuracy load cell used for the calibration, (b) Calibration curves of the load cell and (c) offset error.

Output voltages corresponding to a loading and unloading process from 0.1kN to 2.5kN and vice-versa, were monitored as given in Fig. 6.16b and Fig. 6.16c.

6.4.7 Required variables from suction controlled triaxial test

As mentioned above, the laser system was used to measure the radial displacement and to scan the vertical profile of the sample. During the shearing phase, if lasers are not used for scanning, they are fixed at the middle of the sample height. During this phase, the undergoes inhomogeneous deformations (barrel shape). While the axial strain is measured globally on the whole sample by means of an external LVDT, the radial strain is in this case measured locally. Thus, it follows:

$$\varepsilon_v = \varepsilon_{a(LVDT)} + 2\varepsilon_{r(LASER)} \tag{6-24}$$

where $\varepsilon_{a(LVDT)}$ and $\varepsilon_{r(LASER)}$ are the axial global strain and radial strains referred to the centre of the sample. The correction involved the computation of a "*c*" parameter based on the scanning of the entire sample profile performed every few hours. The "*c*" parameter is applied to the radial strain:

$$\varepsilon_{v(GLOBAL)} = \varepsilon_{a(LVDT)} + 2c\varepsilon_{r(LASER)} \tag{6-25}$$

If the laser system is placed at the middle of the sample height, as in the current research, the real volume can be computed:

$$V_r = \int_{-\frac{h_i}{2}}^{\frac{h_i}{2}} \pi r_i^2 dr \tag{6-26}$$

where r_i and h_i are the radius and height of the sample at each –*i* scanning. The radius of the equivalent cylindrical sample can be obtained:

$$\overline{r_i} = \sqrt{\frac{V_r}{\pi h_i}} \tag{6-27}$$

The equivalent radial strain $\overline{\varepsilon_{ri}}$ can be computed by knowledge of the initial radius r_0:

$$\overline{\varepsilon_{ri}} = \frac{\overline{r_i} - r_0}{r_0} \tag{6-28}$$

Assuming ε_r as the radial strain obtained from laser reading at the fixed position of the i-th scanning, the correction parameter to put in eq. 6-25 is given by:

$$c = \frac{\overline{\varepsilon_{ri}}}{\varepsilon_r} \tag{6-29}$$

The corrected volume V_c of the sample during the shearing phase, can be computed by using the volumetric strain (eq. 6-25):

$$V_c = V_0 + V_0\varepsilon_V \tag{6-30}$$

It can be compared to the real volume V_r that is directly obtained by integration of radius with respect to the height at each of the -n scanning profile (Fig. 6.17).

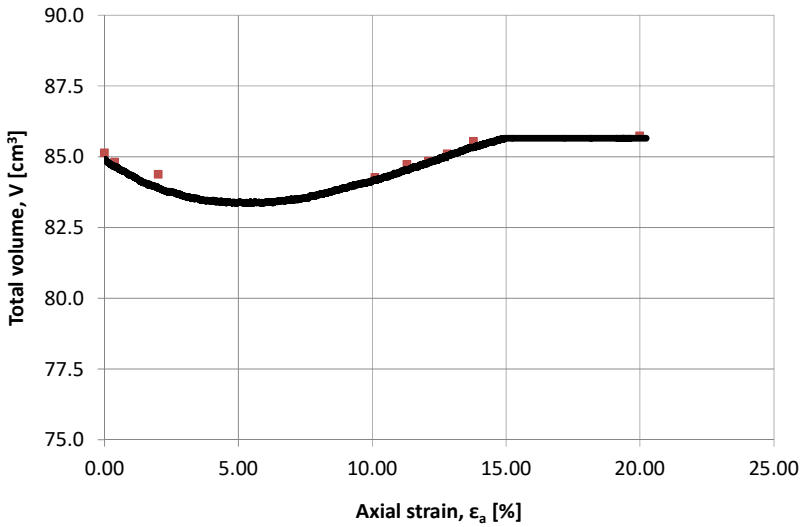

Fig. 6.17 - True volume obtained from scanning readings and calibrated volume (shearing phase, TX_0.70-60-400).

During the shearing phase, the area of the sample changes, so it can be obtained from the corrected volume:

$$A_c = \frac{V_c}{h} \tag{6-31}$$

where h represents the height of the sample. Knowledge of initial height h_0 of the sample and axial displacement Δh measured by the external LVDT, allows to compute the axial strain and so the height h:

$$h = h_0 + h_0 \varepsilon_a \tag{6-32}$$

Finally, knowledge of the corrected area and the axial force F measured by the load cell, allows to compute the axial strain σ_a:

$$\sigma_a = \frac{F}{A_c} \tag{6-33}$$

6.4.8 Sample preparation

Suction controlled triaxial tests were carried out on unsaturated specimens 38mm diameter and 76mm height (Fig. 6.18) at different initial void ratios and water content (Tab. 6.1). Suction controlled triaxial tests were done on statically compacted silt samples. Statical compaction was induced by hand-mixing dry soil powder with a certain amount of demineralized, de-aired water The mixture was put inside an cylindrical mould and it was statically compacted by gradually applying an axial force. A controlled axial displacement Wykeham Farrance loading frame was used to increment the axial load until the desired volume was reached under controlled water content. The specimens were carefully extruded from their mould and then placed inside the triaxial cell in order to be tested.

Fig. 6.18 - Cylindrical mould for suction controlled triaxial tests.

6.4.9 Testing phases

Suction controlled triaxial tests performed by axis translation technique involved three steps: suction equalization phase, consolidation phase and shearing phase at constant water content or at constant suction:

- Suction equalization phase: after assemblage of the triaxial cell, a matric suction is imposed on the specimen, by independent control of the water pressure and air pressure; water and air drainages are open. In this phase, a net pressure (about 10kPa) is also applied by controlling cell pressure and axial stress. Suction equalization phase last until when measures of the water volume change don't change with time. Time required for equilibrium depends on the sample permeability, initial water content and permeability of the porous stone. In the current research the equalization time was about three-four days.
- During the consolidation phase, cell and axial pressures were simultaneously increased of the same amount to maintain an isotropic state of stress. The air pressure was maintained constant, allowing the net stress to increase to a desired target. During this phase, water and air drainages were kept open. The consolidation phase was considered ended when no variations of water volume with time took place.
- The final phase of the triaxial tests consisted in a shearing phase at constant water content or at constant suction. In both cases, the axial stress was increased in strain controlled conditions. If the sample was sheared at constant water content, water drainages were closed. The water pressure was measured by means of an additional pressure transducer connected to the sample. In order to minimize the hydraulic head between sample and transducer, the latter one is placed at the same level of the sample. While top and bottom water lines of the sample were connected to the burette, two additional water drainages of the sample were connected to the air trap and the following three-way valve. This valve, if properly turned on, allows to connect the additional transducer to the sample. The pressure of transducer is regulated to zero when the valve is turned to connect the transducer to atmospheric pressure. If the valve is turned to connect the transducer to the sample, water pressure can be measured during the shearing phase at imposed water content. Air drainages are maintained open, so knowledge of the air and water pressure allows to obtain the suction between the measured water pressure and the imposed air

pressure. This is the procedure followed in the current research to obtain the suction during shearing at imposed water content. In this phase, the burette is not connected to the sample in order to prevent water volume change between the burette and the sample. The shearing phase in the present research occurred at an axial strain rate of about (0.00625mm/min) which implies a duration of the shearing phase of about 1.5 days. When the sample was sheared at constant suction, water and air drainages were maintained open. In order to avoid excess of pore pressure the strain rate is decreased one order of magnitude than the strain rate imposed for shearing at constant water content. About 15 days were then required for a shearing phase performed at constant suction.

An example of stress path in terms of suction and net stress or Bishop effective stress is given in Fig. 6.19 from the initial state to the end of consolidation phase. Point 1 means the initial state of the sample (initial suction s_i unknown), point 2 means the end of the suction equalization phase, while point 3 means the end of the consolidation phase.

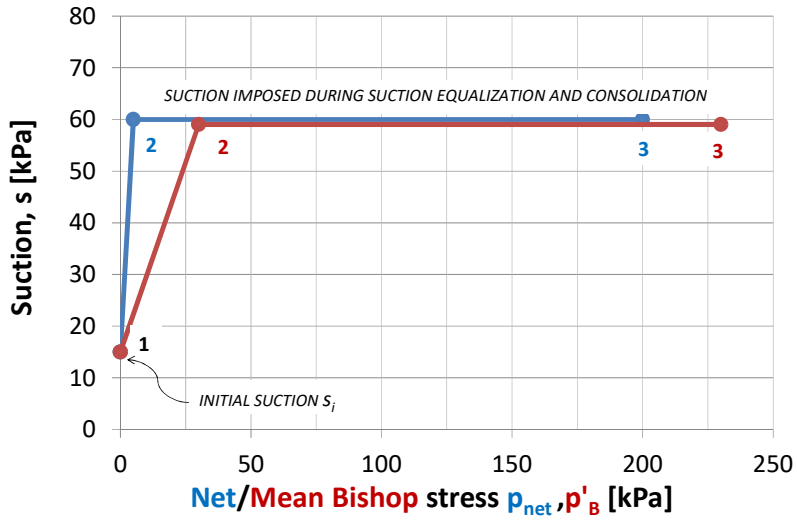

Fig. 6.19 - Example of stress path in (s, p_{net}) plane and (s, p'_B) plane.

It is worth to note that, before suction equalization phase, sample TX_0.80-90-800, sample TX_0.64-60-200b and sample TX_0.80-90-100 were isotropically loaded in undrained conditions until a net stress equal to 100kPa. This preliminary phase required about 20 minutes and it was followed by the suction equalization phase where a matric suctions, respectively, of 90kPa and 60kPa were imposed by means of the axis translation technique.
Only one triaxial test (TX_0.60-175-200) was performed by using the vapour equilibrium technique instead of the axis translation technique. The testing procedure was similar to other tests, except the suction equalization phase where the suction was imposed by means controlling the relative humidity of the sample instead of acting on water and air pressures. A stainless disc allowing the only passage of air was used instead of the bottom porous stone. The upper porous stone was modified by closing the two water drainages and the burette was excluded from the circuits. A K_2SO_4 solution was prepared and connected by means air lines to the specimen, as shown in Fig. 6.20a and Fig. 6.20b. An air pump was used to force chemical vapours passing through the sample in order to reduce the equilibrium time. The weight of solution was monitored, while an isotropic state of stress equal to 50kPa was imposed. The consolidation phase was then performed at net stress equal to 200kPa and the shearing phase was carried out at constant suction level. The vapour equilibrium technique

was found to be ineffective to impose the desired suction value in reasonable times (3 weeks). This was appreciated because very little water, with respect to what expected, was lost during suction equalization. The average suction actually applied during testing was estimated thus on basis of the water content measured at the end of the tes, which was interpreted on basis of the water retention models introduced in the previous chapter.

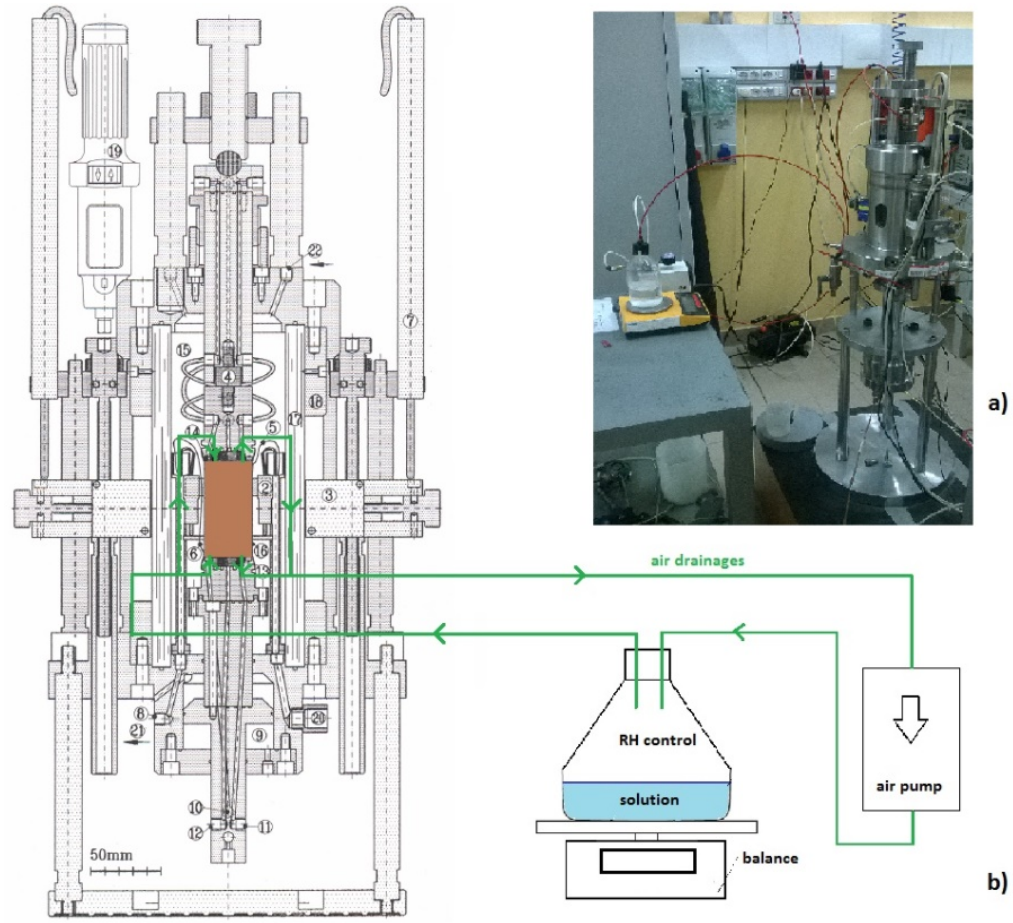

Fig. 6.20 - (a) Picture of the triaxial cell equipped for the vapour equilibrium technique and (b) schematic view (modified from Romero, 1999).

Table 6.5 gives the list of the tested unsaturated triaxial samples with their initial state in terms of percentage of silt and sand, void ratio (e_0) , dry unit weight (γ_d) and water content (w_0). It is worth to note that, into the name of the sample, the first number identifies the initial void ratio, the second number identifies the suction imposed to the specimen and the third number identifies the mean net stress imposed during the consolidation phase. Table 6.6 shows the values of suction (s), deviator stress (q) and net stress (p_{net}) at each phase. Table 6.7 gives the adopted measurement/suction control technique and some comments for each tests, while Tab. 6.8 shows the drainage conditions for each phase.

Tab. 6.5 - List of the suction controlled triaxial tests.

Sample	e_0 [-]	w_0 [%]	γ_d [kN/m^3]
TX_0.70-60-100	0.70	14.9	16.6
TX_0.70-60-200	0.70	14.9	16.6
TX_0.70-60-400	0.70	14.9	16.6
TX_0.60-60-800	0.60	14.9	17.7
TX_0.60-175-200	0.60	6.4	17.7
TX_0.80-90-800	0.80	5.7	15.7
TX_0.64-60-200b	0.64	16.5	17.2
TX_0.80-90-100	0.80	14.1	15.7

Tab. 6.6 - Phases of the suction controlled triaxial tests.

Sample	Constant water content loading	Suction Equalization Phase			Consolidation Phase		
	p_{net}	s	q	p_{net}	s	q	p_{net}
	[kPa]	[kPa]	[kPa]	[kPa]	[kPa]	[kPa]	[kPa]
TX_0.70-60-100	-	s_i→60	0	5-10	60	0	5-10→100
TX_0.70-60-200	-	s_i →60	0	5-10	60	0	5-10→200
TX_0.70-60-400	-	s_i →60	0	5-10	60	0	5-10→400
TX_0.60-60-800	-	s_i →60	0	5-10	60	0	5-10→800
TX_0.60-175-200	-	s_i →175	0	5-10	175	0	5-10→200
TX_0.80-90-800	100	s_i →90	0	100	90	0	5-10→800
TX_0.64-60-200b	100	s_i →60	0	100	60	0	5-10→200
TX_0.80-90-100	100	s_i →90	0	100	-	-	-

Tab. 6.6 - Phases of the suction controlled triaxial tests (continued).

Sample	Wetting Phase			Shearing Phase		
	s	q	p_{net}	s	q	p_{net}
	[kPa]	[kPa]	[kPa]	[kPa]	[kPa]	[kPa]
TX_0.70-60-100	-	-	-	Measured	Measured	Measured
TX_0.70-60-200	-	-	-	Measured	Measured	Measured
TX_0.70-60-400	-	-	-	Measured	Measured	Measured
TX_0.60-60-800	60→20	Const. (0)	Const. (800)	Measured	Measured	Measured
TX_0.60-175-200	-	-	-	Const. (175)	Measured	Measured
TX_0.80-90-800	-	-	-	Measured	Measured	Measured
TX_0.64-60-200b	-	-	-	Const. (60)	Measured	Measured
TX_0.80-90-100	-	-	-	Const. (90)	Measured	Measured

Tab. 6.7 - Suction control or measurement technique adopted and comment for each test.

Sample	Measurement/Suction control Technique	Comments 1	Comments 2 (C.S. = Critical State)
TX_0.70-60-100	Axis translation	Shearing in undrained conditions	C.S. approached
TX_0.70-60-200	Axis translation	Shearing in undrained conditions	C.S. reached
TX_0.70-60-400	Axis translation	Shearing in undrained conditions	C.S. reached
TX_0.60-60-800	Axis translation	Shearing in undrained conditions	C.S. not reached
TX_0.60-175-200	Vapour Equilibrium	Shearing in undrained conditions	C.S. reached
TX_0.80-90-800	Axis translation	Shearing in undrained conditions	C.S. reached
TX_0.64-60-200b	Axis translation	Shearing in drained conditions (imposed suction)	C.S. reached
TX_0.80-90-100	Axis translation	Shearing in drained conditions (imposed suction)	C.S. reached

Tab. 6.8 - Drainage conditions at each phase.

Phase	Constant water content loading		Suction Equalization		Wetting		Consolidation		Shearing	
Sample/Drainage	water	air	water	air	water	air	water	air	water	air
TX_0.70-60-100	-	-	Open	Open	-	-	Open	Open	Close	Open
TX_0.70-60-200	-	-	Open	Open	-	-	Open	Open	Close	Open
TX_0.70-60-400	-	-	Open	Open	-	-	Open	Open	Close	Open
TX_0.60-60-800	-	-	Open	Open	Open	Open	Open	Open	Close	Open
TX_0.60-175-200	-	-	Close	Open	-	-	Close	Open	Close	Open
TX_0.80-90-800	Close	Open	Open	Open	-	-	Open	Open	Close	Open
TX_0.64-60-200b	Close	Open	Open	Open	-	-	Open	Open	Open	Open
TX_0.80-90-100	Close	Open	Open	Open	-	-	-	-	Open	Open

6.5 SUCTION CONTROLLED TRIAXIAL TEST: RESULTS

In order to investigate the hydro-mechanical response of Stava silt tailing in unsaturated conditions, a shearing phase after consolidation was performed for all tests. The maximum axial strain ranged between 15% and 20%. The higher was the axial strain, the greater the possibility for the Stava sample to reach the Critical State. The large majority of the tests lead to appreciate the critical state condition as described by eq. 6-1. The maximum axial strain reached during a few tests only allowed a reasonable prediction of the critical state (TX_0.70-60-100) or a tentative prediction (TX_0.60-60-800). When the Critical State was observed, it was possible to compute the stress ratio M, the shearing resistance angle ϕ'_{cv} and the void ratio e_{cv} at Critical State in order to define a Critical State Line also for unsaturated Stava silt specimens. The *CSL* in unsaturated conditions will be compared with those obtained for the same material tested by Carrera (2008) in saturated conditions.

6.5.1 Description of results of test TX_0.70-60-200

In the following a complete description of the results of one test (TX_0.70-60-200) is given. This description allows appreciating all the aspects of a single test. The other tests will be described in a synthetic manner.

- The suction equalization phase: from the initial state (e_0 = 0.7, Sr = 60%, γ_d = 16.6kN/m^3), a matrix suction equal to 60kPa was imposed to the sample, by increasing simultaneously air and water pressure. In the meantime, a net stress of 5÷10kPa was imposed and kept constant. Water and air drainages were kept open, so water volume changes were monitored.
- Consolidation phase: an isotropic state of stress was imposed, by increasing simultaneously axial and radial stress, until reaching a net stress equal to 200kPa. Also in this phase, water and air drainages were kept open, so water volume exchanges were monitored. This phase was interrupted when no water volume changes in/out of the sample were measured.
- Sample was then sheared in strain controlled conditions (triaxial compression) at constant water content conditions, by closing the water drainages, keeping open air drainages and measuring the excess of pore pressure. Every two hours the entire profile of the sample was scanned in order to obtain the true volume of the sample. This phase was interrupted when an axial strain about 20% was reached (time required: less than two days).

The water volume change with the time for test TX_0.70-60-200 are shown in Fig. 6.21. During the suction equalization phase, due to the imposed suction probably higher than the initial suction of the sample (not measured), a volume of water equal to 3.6cm^3 was expelled from the sample. Then, the water volume change didn't show any variations, so the consolidation phase was commenced. During the consolidation phase, about 0.5cm^3 of water left the sample in the first hours, than no any water volume changes were measured. Because of the undrained conditions during the shearing phase, no water volume changes from the beginning of the shearing phase occurred until the end of the test.
The total volume change with the axial strain during the shearing phase at constant water content is shown in Fig. 6.22a. The red squares represent the total volume of the sample obtained by integration of the entire profile during the laser readings performed every two-three hours. Based on these data, the computed total volume of the sample was calibrated and it is represented by the continuous black line. The total volume corresponding at null axial strain (84.6 cm^3) is the volume at the end of consolidation, just before the beginning of the shearing phase. A reduction of total volume from 84.6cm^3 to 83.4cm^3 can be observed until an axial strain equal to 5%. Then, sample exhibits a dilative behaviour, increasing its total volume from 84.4cm^3 to 86cm^3 until reaching an axial strain of about 15%. Finally, with increasing of axial strain from 15% until the end of the test, no further changes of total volume (Fig. 6.22a), suction (Fig. 6.24a) and deviator stress (Fig. 6.27a) were observed, meaning that critical state conditions were reached.

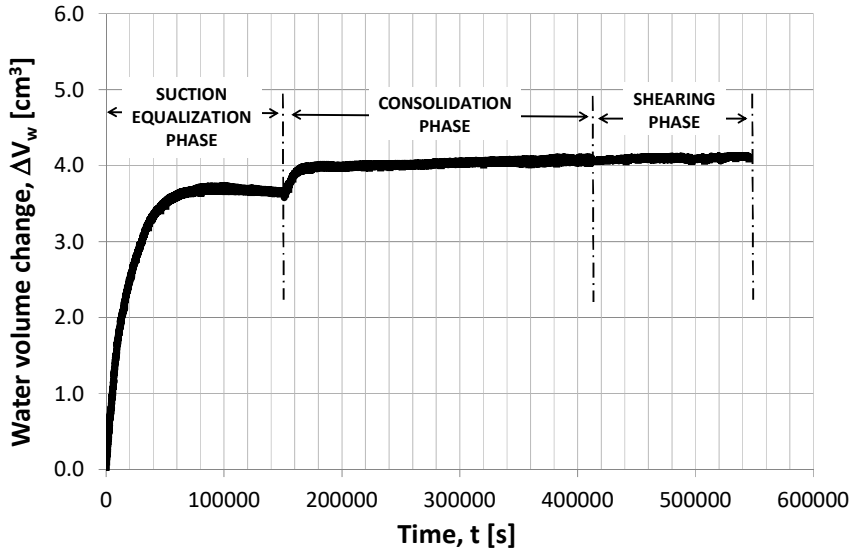

Fig. 6.21 - Water volume change with time (TX_0.70-60-200).

The corresponding volumetric strains occurred during the shearing phase are shown in Fig. 6.22b. A decrease of the total volume until reaching a value of 1.4% was obtained until an axial strain equal to 5%, then the sample started to show a dilative behaviour, from 1.4% until -1.8% when the critical state was reached.

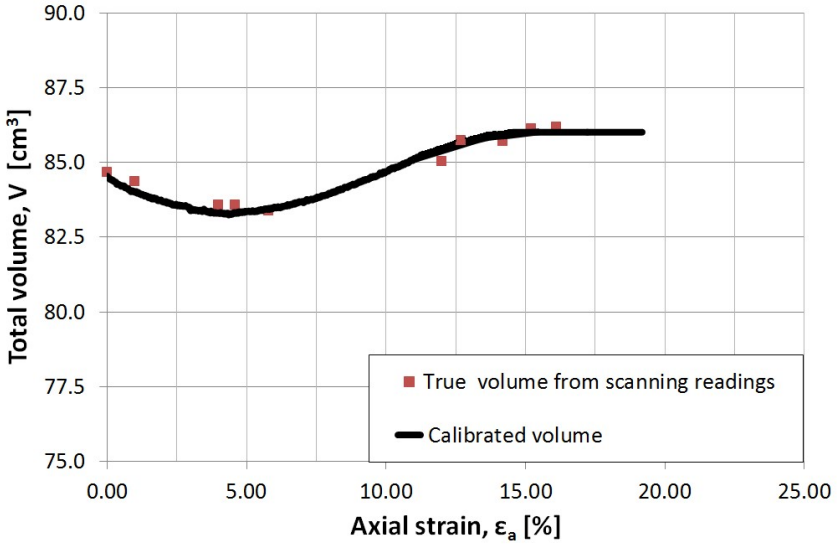

(a)

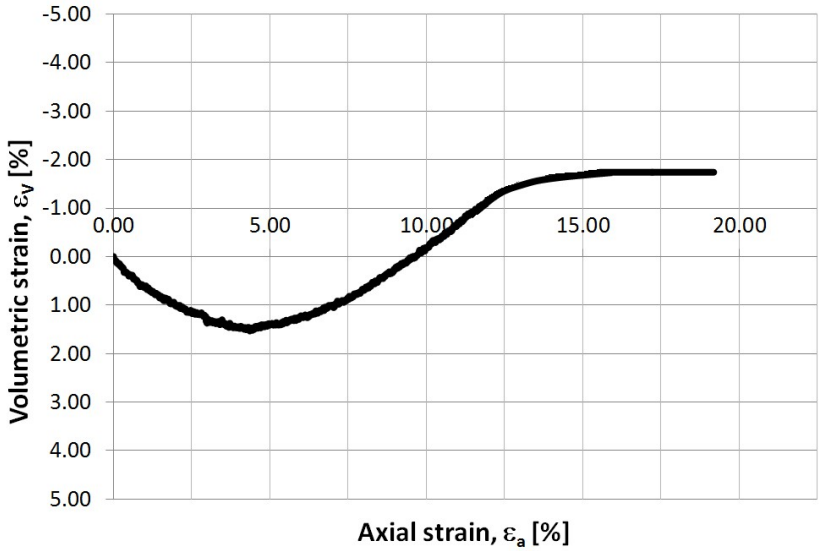

(b)

Fig. 6.22 - (a) Total volume change with axial strain and (b) volumetric strain with axial strain during the shearing phase (TX_0.70-60-200).

The void ratio during the entire test is shown in Fig. 6.23a. A small decrease of the void ratio from the initial value equal to 0.70 until 0.69 can be observed during suction equalization. The void ratio remained nearly constant until the end of suction equalization phase and then it decreased from 0.690 until 0.667 due to the isotropic consolidation (p_{net} = 200kPa). The void ratio changes with the axial strain during the shearing phase at constant water content are more evident in Fig. 6.23b. The void ratio at null axial strain (0.668) is the value at the end of consolidation, just before the beginning of the shearing phase. A reduction in void ratio from 0.668 until 0.648 can be observed in the first step of the shearing phase. Then, after 5% of axial strain, sample exhibits a dilative behaviour, increasing its void ratio from 0.648 to 0.690 until reaching an axial strain of about 15%. Finally, with increasing of axial strain equal from 15% until the end of the test (20%), no further changes of void ratio were observed together with the results of deviatoric stress-axial strain relationship, discussed in the following, this means that critical state conditions were reached.

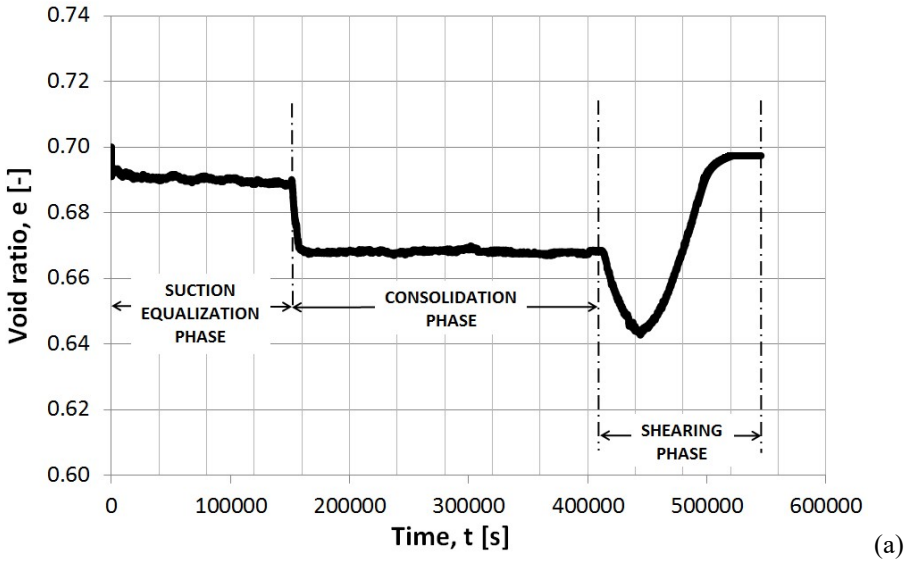

(a)

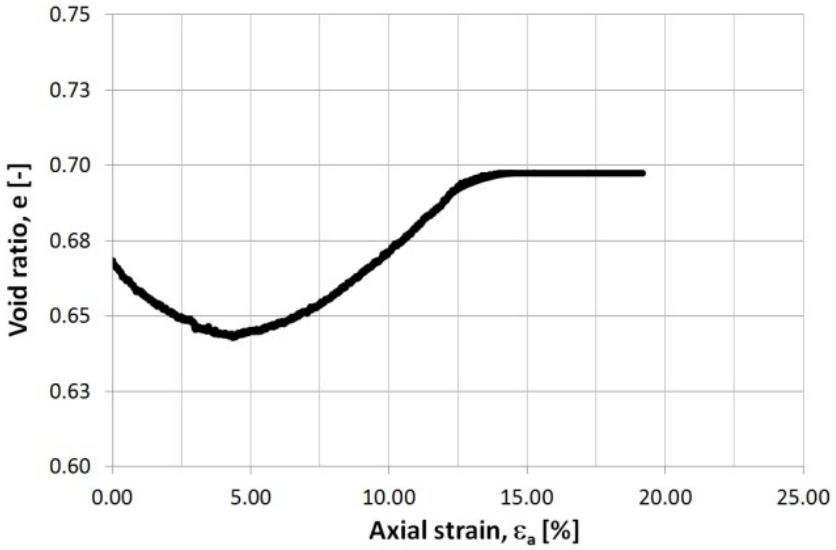

(b)

Fig. 6.23 - (a) Void ratio with time during the entire test and (b) void ratio with axial strain during the shearing phase (TX_0.70-60-200).

The evolution of suction during the entire test is shown in Fig. 6.24a. By using the axis translation technique, a suction equal to 60kPa was imposed on the sample during the suction equalization phase and the consolidation phase. During shearing, suction decreased until a constant value of 42kPa because of the increasing of the pore water pressure from 18kPa to 31kPa, as shown in Fig. 6.24b.

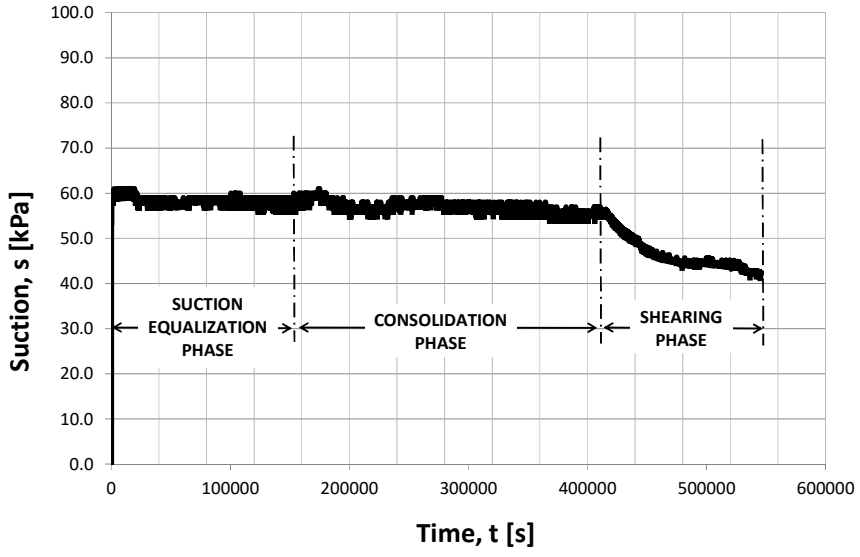

(a)

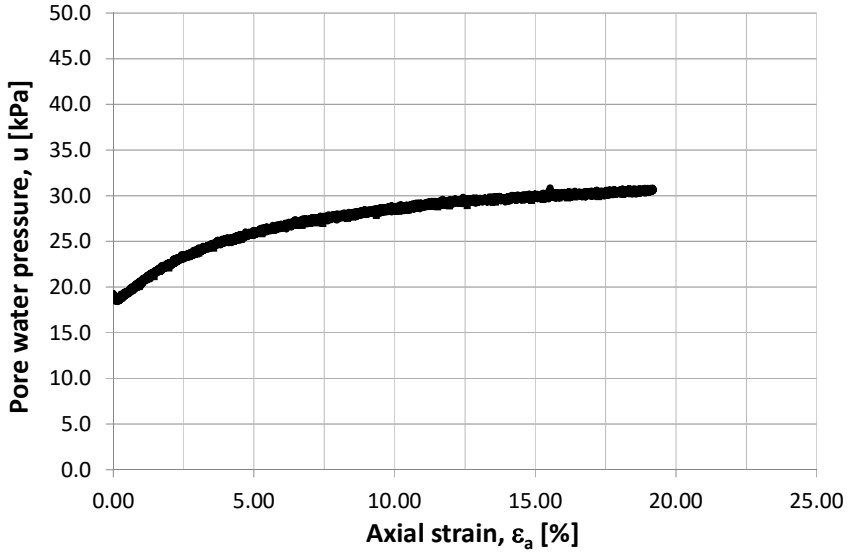

(b)

Fig. 6.24 - (a) Suction with time during the entire test and (b) pore water pressure with axial strain during the shearing phase (TX_0.70-60-200).

The water ratio during the entire test is shown in Fig. 6.25. Because of the drying process (Fig. 6.21) during the suction equalization phase, the water ratio decreased from 0.42 until a constant value of 0.35. During the consolidation phase, the water ratio decreased slightly from 0.35 to about 0.34. Finally, because of the shearing phase performed at constant water content, the water ratio was constant until to the end of the test.

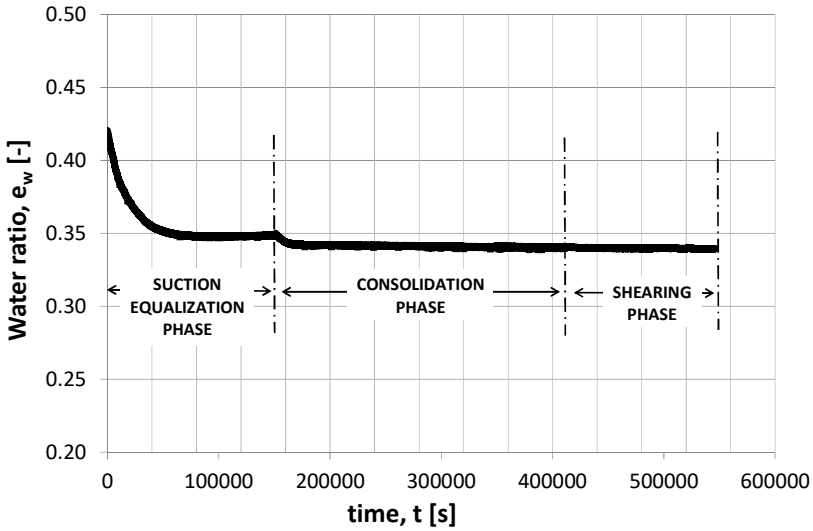

Fig. 6.25 - Shearing phase: water ratio with axial strain (TX_0.70-60-200).

The degree of saturation of the unsaturated specimen during the entire test is given in Fig. 6.26. Due to the drying process (about 3.5cm^3 of water left the sample, as shown in Fig. 6.21) resulting from the imposed suction during the equalization phase, the degree of saturation decreased from the initial value equal to 59%÷60% until a constant value of about 50%÷51%. Then, because of a little expulsion of water (about 0.5cm^3 of water left the sample, Fig. 6.21) and the decrease of void volume during the consolidation phase, the degree of saturation increased from 50% until a constant value of about 52%. Finally, because of the contractive and dilative response during the undrained shearing phase, the degree of saturation increased until 53% and then decreased to a value of about 48%. Because of no total volume variations at critical state and no water volume changes (shearing phase at constant water content), the degree of saturation remained constant at the value of about 48% until the end of the test.

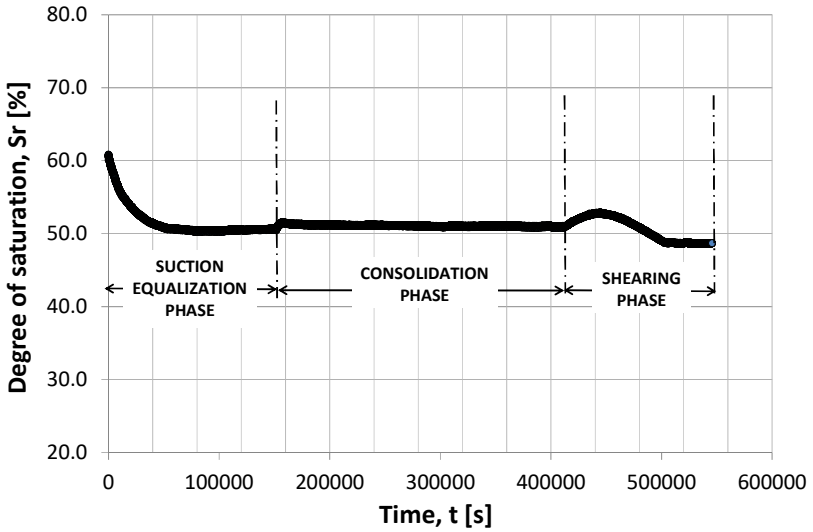

Fig. 6.26 - Degree of saturation with time (TX_0.70-60-200).

The stress-strain behaviour in terms of deviator stress q and axial strain ε_a for the unsaturated sample TX_0.70-60-200 is given in Fig. 6.27a. As can be observed, the deviator stress, starting from zero, increased until a maximum value q_{max} equal to 405kPa around an axial strain of 5%. Then, it gently decreased until a steady value 360kPa at an axial strain of 15% without further appreciable variations. The drops of deviator stress pointed by the arrow are due to the short interruptions of the shearing phase in order to perform the laser scanning of the sample profile. During this operation, that requires 2÷3 minutes, a little decreasing of the axial stress was observed, resulting in a little decreasing of the deviator stress that will be immediately recovered after the sample profile is acquired by means of the laser devices and so the shearing phase is continued.

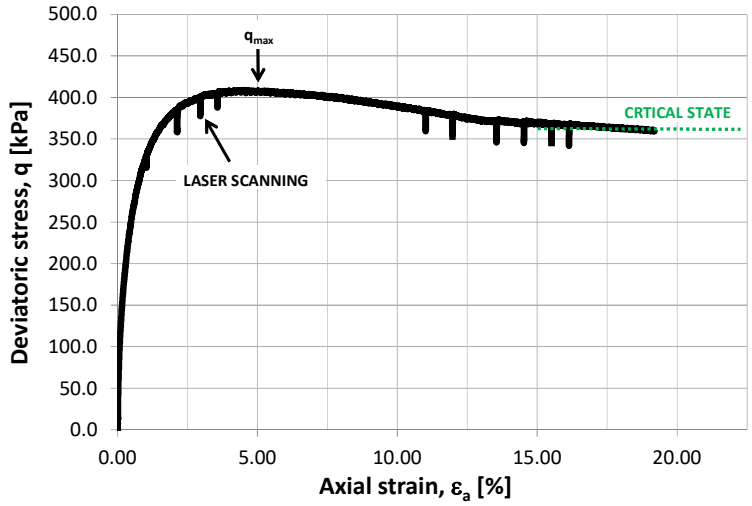

(a)

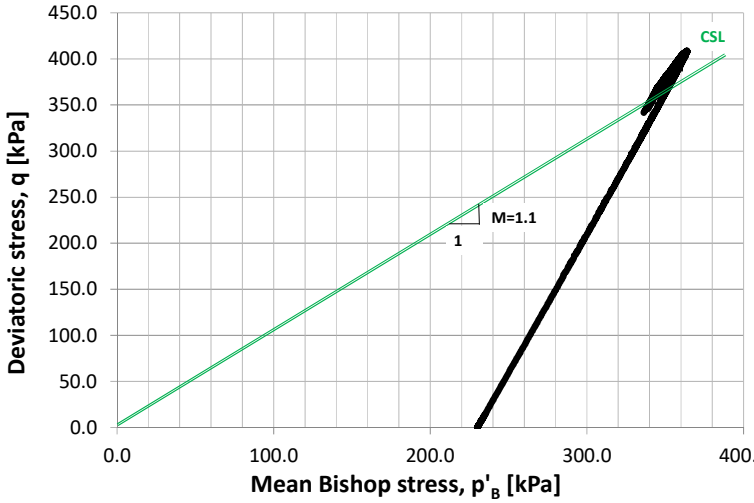

(b)

Fig. 6.27 - (a) Shearing phase: stress-strain behaviour (TX_0.70-60-200). (b) Shearing phase: mean Bishop stress with deviator stress (TX_0.70-60-200).

The stress path during the shearing phase in terms of deviator stress q and mean Bishop stress p'_B is shown in Fig. 6.27b.

It can be observed, the Critical State Line *CSL* can be obtained connecting the axis origin and the final q-p'_B values deviator stress. Indeed, the slope of *CSL* is the stress ratio M (ratio between deviator stress and Bishop effective stress at critical state). Once the stress ratio at critical state is obtained, the corresponding shearing resistance angle ϕ'_{cv} is given by:

$$M = \frac{6\sin\phi_{cv}}{3 - \sin\phi_{cv}} \rightarrow \phi_{cv} = \arcsin\left(\frac{3M}{M+6}\right) \quad (6\text{-}34)$$

In the current case, a stress ratio M equal to 1.1 is obtained, so its corresponding shearing resistance angle ϕ'_{cv} is about 27°.
The hydraulic path followed during the shearing phase of triaxial test TX_0.70-60-200, in terms of suction and degree of saturation, is given in Fig. 6.28. The different test phases correspond at black squares: initial state (1), end of suction equalization phase (2), end of consolidation phase (3) and end of shearing phase (4). It is worth to note that the entire *s*-*Sr* path of triaxial test TX_0.70-60-200 lies inside the estimated water retention curve of the silt sample (OED_SILT_0.7) having initial void ratio e_0 = 0.7. The drying-wetting path occurred during the shearing phase is represented by the green line, from point 3 to point 4. Because of the initial volume contraction during shearing at constant water content, the effective degree of saturation first increased. Then, when sample started to increase its volume until to the end of the test, the effective degree of saturation decreased.

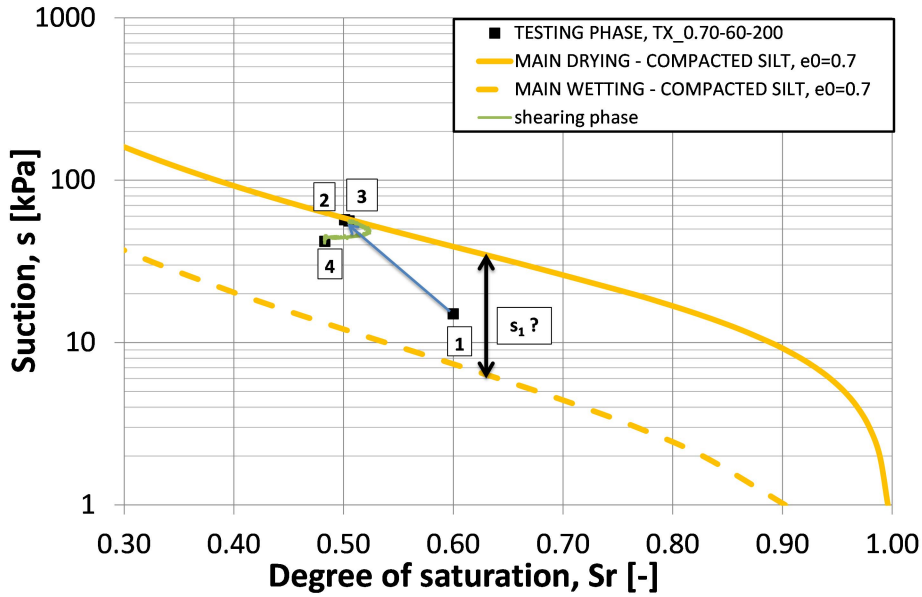

Fig. 6.28 - Water retention curve and stress path for sample TX_0.70-60-200.

6.5.2 Results: TX_0.70-60-100

This section summarizes the experimental results obtained from Stava silt specimen TX_0.70-60-100 prepared at initial void ratio e_0 = 0.70 and degree of saturation Sr_0 = 0.60. First a suction s = 60kPa was imposed, then the sample was consolidated isotropically until reaching a net stress p_{net} = 100kPa. Finally it was sheared under strain-controlled conditions at constant water content, by keeping open the air drainages and closing the water drainage. The volumetric strains ε_v occurred during the shearing phase are shown in Fig. 6.29a.

Specimen first shown a little contraction (ε_v about 0.8%) until an axial strain of about 2%, then it exhibited a dilative behaviour until the end of the test, corresponding to an axial strain of 8%.
Because of the initial reduction of total volume at the beginning of the shearing phase, the void ratio decreased from 0.69 until 0.68. Then, due to the following dilative behaviour, the void ratio increased reaching about 0.72 as given in Fig. 6.29b. It is worth to note that there is no a evidence of null variations in volumetric strains, so the specimen was just approaching the critical state without reaching it. Basing on the theorical model proposed by Gallipoli *et al.* (2003), the dot black line gives a qualitative estimation of the void ratio and volumetric strain at critical state. The matric suction during the entire triaxial test is shown in Fig. 6.31b. By means of the axis translation technique, suction was imposed at 60kPa and it remained constant during the suction equalization phase and consolidation phase.
Because of the increase of void ratio due to the dilative behaviour of the specimen (from an axial strain of 2% until the end of the test) and its corresponding decrease of degree of saturation, one could expect an increase of suction. Despite this, a decrease of matric suction can be observed during the shearing phase (Fig. 6.29c). Hypothesis aimed to explain occurrence of this hydraulic behaviour will be given in next section based on the evolution of water retention with void ratio.
The stress-strain behaviour in terms of deviator stress q and axial strain ε_a for the unsaturated sample TX_0.70-60-100 is given in Fig. 6.30. As can be observed, the deviator stress, starting from zero, increased until a maximum value q_{max} = 240kPa around an axial strain of 2%. Then, it gently decreased until 200kPa at an axial strain of 8%. Again, because no clear evidence of critical state from Fig. 6.29, the dot line gives a qualitative prediction of the steady state in terms of deviator stress. It is worth to note that, in this case as for test that approached or didn't reach the Critical state (TX_0.60-60-800), the deviator stress at critical state was extimated by means of Taylor relationship, where $d\varepsilon_v$ and $d\varepsilon_s$ are, respectively, the variations of volumetric strain and shearing strain.

$$\frac{q}{p'_B} = M - \frac{d\varepsilon_v}{d\varepsilon_s} \tag{6-35}$$

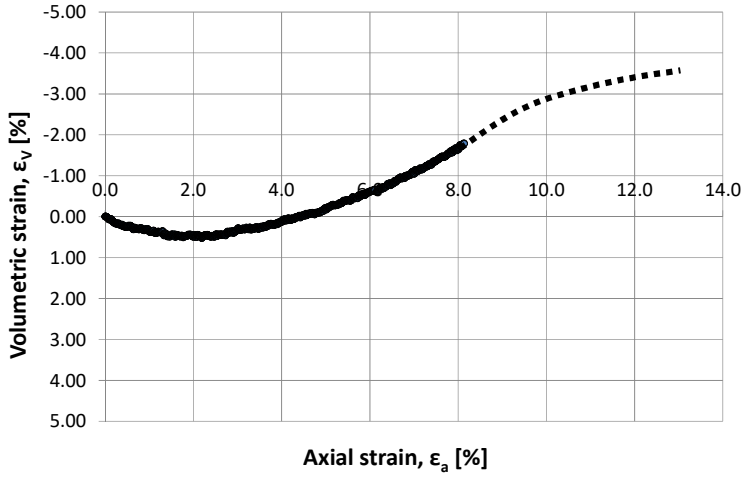

(a)

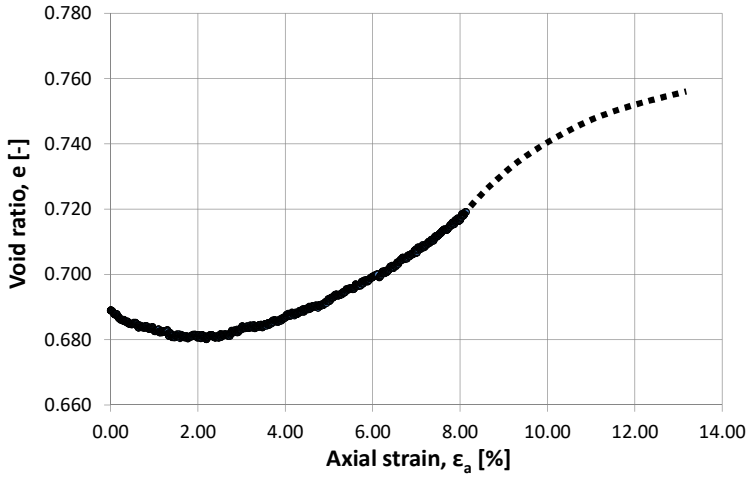

(b)

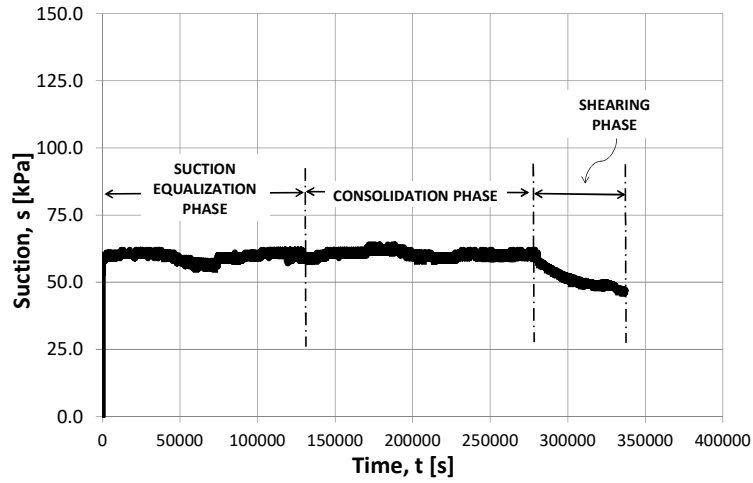

(c)

Fig. 6.29 - (a) Shearing phase: volumetric strain with axial strain. (b) Shearing phase: void ratio with axial strain. (c) - Suction with time during the entire test (TX_0.70-60-100).

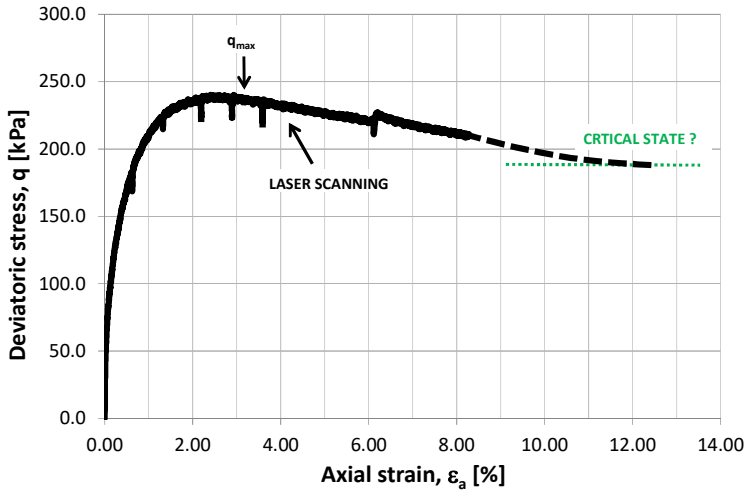

Fig. 6.30 - Shearing phase: deviator stress with axial strain (TX_0.70-60-100).

6.5.3 Results: TX_0.70-60-400

The experimental results obtained from Stava silt specimen TX_0.70-60-400 (initial void ratio e_0 = 0.70) are summarized in this section. The specimen was first imposed a suction of 60kPa, then it was isotropically consolidated until reaching a net stress p_{net} = 400kPa. Finally, it was sheared under strain-controlled conditions at constant water content, by keeping open the air drainages and closing the water drainage. The volumetric strains ε_v occurred during the shearing phase are shown in Fig. 6.31a. Specimen first shown a contraction corresponding at 2% of volumetric strain until an axial strain ε_a = 5%. Then, it exhibited a dilative behaviour until the end of the test, corresponding at an axial strain of 20%. It is worth to note no variations of volumetric strain from an axial strain of 15% until the end of the test, allowing to assume that a critical state condition was reached.
Because of the initial reduction of total volume at the beginning of the shearing phase, the void ratio decreased from 0.68 until 0.65. Then, due to the dilative behaviour, the void ratio increased reaching a value of about 0.69 (Fig. 6.31b) and it remains nearly constant because of no variation of volume.
The matric suction during the entire triaxial test is shown in Fig. 6.31c. As for TX_0.70-60-100 and TX_0.70-60-200, also in this case, the suction was imposed at 60kPa and it remains constant during the suction equalization phase and consolidation phase.
Because of the increase of void ratio due to the dilative behaviour of the specimen (from an axial strain of 5% until the end of the test) and its corresponding decrease of degree of saturation, one could expect an increase of suction. Again, despite this, a decrease of matric suction can be observed during the entire shearing phase (Fig. 6.31c). Hypothesis aimed to explain occurrence of this hydraulic behaviour will be given in next section based on the dependency of water retention on void ratio.

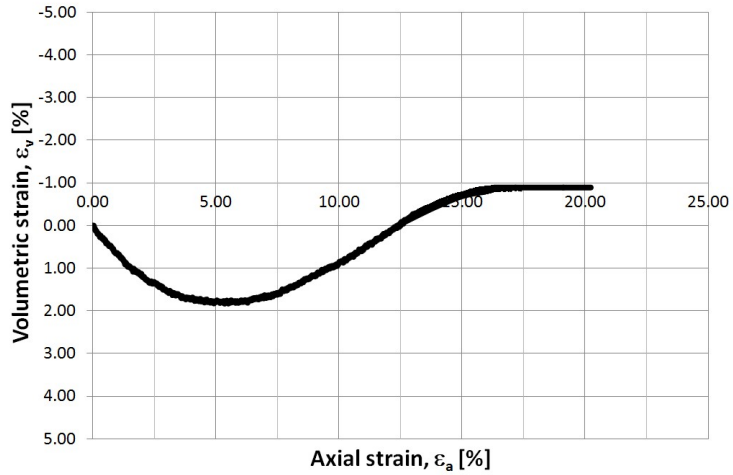

(a)

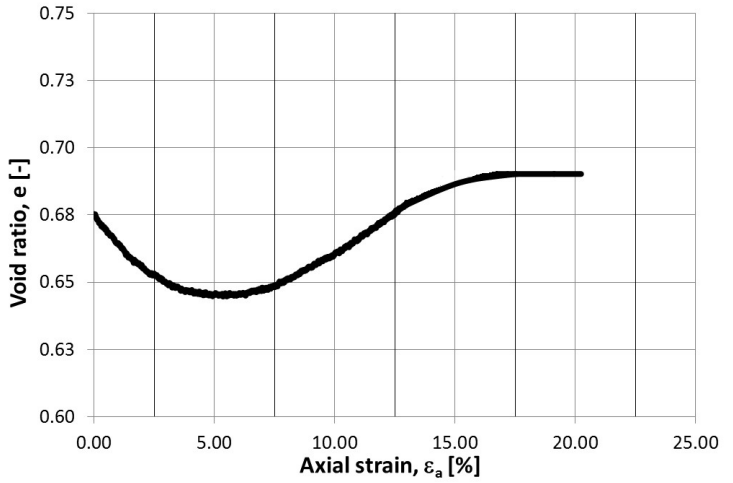

(b)

(b)

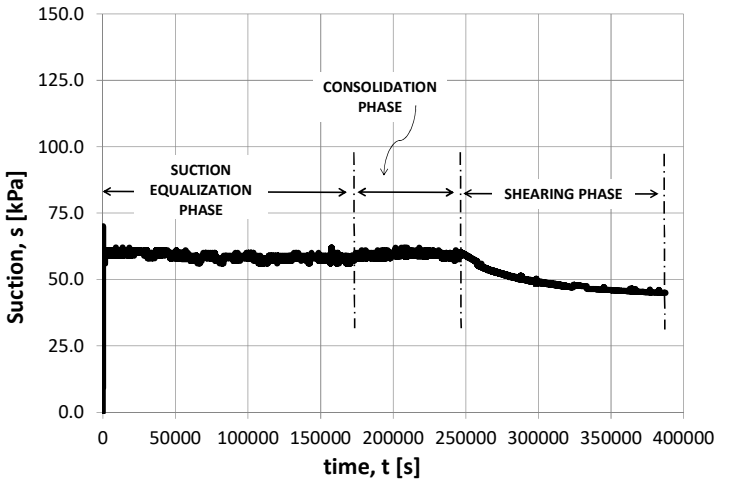

(c)

Fig. 6.31 - (a) Shearing phase: volumetric strain with axial strain. (b) Shearing phase: void ratio with axial strain. (c) Suction with time during the entire test (TX_0.70-60-400).

The stress-strain behaviour in terms of deviator stress q and axial strain ε_a for the unsaturated sample TX_0.70-60-400 is given in Fig. 6.32. It can be observed that deviator stress, starting from zero, increased until a maximum value q_{max} equal to 780kPa around an axial strain of 5÷6%. Then it gently decreased seeming to approach a constant value of 720kPa at the end of the test.

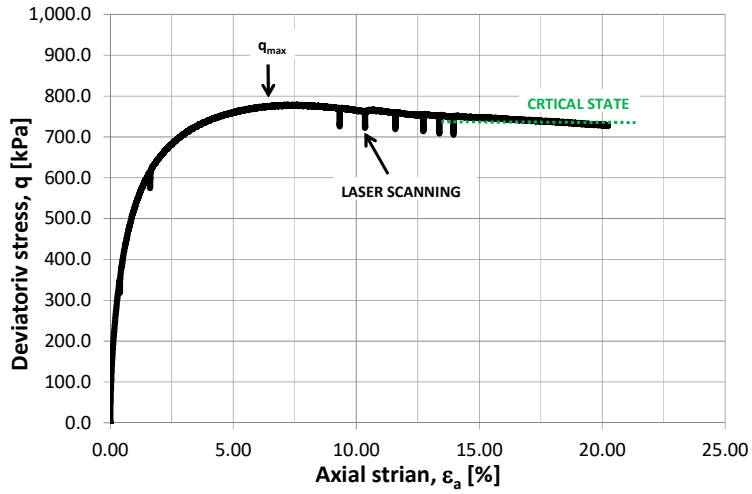

Fig. 6.32 - Shearing phase: deviator stress with axial strain (TX_0.70-60-400).

6.5.4 Results: TX_0.60-60-800

The experimental results obtained from Stava silt specimen TX_0.60-60-800 (initial void ratio e_0 = 0.60) are summarized in this section. A suction of 60kPa was imposed to the specimen by using of the axis translation technique, then it was isotropically consolidated by means of two steps. In the first step net stress was increased from p_{net} = 10kPa to p_{net} = 200kPa, allowing a steady state in terms of water volume change. In the second step, net stress was increased from p_{net} = 200kPa to p_{net} = 800kPa, allowing a steady state in terms of water volume change. Then, the specimen was wetted by increasing the pore water pressure in order to obtain 20kPa of suction. Again, the wetting phase was interrupted only when no variations in water volume were observed. Finally, the specimen was sheared under strain-controlled conditions at constant water content, by keeping open the air drainages and closing the water drainage.

Volumetric strains ε_v occurred during the shearing phase are shown in Fig. 6.33a. Specimen first shown a contraction behaviour corresponding at 2% of volumetric strain until an axial strain of about 7%. Then, it exhibited a dilative behaviour until the end of the test, corresponding at an axial strain of 15%. Due to high net stress imposed during the consolidation phase (p_{net} = 800kPa), the piston that transfers the pressure to the bottom of the sample was not long enough to give an high axial strain of the sample (about 20% as in the previous tests) at the end of the shearing phase. For these reason, the specimen was sheared to a limited axial strain of about 15%.

As given in Fig. 6.33b, because of the initial reduction of total volume at the beginning of the shearing phase, the void ratio decreased from 0.57 until 0.55 and then, because of the increasing of volume, the void ratio increased reaching again about 0.57. As shown in Fig. 6.33a and Fig. 6.33b, a steady state in terms of volumetric strain, and so void ratio was not reached.

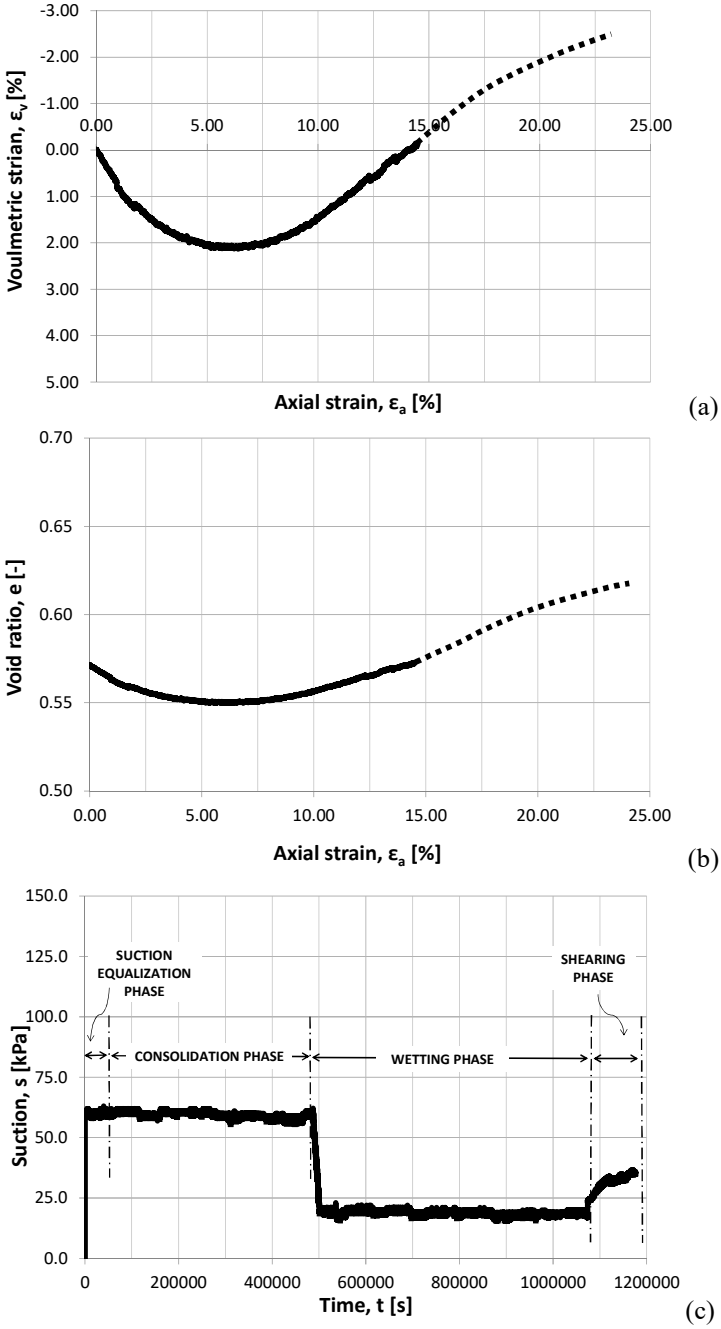

Fig. 6.33 - (a) Volumetric strain with axial strain, (b) void ratio with axial strain, during the shearing phase and (c) suction with time during the entire test (TX_0.60-60-800).

The matric suction evolution during the entire triaxial test is shown in Fig. 6.33c. As for TX_0.70-60-100, TX_0.70-60-200 and TX_0.70-60-400, also in this case the suction was imposed at 60kPa and it remains constant during the suction equalization and consolidation phase. Then, because of the increasing of the pore water pressure during the wetting phase,

suction decreases from 60kPa to 20kPa. Finally, during the shearing phase, the suction increased to 35kPa until the end of the test.
The stress-strain behaviour in terms of deviator stress q and axial strain ε_a for the unsaturated sample TX_0.60-60-800 is given in Fig. 6.34. It can be observed that deviator stress, starting from zero, increased until a maximum value q_{max} = 1600kPa at an axial strain ε_a = 7%. Then, the deviator stress constantly decreased until the end of the test without reaching a well-defined constant value.

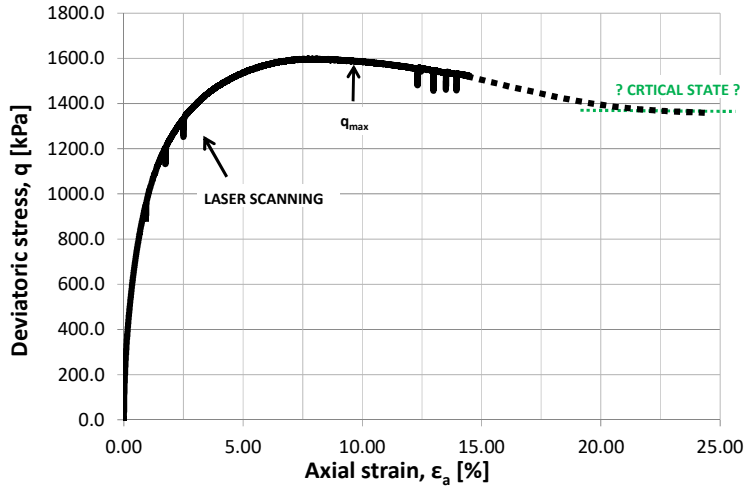

Fig. 6.34 - Shearing phase: deviator stress with axial strain (TX_0.60-60-800).

A stress ratio η equal to 1.14 was obtained. It corresponds at a friction angle equal to 28.7°. It is worth to note that this stress ratio, and it corresponding friction angle, results higher than other ones because in the current case the critical state was not completely reached.

6.5.5 Results: TX_0.60-175-200

The experimental results obtained from Stava silt specimen TX_0.60-175-200 (initial void ratio e_0 = 0.60) are summarized in this section. The initial purpose of this test consisted an imposing a suction of 4MPa to the specimen with a K_2SO_4 salt solution by means of the vapour equilibrium technique (Fig. 6.20). During this phase, the water drainage were closed, so the suction equalization can be considered as performed at constant water content. The specimen was then isotropically consolidated until reaching a net stress p_{net} = 200kPa by maintaining closed the water drainages. Finally, it was sheared under strain-controlled conditions at constant water content. As usually, at the end of the test, specimen was weighted, oven dried at 105°C for 24 hours and then weighted again in order to obtain the water content at the end of the shearing phase. Because the water drainages were kept closed during the entire test, a constant water condition was assumed also for consolidation and suction equalization phase. Knowledge of water content at the end of shearing phase (e = 0.73), allowed to compute the corresponding degree of saturation (Sr = 21.5%). The main drying branch of the water retention curve associated at the same void ratio of the sample at the end of shearing phase allowed to estimate the suction (s = 175kPa).

The volumetric strains ε_v occurred during the shearing phase are shown in Fig. 6.35a. Specimen first shown a very little volume contraction (ε_v about 0.3%) until an axial strain of about 1.5%. Then the specimen exhibited a dilative behaviour until a volumetric strain equal

to 9% the end of the test (axial strain of 15%). It is worth to note that no variations of volumetric strain were observed from axial strain of 8% until the end of the test, allowing to assume that a critical state condition was likely reached.
Because of the small initial reduction of total volume at the beginning of the shearing phase, the void ratio just decreased from 0.59 until 0.58 (Fig. 6.35b). Then, because of the increasing of volume, the void ratio increased reaching about 0.74 (Fig. 6.35b) and it remained nearly constant because of no variation of volume.

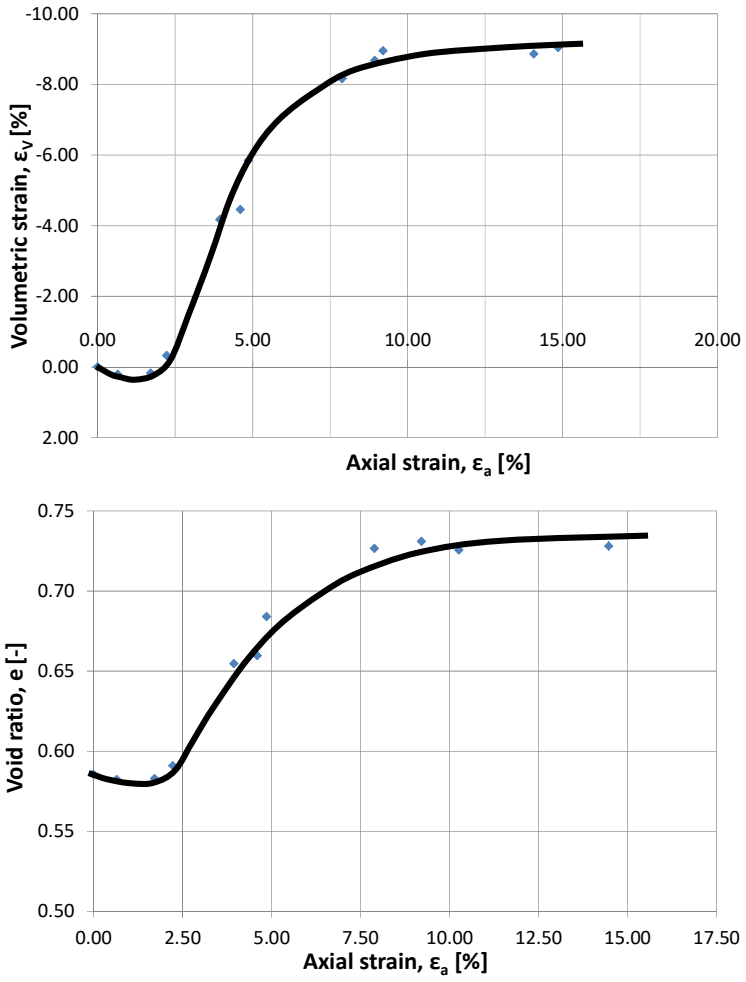

Fig. 6.35 - (a) Shearing phase: volumetric strain with axial strain. (b) Shearing phase: void ratio with axial strain (TX_0.60-300-200).

The stress-strain behaviour in terms of deviator stress q and axial strain ε_a for the unsaturated sample TX_0.60-300-200 is given in Fig. 6.36. The deviator stress, starting from zero, increased until a maximum value q_{max} = 650kPa around an axial strain of 1.5%÷2%. Then, it decreased reaching a value of about 450kPa at an axial strain of 7.5%. Finally, it remained constant until the end of the test.

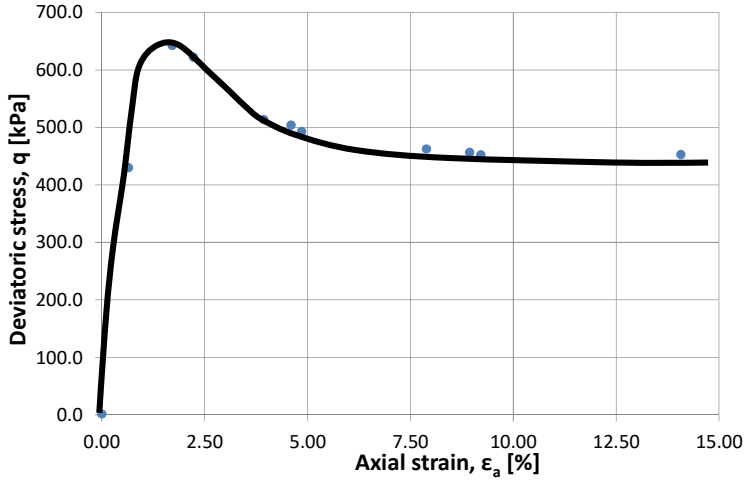

Fig. 6.36 - Shearing phase: deviator stress with axial strain (TX_0.60-350-200).

6.5.6 Results: TX_0.80-90-800

This section summarizes the experimental results obtained from Stava silt specimen TX_0.80-90-800 prepared at initial void ratio $e_0 = 0.80$.
The specimen was first fast loaded until a net stress of 100kPa at constant water content, so a suction of 90kPa was imposed by means of the axis translation technique. Then the specimen was isotropically consolidated until reaching a net stress equal to 800kPa. Again, as for TX_0.60-60-800, due to high net stress imposed during the consolidation phase (p_{net} = 800kPa), the piston that transfers the pressure to the bottom of the sample would not be long enough to give an high axial strain of the sample at the end of the shearing phase. In the current test, this mechanical limitation was solved. The adopted solution consisted of pushing the piston back just before the beginning of the shearing phase in order to have a longer available length. It is worth to note that during the piston pushing back operations, the loading chamber placed at the bottom of the triaxial cell and filled with de-aired water, were closed in order to avoid any undesired unloading of the specimen. Finally it was sheared under strain-controlled conditions at constant water content.
The volumetric strains ε_v occurred during the shearing phase are shown in Fig. 6.37a. Specimen shown a pure contractive behaviour during the entire shearing phase, reaching a constant value of about 5% at an axial strain corresponding at 10%. Then, the volumetric strain remains constant until the end of the test (axial strain of 22%), meaning the critical state was reached.
As shown in Fig. 6.37b, because of the reduction of volume, the void ratio constantly decreased from 0.73 until 0.64 and then it remains about constant because of no variation of volume.
The matric suction during the entire triaxial test is shown in Fig. 6.37c. Initial suction was imposed at 90kPa and kept constant during the suction equalization phase and consolidation phase. Despite an decrease of the void ratio due to the pure contractive behaviour of the specimen and a corresponding increase of degree of saturation, a little increase of the matric suction from 90kPa to 106kPa can be observed.
The stress-strain behaviour in terms of deviator stress q and axial strain ε_a for the unsaturated sample TX_0.80-90-800 is given in Fig. 6.38. It can be observed that deviator stress, starting from zero, monotonically increased until a maximum value q_{max} equal to 1280kPa around an axial strain of 15% and then it remained nearly constant until the end of the test,

corresponding to at an axial strain of 22%.

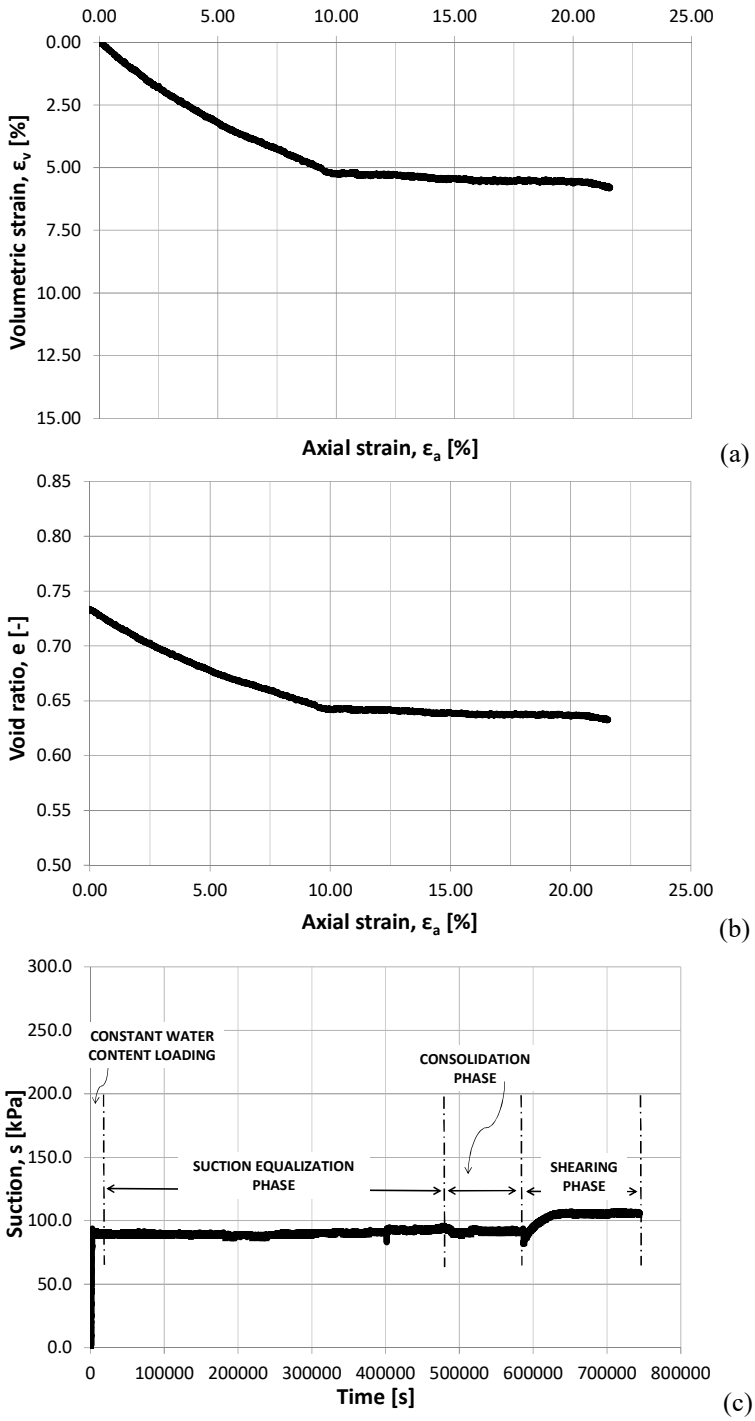

Fig. 6.37 - (a) Shearing phase: volumetric strain with axial strain. (b) Shearing phase: void ratio with axial strain. (c) Suction with time during the entire test (TX_0.80-90-800).

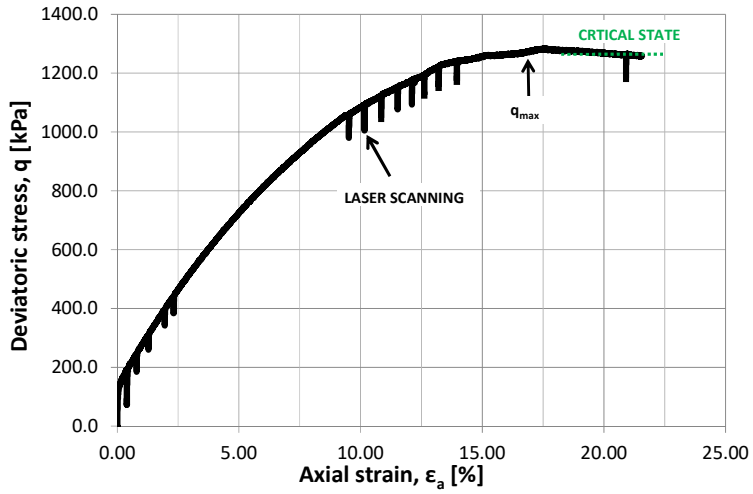

Fig. 6.38 - Shearing phase: deviator stress with axial strain (TX_0.80-90-800).

6.5.7 Results: TX_0.64-60-200b

The experimental results obtained from Stava silt specimen TX_0.64-60-200b (initial void ratio e_0 = 0.64) are summarized in this section. After a fast loading of the sample at constant water content until reaching a net stress p_{net} = 100kPa in undrained condition, a suction of 60kPa was imposed at the specimen in drained conditions by means of open the water drainages. Then it was isotropically consolidated at a net stress p_{net} = 200kPa. Finally the specimen was sheared under strain-controlled conditions at constant suction (drained conditions), by keeping open the air and water drainages.

Volumetric strains occurred during the shearing phase are given in Fig. 6.39a. Specimen first shown a very small contraction corresponding at 0.3% of volumetric strain until an axial strain of about 1%. Then, it exhibited a dilative behaviour with a volumetric strain ε_a = 2.6% until the end of the test (axial strain of 11%). It is worth to note that no variations of volumetric strain occurred from axial strain of 7% to the end of the test, allowing to assume that a critical state condition was likely reached.

As shown in Fig. 6.39b, due to the initial reduction of total volume at the beginning of the shearing phase, the void ratio experienced a little reduction. Finally, because of the increasing of volume, the void ratio increased from 0.59 to a final value of about 0.64.

Because of the reduction of volume due to the initial fast loading (water drainages closed, air drainages open) the degree of saturation increased, from the initial value of 73% up to 76%-77% (Fig. 6.39c). Then, due to the drying process occurred during the suction equalization phase (3.2cm^3 of water left the specimen), the degree of saturation decreased to 68%. A small increase of degree of saturation was observed during the consolidation phase, from Sr = 68% to Sr = 69%. Finally, because of the dilative behaviour occurred during the drained shearing phase, the degree of saturation decreased to a constant value of Sr = 63%.

The stress-strain behaviour, expressed in terms of deviator stress q and axial strain ε_a, is given in Fig. 6.40. The deviator stress, starting from zero, increased until a maximum value q_{max} = 420kPa corresponding at an axial strain ε_a = 3%. Then, the deviator stress gently decreased reaching a value of about 390kPa at an axial strain of 7.5%. Finally, it remained constant until the end of the test.

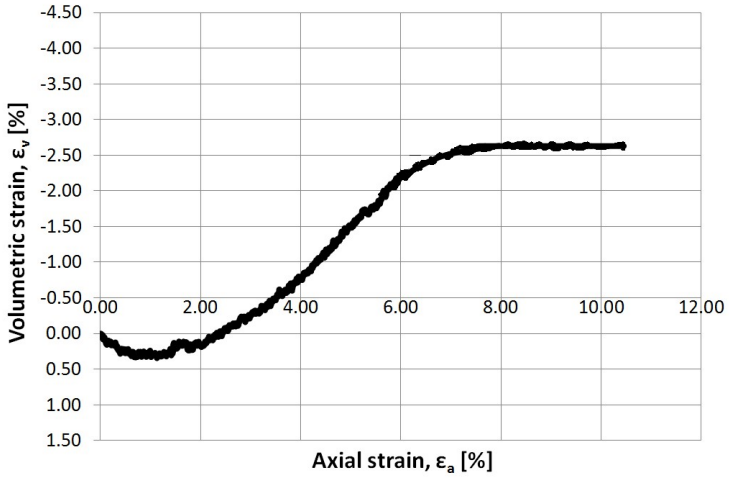

(a)

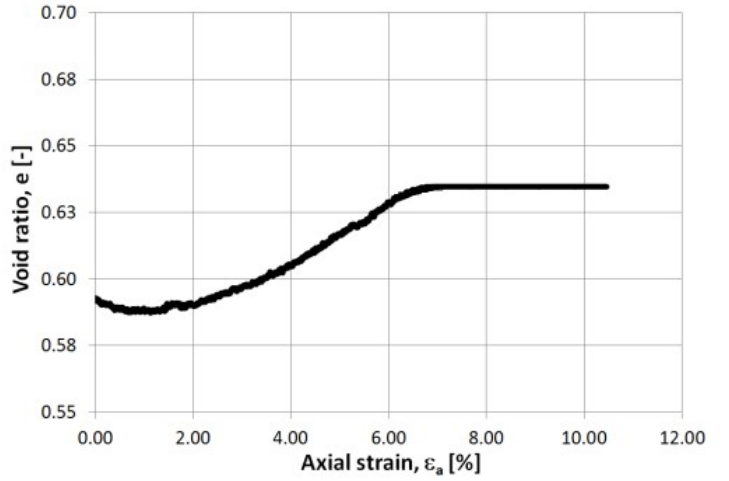

(b)

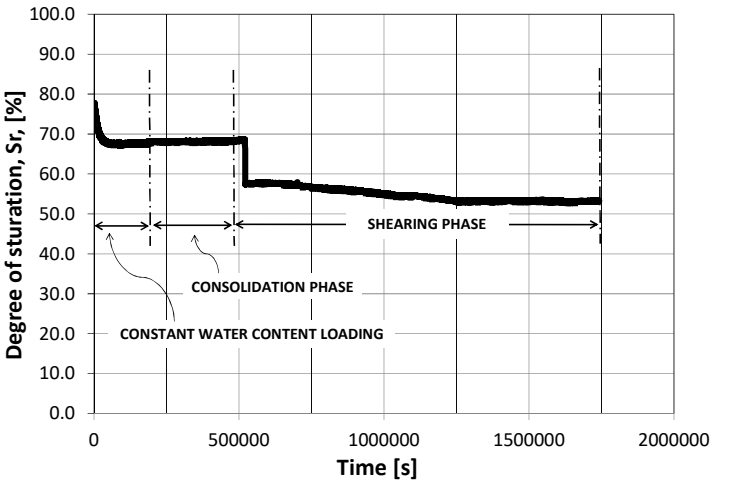

(c)

Fig. 6.39 - (a) Shearing phase: volumetric strain with axial strain. (b) Shearing phase: void ratio with axial strain. (c) Degree of saturation with time during the entire test (TX_0.64-60-200b).

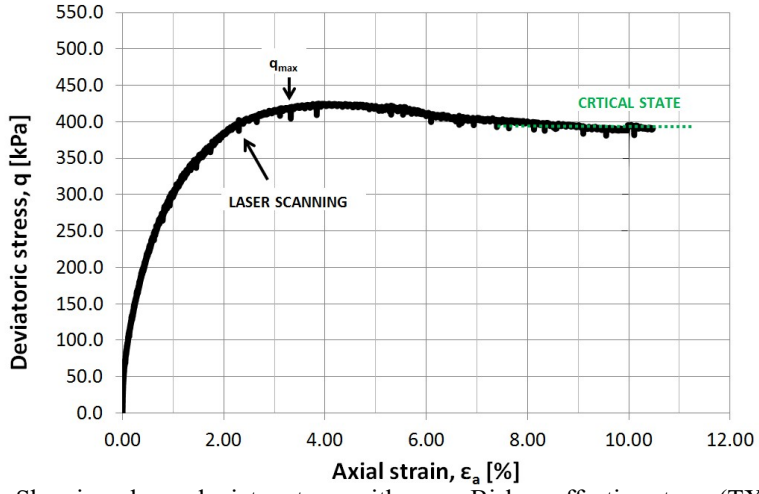

Fig. 6.40 - Shearing phase: deviator stress with mean Bishop effective stress (TX60-200b).

6.5.8 Results: TX_0.80-90-100

This section summarizes the experimental results (Fig. 6.41) obtained from Stava silt specimen TX_0.80-90-100 prepared at an initial void ratio $e_0 = 0.80$.
The specimen was fast loaded until a net stress p_{net} = 100kPa at constant water content. Hence a matric suction s = 90kPa was imposed in drained conditions by means of the axis translation technique. Finally, the specimen was sheared under strain-controlled conditions at constant suction, by keeping open the air and water drainages.
Volumetric strains occurred during the shearing phase are given in Fig. 6.41a. The specimen first shown a contraction corresponding at 1.4% of volumetric strain until an axial strain of about 7%. Then, a dilative behaviour can be observed: the volumetric strain decreases from 1.45% to about 1.2% until the end of the test (axial strain of 17%), approaching the critical state condition.
As given in Fig. 6.41b, because of the initial reduction of total volume at the beginning of the shearing phase, the void ratio shown a reduction from 0.77 to 0.74. After that, because of the increasing of total volume, the void ratio experienced a little increase.
The stress-strain behaviour in terms of deviator stress q and axial strain ε_a is given in Fig. 6.41a. The deviator stress, starting from zero, increased until a maximum value q_{max} = 240kPa around an axial strain of 4%. Then, it gently decreased reaching a value of about 180kPa corresponding at an axial strain of 15%. Then, it seems remain nearly constant until the end of the test at an axial strain of about 17%.

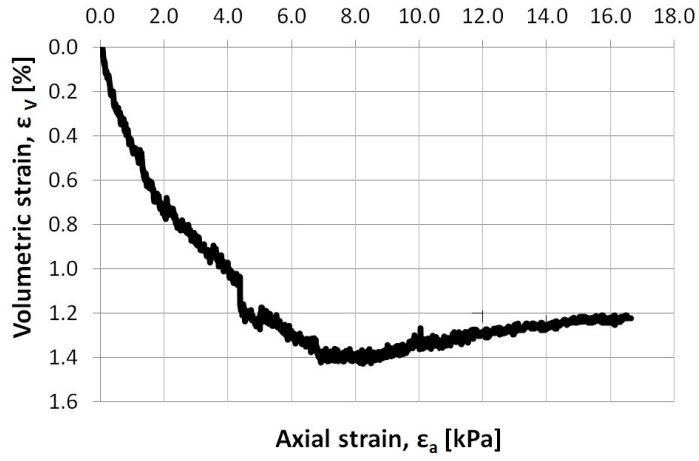

(a)

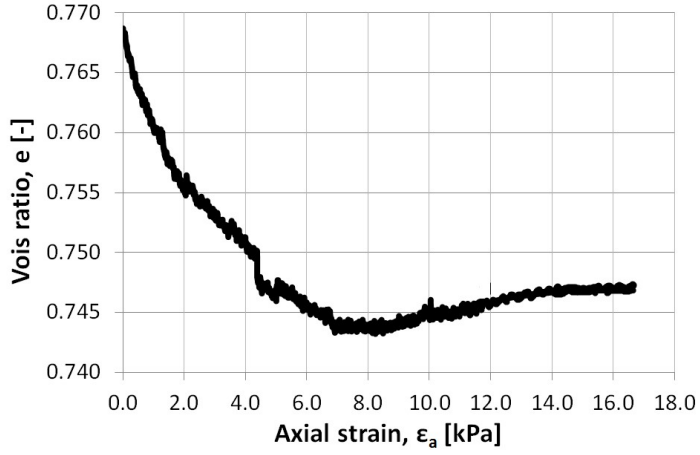

(b)

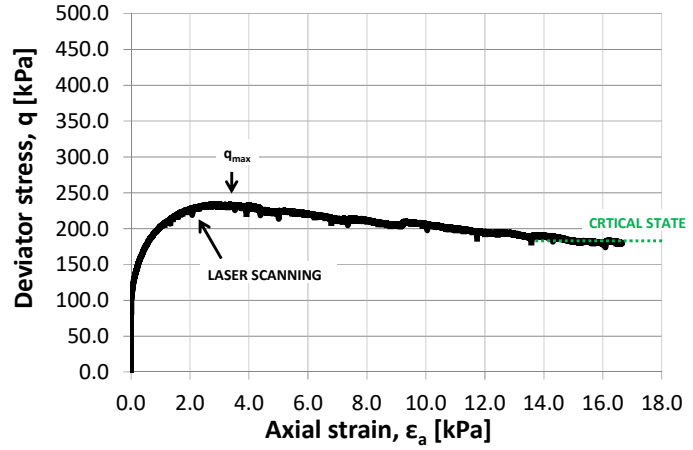

(c)

Fig. 6.41 - (a) Shearing phase: volumetric strain with axial strain. (b) Shearing phase: void ratio with axial strain. (c) Shearing phase: deviator stress with mean Bishop effective stress (TX_0.80-90-100).

6.5.9 *Effect of net stress on hydro-mechanical behaviour*

The hydro-mechanical response of unsaturated silt specimens isotropically consolidated at different net stresses is given in Fig. 6.42, Fig. 6.43, Fig. 6.44 and Fig. 6.45. The three specimens TX_0.70-60-100, TX_0.70-60-200 and TX_0.70-60-400 were prepared at the same initial conditions in terms of void ratio e_0 = 0.70 , water content w_0 and dry weight γ_d. They were equalized at the same suction s = 60kPa, then consolidated at different net stresses, p_{net} = 100kPa, p_{net} = 200kPa, p_{net} = 400kPa, respectively. Finally they were sheared in strain controlled conditions at constant water content.

As shown in Fig. 6.42a the maximum deviator stress of TX_0.70-60-100 is q_{max} = 220kPa corresponding to an axial strain ε_a = 2.5%, The maximum deviator stresses of TX_0.70-60-200 and TX_0.70-60-400 specimens are q_{max} = 400kPa and q_{max} = 780kPa, corresponding to an axial strain ε_a = 4.5% and ε_a = 6.5% respectively. When the three test results are plotted together, the maximum deviator stress increases with increasing the net stress: all stress-strain curves are well ordered and evolve regularly with increasing net stress. It is worth to note that the maximum deviator stress occur at increasing axial strain with increasing the net stress.

Figure 6.42b shows the stress ratio η with the axial strain of the samples TX_0.70-60-100, TX_0.70-60-200 and TX_0.70-60-400 during the shearing phase. It can be noticed that, for all the three specimens, the stress ratio at critical state is about M = 1.1. It is also possible to appreciate the fact that, increasing the confining stress applied during shearing, causes the decrease of the stress ratio at peak conditions η_{peak}.

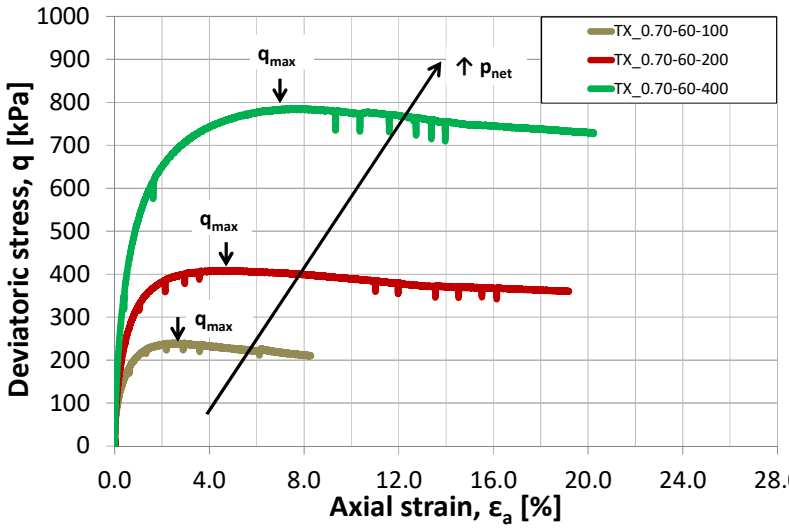

(a)

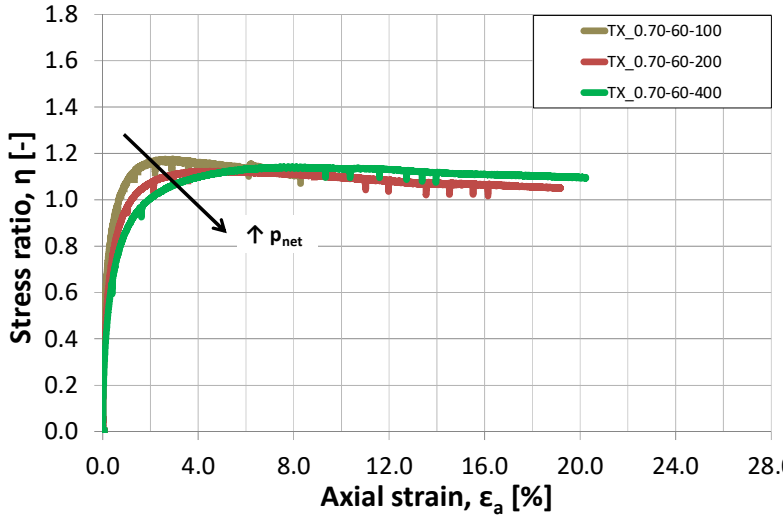

(b)

Fig. 6.42 - The effect of net pressure on mechanical behaviour during the shearing phase in terms of (a) deviator stress q and (b) stress ratio M during the shearing phase.

Figure 6.43 shows the volumetric response of the same samples TX_0.70-60-100, TX_0.70-60-200 and TX_0.70-60-400. It is worth to note that a positive volumetric strain correspond to a decrease of volume and vice-versa. The maximum volumetric contraction of TX_0.70-60-100 is ε_v = 0.4% followed by an increase of volume until an estimated volumetric strain of about -3%. The volumetric contractions of TX_0.70-60-200 and TX_0.70-60-400 specimens are ε_v = 1.2% and ε_v = 2%, followed by a dilative behaviour until volumetric strains of about ε_v = - 1.8% and ε_v = -1.0%, respectively. When the three test results are plotted together, it is clear an increase of compressive behaviour with increasing net stress. All curves are well ordered and evolve with increasing net stress according to the black arrow. On the other hand, a decrease of dilative behaviour with increasing net stress can be observed.

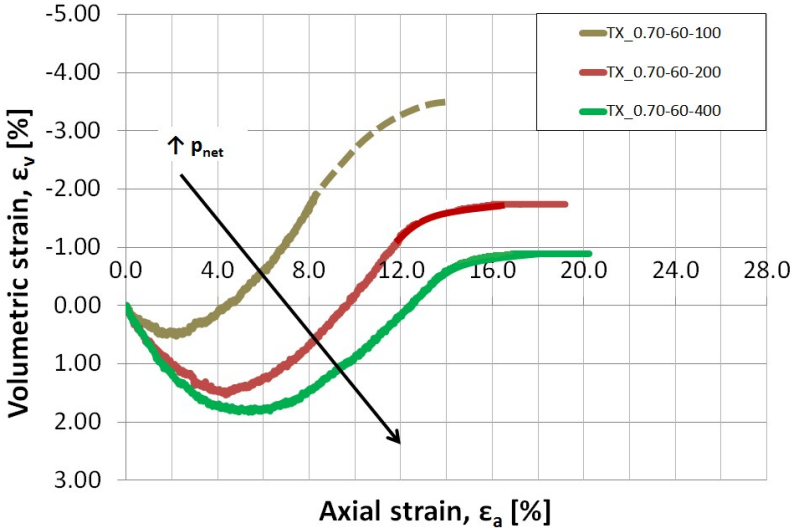

Fig. 6.43 - The effect of net pressure on volumetric behaviour during the shearing phase.

Figure 6.44 shows the stress path in terms of suction and net stress of the same samples TX_0.70-60-100, TX_0.70-60-200 and TX_0.70-60-400 during the entire tests. The numbers from 1 to 4 are referred to TX_0.70-60-400 specimen. The number 1 identifies the initial state, number 2 identifies the end of the suction equalization phase, while number 3 and 4 stands for the end of consolidation phase and the end of the shearing phase, respectively. In all these cases, a suction s = 60kPa was imposed and it did not change during until the end of consolidation phase. Because of the shearing phase performed at constant water content, variations in pore water pressure led changes in suction. Independently from the net stress imposed during the consolidation phase, a decrease of suction can be observed for all the three specimens until a final value of about 44kPa.

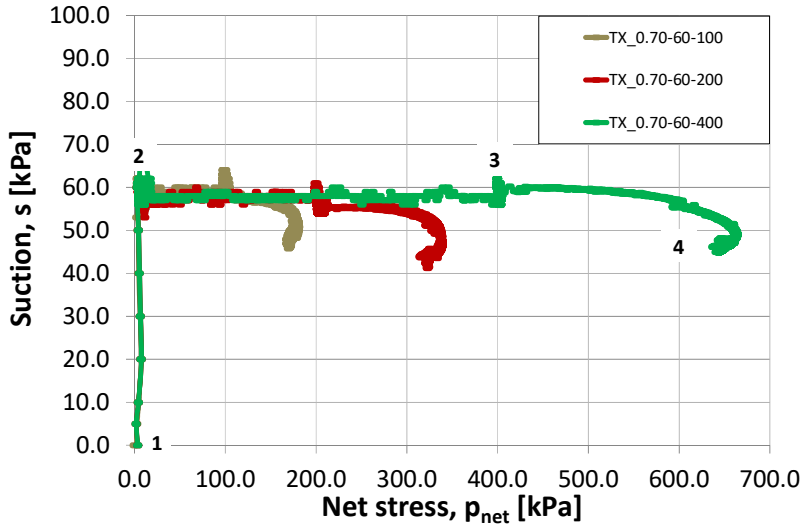

Fig. 6.44 - The effect of net pressure on suction during the shearing phase.

Figure 6.45 shows the water volume change with time of the same samples TX_0.70-60-100, TX_0.70-60-200 and TX_0.70-60-400 during the consolidation phase. All the specimens loss different amounts of water. Sample TX_0.70-60-100 loss a water volume ΔVw = 0.25cm^3, while sample TX_0.70-60-200 and TX_0.70-60-400 loss 0.4cm^3 and 0.5cm^3, respectively. If the three test results are plotted together, it is clear an increase of water volume loss with increasing net stress. All curves are well ordered and evolve with increasing net stress according to the black arrow.

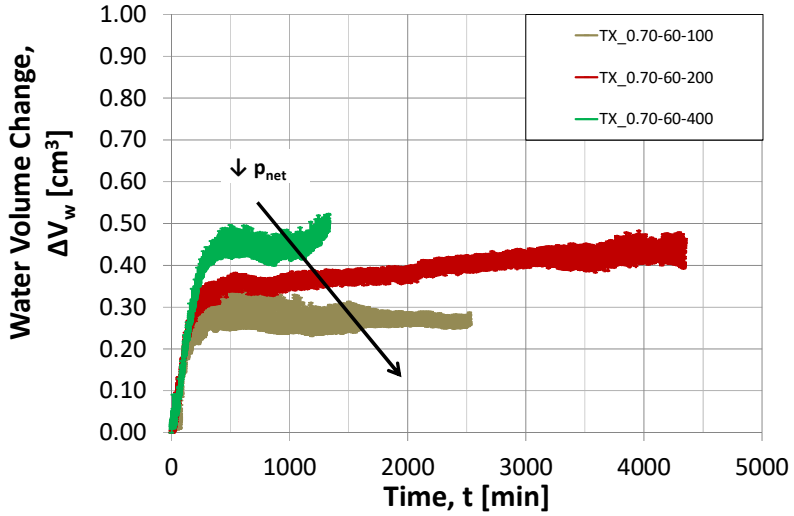

Fig. 6.45 - The effect of net pressure on water volume change during the consolidation phase.

The compression lines in isotropic conditions for specimens TX_0.70-60-100, TX_0.70-60-200 and TX_0.70-60-400 are shown in Fig. 6.46a. Details in terms of suction, degree of saturation and void ratio at the beginning and at the end of the consolidation phase are given in Tab. 6.9. Probably because of inhomogeneity during the sample preparation, little differences of the void ratio at the beginning of the consolidation phase can be observed.

Tab. 6.9 - Suction, degree of saturation and void ratio at the beginning and at the end of the consolidation phase for specimen TX_0.70-60-100, TX_0.70-60-200 and TX_0.70-60-400.

Phase		**TX_0.70-60-100**	**TX_0.70-60-200**	**TX_0.70-60-400**
Beginning of consolidation	s_i [kPa]	60.0	57.0	59.0
End of consolidation	s_f [kPa]	60.0	56.0	58.0
Beginning of consolidation	Sr_i [%]	46.6	50.6	48.9
End of consolidation	Sr_f [%]	46.7	51.0	49.6
Beginning of consolidation	e_i [-]	0.70	0.69	0.70
End of consolidation	e_i [-]	0.69	0.67	0.68

Because of the different net stress applied, during the consolidation phase the three samples experienced different void ratio changes (Δe = 0.015, Δe = 0.021, Δe = 0.028) and different volumetric strain variations ($\Delta\varepsilon_v$ = 0.88%, $\Delta\varepsilon_v$ = 1.24%, $\Delta\varepsilon_v$ = 1.64%, Fig. 6.46b). The maximum void ratio variation was experienced by the sample consolidated at the higher net stress (TX_0.70-60-400 with Δe = 0.028 and $\Delta\varepsilon_v$ = 1.64%), while the minimum void ratio variation was experienced by the sample consolidated at the lower net stress (TX_0.70-60-100 with Δe = 0.015 and ($\Delta\varepsilon_v$ = 0.88%). Within the stress range investigated (p'_B varies from 30kPa to 430kPa), the stiffnesses of specimens TX_0.70-60-100, TX_0.70-60-200 and TX_0.70-60-400 are practically the same because of the same slope of the compression lines in isotropic conditions as shown in Fig. 6.46.

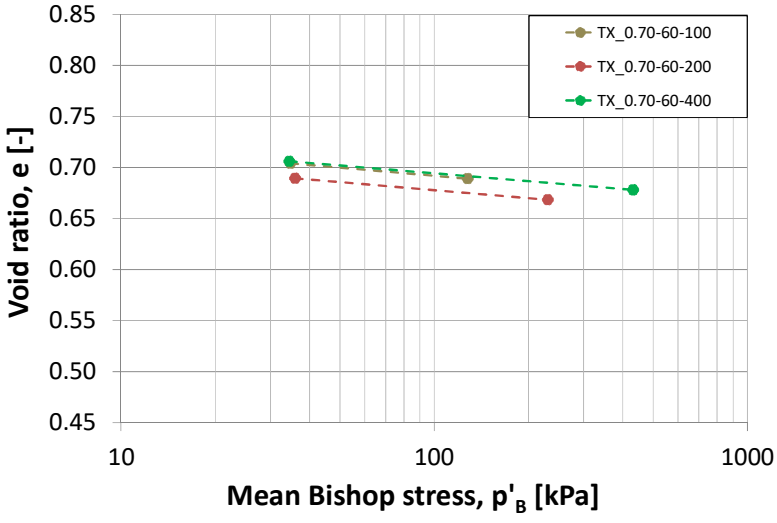

(a)

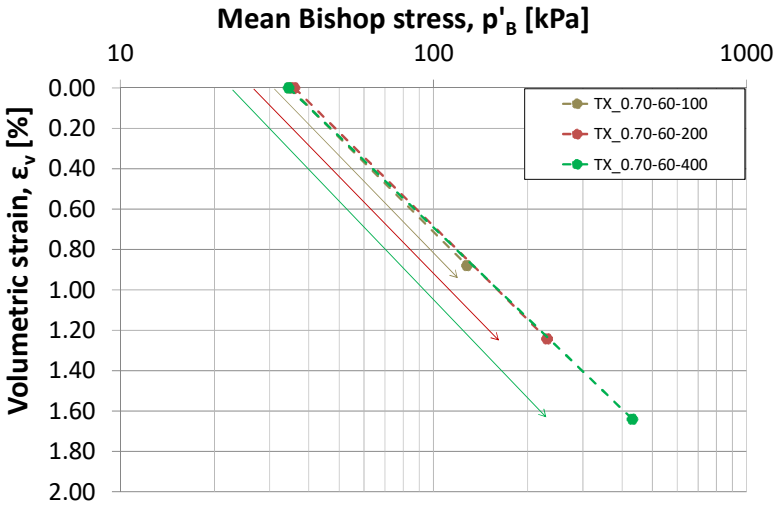

(b)

Fig. 6.46 - (a) Initial and final points of the isotropic compression lines. (b) Initial and final volumetric strain with mean Bishop stress during the isotropic consolidation phase (specimen TX_0.70-60-100, TX_0.70-60-200 and TX_0.70-60-400).

6.5.10 Effect of drainage conditions on hydro-mechanical behaviour

The hydro-mechanical response of unsaturated silt specimens sheared at different drainage conditions is given in Fig. 6.47, Fig. 6.48. The two specimens TX_0.70-60-200 and TX_0.64-60-200b were prepared at initial void ratio e_0 = 0.70 and e_0 = 0.64, respectively. Sample TX_0.70-60-200 was equalized at the suction s = 60kPa, then it was consolidated at net stresses, p_{net} = 200kPa and finally it was sheared at constant water content conditions. On the other side, sample TX_0.64-60-200b was first loaded at net stresses p_{net} = 100kPa at constant water content, then it was equalized at the same suction imposed at sample

TX_0.70-60-200 (s = 60kPa) in order to be consolidated at net stress p_{net} = 200kPa. Finally it was sheared in strain controlled conditions at constant suction (drained conditions).

As shown in Fig. 6.47a the maximum deviator stress of TX_0.70-60-200 is q_{max} = 425kPa, while the maximum deviator stresses of TX_0.64-60-200b is about q_{max} = 405kPa. The residual deviator stress of sample TX_0.70-60-200 and TX_0.64-60-200b is 360kPa and 390kPa, respectively. Figure 6.47b shows the stress ratio η with the axial strain of the two samples during the shearing phase. It can be noticed that, for the sample TX_0.70-60-200, the stress ratio at critical state is about 1.05, while for sample TX_0.64-60-200b the stress ratio is 1.14.

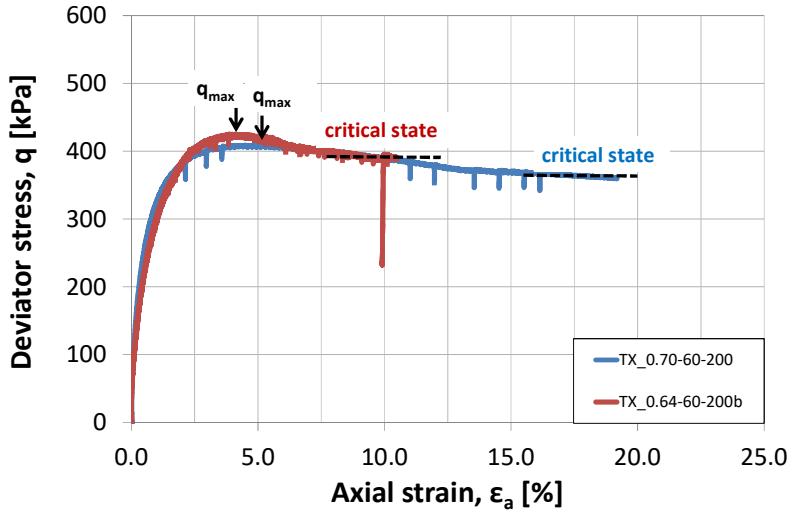

(a)

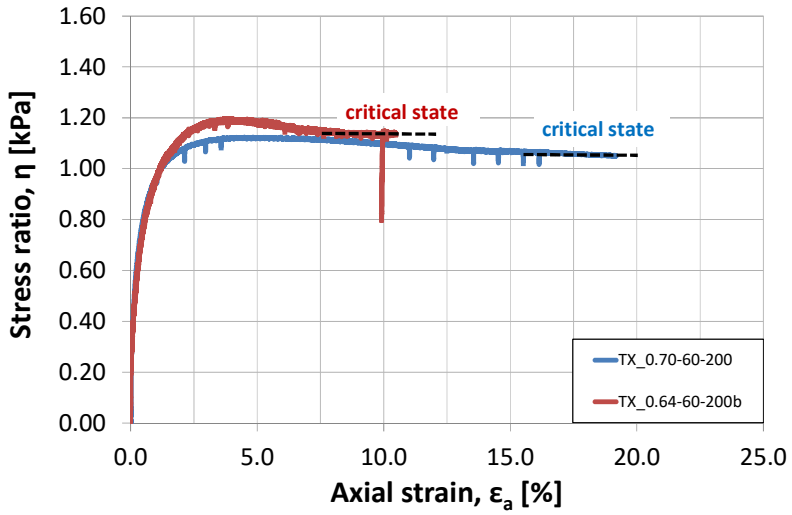

(b)

Fig. 6.47 - (a) The effect of drainage conditions on mechanical behaviour during the shearing phase in terms of (a) deviator stress q and (b) stress ratio M during the shearing phase.

Figure 6.48 shows the stress path in terms of suction with time of the two specimens during the entire tests. Number 1 identifies the initial state, number 2 identifies the end of the suction equalization phase, while number 3 and 4 stands for the end of consolidation phase and the end of the shearing phase, respectively.
As shown in Fig. 6.48, suction imposed at sample TX_0.70-60-200 remained constant until the beginning of the shearing phase. Then, it decreased until a constant value of about 43kPa. On the other hand, for sample TX_0.64-60-200b the measured suction reached the value imposed at the end of the equalization phase (s = 60kPa) and then it remained nearly constant in the following consolidation phase. Because of the low strain rate imposed during the shearing phase, no excess of pore pressure were generated, so the suction didn't change until the end of the test.

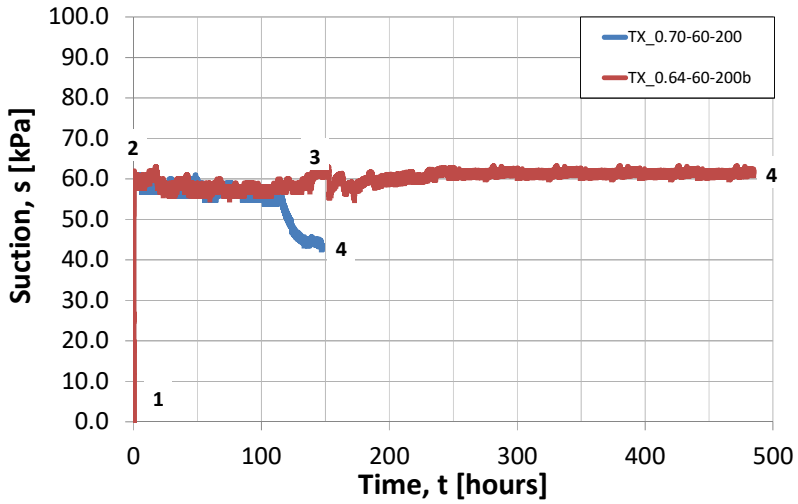

Fig. 6.48 - Effect of drainage conditions on mechanical behaviour during the shearing phase in terms of suction with time.

Figure 6.49 shows the volumetric strain of samples TX_0.70-60-200 and TX_0.64-60-200b with the axial strain during the shearing phase. It can be observed that the sample sheared at constant water content has an higher tendency to contract than the sample sheared at constant suction. After an initial contraction phase, both samples started to dilate. Sample TX_0.70-60-200 reached a volumetric strain of -1.8%, while sample TX_0.64-60-200b reached a volumetric strain of -2.6%. Starting from the volumetric strain corresponding to the maximum reduction of volume, it is possible to observe that both samples dilated, resulting in a variation of volumetric strain equal to 2.9%÷3.0%.

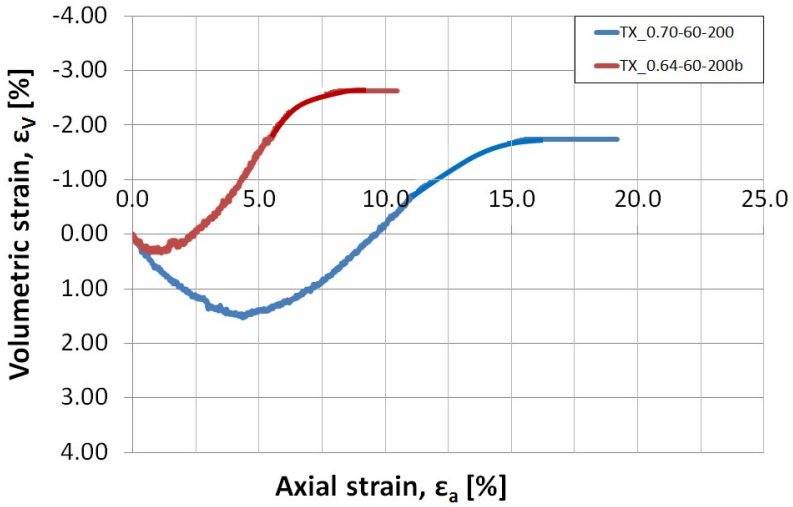

Fig. 6.49 - The effect of drainage conditions on mechanical behaviour during the shearing phase in terms of volumetric strain with axial strain.

6.5.11 Hydro-mechanical coupled behaviour in unsaturated conditions: constant water content shearing phase

The hydraulic path resulting from the suction controlled triaxial test for specimen TX_0.70-60-100, in terms of suction s and water ratio e_w, is given in Fig. 6.50a. Points A and B represent the beginning of the shearing phase and the end of the test, respectively. In the same figure, the water retention curves for void ratios equal to those at the beginning and end of the shearing phase, are also given. Indeed, the green solid and dotted lines represent the main drying and main wetting branches, respectively, at void ratio chosen to be equal to e = 0.69, the same value that triaxial specimen TX_0.70-60-100 had at the end of consolidation phase. In a similar way, the red solid and dotted lines refer to the main drying and main wetting branches, respectively, at void ratio chosen to be equal to e = 0.72, the same value that triaxial specimen TX_0.70-60-100 had at the end of the test. It is worth to note that, because of the need to have the water retention curves corresponding to the values of void ratios at the beginning and at the end of the shearing phase, the water retention curve is obtained by implementing the model proposed by Gallipoli, whose parameters n, m, ψ, Φ were calibrated and summarized in Tab. 5.6. The direction of the hydraulic path during the test is highlighted by the red arrow. Because of the small size of the stress path if compared to the whole water retention curve, a more detailed picture is given in Fig. 6.50b. Since shearing was performed at constant water content, the water ratio is constant, so the hydraulic path is basically a vertical line. The initial point A lies on the main drying branch of water retention curve 0.69. During the shearing phase, the specimen TX_0.70-60-100 exhibited a dilative behaviour, and its void ratio increased from 0.69 to 0.72. A dilative behaviour is associated to changes in the water retention state of the soil toward the drying water retention surface. It is expected that suction increases due to drying. However, suction decreased in order to approach the main drying branch of the water retention curve corresponding to e = 0.72 from the water retention curve corresponding to e = 0.69. This is consistent with the experimental data: indeed, the water retention state moved down, in the same direction of the main drying branch of the water retention curve corresponding to void ratio 0.72. It is worth to note that in the current test, the critical state was not completely reached: the estimated void ratio at critical state is e = 0.74 and this might further decrease

the suction. It is also worth noting that, in the case of a fully saturated soils sheared in undrained conditions and having tendency to dilate, pore pressure decrease is anticipated to "freeze" volume changes. The opposite (pore pressure increase) occurred for this test.

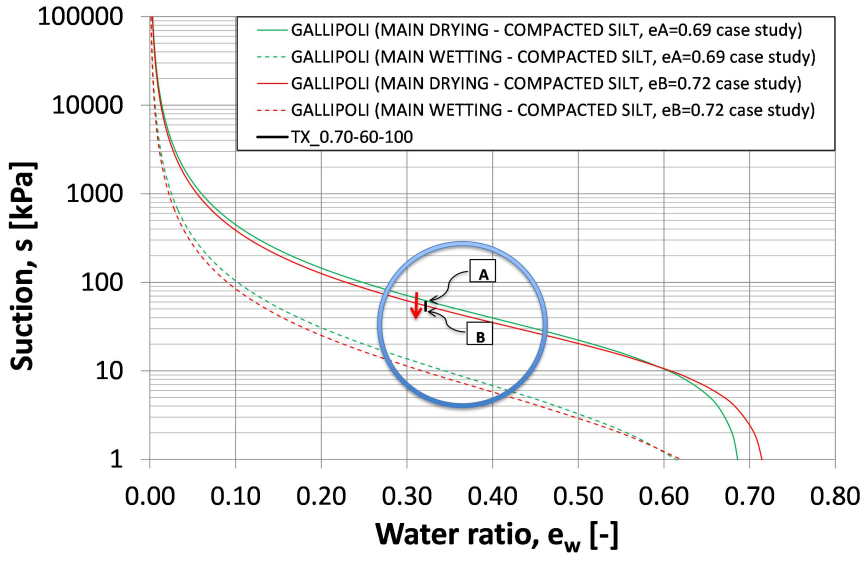

(a)

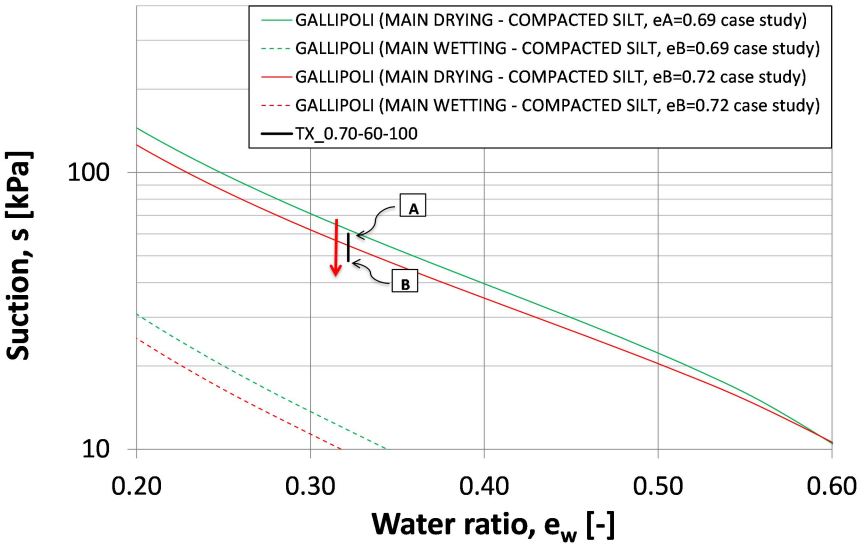

(b)

Fig. 6.50 - (a) Superposition of water retention curve and stress path obtained from suction controlled triaxial test and (b) its detail (TX_0.70-60-100).

Similar results, from the suction controlled triaxial test on specimen TX_0.70-60-200, are given in Fig. 6.51a. Again, points A and B represent the beginning of the shearing phase and the end of the test, respectively. The water retention curves corresponding at void ratios equal to those resulting at the beginning of shearing phase and at the end of the test, are estimated by the model proposed by Gallipoli *et al.* (2003). The green solid and dotted lines refer the main drying and main wetting branches, respectively, at void ratio chosen to be

equal to e = 0.67. Red solid and dotted lines represent the main drying and main wetting branches, at void ratio chosen to be equal to e = 0.70, the same value that triaxial specimen TX_0.70-60-200 had at the end of the test. A more detailed picture is given in Fig. 6.51b. Again, shearing phase of TX_0.70-60-200 test was performed at constant water content, so the water ratio is constant and the stress path is a vertical line.
The initial point A is very close to the main drying branch of water retention curve 0.67. Again, a dilative behaviour is associated to changes in the water retention state of the soil toward the drying water retention surface. It is expected that suction increases due to drying. However, suction decreased in order to approach the main drying branch of the water retention curve corresponding to e = 0.70 from the water retention curve corresponding to e = 0.67. This is consistent with the experimental data: point B moved down, in the same direction of the main drying branch of the water retention curve corresponding at void ratio 0.70. It is worth to note that the final point B does not lie exactly on the main drying curve (e = 0.70). During the shearing phase, the measured decrease of suction is 12÷13kPa, while the decrease of suction estimated by means of the water retention curves is about 4-5kPa. These differences are supposed to be not so relevant because variations of ±5kPa in water and air pressures, due to the experimental devices's accuracy, are common. Also consider that the water retention curves estimated on basis of Gallipoli *et al* (2003) relationship might differ a bit from the physical behavior of the soil.

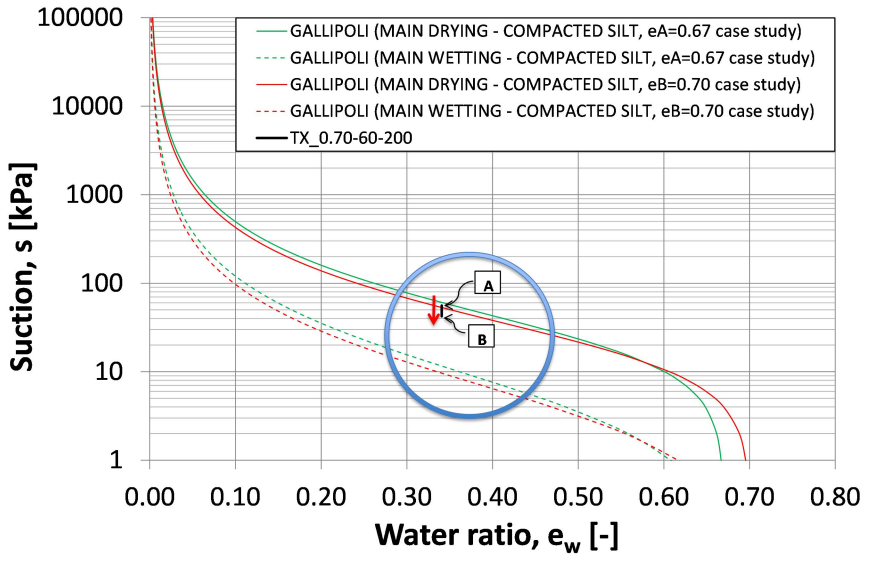

(a)

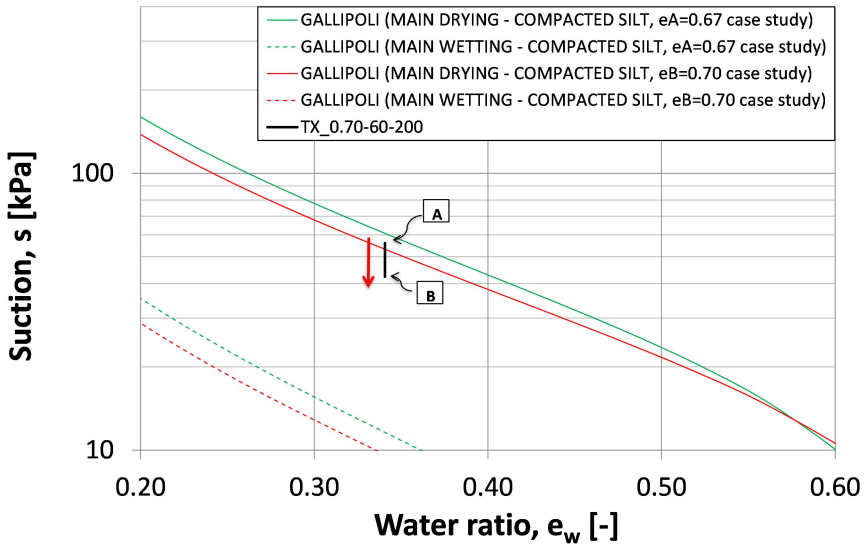

(b)

Fig. 6.51 - (a) Superposition of water retention curve and stress path obtained from suction controlled triaxial test and (b) its detail (TX_0.70-60-200).

It is worth to note that initial (A) and final points (B) of the stress path followed during shearing represented in (s-e_w) plane shown in Fig. 6.51, are the same of those represented in (s-Sr) plane (Fig. 6.28) for the entire stress path during shearing. By observing Fig. 6.28, it can be noticed that points 2 and 3 lie close to the main drying branch. Hence, by observation of whole path 1-2-3-4, the water retention curve (hydraulic behaviour) seems to play a relevant role in the mechanical response, acting as a domain. The hydro-mechanical behaviour in terms of s-Sr obtained from the suction controlled triaxial test lies inside this two dimensional domain that could evolve into a three dimension space if relevant variations of void ratio occur. In this latter case, the water retention curve (*WRC*) should be estimated by means of models able to take into account the void ratio variations (e.g. Gallipoli *et al,* 2003), giving the *WRC* as a surface into the (s-Sr-e) space.

Same considerations can be extended by analysing the results obtained from the suction controlled triaxial test on specimen TX_0.70-60-400 (Fig. 6.52a and Fig.6.52b). Because of the small dilative behaviour due to the high applied net stress at consolidation phase (from e = 0.68 to e = 0.69), the water retention curves estimated by means of Gallipoli model, are very close each other. As pointed by the red arrow, the stress path moves down, toward the main drying branch of the water retention curve corresponding at e = 0.69, with a decrease of suction.

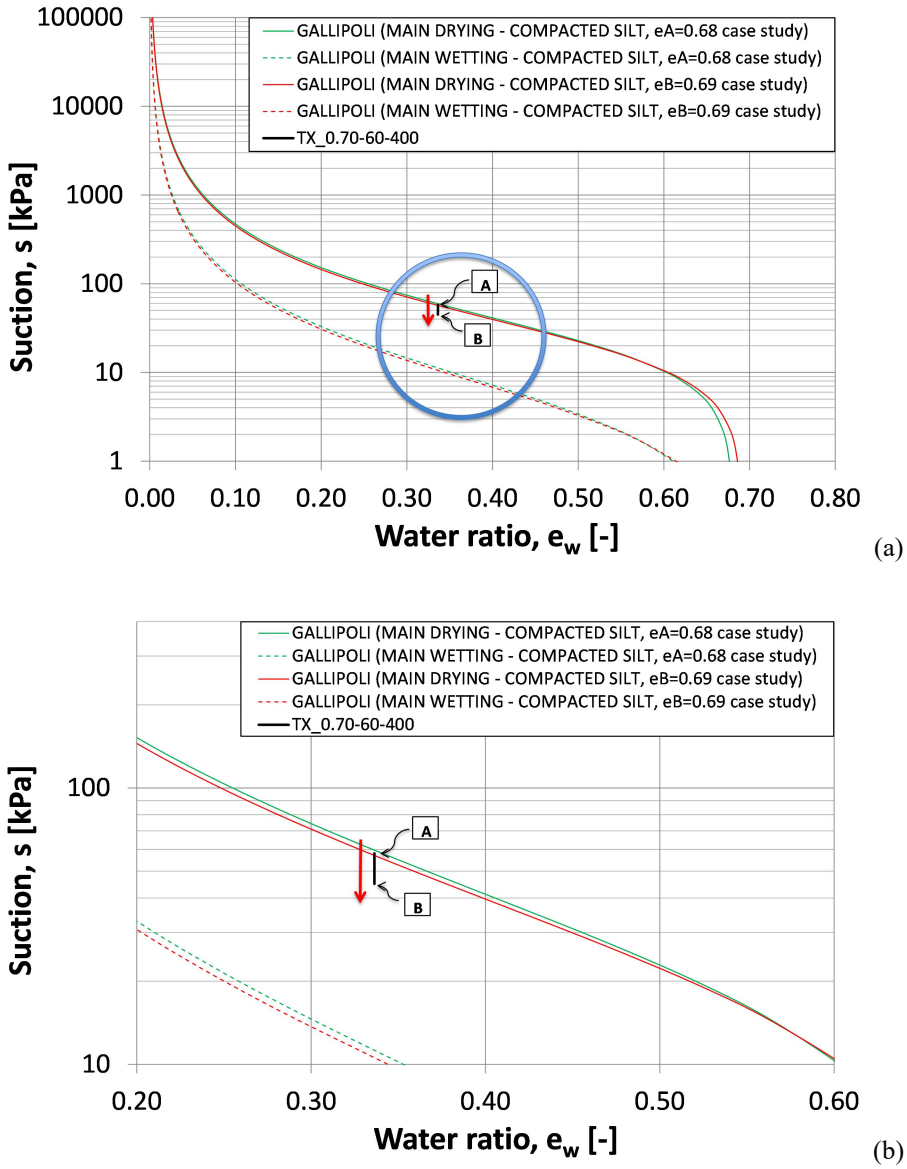

Fig. 6.52 - (a) Superposition of water retention curve and stress path obtained from suction controlled triaxial test and (b) its detail (TX_0.70-60-400).

Similar considerations can be extended by analysing the results obtained from the suction controlled triaxial test on specimen TX_0.60-60-800 (Fig. 6.53a and Fig.6.53b). Because of the wetting phase, point A lies close to the wetting branch corresponding at e = 0.57. Again, because of the small dilative behaviour due to the high applied net stress at consolidation phase, the water retention curves estimated by means of Gallipoli model, are very close each other. As pointed by the red arrow, the stress path moves upward, toward the main drying branch of the water retention curve corresponding at e = 0.58, with an increase of suction.

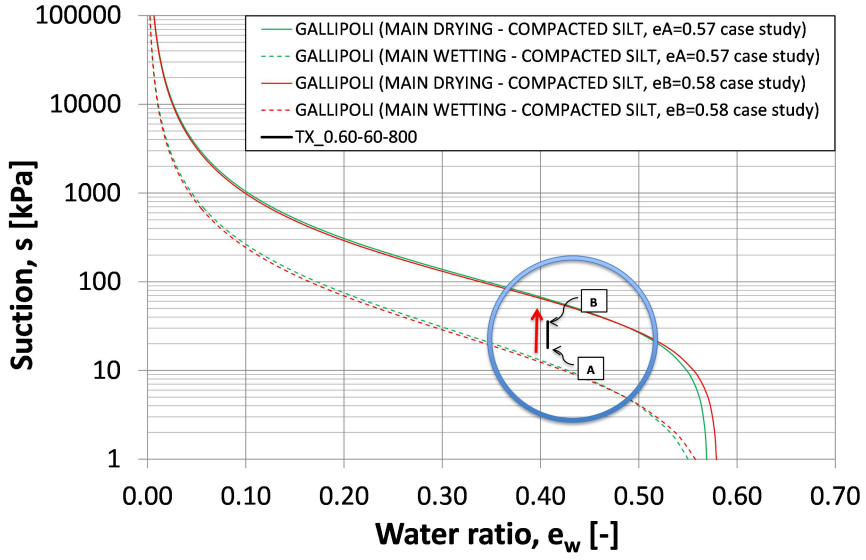

(a)

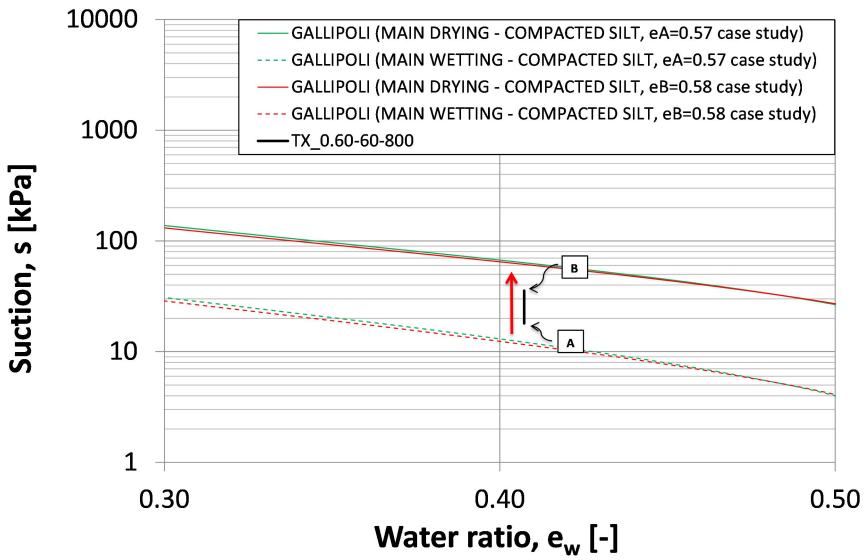

(b)

Fig. 6.53 - (a) Superposition of water retention curve and stress path obtained from suction controlled triaxial test and (b) its detail (TX_0.60-60-800).

Finally, the last sample sheared in undrained conditions, is represented by the specimen TX_0.80-90-800 (Fig.6.54a and Fig.6.54b). During the shearing phase, the specimen experienced a contractive behaviour, so the stress path should move down, toward the main wetting curve at void ratio equal to 0.63. As shown in Fig. 6.54a and Fig.6.54b, in the current case this approach does not work. Indeed, the stress path moves up at higher suction values, toward the main drying e_B = 0.63, instead moving down at lower suction values toward the main wetting e_B = 0.63. It is worth to note that the suction measured during the shearing phase of this test is not believed to be realistic. Indeed, the final suction (s_B = 106KPa) is higher than the declared air entry value of the adopted porous stone (AEV = 100kPa).

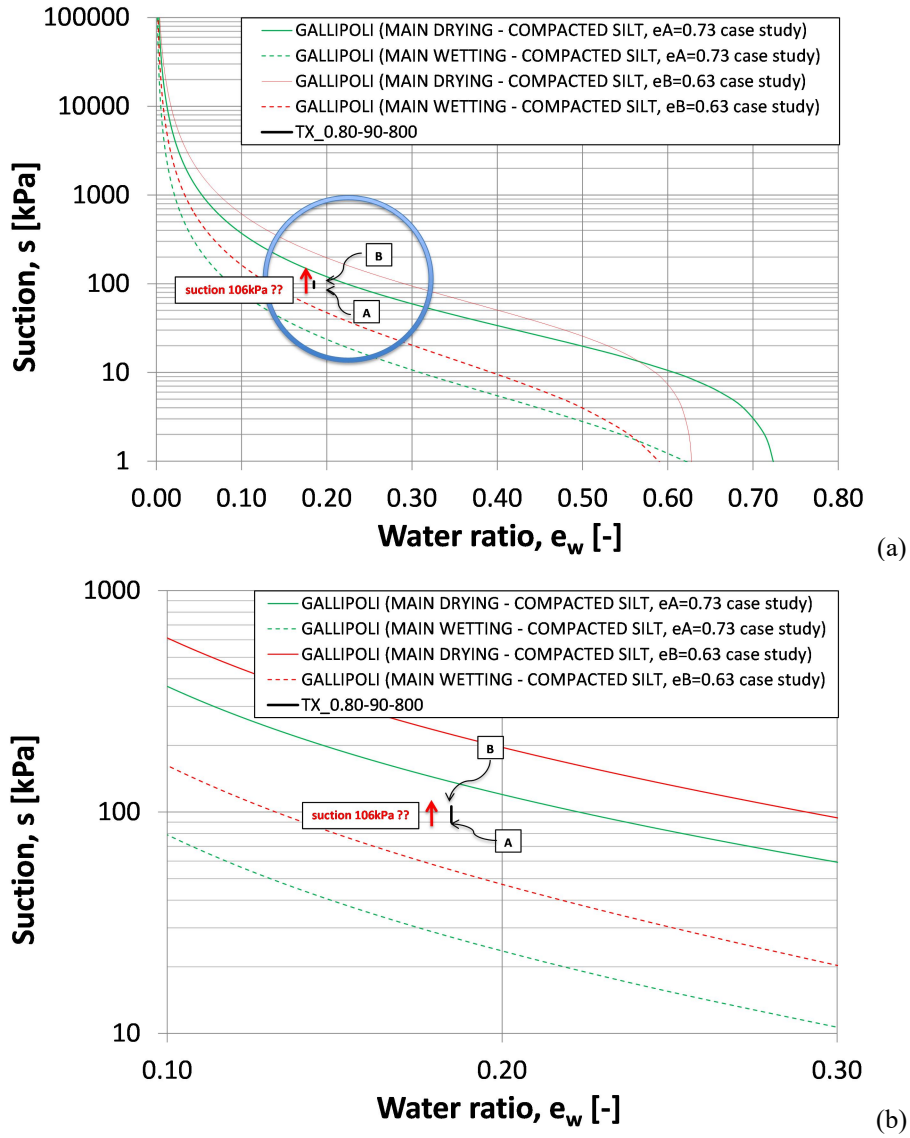

Fig. 6.54 - (a) Superposition of water retention curve and stress path obtained from suction controlled triaxial test and (b) its detail (TX_0.80-90-800).

6.5.12 Hydro-mechanical coupled behaviour in unsaturated conditions: constant suction shearing phase

The stress path resulting from the suction controlled triaxial test for specimen TX_0.60-175-200, in terms of suction *s* and degree of saturation *Sr*, is represented in Fig. 6.55a and Fig. 6.55b. Points A and B represent the beginning of the shearing phase and the end of the test, respectively. Also in this case, the water retention curves for void ratios equal to those resulting at the beginning of shearing phase and at the end of the triaxial test, are estimated by Gallipoli model. The green solid and dotted lines represent the main drying and main wetting branches, respectively, at void ratio chosen to be equal to $e = 0.59$, the same value that triaxial specimen TX_0.60-175-200 had at the beginning of shearing phase. The red

solid and dotted lines refer to the main drying and main wetting branches, respectively, at void ratio chosen to be equal to e = 0.73, the same value that triaxial specimen TX_0.6-175-200 had at the end of the test. The direction of the stress path is highlighted by the red arrow. Because of the shearing was supposed to be in drained conditions (constant suction), the stress path is represented by an horizontal line. During the shearing phase, the specimen TX_0.60-175-200 exhibited a dilative behaviour (void ratio increased from 0.59 to 0.73). Again, a dilative behaviour is associated to changes in the water retention state of the soil toward the drying water retention surface. In order to approach the main drying branch of water retention curve corresponding at e = 0.73, starting from the water retention curve at e = 0.59, the stress path moved left, in the same direction of the main drying branch of the water retention curve corresponding at void ratio 0.73.

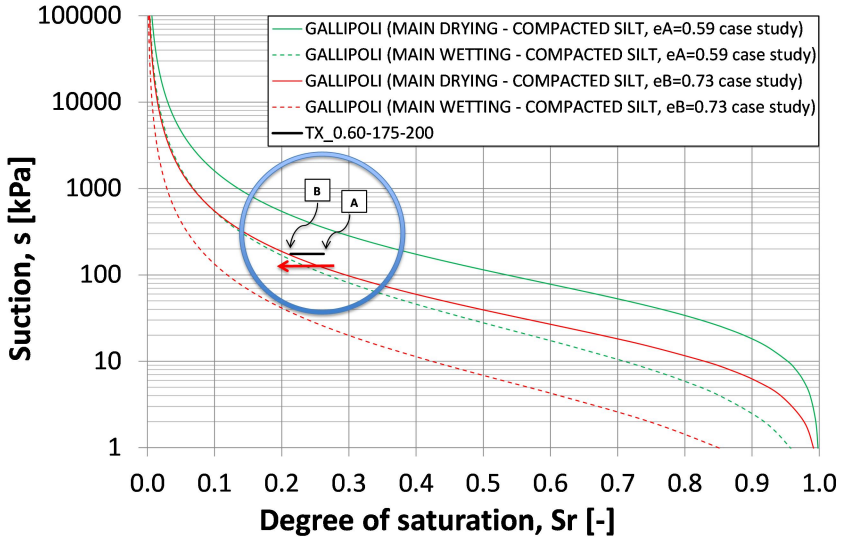

(a)

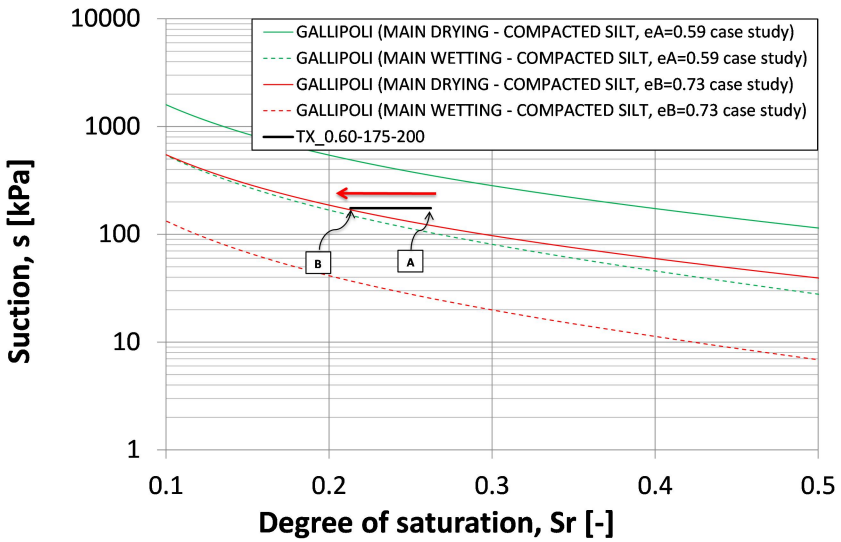

(b)

Fig. 6.55 - (a) Superposition of water retention curve and stress path obtained from suction controlled triaxial test and (b) its detail (TX_0.60-175-200).

The stress path resulting from the suction controlled triaxial test for specimen TX_0.64-60-200b, in terms of suction s and water ratio e_w, is given in Fig. 6.56a and Fig. 6.56b. Points A and B represent the beginning of the shearing phase and the end of the test, respectively. Again, the green solid and dotted lines represent the main drying and main wetting branches, respectively, at void ratio chosen to be equal to e = 0.59, the same value that triaxial specimen TX_0.64-60-200b had at the beginning of shearing phase. The red solid and dotted lines refer to the main drying and main wetting branches, respectively, at void ratio chosen to be equal to e = 0.64, the same value that triaxial specimen TX_0.64-60-200b had at the end of the test. The direction of the stress path is highlighted by the red arrow. The initial point A is very close the main drying branch of water retention curve 0.59. During the shearing phase, the specimen TX_0.64-60-200b exhibited a dilative behaviour (void ratio increased from 0.69 to 0.72). Again, a dilative behaviour is associated to changes in the water retention state of the soil toward the drying water retention surface. It is expected that suction increases due to drying. Because of the constrain represented by the drained conditions (constant suction) imposed during the shearing phase, the stress path is an horizontal line. In order to approach the main drying branch of water retention curve corresponding at e = 0.64, starting from the water retention curve at e = 0.59, the stress path moved left, in the same direction of the main drying branch of the water retention curve corresponding at void ratio 0.64.

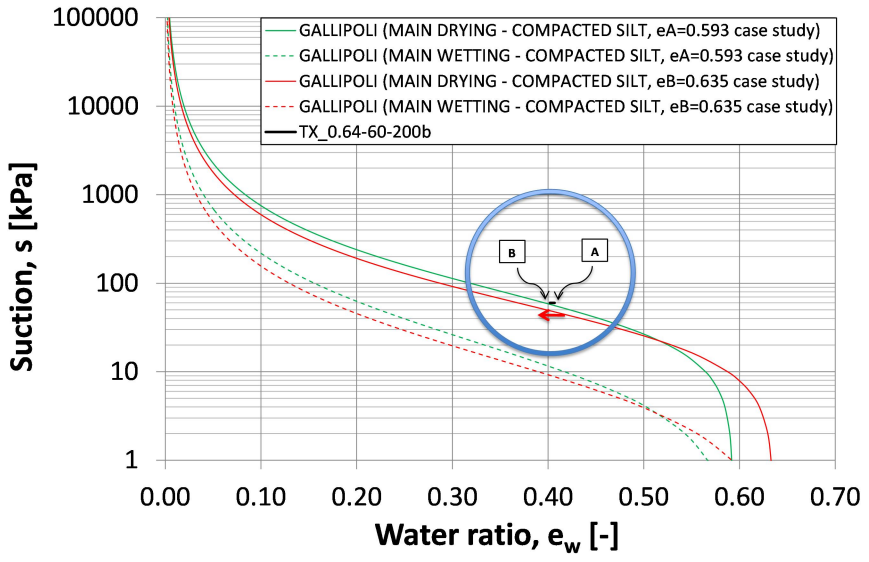

(a)

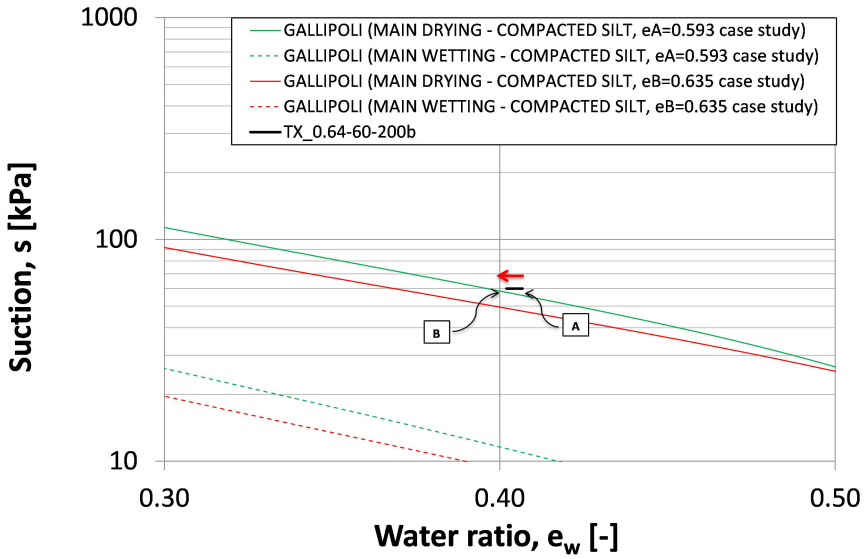

(b)

Fig. 6.56 - (a) Superposition of water retention curve and stress path obtained from suction controlled triaxial test and (b) its detail (TX_0.64-60-200b).

The stress path resulting from the suction controlled triaxial test for specimen TX_0.80-90-100, in terms of suction s and water ratio e_w, is represented in Fig. 6.57a and Fig. 6.57b. Again, the green solid and dotted lines represent the main drying and main wetting branches, respectively, at void ratio equal to e = 0.77, the same value that triaxial specimen TX90-100 had at the beginning of shearing phase. In the same way, the red solid and dotted lines refer to the main drying and main wetting branches, respectively, at void ratio chosen to be equal to e = 0.74, the same value that triaxial specimen TX_0.80-90-100 had at the end of the test. The direction of the stress path is highlighted by the red arrow. Again, because of the shearing phase was performed at constant suction (drained conditions), the stress path is represented by an horizontal line. The initial point A is little bit out from the domain represented by the water retention curve 0.77. This is supposed to be due at calibration of Gallipoli parameters n, m, ψ, Φ used for the estimation of the water retention curve. If two water retention tests were performed on silt samples having initial void ratio e_0 = 0.77 and e_0 = 0.74 and experimental data were fitted by means of two different sets of Van Genuchten parameters, the stress path probably would be completely inside the hydraulic domain.
During the shearing phase, the specimen TX_0.80-90-100 predominantly exhibited a contractive behaviour (void ratio decreased from 0.77 to 0.74). A contractive behaviour is associated to changes in the water retention state of the soil toward the wetting water retention surface. It is expected that suction decrease due to wetting, but because of the drained conditions (constant suction) during the shearing phase, the stress path is represented by an horizontal line. In order to approach the main wetting branch of water retention curve corresponding at e = 0.74 starting from the water retention curve at e = 0.77, stress path moved left, in the same direction of the main wetting branch of the water retention curve corresponding at void ratio 0.74 (green dotted line). This trend would have been evident if the specimen lost more water, leading a bigger decrease of degree of saturation, so resulting closer to the main wetting curve corresponding at void ratio 0.74.

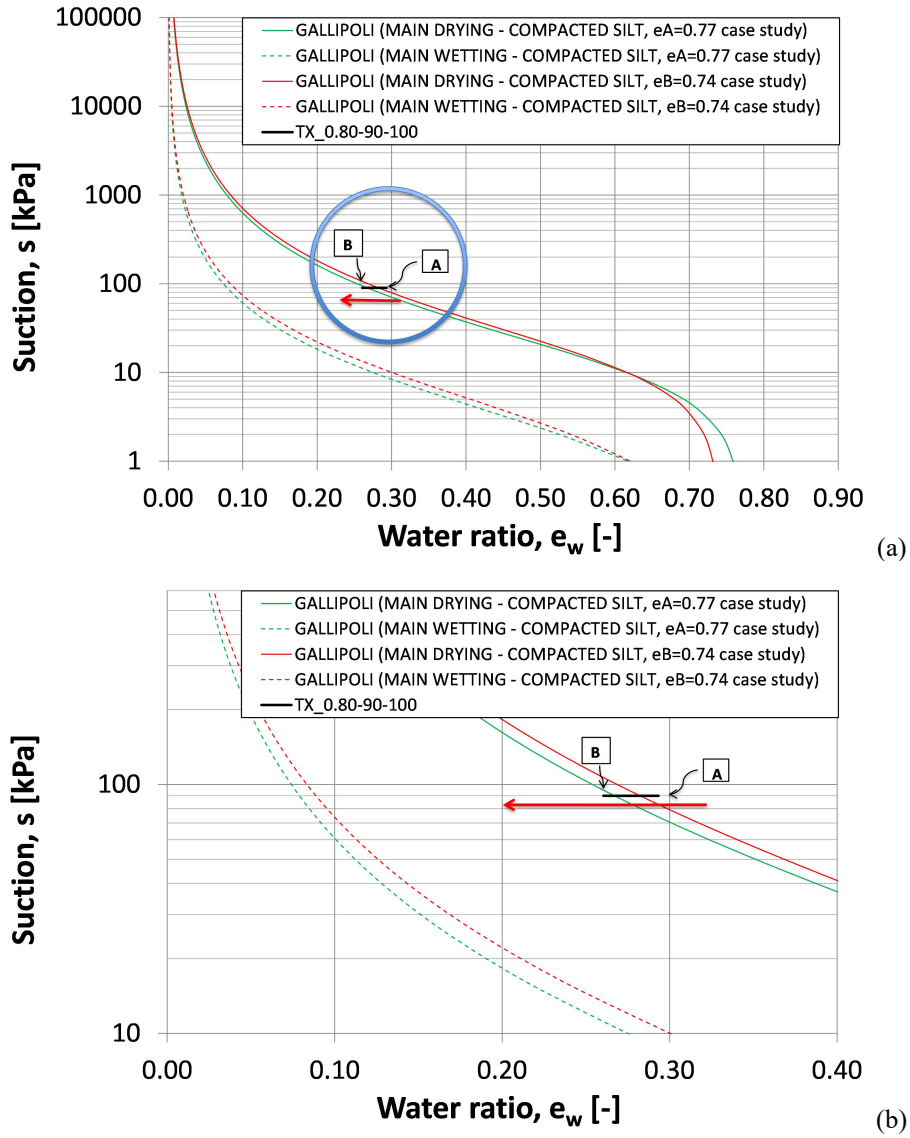

Fig. 6.57 - (a) Superposition of water retention curve and stress path obtained from suction controlled triaxial test and (b) its detail (TX_0.80-90-100).

By observing of all the stress path occurred during the shearing phase (from Fig. 6.50 to Fig. 6.57), the water retention curves seems to play as a domain, affecting the mechanical behaviour. In most of cases, the hydro-mechanical behaviour in terms of s-e_w (or s-Sr) obtained from the suction controlled triaxial test lies inside the water retention surfaces corresponding at the different void ratios at the beginning and at the end of the shearing phase. For this reason, all the water retention curve have been estimated by means of the Gallipoli model, and plotted in a two-dimensions graphs (Fig. 6.50-6.57) in order to have a simpler visualization. These two dimensional graphs are cross sections at constant void ratio of the WRC surface into the three dimensions space (s-Sr-e) or (s-e-e_w). All the triaxial stress paths, plotted in the three domain defined by the water retention surface in the (s-e-e_w) space is plotted in Fig. 6.58.

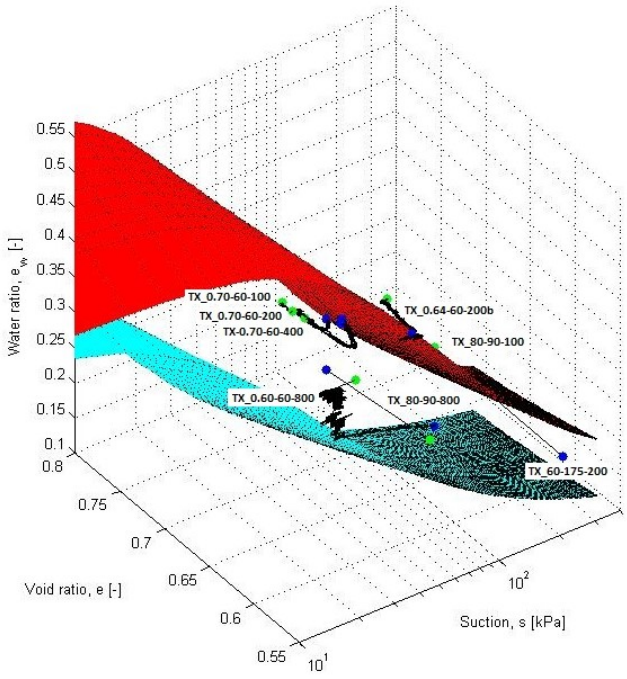

Fig. 6.58 - 3D representation of the *WRC* obtained from the water retention tests, and the stress paths obtained from the suction controlled triaxial tests in the (e, e_w, s) space.

6.5.13 The critical state in unsaturated conditions in (e_w-p'_B-Sr) plane and in (q-p'_B) plane

The final states of the triaxial tests are given in Fig. 6.59. They are represented by means of coloured symbols (squares, triangles, crosses and circles) on the (e_w-p'_B) plane.

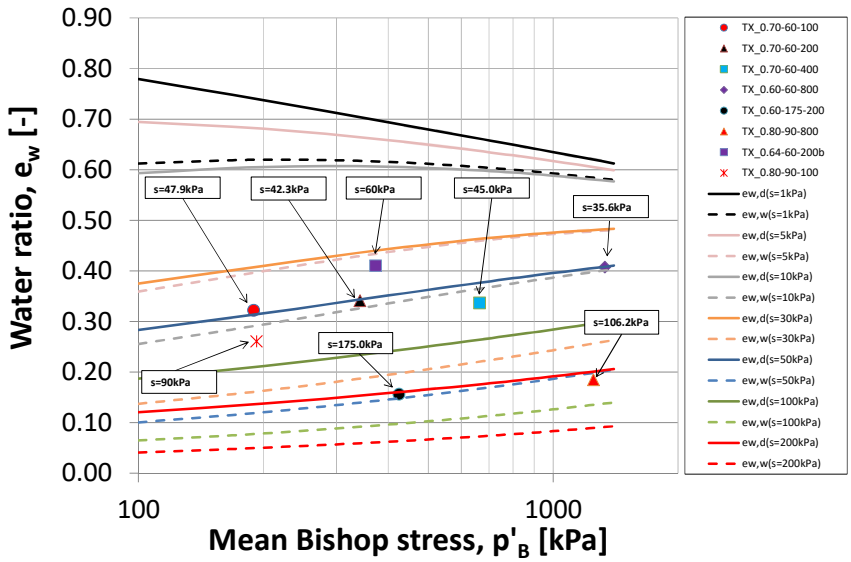

Fig. 6.59 - Points at Critical state in (e_w-p'_B) plane.

The coloured iso-suction curves have been obtained from the water retention curves on the (s-e_w) plane by implementing the Gallipoli model at different void ratios evaluated in the compressive plane at critical state, for different values of mean Bishop stresses. They represent the suction levels for drying (solid) and wetting (dotted) branches at different Bishop effective stress (or void ratio) levels. Each triaxial test is provided with the values of suction s at critical state or at the end of the test if the critical state was approached or not reached. Despite a certain scattering, it is possible to observe that points related at tests TX_0.70-60-100, TX_0.70-60-200, TX_0.70-60-400, TX_0.60-60-800, TX_0.80-90-800 and TX_0.60-175-200 are quite close to the curve corresponding at the suction value reached at the end of the test.

The final state of the triaxial tests is given in Fig. 6.60: the deviator stress q at the end of the shearing phase is reported with the mean Bishop stress p'_B. Each test, identified by a red square, is provided with the values of void ratio e, water ratio e_w, suction s, degree of saturation Sr and Bishop effective stress p'_B at critical state or at the end of the test when the critical state was approached or not reached. The experimental data were fitted by the critical state line represented by the solid black line.

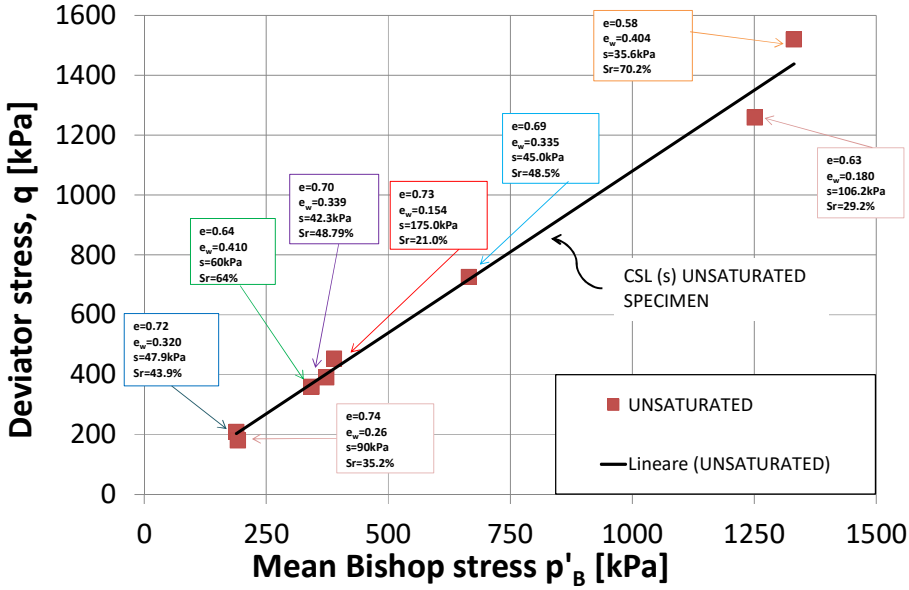

Fig. 6.60 - Critical state line *CSL(s)* for unsaturated samples tested in the current research.

A comparison between the previous two set of results, respectively unsaturated tests (current research) and saturated tests (Carrera, 2008), is given in Fig. 6.61 in terms of deviator stress q - p'_B (unsaturated tests identified with the red squares) and deviator stress q - p' (saturated tests represented with blue circles). It is possible to note that the two set of data lie in quite a narrow area around a unique critical state line identified by the solid double line.

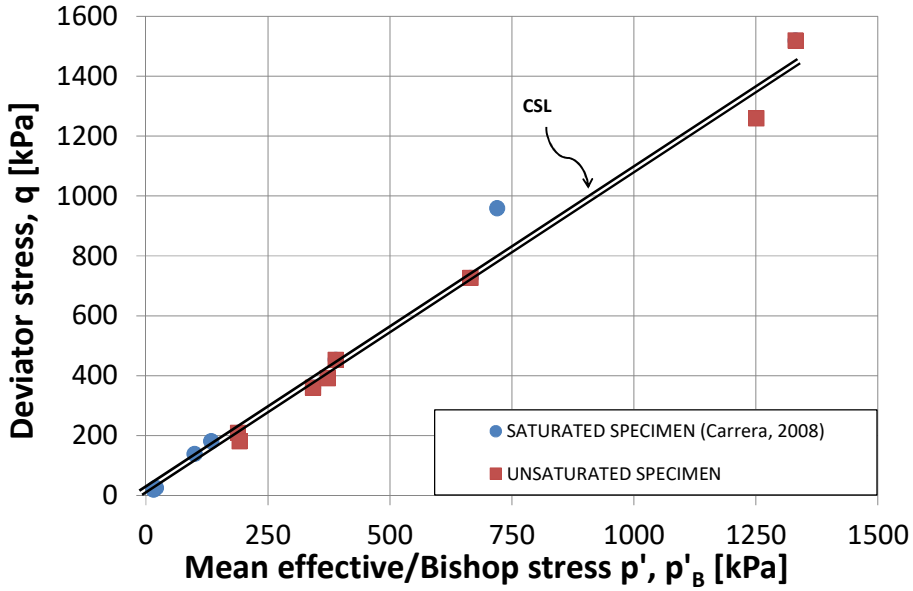

Fig. 6.61 - Critical state line for saturated silt samples and unsaturated silt samples.

Such experimental results suggest that, for the interval of stresses investigated in the current research, the "bonding effect" due to water menisci and to the matric suction (Gallipoli *et al*., 2003) seems to have not a relevant effect on the shear strength at critical state conditions. Similar results were obtained by Nicotera *et al*. (2015), that performed an hydro-mechanical characterization campaign on normal-consolidated and over-consolidated pyroclastic silty-sand by means of triaxial tests in saturated conditions (drained shearing phase) phase and suction controlled triaxial tests at different mean net stresses, suction levels and void ratios. In both cases, for saturated and unsaturated silty-sand samples, the Authors observed that the data in terms of deviator stress and effective stress were quite aligned, so they identified a unique *CSL*. Indeed, a unique stress ratio *M* and the same friction angle at was estimated by the Author. Even if the suction seemed not to influence the hydro-mechanical behaviour, the experimental data obtained by Nicotera *et al*. (2015) showed that the conditions of saturation affect the stress-strain curve: saturated normal-consolidated specimens showed lower values of dilatancy than the unsaturated specimens. Similar results obtained from suction controlled triaxial have been reported by other authors, Tarantino and Tombolato, 2005; Thu *et al.* (2006) on compacted silt, Tarantino (2007) on compacted non-active clay, Kayadelen *et al*. (2007) on residual clayey soils and Chiu *et al*. (2010) on aged compacted clay, and Capotosto and Russo (2011) on compacted silt.

6.5.14 The critical state in unsaturated conditions: (e-p'$_B$) plane

The final conditions of the suction controlled triaxial tests obtained in the current research are given in the compressive plan in terms of void ratio *e* and mean Bishop stress p'_B (Fig. 6.62a). In the same figure, the final conditions of the triaxial tests on the Stava silt specimens performed in saturated conditions by Carrera (2008), are reported in terms of void ratio *e* and mean effective stress *p'*. The empty red points represent the final state of saturated samples. They are connected by a dotted red line that represents, in that interval of mean effective stress investigated, the critical state line of the Stava silt specimen in saturated conditions. The solid coloured points represent the final state of unsaturated samples. They are connected by a dotted black line that represents, in that interval of mean Bishop stress

investigated, the critical state line of the Stava silt specimen in unsaturated conditions found in this research. For each unsaturated test, the value of void ratio e, water ratio e_w, suction s, degree of saturation Sr and mean Bishop stress p'_B are given. The void ratio found in this experimental study generally lie above those found by Carrera (2008). The critical state lines is more flat for low values of stress and is more steeper for high stress values.

The final conditions of the suction controlled triaxial tests obtained in the current research, together with the stress paths followed during the entire test, are given in Fig. 6.62b. It is possible to observe that all unsaturated samples whose state in terms of initial void ratio e_0 lies below the critical state *CSL(s)*, approached the critical state line by, predominantly, experiencing an increase of volume and so a dilative behaviour under shearing. This is the case of sample TX_0.70-60-100, TX_0.70-60-200, TX_0.70-60-400, TX_0.60-175-200, and TX_0.60-60-800. On the other hand, all unsaturated samples whose state in terms of initial void ratio e_0 lies above the critical state, achieved the *CSL(s)* by means of a decrease of volume, and so a contractive behaviour. This is the case of sample TX_0.80-90-800 and sample TX_0.80-90-100.

It is hence possible to state the critical state in unsaturated condition was reached by means of two ways, depending on the initial state (e.g. the initial density) of the sample with respect to the critical state. Specimens that are denser than the critical state, approached the *CSL* by changing their water retention state toward the drying water retention surface (TX_0.70-60-100, TX_0.70-60-200, TX_0.70-60-400, TX_0.60-175-200, and sample TX_0.60-60-800). On the other hand, samples that are looser than the critical state, shown a contract in their volume and approached the *CSL* by changing their water retention state toward the wetting water retention surface (TX_0.80-90-800, TX_0.80-90-100). No tests have been successfully performed on very loose sample, e.g. at initial void ratio higher than 0.80, due to experimental difficulties. Indeed, at these conditions of very low density, all the unsaturated triaxial samples collapsed because of the weight of the top cap and load cell (about 3kg) during the assemblage operations of the cell or during the suction equalization phase.

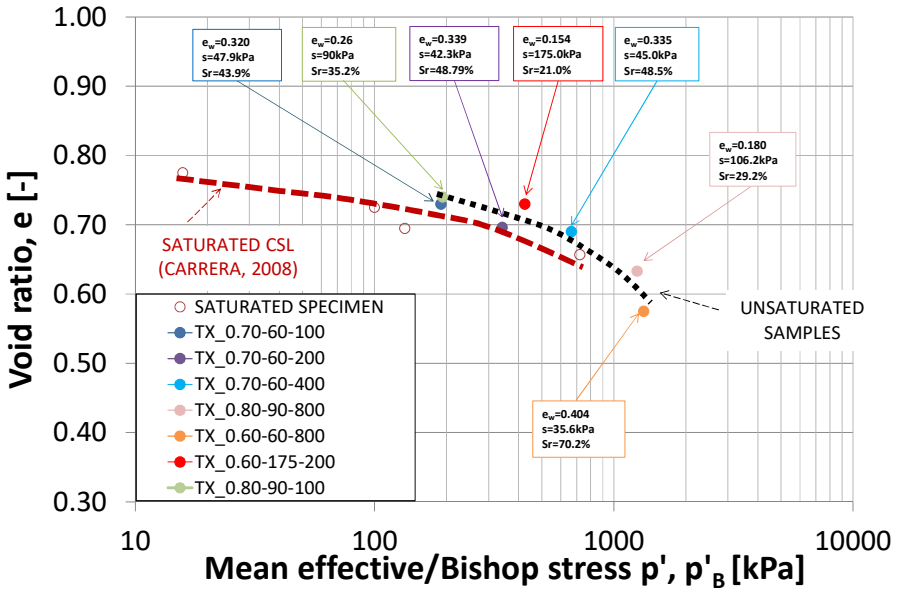

(a)

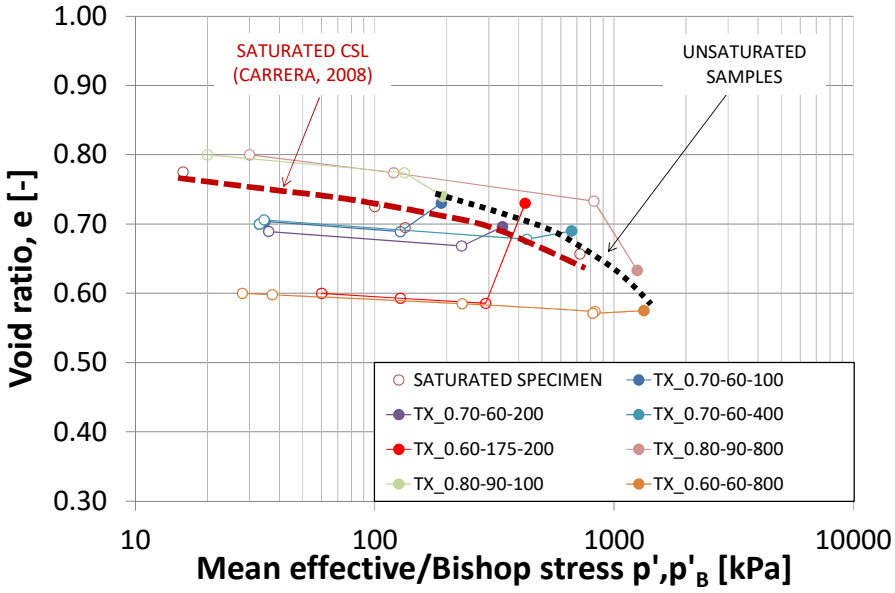

(b)

Fig. 6.62 - (a) Critical state line of saturated silt specimens (Carrera, 2008) and unsaturated silt specimens (current study) at the end of the test. (b) Evolution of void ratio and Bishop effective stress at the different phases of the triaxial tests.

The void ratio of unsaturated samples at critical state was then corrected by means of the model proposed by Gallipoli *et al.* (2003b), summarized in section 6.1.2. It is worth to note that the critical state void ratios in unsaturated conditions were predicted by knowledge of the critical state void ratio in saturated conditions obtained by Carrera (2008). Because the latter ones are comprised in a stress interval of a mean effective stress ranging between 15kPa and 720kPa, the critical state void ratio was estimated just for unsaturated specimen consolidated at a Bishop effective stress less than 720kPa, especially TX_0.70-60-100, TX_0.70-60-200, TX_0.70-60-400, TX_0.60-175-200 and TX_0.80-90-100. The results in terms of mean Bishop stress and theorical void ratio predicted by Gallipoli model are given in Fig. 6.63a.

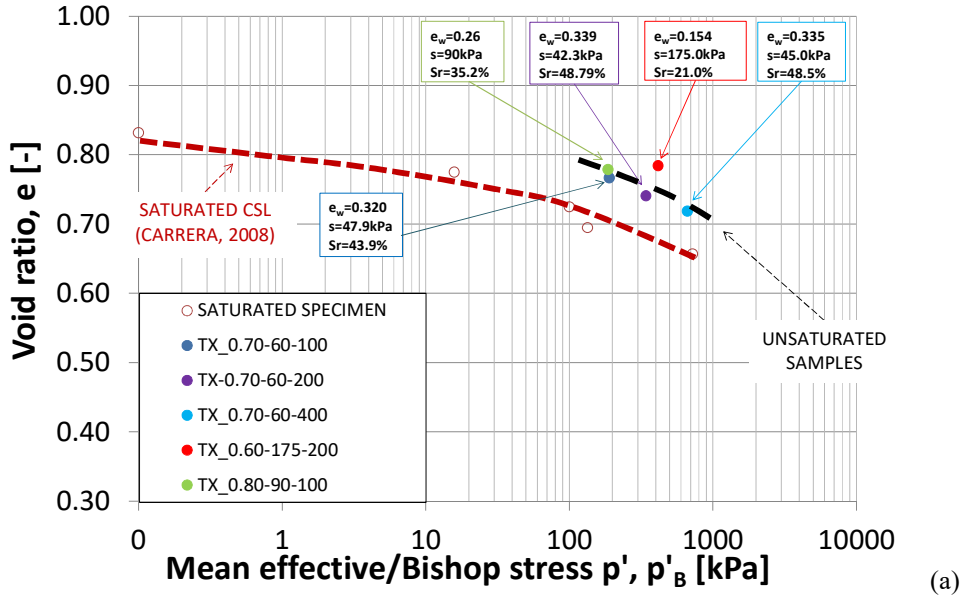

(a)

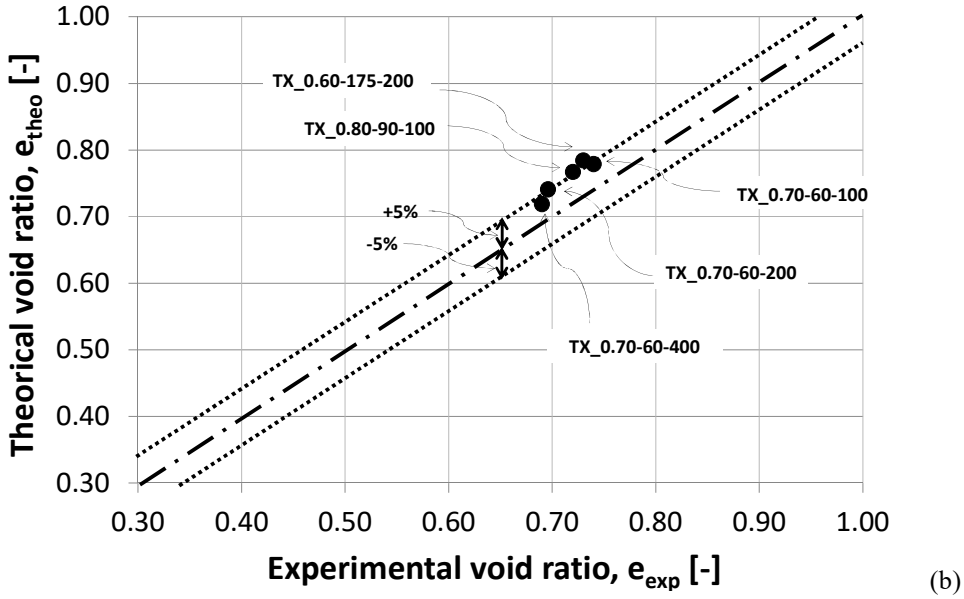

(b)

Fig. 6.63 - (a) Final conditions of unsaturated specimen in terms of Bishop effective stress and theorical void ratio predicted by Gallipoli model. (b) Experimental void ratio and theorical void ratio predicted by Gallipoli model.

Again, in the stress range investigated, all the predicted critical state void ratios in unsaturated conditions (coloured solid points, Fig. 6.63a) are close to the experimental critical state void ratio in saturated conditions (red empty points, Fig. 6.63a), resulting in two very close critical state lines. All the theorical void ratios appear to be quite well aligned, so a unique *CSL* can be obtained (dotted black line). This is confirmed by the good agreement between the theorical critical state void ratio and the experimental critical state void ratio in unsaturated conditions, plotted in Fig. 6.63b.

6.6 SUMMARY AND FINAL CONSIDERATIONS

A detailed understanding of the hydro-mechanical behaviour of tailings in unsaturated conditions is fundamental to approach the stability problems of tailing dams in terms of shear strength. For these purposes, the hydro-mechanical response of unsaturated silt tailings was studied in terms of suction controlled triaxial tests and oedometer tests on unsaturated silt specimens.

A campaign of oedometer tests was performed in order to investigate the dependency of preconsolidation stress σ_p and stiffness on suction in unsaturated conditions at different suction levels.

An experimental campaign of suction-controlled triaxial test was aimed to study the hydro-mechanical response of the silt tailing. After consolidation, a shearing phase was performed for all tests at constant water content or at constant suction, in order to reach the Critical State and define a Critical State Line also for unsaturated Stava silt samples. A critical state condition was reached for almost the all samples. The critical state was approached both from drying side and from wetting side. A possible interpretation of such behaviour by means of the water retention curve has been proposed. The Critical State Line in unsaturated conditions was compared with those obtained for the same material tested by Carrera (2008) in saturated conditions. If plotted on (q-p'_B) plane, the two set of experimental data, in saturated and unsaturated conditions, lie in a narrow area around a unique critical state line. Also in the compressive plane, the *CSL* for unsaturated samples reveals to be quite close to the *CSL* for saturated samples, increasing its slope at high stress values. Finally, the experimental void ratios at critical state were successfully compared with those predicted by the model proposed by Gallipoli.

REFERENCES

1. Alonso E., Gens A. and Josa A. 1990. A constitutive model for partially saturated soils . Geotechnique **40** (3), 405–430.

2. Azizi A. 2016. Effects of hydraulic repeated loads on the hydro-mechanical response of an unsaturated silty soil . Ph.D. thesis, Politecnico di Torino.

3. Carrera A. 2008. Mechanical behaviour of Stava tailings. Ph.D. thesis, Politecnico di Torino.

4. Capotosto A. and Russo G. 2011. Yielding and critical state behaviour of a lime stabilized compacted alluvial soil. Proc. 5th International Symposium on Deformation Characteristics of Geomaterials, Seoul, 1–3 September 2011, pp. 738–745.

5. Chiu A.C.F.; Zhao X. and Yuan J.P. 2010. State Boundary Surfaces for an Aged Compacted Clay, J. Geotech. Geoenviron. Eng., **136**(9): pp. 1251-1262.

6. Estabragh A. R. and Javadi A.A. 2008. Critical state for overconsolidated unsaturated silty soil. Can. Geotech. J., **45**(3), 408–420.

7. Estabragh A.R. and A. A. Javadi A.A. 2014. Roscoe and Hvorslev Surfaces for Unsaturated Silty Soil, International Journal of Geomechanics, pp. 230–238.

8. Fisher R.A. 1926. On the capillary forces in an ideal soil: correction of formulae given by W. B. Haines. J. Agric. Sc. Vol. **16**(3), pp. 492–505.

9. Gallipoli D., Wheeler S.J., Karstunen M. 2003. Modelling the variation of degree of saturation in a deformable unsaturated soil. Géotechnique, **53**, 1: pp. 105–112.

10. Houlsby G. T., Wroth C. P. and Wood D. M. 1982. Predictions of the results of laboratory test on a clay using a critical state model. Proc., Int. Workshop on Constitutive Behaviour of Soil, Balkema, Rotterdam, Netherlands, 99–121.

11. Jommi C. 2000. Remarks on the constitutive modelling of unsaturated soils. Experimental evidence and theoretical approaches in unsaturated soils, Proc. Of an International Workshop, Balkema, Rotterdam, pp. 139–153.

12. Jotisankasa A., Coop M. and Ridley A. 2009. The mechanical behaviour of an unsaturated compacted silty clay. Geotechnique **59** (5), 415–428.

13. Kayadelen C., Sivrikaya O., Taşkıran T. and Güneyli H. 2007. Critical-state parameters of an unsaturated residual clayey soil from Turkey. Engineering Geology, **94**: pp. 1-9.

14. Khalili N., Geiser F. and Blight G. E. 2004. Effective stress in unsaturated soils: Review with new evidence. Int. J. Geomech., 10.1061/ (ASCE)1532-3641(2004)4:2(115), 115–126.

15. Loret B. and Khalili N. 2002. An effective stress elasto-plastic model for unsaturated porous media. Mech. Mater., **34**(2), 97–116.

16. Nicotera M.V., Papa R., and Urciuoli G. 2015. The hydro-mechanical behaviour of unsaturated pyroclastic soils: An experimental investigation. Engineering Geology **195**: pp. 70–84.

17. Maâtouk A., Leroueil S. and La Rochelle P. 1995. Yielding and critical state of a collapsible unsaturated silty soil. Geotechnique **45** (3), 465–477.

18. Nocera E. 2017. Studio sperimentale del comportamento idromeccanico in condizioni non sature del limo di Stava. MSc. thesis, Politecnico di Torino.

19. Romero E. 1999. Characterisation and thermo-hydromechanial behavior of unsaturated Boom clay: an experimental study. Ph.D. thesis, UPC.

20. Romero E. and Vaunat J.. 2000. Retention curves in deformable clays. Experimental evidence and theoretical approaches in unsaturated soils, A. A. Balkema, Rotterdam, pp. 91–106.

21. Tarantino A., Tombolato S. 2005. Coupling of hydraulic and mechanical behaviour in unsaturated compacted clay. Géotechnique, **55**, 4: pp. 307–317.

22. Tarantino A. 2007. A possible critical state framework for unsaturated compacted soils. Technical Note, Géotechnique, **57**, 4: pp. 385-389.

23. Tarantino A. and Mountassir G. 2013. Making unsaturated soil mechanics accessible for engineers: Preliminary hydraulic–mechanical characterisation & stability assessment. Engineering Geology, 165 pp. 89-104.

24. Toll D.G. 1990. A framework for unsaturated soil behaviour. Géotechnique, **40**, 1: pp. 31-44.

25. Toll D.G., Ong B.H. 2003. Critical-state parameters for an unsaturated residual sandy clay. Géotechnique, **53**, 1: pp. 93-103.

26. Vanapalli S.K., Fredlund D.G., Pufahl D.E. and Clifton A.W. 1996. Model for the prediction of shear strength with respect to soil suction. Canadian Geotechnical Journal, Vol. 33, pp. 379–392.

27. Wang Q., Pufahl D.E. and Fredlund, D.G. 2002. A study of critical state on an unsaturated silty soil. Canadian Geotechnical Journal 39, 213-218.

28. Wheeler S.J. and Sivakumar V. 1995. An elasto-plastic critical state framework for unsaturated soil. Géotechnique, **45**, 1: pp. 35-53.

29. Wheeler S.J. and Sivakumar V. 2000. Influence of compaction procedure on the mechanical behaviour of an unsaturated compacted clay. Part 2: Shearing and constitutive modelling. Géotechnique, **50**, 4: pp. 369–376.

7 Liquefaction response of Stava tailings in unsaturated conditions

Because of the importance of the static liquefaction phenomenon with reference to tailing storage facilities in terms of failure, this section is aimed at provide an experimental investigation of the static liquefaction resistance of Stava silty tailings. After giving an initial review of the state-of-art concerning the main factors influencing the liquefaction resistance, innovative aspects and aims of the current investigation are presented. The experimental procedures adopted in the current work are given and results in terms of preparation technique, void ratio and degree of saturation on static liquefaction resistance of Stava tailings are then shown, together with a comparison between experimental data and theoretical relationships between *B*-value and degree of saturation.

7.1 GENERAL FEATURES OF LIQUEFACTION

Liquefaction of soils is a phenomenon that can experience when dynamic, shock (dynamic liquefaction) or monotonic (static liquefaction) loads are applied under undrained conditions and the mass of soil tends to flow as a fluid.
Static liquefaction consists in a temporary decrease of the shear strength of loose, saturated soil until new stability conditions are reached. When the soil is sheared, the applied load is transferred to the water filling the soil pores. Because of the undrained conditions, the loose soil cannot contract, resulting in increase of pore pressure and, according to Terzaghi principle, a decrease of mean effective stress will occur. In certain conditions, the shear strength of the soil will suddenly decrease close to zero, allowing the soil behave as a fluid with large deformations (Fig. 7.1).

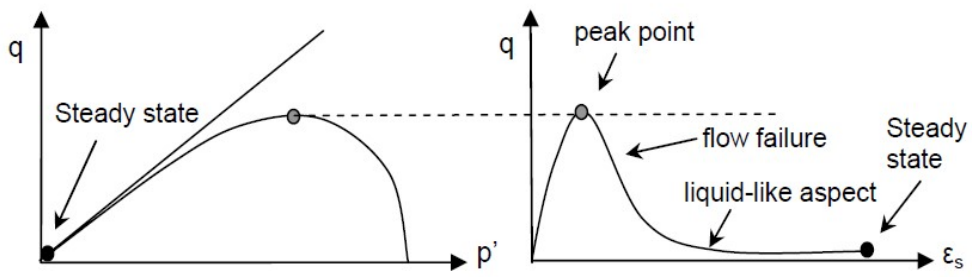

Fig. 7.1 - Occurrence of liquefaction phenomena in strain controlled test (Carrera, 2008).

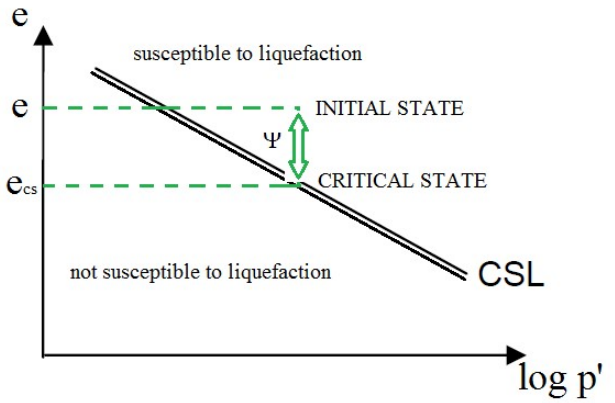

Fig. 7.2 - State parameter and state criteria for liquefaction susceptibility.

Been and Jefferies (1985) characterized the tendency of a granular soil to liquefy or not, depending on the state parameter ψ (Fig. 7.2). The Authors defined the state parameters as the difference between the initial void ratio e and the void ratio at critical state e_{cs}. A positive state parameter is related to a loose specimen susceptible to liquefaction (contractive behaviour) and vice-versa.

7.2 FACTORS INFLUENCING THE LIQUEFACTION RESISTANCE: LITERATURE REVIEW

The effects of factors such as degree of saturation, relative initial density/void ratio, preparation technique, confining pressure, initial shear stress and fine content on liquefaction response of saturated sandy soils are exposed from the experimental point of view. These literature studies on saturated soils will provide a good reference for interpreting the results obtained by means of undrained triaxial tests on Stava silty tailings.

7.2.1 Effects of degree of saturation

The first studies regarding cyclic liquefaction strength in unsaturated conditions were performed by Martin *et al*. (1978) and Mulilis *et al*. (1978) on Monterrey sandy samples. These Authors shown that, for the range of *B*-values investigated (between 0.91 and 0.97), the Skempton's coefficient has not a big influence on the liquefaction strength of the tested soil**.** In recent years, the dynamic liquefaction resistance in unsaturated conditions have been studied by means of cyclic triaxial tests (Kokusho 2000; Yang and Sato 2001; Pietruszczak *et al*. 2003; Atigh and Byrne 2004; Mathiroban and Grozic 2004; Arab *et al.* 2015). According to Martin *et al.* (1978), Yoshimi *et al.* (1989), Ishihara *et al.* (2001, 2004), Yang (2002), Yang *et al.* (2004), Bouferra (2000), Bouferra *et al*. (2007) the liquefaction strength of sandy soils tends to increase if the degree of saturation decreases. Results obtained from cyclic torsional shear tests performed by Yoshimi *et al.* (1989) on reconstituted Toyoura sandy samples (Dr = 60%), showed that the degree of saturation has a fundamental influence on the cyclic liquefaction strength of the soil. Figure 7.3a shows that the liquefaction strength of Toyoura sand decreases with the degree of saturation. The liquefaction resistance, defined as the fraction of shear stress ratio at given degree of saturation to the shear stress ratio at full saturation, at degree of saturation equal to 90% is about two times that at fully saturated conditions and it increases at three times when the soil is at 70% of saturation. The highest gain in terms of liquefaction resistance is obtained reducing the degree of saturation from 100% to 70%. Further reductions of degree of saturation will not allow big gains in terms of

liquefaction resistance, just from 3.0 to 3.7 times the resistance at fully saturated conditions. Same results are given in terms of liquefaction resistance and *B*-value, as shown in Fig. 7.3b where the liquefaction resistance decreases with the increasing of *B* parameter from 0 to 1. When *B*-value is close to zero, the liquefaction strength continues to increase from 2.5 to 3.7 times the liquefaction resistance at fully saturated conditions, meaning a *B*-value equal to zero corresponds at a degree of saturation ranging between 0% and 85%. On the other hand, the liquefaction resistance shows little variations, from 1.5 to 1 time the liquefaction resistance at fully saturated conditions, for *B*-values ranging between 0.2 and 1.

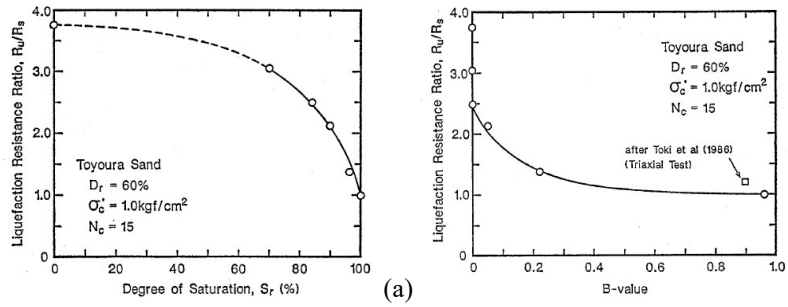

Fig. 7.3 - (a) Relationship between liquefaction resistance and degree of saturation. (b) Relationship between liquefaction resistance and B parameter (Yoshimi *et al.,* 1989).

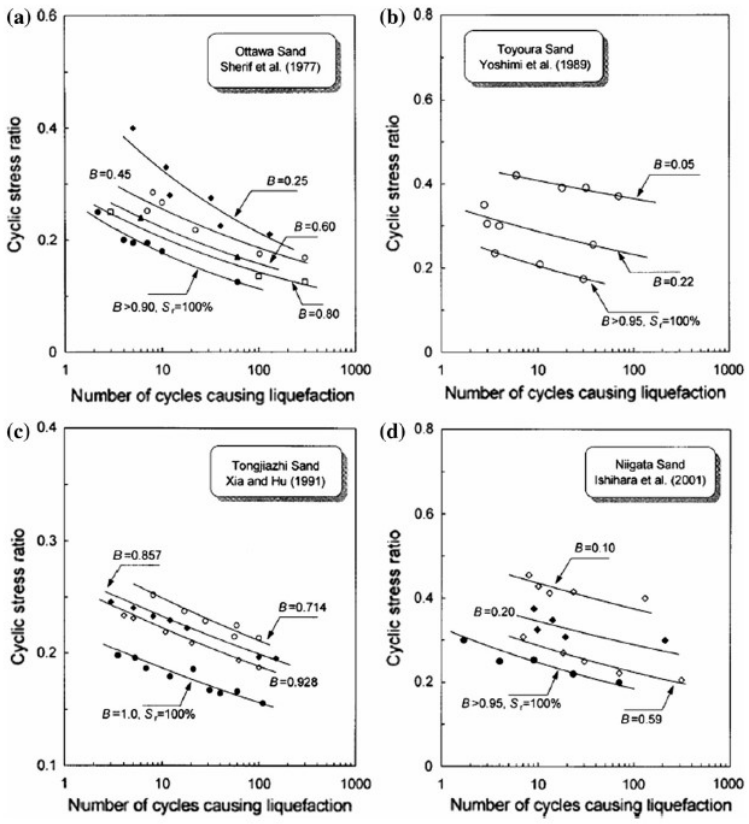

Fig. 7.4 - (a) *B*-value effects on liquefaction resistance on: (a) Ottawa sand, (b) Toyoura sand, (c) Tongjiazhi sand, (d) Nigata sand (Yang *et al*., 2004).

Figure 7.4 shows some literature results (Sherif *et al*., 1977; Yoshimi *et al.,* 1989; Xia and Hu, 1991; Ishihara *et al.,* 2001) concerning the variation of dynamic liquefaction resistance

in terms of cyclic stress ratio (CSR required to cause liquefaction at 20 cycles) with the number of cycles causing the liquefaction), for different sandy soils tested at different *B*-values. For all the tested sands, the liquefaction strength decreases as the *B* Skempton parameter increases.

The Authors also obtained a relationship (Fig. 7.5) between the *B* parameter and the normalized cyclic strength for different types of soils. The normalized cyclic resistance is expressed as the ratio between the liquefaction strength for low values of *B* parameter (cyclic stress ratio CSR_{PS} required to have liquefaction at 20 cycles under unsaturated conditions) and the liquefaction resistance in fully saturated conditions (cyclic stress ratio CSR_{FS} required to obtain liquefaction at 20 cycles under fully saturated conditions). A linear correlation can be observed and the normalized liquefaction strength decreases as the *B*-value increases.

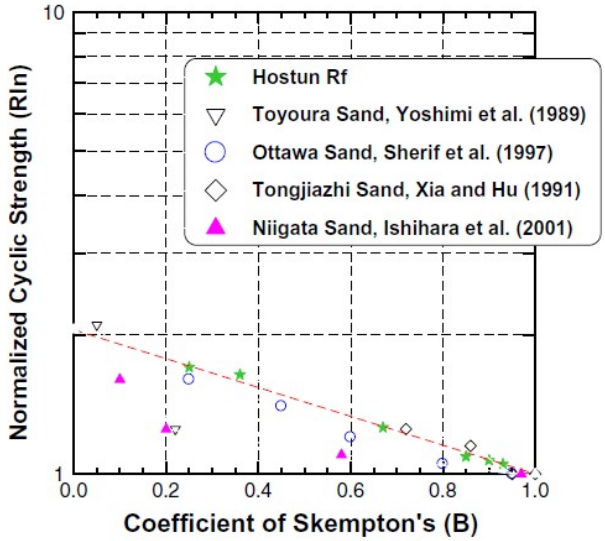

Fig. 7.5 - Relationship between normalized liquefaction resistance and *B*-value (Yang *et al.*, 2004).

A relationship between the normalized dynamic liquefaction resistance (expressed as the ratio between the cyclic resistance ratio in unsaturated conditions and the cyclic resistance ratio in saturated conditions for 20 loading cycles) and the P-wave velocity V_p (connected to the degree of saturation) for different sandy soils proposed by Hossain *et al.* (2013) is given in Fig. 7.6. It is noteworthy that liquefaction resistance increases significantly with the decrease of the P-wave velocity (degree of saturation or *B*-value). It is clear that the liquefaction resistance at degree of saturation equal to 90% (V_p =400m/s) is more than two times that at full saturated conditions (Sr = 100%, V_p = 1900m/s).

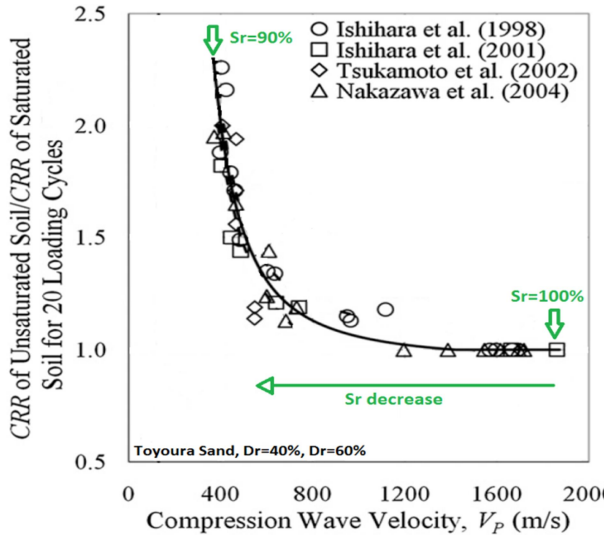

Fig. 7.6 - Relationship between normalized liquefaction resistance and P-wave velocity (modified from Hossain *et al*., 2013).

Aimed at study the effects of gas on the undrained response of soils with pore water containing dissolved gas in marine sediments (gassy soils), the liquefaction resistance of unsaturated granular soil was experimentally investigated by Grozic *et al.* (1999) by means of monotonic compression triaxial tests on saturated and gassy Ottawa sand. The Authors observed that under undrained shearing, gassy Ottawa sand shown a stress-hardening behaviour for degree of saturation lower than 90%, while a strain-softening response is obtained for degree of saturation is higher than 90%. Similar results based on numerical modelling on the same material in the same stress conditions were obtained by Grozic *et al.* (2005).

Della (2010) performed drained and undrained monotonic compression triaxial tests on medium-dense Chlef sandy specimen by varying the *B*-value from 0.13 to 0.90 In order to investigate the influence of saturation on the mechanical response of granular soils. The experimental results shown that a decrease in the Skempton's parameter leads to an increase of the dilative tendency, a decrease in the pore water pressure and reduces the contractive behaviour. The residual strength increases with the decreases in the *B*-value.

He *et al.* (2014) performed undrained compression and extension monotonic triaxial tests on Ottawa sand on different void ratio aimed at investigate the relationship between degree of saturation and static liquefaction resistance. The tests were performed in order to evaluate the effectiveness of induced desaturation processes as a tool for the liquefaction mitigation. The Authors observed that, sand (*Dr* = 10%) in undrained compression triaxial test and sand (*Dr* = 30%) in undrained extension triaxial test, show a relevant undrained shear strength with a transition from stress-softening to stress-hardening when the degree of saturation is lowered from fully saturated conditions to 88%.

In recent years Arab *et al*. (2015) studied the influence of the saturation conditions on both static and dynamic liquefaction potential in terms of undrained shear strength by means of monotonic and cyclic undrained triaxial tests at strain controlled conditions on Hostun sand. Results of the monotonic undrained triaxial tests at different *B*-values (*Dr* = 4%, confining pressure of 100kPa) shown that samples sheared at high *B*-values exhibited low peak shear strengths. The increase of the pore pressure, in turn, leads to a reduction of the mean

effective stress, and so to a decrease of the undrained shear strength. Furthermore, results show that an increase of the *B*-value from 0.89 to 0.95 leads to a linear reduction of the peak and mobilized shear strength, while an increase of the *B*-value from 0.89 to 0.95 leads to a linear increase of the pore water pressure.

7.2.2 Effects of fine content

Some literature results concerning the effects of fine content on both static and dynamic liquefaction can be found, often with contradictory conclusions. Sometimes an increasing of the fine fraction seems to cause a decreasing liquefaction strength (Shen *et al*., 1977; Troncoso and Verdugo, 1985; Lade and Yamamuro, 1997, Pitmann *et al*., 1994; Bouferra and Shahrour, 2004; Carrera, 2008).
In 1977, Shen *et al*., by performing cyclic triaxial tests on different sandy-silt mixtures, observed a decrease of dynamic liquefaction resistance with increasing the fine content. In 1985 Tronsco and Verdugo performed cyclic triaxial tests on tailing sandy mixtures with different fine contents. They show that decreasing the silt content, mixtures are less prone to liquefaction, because the soil becomes less compressive and more dilative, resulting in higher liquefaction resistance.
These data are confirmed by results obtained by Carrera in 2008 on Stava tailings from undrained monotonic triaxial tests that will be described in section 7.3. Results obtained by Lade and Yamamuro (1997) from monotonic triaxial tests on dry pluviated samples (Ottawa sand), shown a decrease of maximum *q/p'* ratio as the fine content increases from clean sand to a mixture made of 50% of fines and 50% of sand (Fig. 7.7a). Also other experimental results show that an increase of the fine content until 15÷30% leads to a decrease of the liquefaction resistance, followed by an inversion of behaviour when the fine content exceeds that value. This transitional behaviour was observed by Bouferra and Shahrour (2004) by performing monotonic triaxial tests on Hostun sand mixed with kaolin clay. The authors shown that an increase in the *fc* up to 15÷30% decreases the liquefaction strength of the mixture (Fig. 7.7b), relating this behaviour to the role that fine fraction has in decreasing the dilating behaviour of the mixture until a limit value equal to 30%.

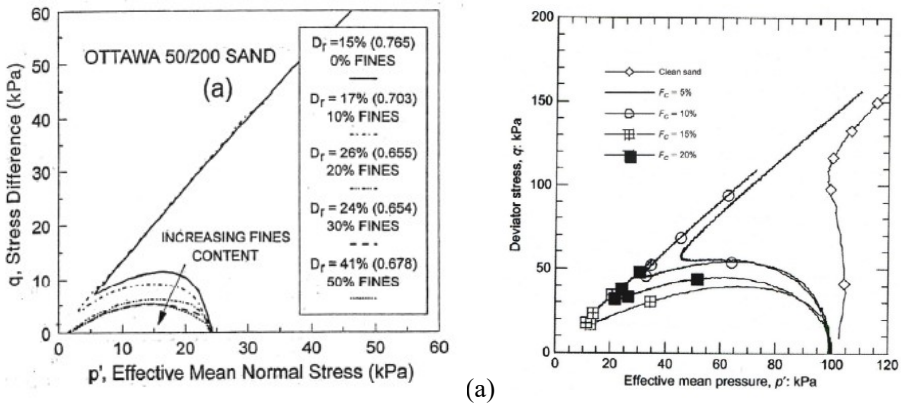

(a) (b)

Fig. 7.7 - (a) Effect of fine content on liquefaction resistance. (a) An increase of fine content leads to a decrease of the liquefaction strength. An increase of the relative density *Dr* with the fine content can be observed (Lade and Yamamuro, 1997). (b) An increase of fine content until 15-30% leads to a decrease of the liquefaction resistance. When fine content is higher than 15-30% the liquefaction resistance starts to increase (Bouferra and Shahrour, 2004).

The susceptibility of sand-silt mixtures to liquefy can be explained according to Yamamuro and Lade (1997) who stated that the liquefaction potential of a sand decreases with decreases in the fines content, as shown in Fig 7.8.

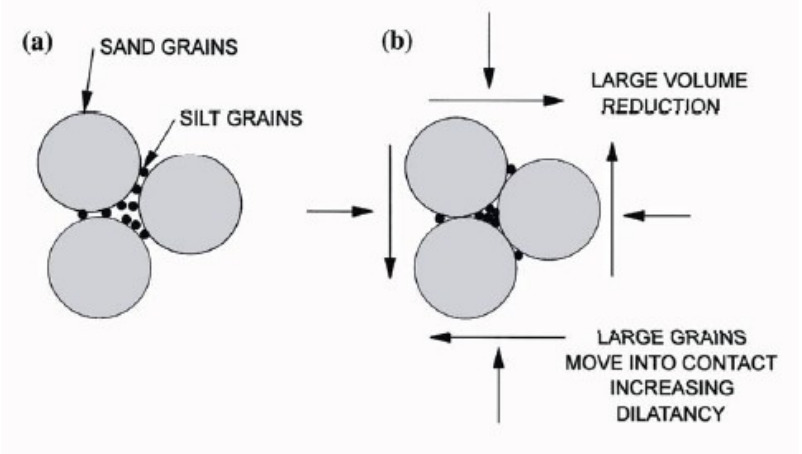

Fig. 7.8 - (a) Silty sand in loose state and (b) silty sand compressed and sheared (Yamamuro and Lade 1997).

Even if the presence of fine particles filling the void spaces between the sand particles (Fig. 7.8) increases the density of the soil, it has a limited effect on its liquefaction strength. Indeed, some of the fine particles do not fill only the void spaces between the sand particles, but also the spaces between the contact points of sand grains, causing a little separation between the sand particles. If the soil is compressed and sheared, the fine particles at the contact points of sandy grains will slide into the pores, so the silty sand mixture becomes more compressible and more prone to liquefy (Yamamuro and Lade 1997).
On the other hand, some investigations (Ishihara 1993) shown that the presence of non-plastic fines has a limited effect by on liquefaction potential, while some other Authors concluded that an increase of the fine content, increases the liquefaction strength (Tokimatsu and Yoshimi 1983; Seed *et al*. 1983; Robertson and Campanella 1985; Kuerbis *et al*. 1988; Pitman *et al*. 1994). In 1994, Pitman *et al*. studied the effects of different percentages of fine fractions (plastic kaolinite and non-plastic quartz) on the Ottawa sand obtaining an increase of static liquefaction strength with increasing of fines independently from their plasticity.

7.2.3 Effects of relative density

The effect of initial density on stress-strain behaviour on saturated sandy soil was shown by Ishihara (1996) by performing undrained shear tests. In case of dense sand, the shear stress increases with the shear strain resulting in hardening behaviour. On the other hand, the shear stress reaches a peak value and then it decreases (softening behaviour) in case of loose sand, while the medium dense sand initially exhibits softening and then hardening behaviour.
Results in terms of stress-strain and pore pressure behaviour of saturated Sacramento River Fine Sand at different relative density are given by Kramer and Seed (1988). The authors performed four isotropically consolidated undrained triaxial tests at different relative densities. Loose samples (Dr = 32% and Dr = 37%) showed a softening behaviour and liquefied with an increase of the pore water pressure that remained constant when the peak value is reached. The medium dense sample (Dr = 44%) initially liquefied at about 10% axial strain and then it showed hardening behaviour, with a first increase of the pore water

pressure that then slightly decreased at 10% of axial strain, when the sample began to show hardening behaviour. A significant hardening behaviour is clear for dense sample (*Dr* = 47%) with a constant decrease of the pore water pressure. These experimental results allow to state that the liquefaction strength of the tested sandy soil increases with increasing the relative initial density.

7.2.4 Effects of preparation techniques and initial shear stress

Results obtained from isotropic consolidated undrained triaxial tests by Chu *et al.* (2003) on loose sandy gold tailing samples shown that moist tamped samples are more susceptible to liquefaction. They exhibit a contractive behaviour with a great loss of shear resistance, while same specimens prepared by means of wet pluviated technique have an higher liquefaction strength. These variations in stress-strain behaviour are supposed due to the different soil fabric created by using different techniques.

Similarly, results obtained by Vaid and Sivathayalan in 2007 by performing undrained shear tests on Syncrude sand, shown an high loss of shear strength for samples created by using the moist tamped technique, while samples created by means of air pluviated method seemed to be stiffer with a less contractive behaviour. On the other hand, sample prepared by using water-pluviated technique shown a higher liquefaction resistance despite their higher void ratio (e = 0.777) if compared to those of moist tamped samples (e = 0.767).
Another factor affecting the liquefaction resistance is the initial shear stress. Results obtained by Kramer and Seed (1988) performing undrained triaxial tests on anisotropically consolidated samples (Sacramento River Fine sand) shown a decrease of liquefaction strength (susceptibility to liquefaction) with the increase of k_0 (2.25). On the other hand, samples consolidated with lower stress anisotropy (k_0 = 1.50) show an higher liquefaction resistance.

7.2.5 Effects of confining pressure and loading path

An example of the effects of confining pressure on liquefaction response was shown by Kramer and Seed 1988. Undrained triaxial tests performed at different confining pressures (ranging between 100kN/m^2 and 500kN/m^2) on Sacramento River Fine Sand, shown that liquefaction strength decreases with decreasing confining pressure (Fig. 7.9a).

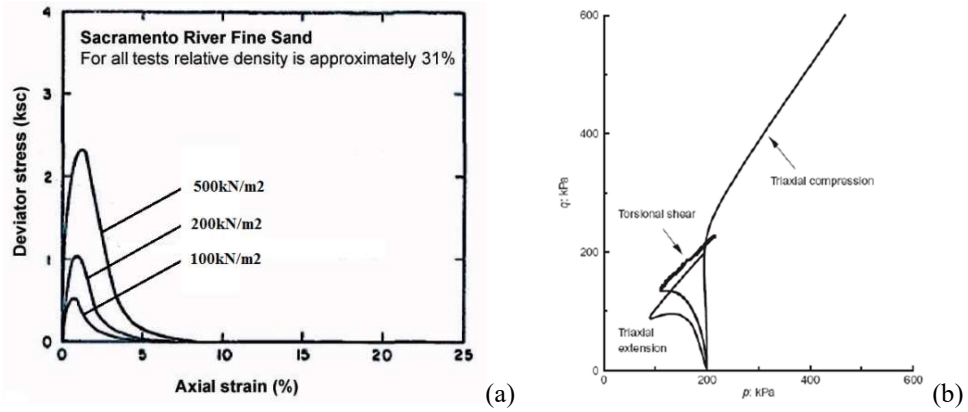

Fig. 7.9 - Effects of confining pressure (a) and loading path (b) on static liquefaction (modified from Kramer and Seed 1988; Yang *et al*., 2008).

Also the loading path was shown to affect the liquefaction behaviour. Yang *et al*. (2008) performed triaxial compression, triaxial extension and torsional shear tests on Toyoura sandy samples at the same density. They show an higher strain hardening, and so an higher liquefaction resistance of samples sheared in triaxial compression then samples sheared in triaxial extension. The stress-strain behaviour of sample subjected to torsional stress is between triaxial compression and extension (Fig. 7.9b).

7.3 SUSCEPTIBILITY TO LIQUEFACTION OF STAVA TAILINGS IN SATURATED CONDITIONS: PREVIOUS LITERATURE RESULTS

Carrera (2008) investigated static liquefaction of different graded saturated samples of Stava tailings. The mixtures investigated were: pure sand, 90% sand - 10% silt (9010), 70% sand - 30% silt (7030), 50% sand - 50% silt (5050), 30% sand - 70% silt (3070) and pure silt. The soil mixtures having a silty fines content ranging between 0 and 30% are representative of the material of the embankment; the pure silt corresponds to the tailings of the 'pond'; the mixtures from 30% to 70% of silts are representative of the 'beach', so the higher the silt content, the closer is the pond. The triaxial cells were all stress-path controlled, with internal axial and radial displacement transducers. The sample sizes were 38mm in diameter and 76mm high, or 70mm in diameter and 140mm high. Each sample was saturated under back pressure in order to reach a *B*-value corresponding to 0.96 that was considered as fully saturation state. Soil specimens were generally isotropically compressed and then sheared under undrained conditions.

Many samples were prepared using the moist tamping technique because it allows loose samples to be created and thus liquefaction phenomena to be studied. Furthermore, the structure created by moist tamping method is similar to that of the moist, unsaturated materials that were placed in the Stava dams. Figure 7.10 gives the stress path of pure silt samples that shown a susceptibility to liquefaction. The only test that reached a complete liquefaction was Test 039 for which the instability line was obtained. Only samples that reached a state in which isotropic and deviatoric stresses tended to zero were considered as having undergone liquefaction. Except Test 012, of which the void ratio is unknown, the maximum deviatoric stress q_{max} was observed to shift towards the Critical State envelope as the confining stress increases. The void ratios at liquefaction (e_{liq}) were then compared with the maximum and minimum void ratios, e_{max} and e_{min} derived as rough estimations from oedometer tests for each mixture.

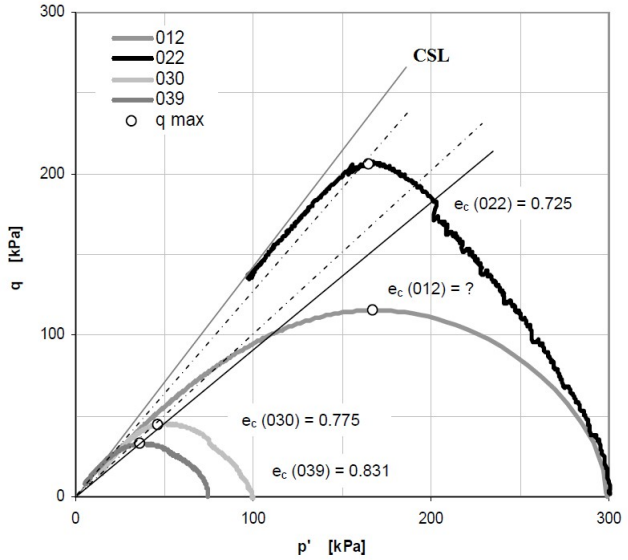

Fig. 7.10 - Stress paths from triaxial tests of silty sample that gave contractive behavior. The black solid line is the instability line of the only sample that reached true liquefaction (No. 039), the grey solid line is the *CSL*, the dotted lines are the possible instability lines for sample tested at high *p'* (Carrera, 2008).

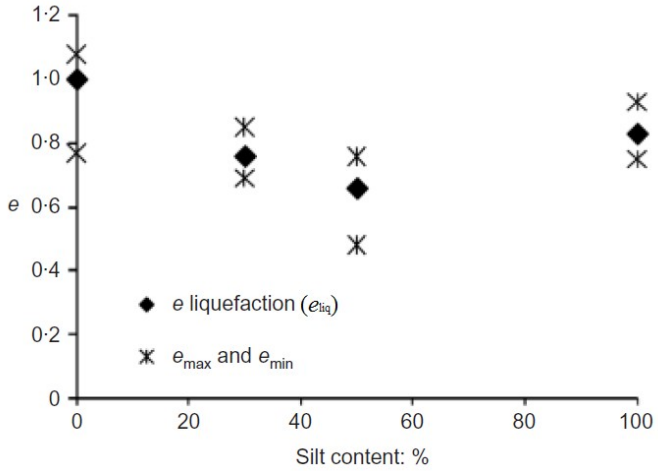

Fig. 7.11 - Void ratios of the Stava samples that liquefied at different fine contents and their respective maximum and minimum void ratios (Carrera *et al*., 2011).

The void ratio at which all the samples liquefied was observed to be comprised in the range between the e_{max} and e_{min} of each material: as shown in Fig. 7.11, samples made of pure sand are prone to liquefaction only for very high void ratios (about 1.0), while mixtures 30% fines - 70% sand material, 50% sand - 50% fines and 100% fines can reach liquefaction at lower void ratios. It is worth noting that the maximum and minimum void ratios were different, so a comparison among different mixtures cannot be done considering only the void ratio at

liquefaction e_{liq}, but also its position with respect to its extremes, e_{max} and e_{min} . It was observed that only sandy samples in a state very close to their maximum void ratio can reach liquefaction, while the pure silt and the mixture 30% fines - 70% sand can liquefy at void ratios that are half way between e_{max} and e_{min}, so it was concluded that sandy tailings were less susceptible to liquefaction than the other mixtures.

7.4 CRITICAL REVIEW OF THE STATE-OF-ART AND AIMS OF THE CURRENT RESEARCH

By analysing literature studies, it is possible to notice a big amount of study concerning the cyclic liquefaction resistance concerning the effects of degree of saturation on dynamic liquefaction resistance. They are basically investigated by means of cyclic triaxial and torsional shear tests just on sandy soils (Sherif *et al*., 1977; Martin *et al*., 1978; Mulilis *et al*., 1978; Yoshimi *et al.*, 1989; Xia and Hu, 1991; Bouferra, 2000; Kokusho 2000; Ishihara *et al.,* 2001; Yang and Sato 2001; Yang, 2002; Pietruszczak *et al*. 2003; Atigh and Byrne 2004; Yang *et al.*, 2004; Mathiroban and Grozic 2004; Ishihara *et al.*, 2001, 2004; Bouferra *et al*., 2007) in unsaturated conditions, showing a decrease of dynamic liquefaction resistance with increasing of the *B*-value, or degree of saturation. This huge amount of studies is motivated by the engineering interest at investigate the behaviour of coarse soils under dynamic loads (i.e. earthquakes).
In 2008, Carrera, under saturated conditions, studied the static liquefaction resistance of Stava tailing mixtures at different grain size distributions, showing the high liquefaction susceptibility also of silty fraction. By considering that silty tailings represent an extensive part of tailing storage facilities, or the fact that sand used to rise the embankment is usually mixed with fines (10%÷40%), the Author demonstrated that the static liquefaction tendency should not be evaluated only for sandy tailings that constitute the embankment, but also for silty tailings or mixtures with different percentages of fine fractions.
In recent years, few studies (Grozic *et al.,* 1999; Grozic *et al.,* 2005; Della, 2010; He *et al.*, 2014; Arab *et al*., 2015) can be found in literature concerning the investigation of the effect of degree of saturation on static liquefaction resistance in unsaturated conditions, again only for sandy soils, showing an increase of the liquefaction resistance with decreasing the *B*-value.
Similarity, the effect of initial density/void ratio on liquefaction response was investigated just on sandy soils in saturated conditions by means of shear tests (Ishihara 1996), showing a stress-hardening behaviour for dense saturated samples.
Finally, investigations performed by Chu *et al.*, 2003; Vaid and Sivathayalan, 2007, again on sandy soils, shown a certain influence of the preparation technique on liquefaction resistance in terms of stress-strain behaviour.
These observations lead to state that:

- despite the importance of investigating the static liquefaction of silty tailings demonstrated by Carrera (2008) at saturated conditions, no further studies seems to be made in order to evaluate the static liquefaction resistance of silty soils (in particular, tailing materials) under unsaturated conditions;
- such studies should also take into account the influence on static liquefaction, under unsaturated conditions, of the initial void ratio on silty tailings;
- as for saturated conditions, these studies should also evaluate the influence of preparation technique on silty soils (especially tailings), under unsaturated conditions;

- as for saturated conditions, these studies should also quantify the influence of preparation technique, with respect to the initial degree of saturation (or *B*-value) and void ratio.

For these reasons, the current study is aimed at investigating the static liquefaction response of silty tailings in unsaturated conditions. The soil used in this research is the Stava silty fraction characterized in chapter 4 and investigated by means of suction-controlled oedometer tests (chapter 5) and suction-controlled triaxial tests (chapter 6). Since the literature on static liquefaction of fine materials (i.e. silty tailings) in unsaturated conditions of which the Author is aware is quite scarce, the work was devoted to investigate the effects of those factors whose relevance is already demonstrated for cyclic liquefaction and static liquefaction just for sandy materials (preparation techniques, initial degree of saturation and void ratio). These factors have been investigated by means of conventional triaxial tests with shearing phase carried out at strain-controlled and undrained conditions on Stava unsaturated silty samples. Finally, different theoretical *B-Sr* relationships are compared with experimental *B-Sr* values. Then, they are compared with literature results obtained on sandy soils in order to verify if they can be used as predictive tool to estimate the degree of saturation reached during the saturation phase of triaxial tests.

7.5 CONVENTIONAL TRIAXIAL APPARATUS

The mechanical behaviour of Stava tailings, in terms of static liquefaction response, was investigated in both unsaturated and very close to saturated conditions by means of nine stress-path triaxial compression tests carried out on silty specimens (Tab. 7.1). These triaxial tests were performed by using a conventional Bishop and Wesley's cell (Fig. 7.12a) with double drainage.


(a)
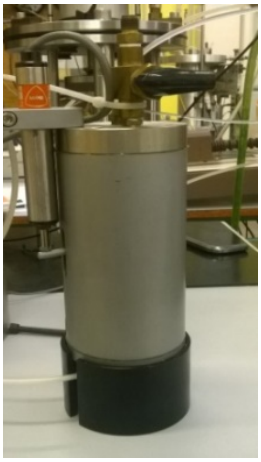
(b)

Fig. 7.12 - (a) Picture of the conventional triaxial cell and (b) volume-meter used to quantify the water volume change.

In the current research, compression tests under strain controlled conditions were performed. The triaxial sample was externally prepared and then placed inside the cell, or it was prepared inside the cell as described in the following section. The apparatus is provided with a bottom and a top water drainages externally connected with two differential diaphragm pressure transducers (maximum pressure 1000kPa, accuracy ±0.5kPa) aimed to record the pore water pressures.

Axial displacements of the samples are measured by using an external linear variable differential transducer (LVDT). The full range of LVDT transducers is 2.5mm and the accuracy is ±5µm.

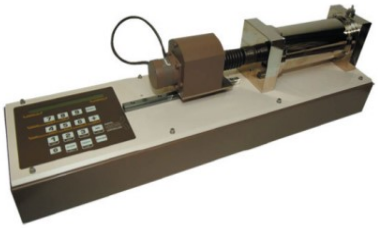

(a)

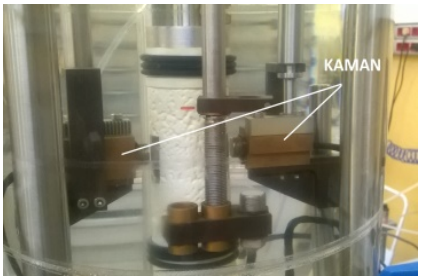

(b)

Fig. 7.13 - (a) Advanced digital pressure-volume controller and (b) picture of the Kaman transducers used for radial displacements measurements.

The axial force is measured by means of a load cell (maximum applicable load 3kN, accuracy ±3N) placed above the sample. A volume-meter (capacity 50cm^3, accuracy ±40mm^3) allows to quantify the water volume exchange with the soil sample (Fig. 7.12b). The strain control shearing phase was performed by means of an axial force given by a piston connected to an hydraulic mean consisting in a digital pressure-volume controller (Fig. 7.13a).
The radial displacements were measured by means of two non-contact 'Kaman' sensors, connected at the bottom of the cell. The full range of Kaman transducers is 2.5mm and the accuracy is ±5µm. They are placed inside the cell (Fig. 7.13b), at the opposite sides, at half height of the sample and their position can be easily adjusted during each phase of the test. These sensors measure variations of sample radius and the output voltage is proportional to the distance between their face and the target. The target is a piece of aluminium attached to the latex membrane surrounding the sample.

7.5.1 Preparation technique

Triaxial tests were carried out on silt samples (Tab. 7.1) at different initial void ratios and water content. All samples were 38mm diameter and 76mm height. The moist tamping technique was the method adopted to compact all the triaxial samples.

Samples TX1 and TX2 were prepared by hand-mixing a certain amount of dry soil with the required amount of demineralized, de-aired water in order to obtain a degree of saturation equal to 60% corresponding a water content equal to 21,2%. The mixture was then put into an hermetic cylindrical mould, so it was statically compacted by means of three layers (25.3 mm height each one), outside the triaxial cell (Fig. 7.14a) until reaching the total height. The samples were then extracted from the mould and placed inside the triaxial cell. An initial degree of saturation equal to 60% was the maximum value in order to have a sample stiff enough to sustain itself once after its extraction from the mould and placement inside the cell.

(a)

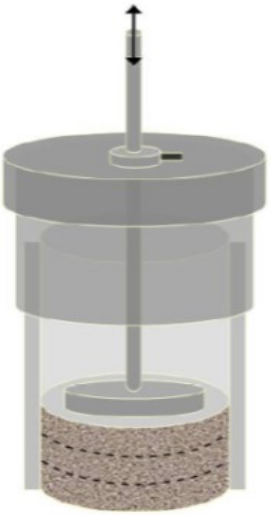

(b)

Fig. 7.14 - (a) static compaction technique used for samples TX1 and TX2. (b) Moist tamped method inside the triaxial cell used for samples TX3, TX4, TX5, TX6, TX7, TX8 and TX9 (Carrera, 2008).

The list of triaxial tests and their main characteristics in terms of initial void ratio (e_0), initial water content (w_0) and initial dry weight (γ_d) is given in Tab. 7.3.

Tab. 7.1 - List and main characteristics of the conventional triaxial tests performed.

Sample	Preparation technique	e_0 [-]	w_0 [%]	γ_d [kN/m^3]	Comments
TX1	Externally compacted	1.00	21.2	1.39	Not liquefied
TX2	Externally compacted	1.06	21.2	1.39	Not liquefied
TX3	Compacted inside the cell (MT)*	1.22	5.0	1.28	Liquefied
TX4	Compacted inside the cell (MT)*	1.23	5.0	1.28	Liquefied
TX5	Compacted inside the cell (MT)*	1.20	5.0	1.28	Liquefied
TX6	Compacted inside the cell (MT)*	1.25	5.0	1.28	Liquefied
TX7	Compacted inside the cell (MT)*	1.34	5.0	1.28	Not liquefied
TX8	Compacted inside the cell (MT)*	1.20	5.0	1.28	Interrupted at wetting phase, B too high
TX9	Compacted inside the cell (MT)*	1.20	5.0	1.28	Liquefied

* MT = moist tamping technique.

Samples TX3, TX4, TX5, TX6, TX7, TX8 and TX9 were prepared by using the moist tamping method (Fig. 7.14b) inside the triaxial cell. Five layers of a certain height and

constant density were created. Imposing the initial void ratio, total volume, the total weight of dry soil is obtained. The total weight is divided into five parts and each one will occupy $1/5^{th}$ of the total volume, assuring that the density is homogeneous. The dry soil of each layer is mixed with 5% in weight of demineralized, de-aired water. The mixture corresponding to the first layer is then put into a split mould inside the triaxial cell and a tamper is adopted to gently compact the layer until reaching $1/5^{th}$ of the total height. Some furrows have been traced on the surface to obtain a better connection between the following layer. The procedure was then repeated until the last layer, reaching the total height of the sample.
The addition of a small amount of water corresponding to water content of 5% is necessary to have water surface tension between grains that create an apparent cohesion. The apparent cohesion allows to prepare loose samples because high void ratios are necessary to investigate the phenomenon of liquefaction. Furthermore, according to Yang *et al*. (2008), the moist tamping method allows an higher homogeneity in the 3 dimensions than using different techniques such as wet pluviation or static compaction with only one layer.

7.5.2 Triaxial testing phases

A split mould was placed inside the cell, so a latex membrane was added. Before mounting the sample, all the drainages attached to apparatus were de-aired. The sample was then prepared inside the cell by moist tamping technique as previously described. Two porous filters were used to allow drainage from both faces of the sample, then a suction of 10kPa was applied to sustain the sample, so the mould was taken out. Two metallic (conductive) papers are glued at the opposite sides of the latex membrane in order to have two targets for the radial displacements measurement. The plastic cell and the top cap were then placed and the triaxial cell was filled with water. Suction was then reduced to zero and simultaneously the cell pressure was increased until 10kPa. Each triaxial test consisted of the following phases:

1) saturation consisting of upward flushing with de-aired water, followed by back pressuring;
2) consolidation phase by means of an isotropic compression;
3) shearing in undrained conditions.

The saturation phase was performed in two different steps:

a) flushing of air bubbles by circulating de-aired water throughout the triaxial system (specimen, drainages, etc.) under an effective confining stress equal to 10kPa. Flushing was realized by connecting samples drainages with an plastic box containing de-aired water. It was placed at a certain height above the sample, in order to have a proper hydraulic head to allow flushing of water into the tailing sample in the upward direction. This step was also aimed to ensure that drainages were completely filled with water. This is a fundamental requirement for the *B*-checking procedure in the following steps. Usually, flushing it is not solely sufficient to obtain high degree of saturation, so it is generally followed by a back-pressuring phase. In each test the flushing phase induced a large volume reduction with an axial strain corresponding at about 4%, depending on the initial degree of saturation of the sample.
b) In the current research, dissolution of residual air inside the sample was performed by through application of backpressure, and check out Skempton *B*-parameter. It consists in increasing, at each step, the back pressure maintaining unchanged the isotropic effective stress. This operation was performed when drainages are closed, by increasing the confining pressure and measuring over few minutes the change in

pore pressure, so the level of saturation is evaluated by means of the Skempton parameter *B*:

$$B = \frac{\Delta u}{\Delta \sigma_3} \tag{7-1}$$

where Δu is the measured change in pore pressure and $\Delta \sigma_3$ is the imposed change in cell pressure. After that, back pressure is increased and drainages are opened. In the current research, each *B*-check phase induces a little volume reduction with a total axial strain corresponding to about 1%.

The consolidation phase was performed in drained conditions. Samples were isotropically consolidated under an effective confining stress by increasing simultaneously radial and axial stresses in order to achieve the required effective stress. Consolidation phase has been concluded when measures of the water volume change between sample and volume-meter show no further variations.

The shearing phase was carried out in undrained conditions at constant radial effective stress. This phase was carried out in strain-controlled conditions at a strain rate equal to 0.012mm/min. The reduction of shear strength and consequent flow would happens in a very short time (i.e. less than one second) if the test is load controlled. Due to the fact that the in strain controlled tests the loss of strength is not fast, and in order to collect more data as possible between the peak and the steady state, all the triaxial tests performed in this research are performed in strain controlled conditions. Furthermore Sladen *et al*. (1985) demonstrated that there are no differences between the stress path coming from strain controlled and load controlled triaxial tests.

At the end of the shearing phase, sample was extracted from the cell and it was weighted. After that, it was oven dried for 24 hours at 105°C. Finally, it was weighted again in order to obtain the mass of water and so the degree of saturation at the end of the isotropic consolidation, assuming no variations of water content occur during the undrained shearing phase.

7.5.3 Required variables

The axial strain ε_a of the sample can be computed from the initial height h_0 and the axial displacement Δh obtained from the external LVDT:

$$\varepsilon_a = \frac{\Delta h}{h_0} \tag{7-2}$$

The radial strain ε_r can be computed from the initial radius r_0 and the radial displacement Δr measure by Kaman transducers:

$$\varepsilon_r = \frac{\Delta r}{r_0} \tag{7-3}$$

Knowledge of the initial total volume V_0, and the volumetric strain ε_v from axial and radial strain, allows to compute the total volume *V*:

$$V = V_0 - \varepsilon_v V_0 \tag{7-4}$$

The radius r at each step is computed from the initial radius r_0:

$$r = r_0 - \varepsilon_r r_0 \tag{7-5}$$

Axial stress at each step is computed by knowledge of the current area A and the axial force F measured by the load cell:

$$\sigma_a = \frac{F}{A} = \frac{F}{r^2\pi} \tag{7-6}$$

When measures of radial displacements were not available or unacceptable due to unsticking of metallic targets from the latex membrane, the area A of the sample at each step was computed by knowledge of initial area A_0 and axial strain ε_a:

$$A = \frac{A_0}{1 - \varepsilon_a} \tag{7-7}$$

Radial stress σ_r is the imposed confinement pressure, so the deviatoric stress q can be obtained:

$$q = \sigma_a - \sigma_r \tag{7-8}$$

Knowledge of pore water pressure u measured by transducers at each step, allows to compute the effective axial stress σ'_a and the effective radial stress σ'_r:

$$\sigma'_a = \sigma_a - u \tag{7-9a}$$

$$\sigma'_r = \sigma_r - u \tag{7-9b}$$

The mean effective stress p' is then computed:

$$p' = \frac{\sigma'_a + 2\sigma'_r}{3} \tag{7-10}$$

The excess of pore pressure Δu during the shearing phase, allows to obtain the mean stress p:

$$p = p' + \Delta u \tag{7-11}$$

Finally, at each phase, knowledge of volume of voids and volume of soil particles, allows to obtain the void ratio.

7.5.4 Theorical relationships between B-values and degree of saturation

In laboratory testing, the B-value is often used as an indicator of the degree of saturation of the soil sample. The relationship between B-parameter and degree of saturation is not linear, nor unique, but it is expected to depend on the fabric of the tested sample. The B-value is an experimental parameter proposed by Skempton in 1954. Defined as the ratio of variation in pore pressure Δu to the variation of the applied confining stress $\Delta\sigma_3$ under undrained conditions (eq. 7-1), it allows a quantification of the distribution of the applied stress between the fluid and the solid skeleton. The classical definition proposed by Skempton was extended by Bishop in 1973 in order to include, in undrained conditions, the influence of the bulk modulus of the solid skeleton for any porous media characterized by interconnected

pores. The Author assumed that skeleton is elastic and isotropic, while the pore fluid is linearly compressible. In the current research the solid phase was assumed incompressible, while the fluid phase (pore air and pore water) was considered compressible, so the Skempton's *B*-parameter is defined as:

$$B = \frac{K_f}{K_f + \phi K} = \frac{1}{1 + \phi\left(\frac{K}{K_f}\right)} \tag{7-12}$$

The pore fluid modulus of an air-water mixture can be computed by considering the bulk modulus of the two phases correlated with their volume fractions, by introducing a lower and an upper bound. In general terms, the upper Voigt bound K_{fV} of the fluid modulus of N phases can be computed as:

$$K_{f_V} = \sum_{i=1}^{N} f_i K_i \tag{7-13}$$

where f_i represents the volume fraction of each phase, while K_i is the corresponding elastic modulus. In the current research, where the phases are water and air, eq. 6-13 can be rewritten as:

$$K_{f_V} = S_a K_a + S_r K_w = (1 - S_r) K_a + S_r K_w \tag{7-14}$$

where K_a and K_w represent the bulk modulus of air and water, which are weighted by their volume fractions introducing the degree of saturation of water *Sr* (volume of water/volume of voids) and air *Sa* = 1-*Sr* (volume of air/volume of voids). According to Reuss (1929), the lower Reuss bound of the fluid modulus K_{fR} of N phases can be computed as follow:

$$\frac{1}{K_{f\,R}} = \sum_{i=1}^{N} \frac{f_i}{K_i} \tag{7-15}$$

Having two fluids, pore air and pore water, eq. 7-15 can be rewritten as:

$$K_{f\,R} = \frac{K_w K_a}{(1 - S_r) K_w + S_r K_a} \tag{7-15}$$

In the present research, the theoretical relationship between *B*-value and degree of saturation is computed by using both lower and upper bounds of the fluid modulus. By putting eq. 7-15 and eq. 7-14 inside eq. 7-12, lower *B*-values (eq. 7-16a) and upper *B*-values (eq. 7-16b) can be obtained as a function of the degree of saturation *Sr*:

$$B = \frac{\frac{K_w K_a}{(1-S_r)K_w + S_r K_a}}{\frac{K_w K_a}{(1-S_r)K_w + S_r K_a} + \left(\frac{e}{1+e}\right) K} \tag{7-16a}$$

$$B = \frac{(1 - S_r) K_a + S_r K_w}{(1 - S_r) K_a + S_r K_w + \left(\frac{e}{1+e}\right) K} \tag{7-16b}$$

The bulk modulus K of silty tailing is obtained by knowledge of variation in mean effective stress $\Delta p'$ and variation in volumetric strain $\Delta\varepsilon_v$ of the sample during the consolidation phase:

$$K = \frac{\Delta p'}{\Delta \varepsilon_v} \tag{7-17}$$

The computed poro-elastic parameters for the estimation of theoretical *B-Sr* relationship (eq. 7-16) are summarized in Tab. 7.2.

Tab. 7.2 - List of poro-elastic parameters used for the estimation of theoretical *B-Sr* relationship (Voigt and Reus bounds).

Porosity of tested soil, Φ[-]	**Bulk modulus of pore air, K_a [GPa]**	**Bulk modulus of pore water, K_w [GPa]**
0.5	0.000142	2.2

The *B-Sr* theoretical relationship was also estimated by using another relationship, the equation proposed by Lade and Hernandez (1977):

$$B = \frac{1}{1 + \phi K\left(\frac{Sr}{K_w} + \frac{1-Sr}{u_w}\right)} \tag{7-18}$$

where Φ is the porosity of the soil, K is the bulk modulus of the soil skeleton (obtained, for each test, by using eq. 7-17), K_w is the bulk modulus of water (2.2GPa), u_w is the water pressure.

Theoretical *B-Sr* relationship was then compared with experimental results in terms of measured *B*-values and computed degree of saturation. During the saturation phase, at each step of *B*-value check, the measured *B*-value was associated to its corresponding degree of saturation. At each step it was computed by knowing the initial water volume (V_{w0}), water volume exchanged due to flushing ($V_{w,flu}$) and the measured water volume exchanged with volume-meter ($V_{w,vol}$) during back pressuring:

$$V_w = V_{w0} + V_{w,flu} + V_{w,vol} \tag{7-19}$$

The volume of voids V_v is computed by subtracting at total volume V, the volume of soil particles V_s :

$$V_v = V - V_s = V - \frac{M_s}{G_s} \tag{7-20}$$

where M_s is the mass of soil particles obtained after the oven drying process and G_s is the specific weight of the soil.

Few literature studies can be found concerning the relationship between *B*-value and its corresponding degree of saturation. Figures 7.15a,b give a comparison of the experimental relationship between the degree of saturation and measured *B*-value obtained before cyclic liquefaction for some sandy soils with some theoretical *B-Sr* relationships (Lade and Hernandez, 1977; Xia and Hu, 1991). The reference sands tested by Yoshimi *et al*., 1989 (by

means of torsional shear test), Raghunadan and Ashish, 2011 (by means of cyclic triaxial tests) are Toyoura sand and Kutch Gujarat river sand, respectively.

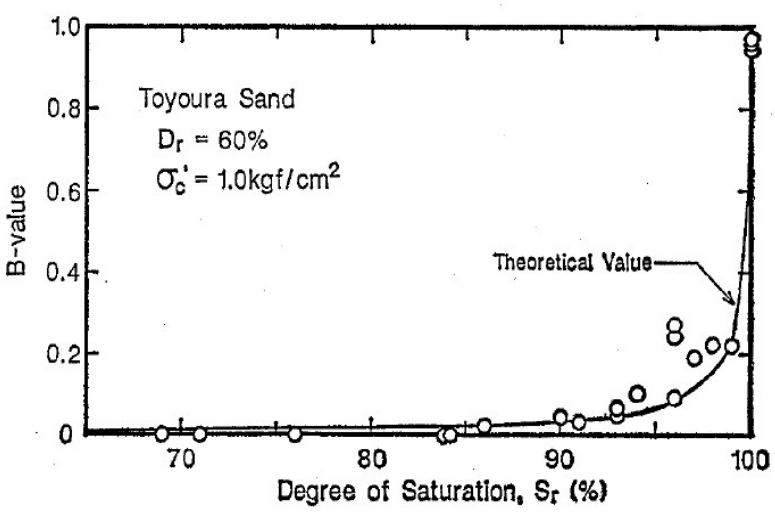

(a)

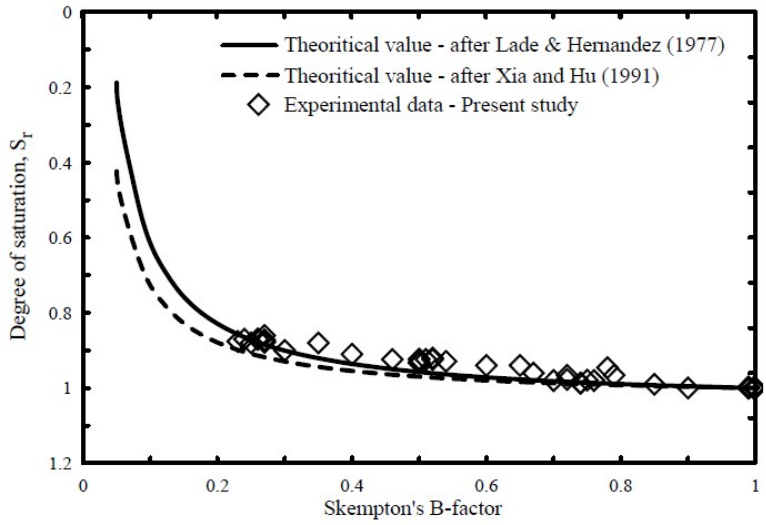

(b)

Fig. 7.15 - Comparison between theoretical and experimental relation of degree of saturation and Skempton's *B*-factor proposed by (a) Yoshimi *et al*., 1989, (b) Raghunadan and Ashish, 2011.

The circles shown in Fig. 7.15a give the experimental relationship between the degree of saturation *Sr* and the measured *B*-values of Toyoura sand having initial relative density of 60%. They are compared with the theoretical *B-Sr* relationship proposed by Lade and Hernandez (1977). It is possible to notice big variations in degree of saturation associated with little changes of *B*-values until *B*-parameter reaches about 0.2. After that value, big variations in *B*-value cause little changes of degree of saturation. Experimental and theoretical results agree quite well.

The diamonds shown in Fig. 7.15b give the experimental relationship between the measured *B*-values and degree of saturation of Kutch Gujarat river sand, compared with the theoretical *B-Sr* relationship. Again, little variations of degree of saturation can be observed for big changes of *B*-values (from $B = 0.2$ to $B = 1$): experimental results show good agreement with theoretical expressions proposed by Lade and Hernandez (1977) and Reuss average. Similar observations can be extended to experimental results obtained on Hostun RF sand by Arab *et al.,* 2015.

7.6 RESULTS

In this section, experimental results obtained in the current research are exposed in terms of susceptibility to static liquefaction and relationships between *B*-value and degree of saturation of Stava silty tailings.

7.6.1 Susceptibility to static liquefaction of Stava tailings in unsaturated conditions

Figure 7.16 shows the variations of deviator stress q with the axial strain ε_a for test TX3, during the undrained shearing phase at cell pressure of 80kPa. The results show that the deviator stress increased to a peak value of about 33kPa at an axial strain of 0.5% and then decreased to12kPa, after which it remained nearly constant until the end of the test.

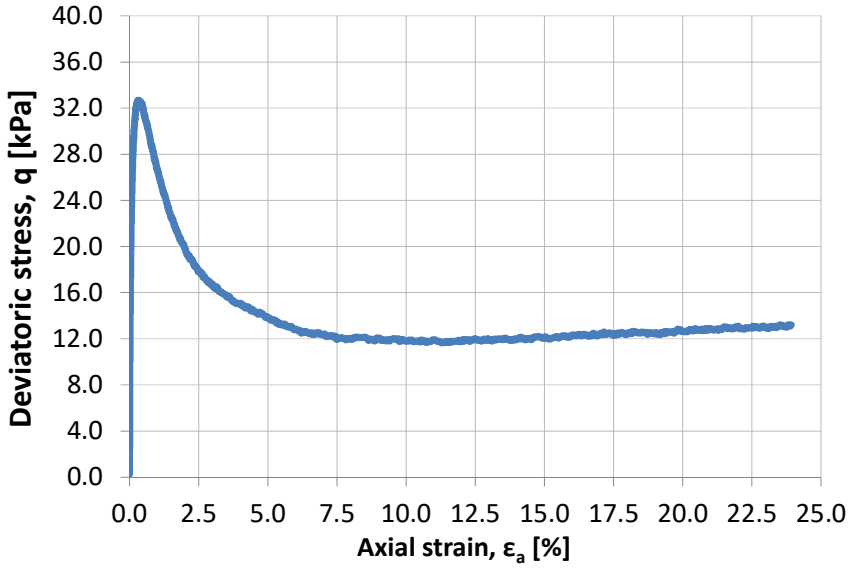

Fig. 7.16 - Specimen TX3: undrained response on q-ε_a plane.

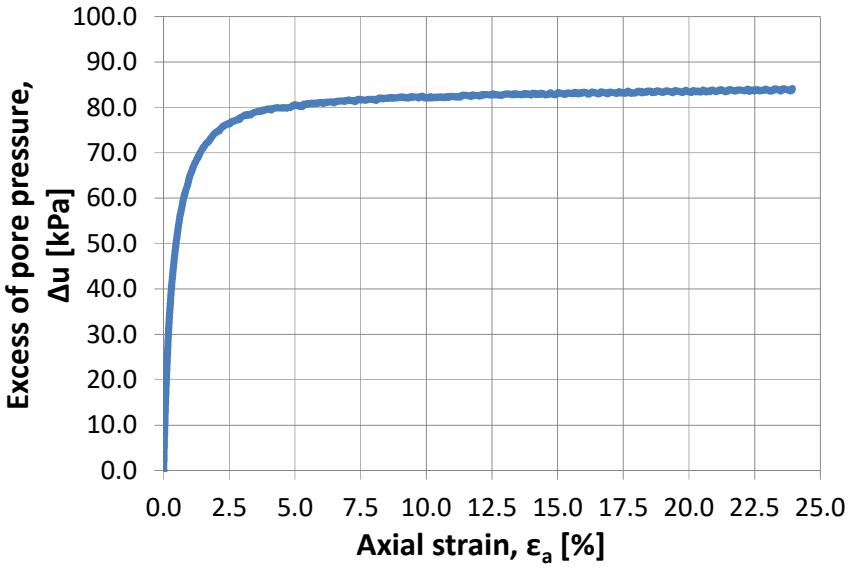

Fig. 7.17 - Specimen TX3: undrained response on Δu-ε_a plane.

In this case, the sample clearly shown a softening behaviour. Being undrained and very close to saturated conditions, the specimen cannot contract, so the pore pressure starts to increase, until an excess of pore pressure equal to 80kPa was reached as shown in Fig. 7.17.
Figure 7.18 shows the variations of deviator stress q with the total mean stress p and with the effective stress p'.

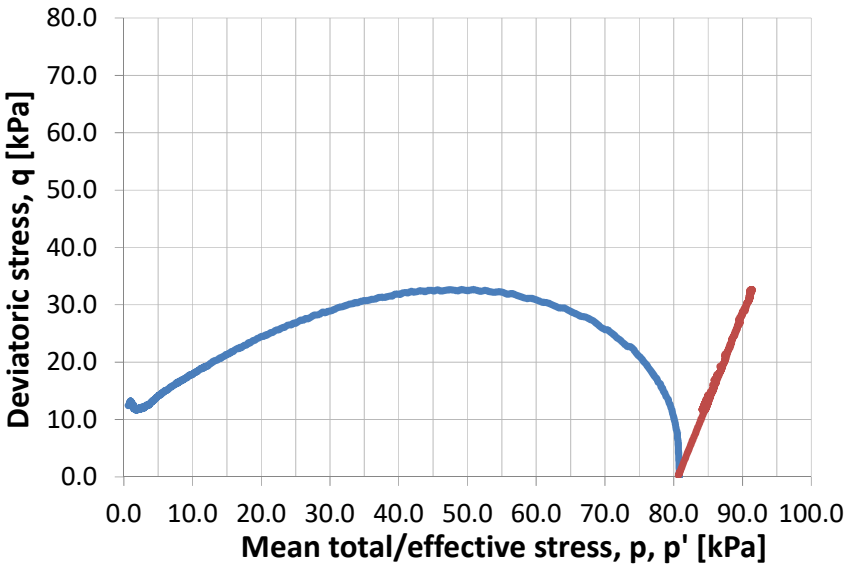

Fig. 7.18 - Specimen TX3: undrained response on q-p,p' plane.

Starting from the pressure imposed during the isotropic consolidation phase (80kPa), the sample shows a tendency to contract and a decrease of both mean effective stress p' and deviator stress q until residual values of 0kPa and 12kPa, respectively.
Figure 7.19 shows the variations of deviator stress q with the axial strain ε_a for test TX1,

during the undrained shearing phase at cell pressure of 80kPa. It is worth to note that TX1 and TX2 were prepared by means of static compaction, consisting in three layers, externally to the triaxial cell, with an initial degree of saturation equal to 60%, while the rest of the specimens were prepared by moist tamping inside the cell. The deviator stress increased to a peak value of about 38kPa at an axial strain of 1.1%, then it maintained this constant value until 3% of axial strain, finally it increased until the end of the test (hardening behaviour). After a small compressive behaviour where the pore pressure reached a peak of 60kPa, the sample showed a tendency to dilate inhibited by the undrained conditions in a quasi-saturated state. The pore pressure starts to decrease, until a final value of about 15kPa, as shown in Fig. 7.20.

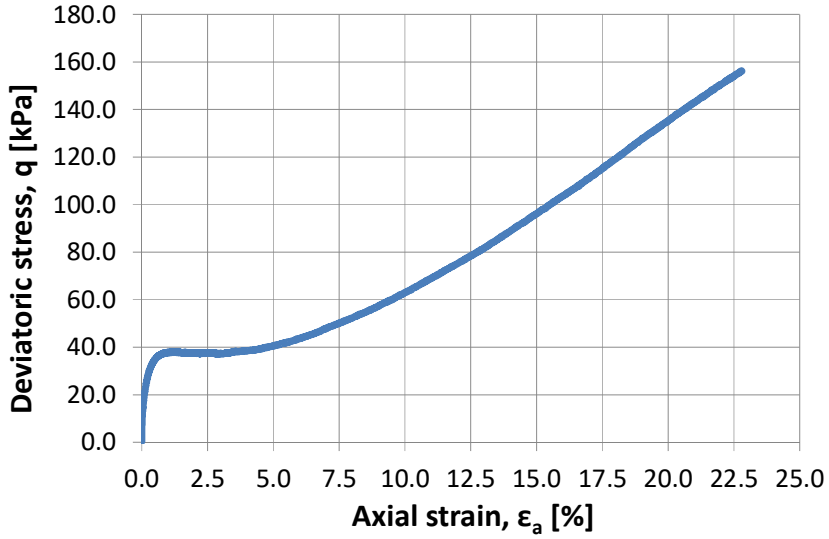

Fig. 7.19 - Specimen TX1: undrained response on q-ε_a plane.

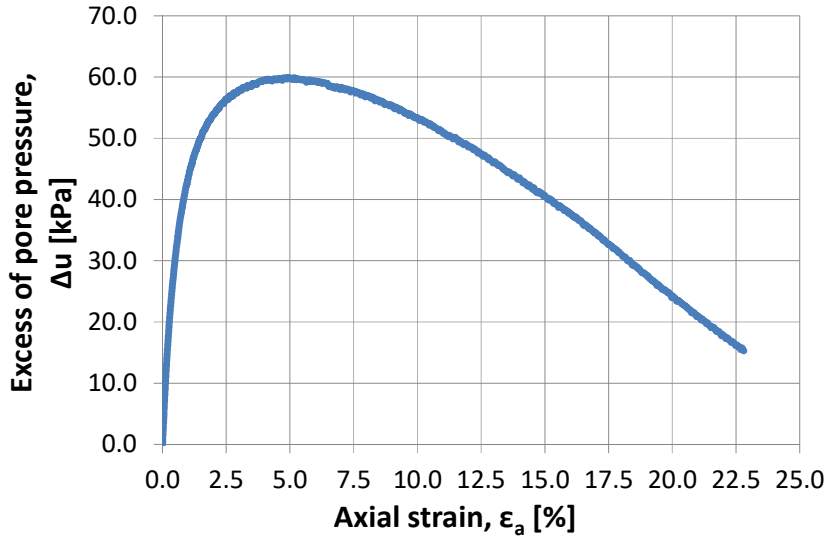

Fig. 7.20 - Specimen TX1: undrained response on Δu-ε_a plane.

Figure 7.21 gives the variations of deviator stress q with the mean total stress p and the mean

effective stress *p'*. It is worth to note the Phase Transformation point A (*q* = 38kPa, *p'* = 33kPa) in the *q-p'* plane where the stress path shows a change of behaviour, from contractive to dilative with a constant increase of deviator stress.

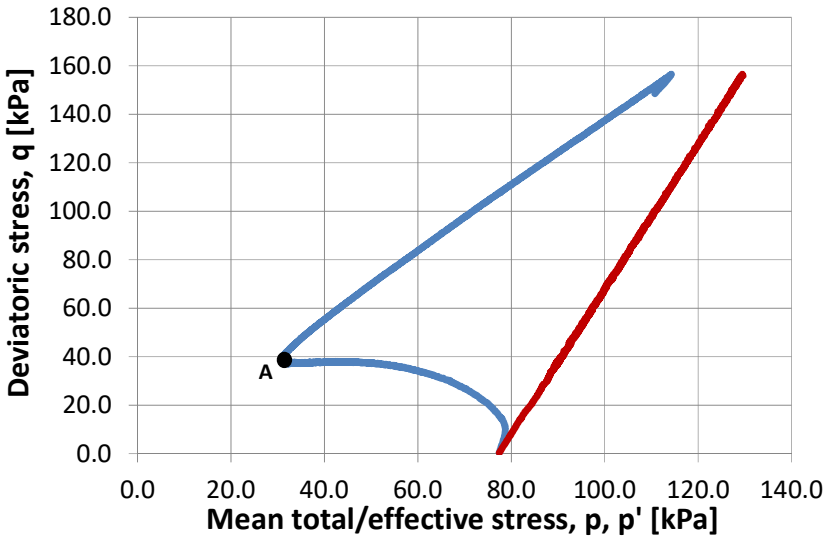

Fig. 7.21 - Specimen TX1: undrained response on *q-p,p'* plane.

Figure 7.22 shows the variations of deviator stress *q* with the axial strain ε_a for test TX7. The experimental results show that the deviator stress increased to a peak value of about 34kPa at axial strain of 0.5%. With increasing axial strain, a small decrease of deviator stress occur reaching a value of about 30kPa at 3% of axial strain, after which it remained nearly constant until the end of the test.

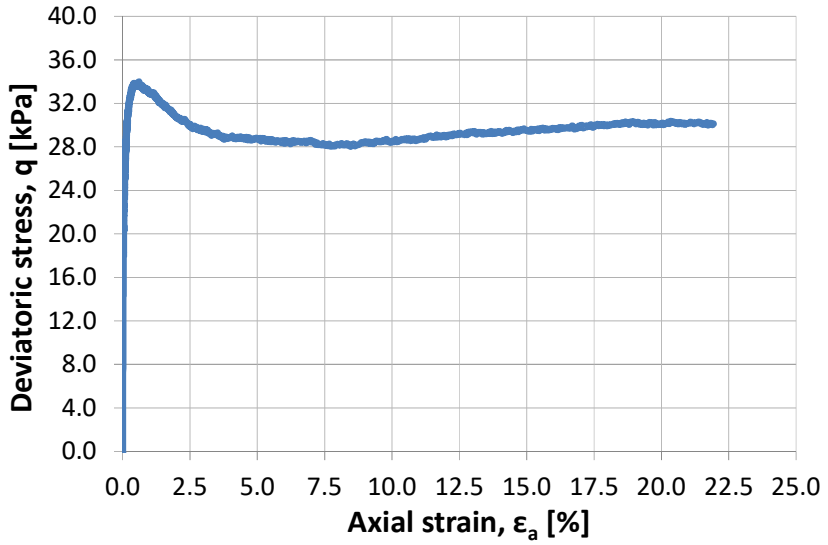

Fig. 7.22 - Specimen TX7: undrained response on q-ε_a plane.

Figure 7.23 shows the variations of deviator stress *q* with *p* and *p'*.

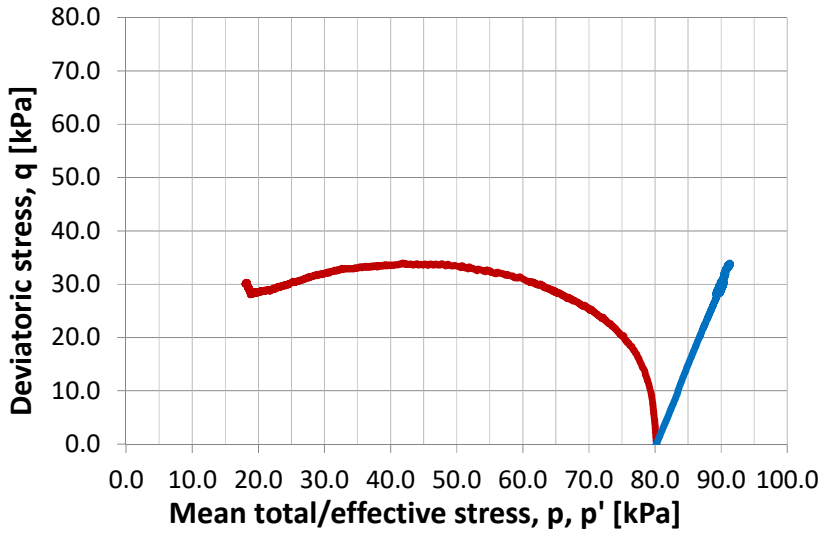

Fig. 7.23 - Specimen TX7: undrained response on *q-p,p'* plane.

Starting from the isotropic state of stress imposed during the consolidation (80kPa), the sample shows a tendency to contraction by means of a decrease of both mean effective stress *p'* and deviator stress *q* until residual values of 18kPa and 28kPa, respectively.
Variations of deviator stress *q* with the axial strain ε_a for tests TX1, TX6 and TX7 are represented in Fig. 7.24. It is worth noting that sample TX1, Tx6 and TX7 are prepared by means of different techniques, saturated at different degree of saturation and they have different void ratio e_c.

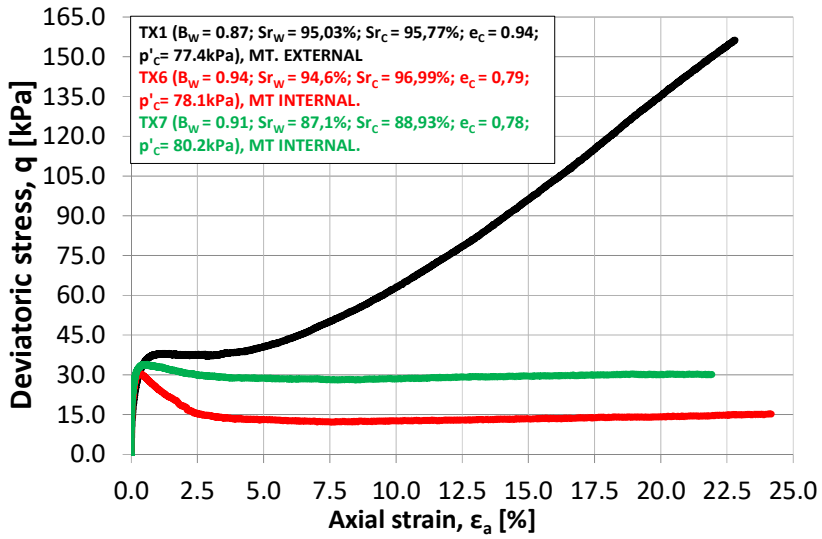

Fig. 7.24 - Undrained response of externally compacted specimen TX1 and moist tamped specimens TX6, TX7 on *q*-ε_a plane.

Sample TX1 shows a clear strain-hardening behaviour if compared to mechanical response of samples TX6 and TX7 that show a partial or complete strain-softening behaviour. Despite

sample TX1 had a void ratio at the end of consolidation (e_c = 0.94) higher than those of samples TX6 (e_c = 0.79), and TX7 (e_c = 0.78), the hardening response of samples TX1 is evident, suggesting a fundamental role of the sample preparation technique also on unsaturated silty soils on the mechanical response of Stava tailing, as previously reported by Vaid and Sivathalayan (2007) on Sincrude sand. Therefore, if all samples were prepared by using the same technique, looser samples (TX1)should be more prone to liquefy than denser ones (TX6 and TX7).

7.6.2 Effect of the preparation technique on static liquefaction in unsaturated conditions

A clear example of the importance of preparation technique on the liquefaction resistance is given by comparing results of stress-strain behaviour for sample TX1 and TX4 (Fig. 7.25a) prepared by means of different techniques. Despite the two samples are quite comparable, especially in terms of degree of saturation Sr_c, at the end of consolidation phase, sample TX1 shows a relevant stress-hardening behaviour, while the sample TX4, even if denser than sample TX1, approaches the steady state by means of a stress-softening behaviour with a lower maximum deviator stress, about 30kPa at 0.5% axial strain instead of 35kPa at 1% axial strain as for sample TX1. Indeed, in this range of degree of saturation, the preparation technique seems to be more relevant than the initial density in terms of stress-strain behaviour, and hence in terms of liquefaction resistance.
The response of specimens TX3 and TX5 is also shown in terms of deviator stress-mean effective stress as given in Fig. 7.25b. The externally compacted specimen (TX1) clearly shows a transition behaviour: a contractive tendency can be observed until a deviator stress of about 40kPa when a dilative tendency begins to be evident until the end of the test. On the other hand, the moist tamped specimen (TX4) is characterized by a pure contractive tendency.

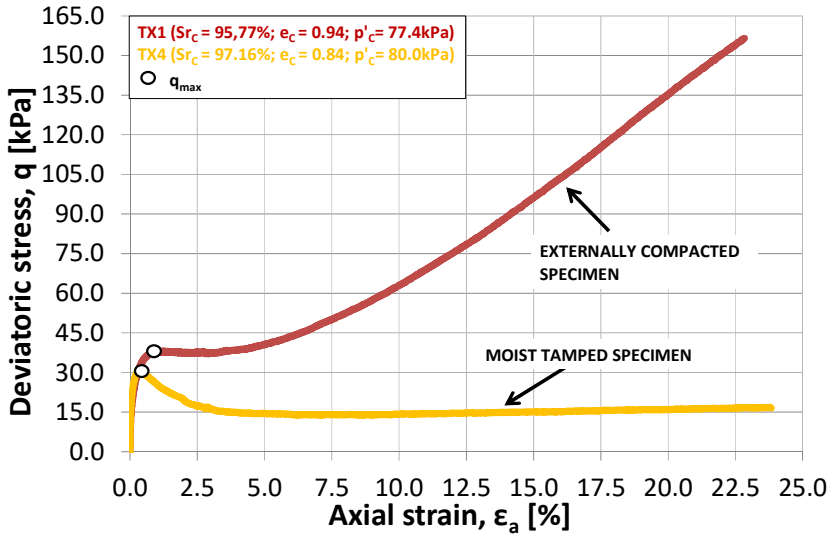

(a)

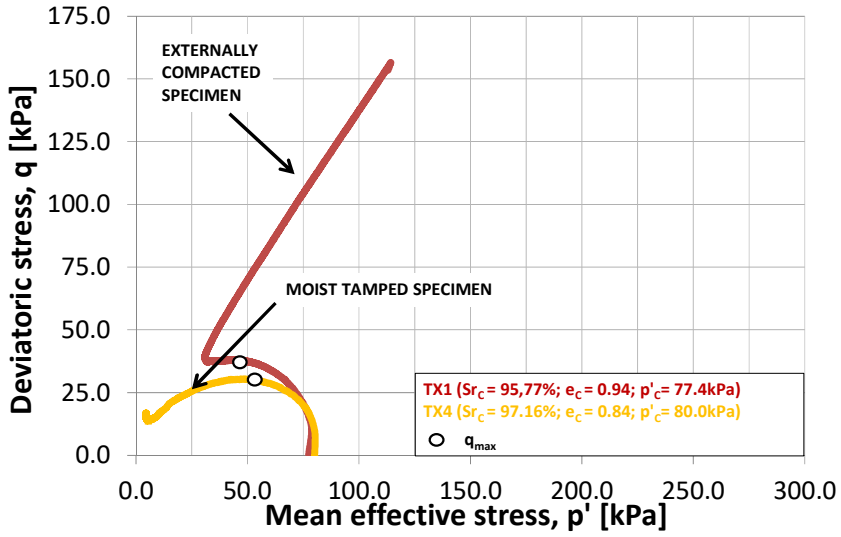

(b)

Fig. 7.25 - Effect of preparation technique on the stress-strain behaviour in (a) q-ε_a and (b) q-p' plane (externally compacted specimen TX1 and moist tamped specimen TX4).

Finally, it is worth to note that the maximum deviator stress q_{max} of the moist tamped specimen is lower than those of the externally compacted specimen. This aspect will be discussed in section 7.6.7.

7.6.3 Effect of volumetric water content of static liquefaction in unsaturated conditions

Figure. 7.26 gives a comparison of the stress-strain behaviour of samples TX3, TX5, TX6, TX7, all prepared by means of the same technique (moist tamping method).

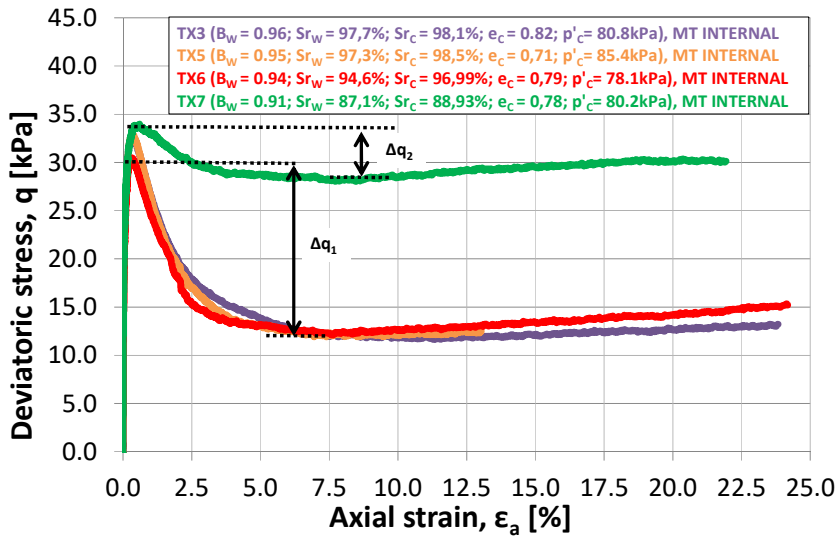

Fig. 7.26 - Undrained response: effect of degree of saturation and void ratio on the stress-strain behaviour (moist tamped specimens TX3, TX5, TX6 and TX7).

Except sample TX7, all other samples exhibit practically the same decrease of deviator stress Δq_1 with similar deviator peak values q_{max} (about 30÷32kPa) at the same axial strain ε_a (about 0.5%), and similar residual deviator values (about 12÷15kPa). The exception is represented by sample TX7 that gives a little loss of deviator stress Δq_2, and so an higher residual deviator value, 30kPa instead of 12kPa÷15kPa. Because of the same preparation technique, a proper comparison between sample TX7 and samples TX3, TX5, TX6 can be based on the different values of void ratio e_c or the degree of saturation at the end of consolidation phase Sr_c, (or the degree of saturation Sr_w at the end of the saturation phase).
If the volumetric water content is computed for each specimen of Fig. 6.26, the combined defect of void ratio and degree of saturation can be quantified. Specimen TX7 shows the lowest volumetric water content (ϑ = 0.693) if compared to values of the other specimens TX3 (ϑ = 0.804), TX5 (ϑ = 0.700) and TX6 (ϑ = 0.766). For these range of void ratios and degrees of saturation, the only consideration can be made is that just a little variation in volumetric water content is enough to move the mechanical behaviour of Stava silty samples from a quasi-strain-hardening behaviour (TX7) to a strain-softening behaviour (TX3, TX5, TX6).

7.6.4 Effect of void ratio of static liquefaction in unsaturated conditions

No many advantages can be obtained by analysing the void ratios e_c: they range between 0.71 and 0.82 because of the different volumetric strains occurred during saturation and consolidation phase, probably due to undesired heterogeneity in the soil fabric/structure of the samples.

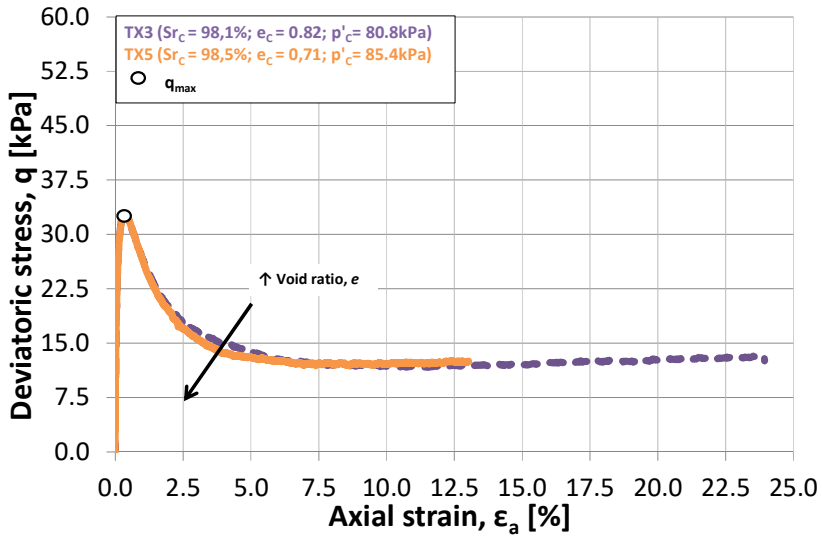

(a)

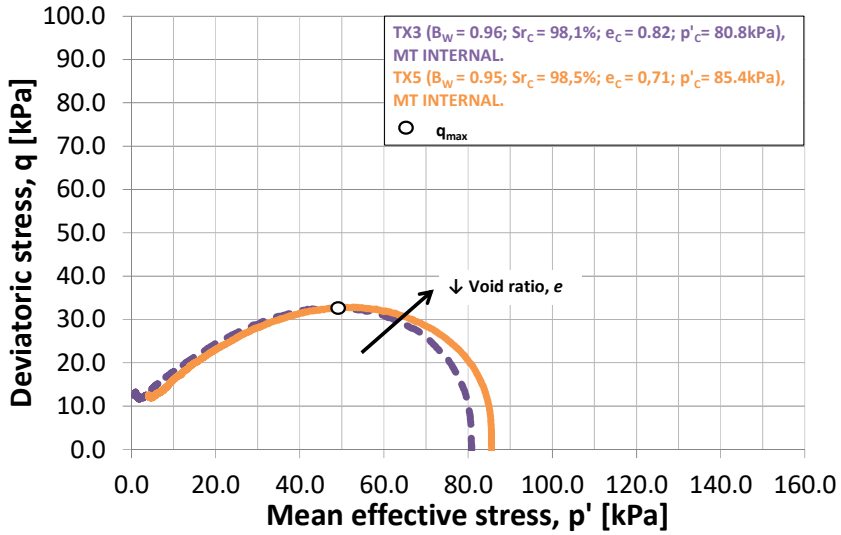

(b)

Fig. 7.27 - Effect of void ratio on the stress-strain behaviour in (a) q-ε_a and (b) q-p' plane (moist tamped specimens TX3 and TX5).

Despite these differences in void ratio, the stress-strain behaviour, for instance, of sample TX3 (e_c = 0.82) is very similar to those of sample TX5 (e_c = 0.71) as shown in Fig. 7.27a, so the void ratio alone seems not to be the main factor governing the static liquefaction response of Stava silty tailing. The response of specimens TX3 and TX5 is also given in terms of deviator stress-mean effective stress as given in Fig. 7.27b. The two specimens show practically the same stress-behaviour with very similar maximum deviator stresses q_{max} and residual values of deviator q and mean effective stresses p'.

7.6.5 *Effect of degree of saturation on static liquefaction in unsaturated conditions*

The degree of saturation represents the last variable to analyse in order to justify the different mechanical response of sample TX7 with respect to the other ones. Fig. 7.28a,b show the effect of degree of saturation on the stress-strain behaviour of sample TX7 and sample TX6. The two sample have very similar void ratio (e_c = 0.78 for sample TX7 and e_c =0.79 for TX6), but different degree of saturation. The degree of saturation of sample TX7 at the end of consolidation phase is 89%, while sample TX6 has a degree of saturation of about 97%, so the difference in stress-strain behaviour is due only to their different degree of saturation. Sample TX7 shows an higher maximum deviator stress (q_{max} = 34kPa) than those of sample TX6 (q_{max} = 30kPa) and a lower loss of strength (Δq_2 = 5kPa instead of Δq_1 = 18kPa). Hence, a decrease of degree of saturation seems to shift the mechanical behaviour from a strain-softening behaviour to a strain-hardening behaviour. It can be noticed that for degree of saturation lower than 90%, the static liquefaction resistance seems to be about twice greater than those for degree of saturation higher than 90%. Indeed sample TX7 (Sr_w = *88.9%*) exhibits a residual deviator stress q_{res} = 29kPa÷30kPa, while specimens TX3-TX4-TX5-TX6-TX9 (Sr_w = *93÷96%*) exhibits a residual deviator stress q_{res} = 14kPa÷15kPa, leading to think that a degree of saturation corresponding at about 90% seems to represent a border value. It is worth noting that these considerations about the static liquefaction resistance on Stava silty tailing are in good agreement with experimental evidences obtained by Yoshimi *et al.,* 1989 (Fig. 7.3a) on reconstituted Toyoura sandy samples, by performing cyclic torsional shear tests. Also in that case, the Author observed that, at low number of cycles (10-20) and low

frequencies, the liquefaction resistance at degree of saturation equal to 90%, is about two times that at fully or close to saturated conditions. Furthermore, results of the current research on fine material can be well compared with experimental evidences obtained on coarse soils by Grozic *et al.* (1999), Della (2010), He *et al.* (2014), Arab *et al*. (2015). Both, literature data on Ottawa sand and the currents work on Stava silty tailings, show an increase of the liquefaction resistance with decreasing the degree of saturation (or *B*-value), finding a degree of saturation of 90% as a border value between strain-hardening and strain-softening behaviour.

The response of specimens TX6 and TX7 in terms of deviator stress-mean effective stress is finally given in Fig. 7.28b. Both specimens TX6 and TX7 show a pure tendency to contract, but the steady state is reached at an higher deviator stress and mean effective stress for TX7 respect to TX6. The maximum deviator stress q_{max} of the specimen that does not liquefy (TX7) is higher than those of the specimen that liquefies. Again this aspect will be discussed in section 7.6.7.

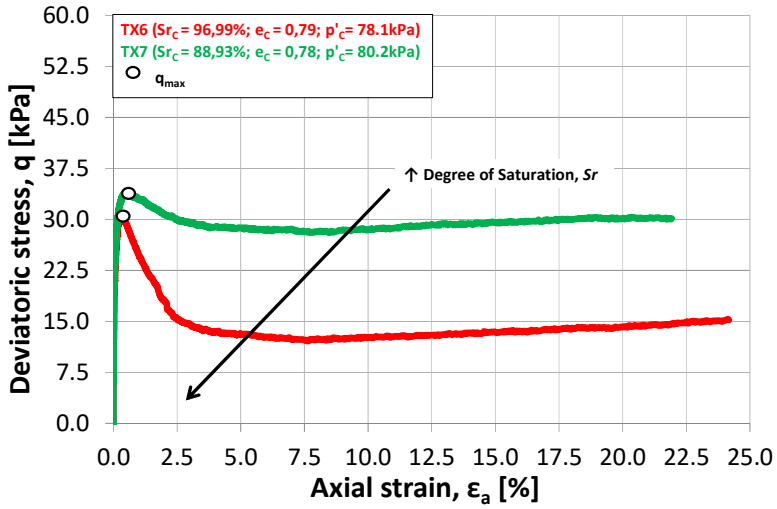

(a)

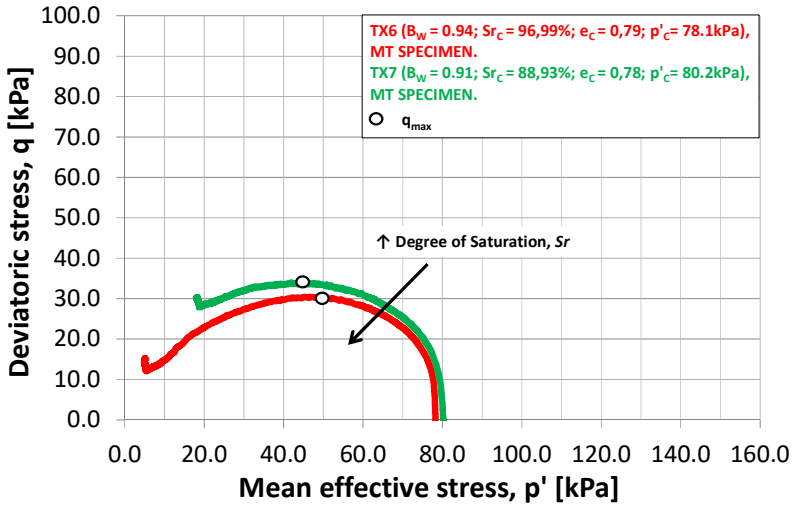

(b)

Fig. 7.28 - Effect of degree of saturation on the stress-strain behaviour in (a) q-ε_a and (b) q-p' plane (moist tamped specimens TX6 and TX7).

7.6.6 *Static liquefaction resistance in unsaturated conditions*

Similarity to Liquefaction Resistance Ratio (Fig. 7.3a) or Cyclic stress Ratio (Fig. 7.4) used for quantifying the dynamic liquefaction strength, in the current research the "static liquefaction resistance ratio" (*SLRR*) is introduced. If the ratio between the residual deviator stress and the confinement pressure (q_{res}/p'_C) of each test is normalized by the ratio between the residual deviator stress and the confinement pressure (q_{res}/p'_C) of the specimen saturated at the highest degree of saturation (assumed as the saturated conditions) and then plotted in terms of Sr_{co}, one can have an idea of variation of static liquefaction resistance (Fig. 7.29).

$$SLRR = \left(\frac{q_{res}}{p'_C}\right)_{uns} \Big/ \left(\frac{q_{res}}{p'_C}\right)_{sat} \tag{7-21}$$

Despite a certain scatter of the experimental points, it is evident a certain decreasing of the static liquefaction resistance with the degree of saturation. Resistance of samples saturated under 90% seems to be more than two times those of samples fully saturated or close to saturated conditions

According to He *et al.*, (2014), the equation proposed by Okamura and Soga (2004) for cyclic loading conditions can be generalized in order to evaluate the liquefaction resistance under monotonic loading conditions, giving the liquefaction resistance ratio *LLR* depending on the degree of saturation:

$$LRR = \log(\alpha \cdot \varepsilon_v^* + 10) \tag{7-22}$$

where α is a parameter to be calibrated and ε_v^* is the potential volumetric strain:

$$\varepsilon_v^* = \frac{p'_c}{p_0 + p'_c}(1 - Sr)\frac{e}{1 + e} \tag{7-23}$$

In eq. 7-23 p_0 is the pressure of the pore fluid (water in the current case), p'_C is the effective confinement stress, e is the void ratio. The influence of the degree of saturation on the liquefaction resistance ratio *LLR* is given in Fig. 7.30 for moist tamped specimens. It is worth to note that, in order to obtain the same value of *LLR* (eq. 7.22) and *SLRR* (eq. 7.21), the α parameter was calibrated and set equal to 5800 for TX7 and 800 per all other tests. In this case, it can be noticed that the liquefaction resistance at degree of saturation of 89% (specimen TX7) is about 2.0 times greater than those of other moist tamped specimens.

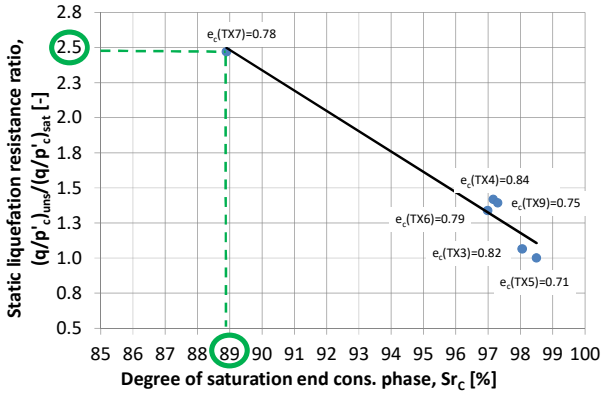

Fig. 7.29 - Degree of saturation effect on the static liquefaction resistance (moist tamped specimens TX3, TX4, TX5, TX6, TX7, TX9).

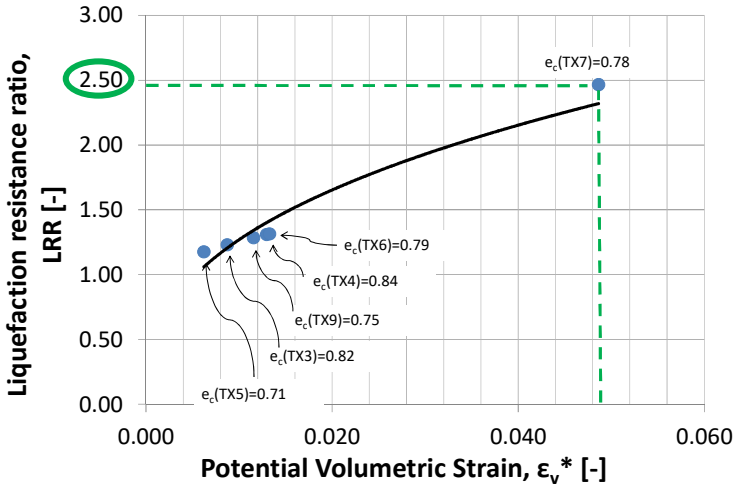

Fig. 7.30 - Degree of saturation effect on the liquefaction resistance ratio (moist tamped specimens TX3, TX4, TX5, TX6, TX7, TX9).

Again, according to He *et al.*, (2014), another equation can be used to evaluate the static liquefaction resistance at different degrees of saturation. This equation, proposed by Yang *et al.*(2004) for cyclic loading conditions, gives an exponential relationship between the liquefaction resistance and the *B*-value:

$$(CSR)_{UNS} = (CSR)_{FS} 10^{(\beta(1-B))} \tag{7-24}$$

where CSR_{UNS} is the cyclic strength stress ratio under unsaturated conditions, CSR_{FS} is the cyclic strength stress ratio under fully saturated conditions, B is the Skempton parameter and β is a parameter to be calibrated. The influence of the degree of saturation on the liquefaction resistance ratio *LLR* is given in Fig. 7.31 for moist tamped specimens.

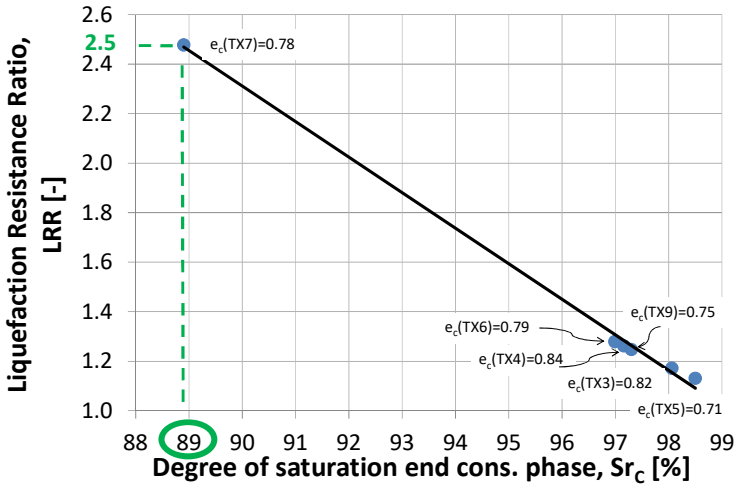

Fig. 7. 31 - Effect of degree of saturation on the liquefaction resistance ratio (moist tamped specimens TX3, TX4, TX5, TX6, TX7, TX9).

In the current research, the cyclic strength stress ratio under fully saturated conditions is

assumed equal to one and eq. 7-24 was applied by using the degree of saturation instead of the B-value. It is worth to note that the β parameter was calibrated and set equal to 3.5 in order to have a good accordance between results shown in Fig. 7.29 and Fig. 7.31. In both cases, the liquefaction resistance at degree of saturation of 89% (specimen TX7) is about 2.4 times greater than those of other moist tamped specimens.

Finally, the excess of pore pressure Δu normalized by the confinement pressure p'_C for tests TX3, TX4, TX5, TX6, TX7, TX9 with degree of saturation at the end of consolidation phase Sr_{CO} is shown in Fig. 6.32. An increasing of Δu with Sr_{CO} can be observed. Indeed a contractive behaviour at high degree of saturation is expected but, because of the undrained conditions and being undrained and very close to saturated conditions, the sample cannot contract, leading the pore pressure to increase. This increment of Δu increases when the sample is more prone contract, meaning at an higher degree of saturation.

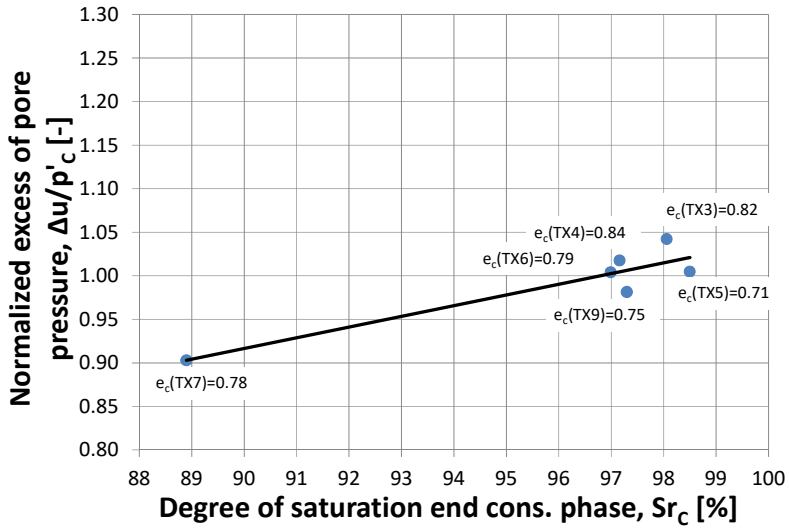

Fig. 7.32 - Degree of saturation effect on the normalized excess of pore pressure (moist tamped specimens TX3, TX4, TX5, TX6, TX7, TX9).

7.6.7 *The steady state in unsaturated conditions*

The undrained response in terms of variations of deviator stress q with the mean effective stress p' for all tests is represented in Fig. 7.33. Also in this plot, the transitional response from contractive to dilative behaviour is evident for samples TX1 and TX2. Starting from the mean effective stress imposed at consolidation phase p'_C, after reaching a peak value q_{peak}, all samples prepared by means of the moist tamped technique and compacted in five layers inside the triaxial cell show a decrease of deviator stress with the mean effective stress p' reaching a residual deviator stress q_{res} equal to 14kPa, with the only exception of sample TX7. Figure 7.33 allows to obtain the critical state envelope (*CSL*), represented by the double solid line, and so the stress ratio M at critical state can be computed. Once the stress ratio at critical state is obtained, the corresponding angle of shearing resistance ϕ_{cv} is given by:

$$M = \frac{6\sin\phi_{cv}}{3 - \sin\phi_{cv}} \rightarrow \phi_{cv} = \arcsin\left(\frac{3M}{M+6}\right) \tag{7-25}$$

The same value of stress ratio can be obtained taking into account only TX1, TX2, only TX3, TX4, TX5, TX6, TX7, TX9 or considering the entire set of tests. The resulting value of M is equal to 1.3 and this value corresponds at an angle of shearing resistance equal to 33°. The position of the peak values q_{max} have been plotted in the q-p' chart as shown in Fig. 7.33. The solid line passing through the q_{max} of liquefied samples is the Instability Line. It should be noted (Fig. 7.33) that no significant differences of q_{max} can be detected between samples TX3, TX4, TX5, TX6, TX7 and TX9. In the same way, no variations in peak deviator stress can be appreciated by considering samples TX1 and TX2.

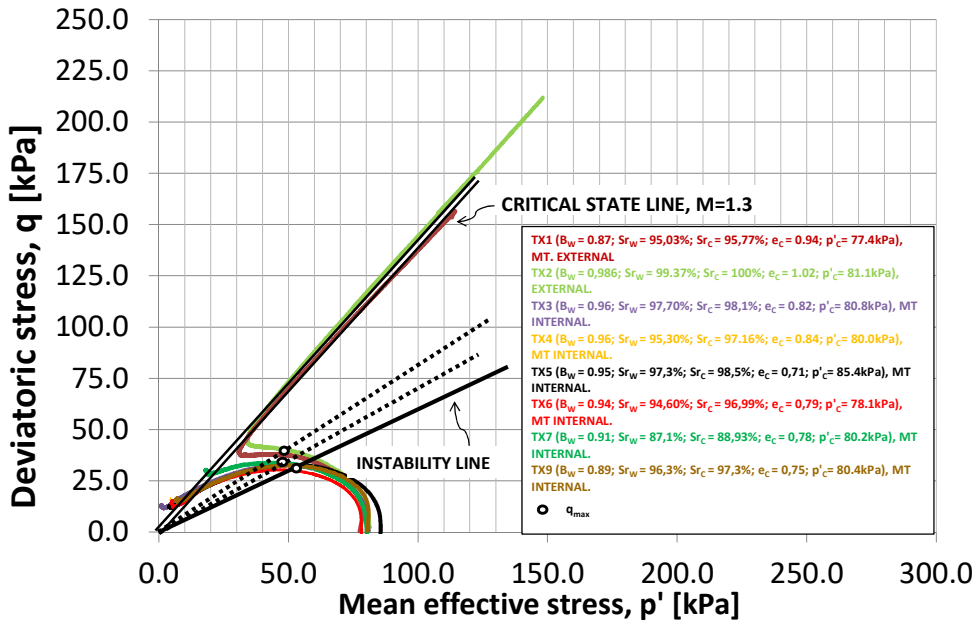

Fig. 7.33 - Undrained response: all specimens, q-p'.

A great value of q_{max} can be observed for samples that exhibit a transitional behaviour (TX1, TX2) than those of samples that show a pure softening behaviour (TX3, TX4, TX5, TX6 and TX9). The same value of q_{max} can be observed for samples that liquefy (TX3, TX4, TX5, TX6 and TX9) and for the sample that did not liquefy (TX7), all prepared by means of the same technique. The results of tests that exhibit a transitional behaviour because of a different preparation technique (TX1, TX2) or results of sample that did not liquefy (TX7) because of a different degree of saturation, show that the deviator peaks of the stress path move toward the *CSL*. According to Carrera (2008), it seems that triaxial tests that show a deviator stress peak that lies in the region between the *CSL* and the Instability Line are not or less prone to liquefy.

Similar value of stress ratio was obtained on the same silty Stava tailing by means of triaxial tests in saturated conditions (triangles: Carrera, 2008) and in unsaturated conditions (circles: current research) as shown in Fig. 7.34. The Critical State Line in q-p' plane of Stava silty tailing in saturated and unsaturated conditions is also given in Fig. 7.34. It is worth noting that in the current research all silty samples were consolidated at the same mean effective stress (p'_c = 79÷83kPa) reported by Carrera for saturated sample observed to liquefy. Furthermore, in the current research the initial void ratio e_0 at which silty samples are prepared were chosen in order to approach, at the end of consolidation phase, the same value

of e_c reported by Carrera (2008). Indeed a void ratio e_c equal to 0.83 for test 039 was obtained at the end of consolidation by Carrera (2008), while in the current work all the e_c range between 0.71 and 0.84.

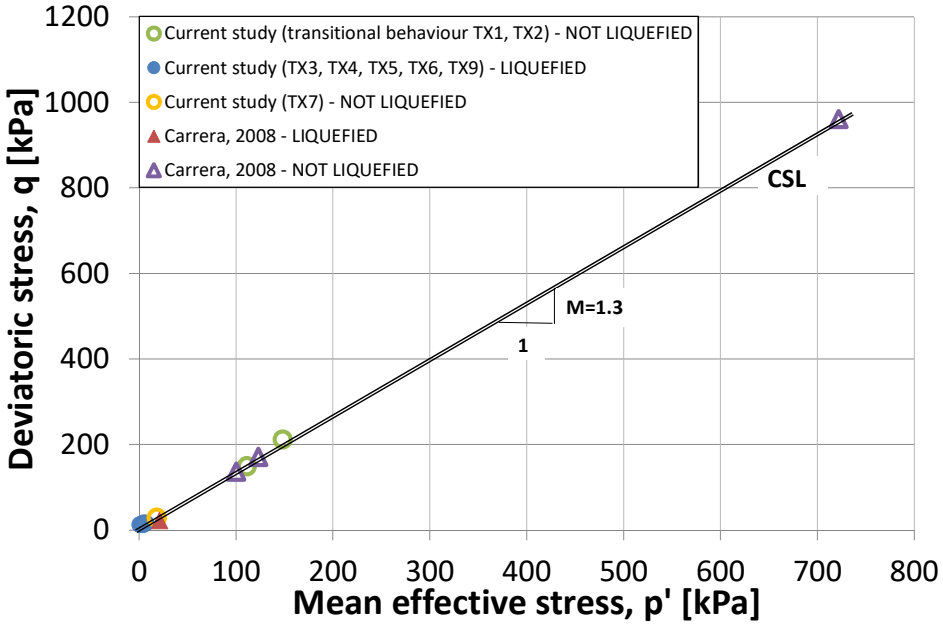

Fig. 7.34 - Saturated and unsaturated undrained response in *q-p'* plane.

According to Ishiara (1993), the residual strength S_{us} can be computed by knowledge of the residual deviator stress q_{res} and the corresponding friction angle ϕ_{cv}:

$$S_{us} = \frac{q_{res}}{2}\cos(\phi_{cv}) \tag{7-26}$$

The influence of the degree of saturation on the residual strength is given in Fig. 7.35 for moist tamped specimens.

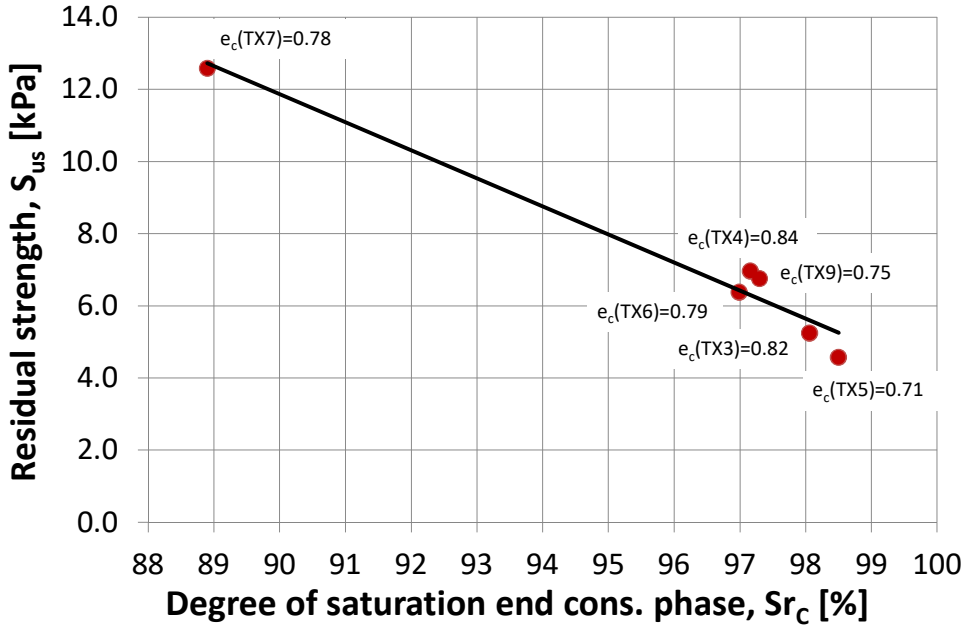

Fig. 7.35 - The effect of the degree of saturation on the residual strength (specimen TX3, TX4, TX5, TX6, TX7, TX9).

7.6.8 Relationships between B-value and degree of saturation

In the current research, a comparison between experimental and theoretical relationship of *B*-value and degree of saturation *Sr* is given in Fig. 7.36 for tailing samples TX1 and TX2.
Red and green dots represent the experimental values of the measured *B*-coefficient and their corresponding degree of saturation, respectively for TX1 and TX2, during the entire saturation phase. The continuous line represents the theoretical lower Reuss bound, while the dashed line represents the theoretical upper Voigt bound. For each sample is also given the bulk modulus *K* of the soil skeleton. It is possible to notice that lower bound curve moves at low degree of saturation with decreasing of the bulk modulus *K*. Both sets of experimental points lies with the domain made by upper Voigt and lower Reuss bounds. Furthermore, all experimental points are in good agreement with the theoretical *B*-*Sr* relationships, especially they are close to the lower Reuss bound. It worth noting that a big variation of Skempton coefficient results in a small variation of degree of saturation, i.e. in TX2 a variation from 0.5 to 1.0 in *B*-value just corresponds at a changing in degree of saturation from 96.6% to 99.3%.

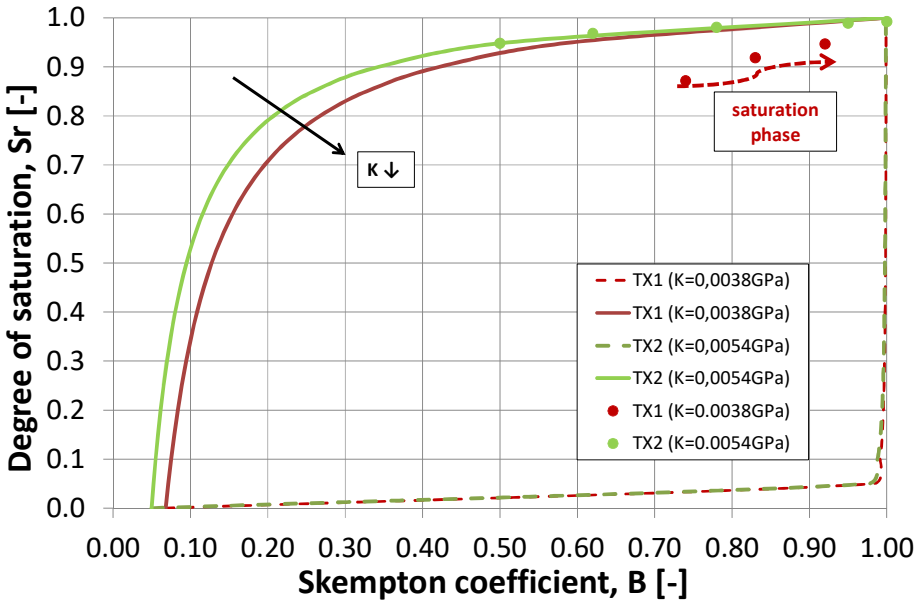

Fig. 7.36 - Comparison of experimental and theoretical relation of Skempton coefficient *B* and degree of saturation *Sr* (externally compacted specimens).

Similar results are plotted in Fig. 6.36 for samples prepared by moist tamped technique and compacted in five layers inside the triaxial cell. Again, circles represents the experimental values of the measured *B*-value and their corresponding degrees of saturation, respectively for TX2, TX3, TX4, TX5, TX6, TX7 and TX9 during the saturation phase. The continuous lines are the theoretical lower Reuss bound and dashed lines are the theoretical upper Voigt bound. Again, lower bound curve shifts at low degree of saturation with decreasing of the bulk modulus *K*. Except TX7, bulk modulus *K* of all other samples are quite similar, ranging between 0.0023GPa and 0.0029GPa, so their corresponding theoretical Reuss bounds are very closed. Only sample TX7 show a lower bulk modulus than other ones because it experienced an higher volumetric strain during saturation and consolidation phase. This is due to its initial void ratio e_0 (about 1.32), higher than other ones e_0 ranging between 1.2 and 1.25. All the experimental points lie with the domain made by upper and lower bounds. As in the previous case, experimental points are in good agreement with the theoretical *B*-*Sr* relationships, close to the lower bound. Considerable variations of *B*-value results in a small variation of *Sr*.

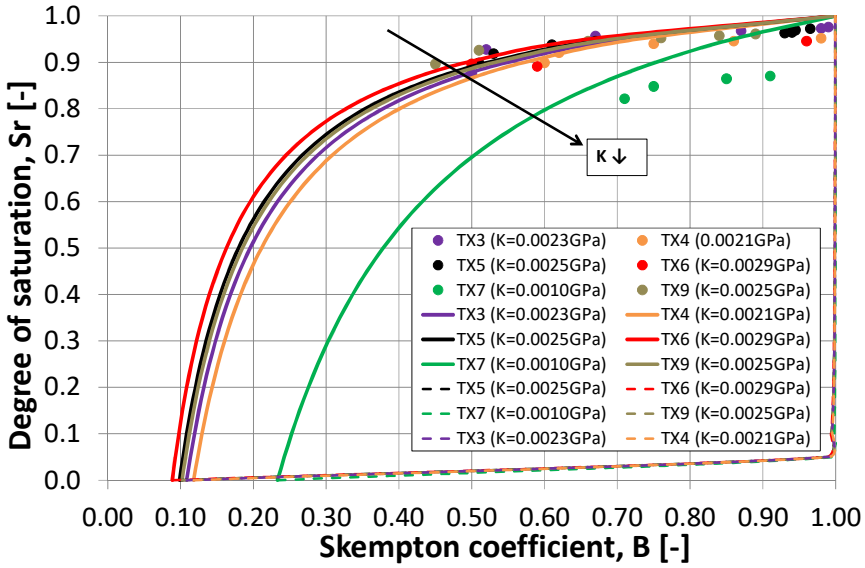

Fig. 7.37 - Comparison of experimental and theoretical relation of Skempton coefficient *B* and degree of saturation *Sr* (moist tamped specimens).

Because of good agreement between experimental and theoretical data shown in Fig. 7.36 and Fig. 7.37, the estimation of theoretical Reuss bound based on the poro-elastic parameters listed in Tab. 7.2 seems to represent a good tool aimed to predict the degree of saturation basing on the *B*-value obtained during the saturation process.
A comparison between theoretical Sr_{theo} and experimental degree of saturation Sr_{exp} (obtained during the entire saturation phase of tests performed in the current study) and literature data (Fig. 7.15) is given by Fig. 7.38. Especially for degree of saturation higher than 95%, theoretical and experimental data seem to have a good accordance.

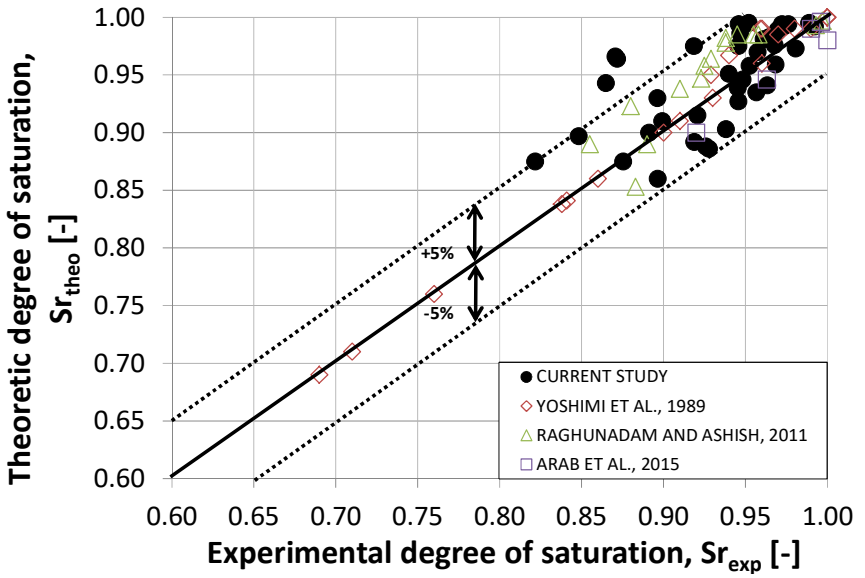

Fig. 7.38 - Comparison between experimental and theoretical degree of saturation.

A comparison between *B-Sr* experimental data and *B-Sr* theoretical relations proposed by Lade and Hernandez (eq. 7-18), together with Reuss lower bound (eq. 7-16a), is shown in Fig. 7.39 separately for sample TX1, TX2, TX3, TX4, TX5, TX6, TX7, and TX9.

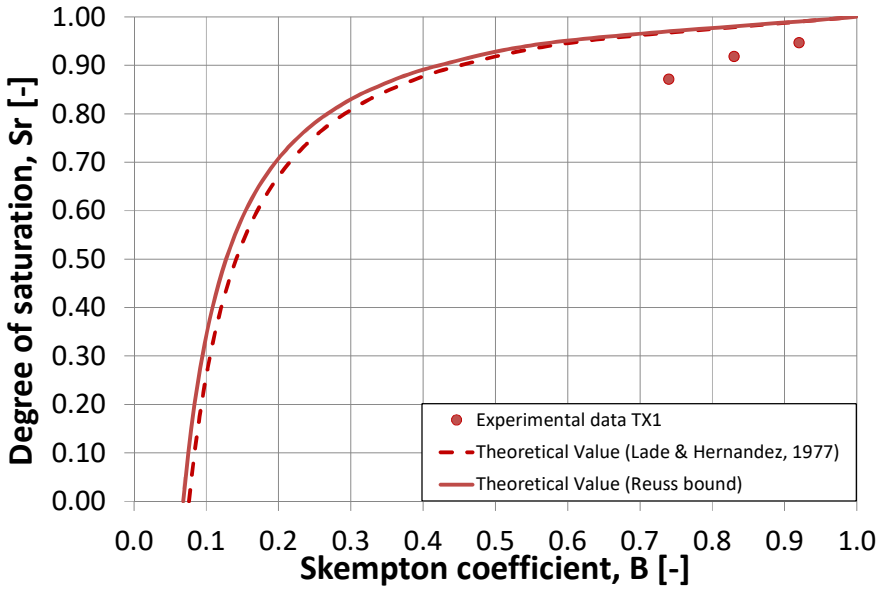

(a)

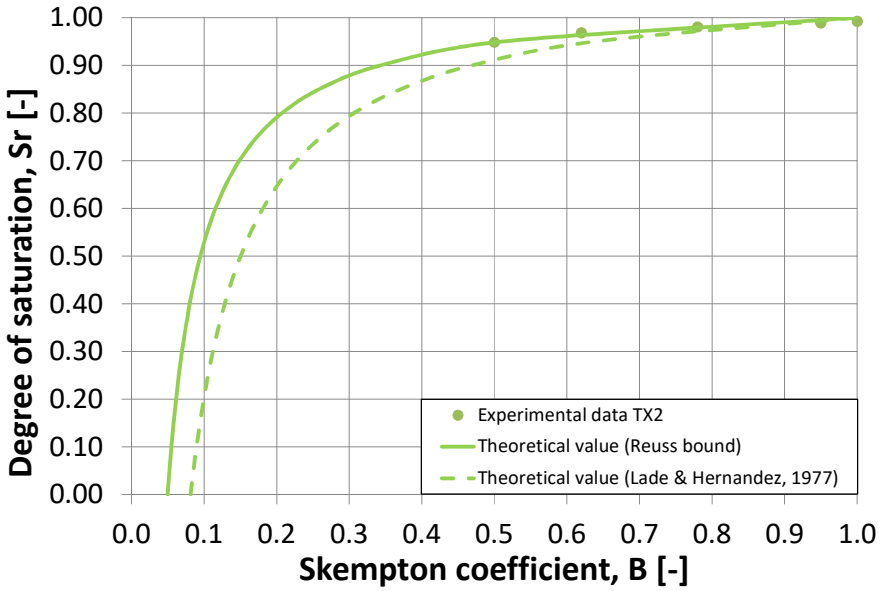

(b)

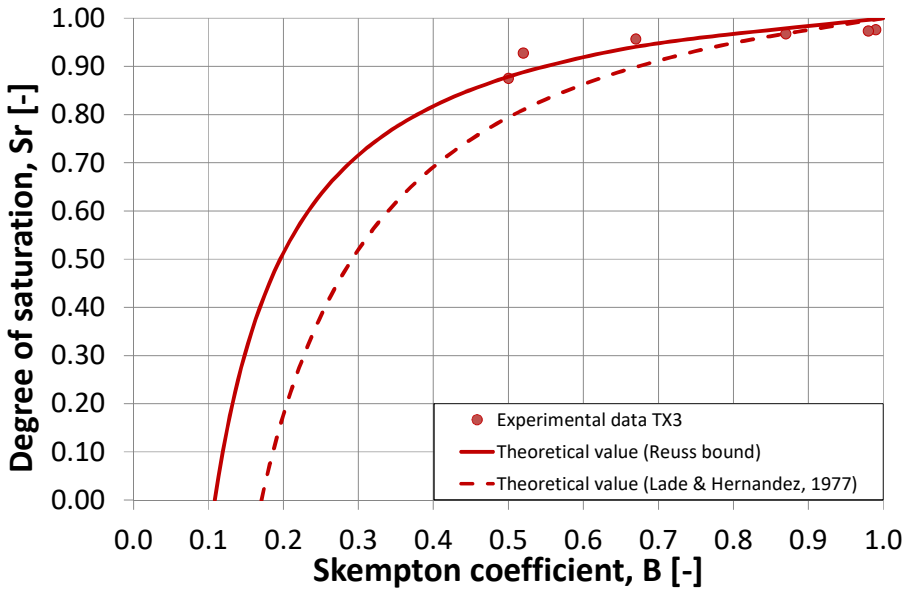
Degree of saturation, Sr [-]
1.00
0.90
0.80
0.70
0.60
0.50
0.40
0.30
0.20
0.10
0.00
0.0 0.1 0.2 0.3 0.4 0.5 0.6 0.7 0.8 0.9 1.0
Skempton coefficient, B [-]
Experimental data TX3
Theoretical value (Reuss bound)
Theoretical value (Lade & Hernandez, 1977)

(c)

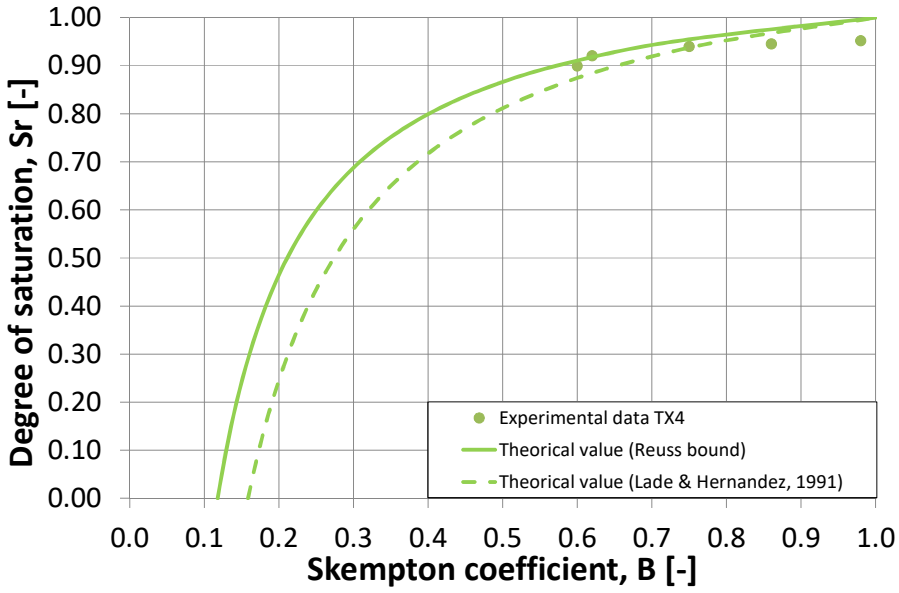
Degree of saturation, Sr [-]
1.00
0.90
0.80
0.70
0.60
0.50
0.40
0.30
0.20
0.10
0.00
0.0 0.1 0.2 0.3 0.4 0.5 0.6 0.7 0.8 0.9 1.0
Skempton coefficient, B [-]
Experimental data TX4
Theorical value (Reuss bound)
Theorical value (Lade & Hernandez, 1991)

(d)

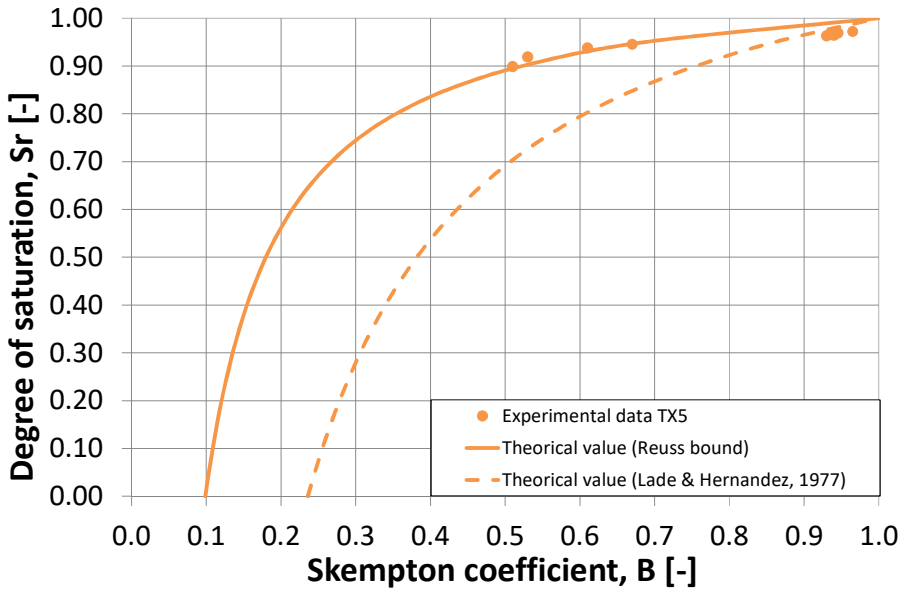
Degree of saturation, Sr [-]
1.00
0.90
0.80
0.70
0.60
0.50
0.40
0.30
0.20
0.10
0.00
0.0
0.1
0.2
0.3
0.4
0.5
0.6
0.7
0.8
0.9
1.0
Skempton coefficient, B [-]
Experimental data TX5
Theorical value (Reuss bound)
Theorical value (Lade & Hernandez, 1977)

(e)

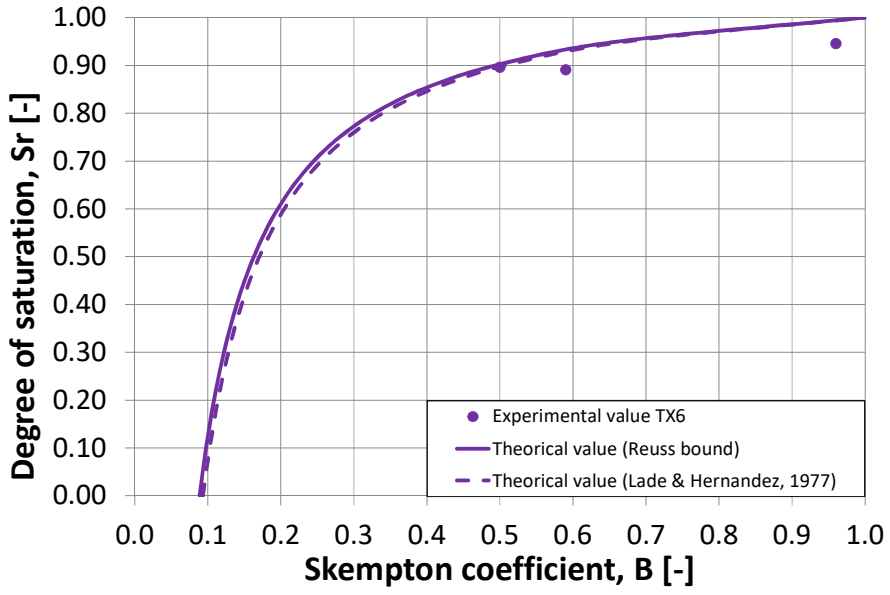
Degree of saturation, Sr [-]
1.00
0.90
0.80
0.70
0.60
0.50
0.40
0.30
0.20
0.10
0.00
0.0
0.1
0.2
0.3
0.4
0.5
0.6
0.7
0.8
0.9
1.0
Skempton coefficient, B [-]
Experimental value TX6
Theorical value (Reuss bound)
Theorical value (Lade & Hernandez, 1977)

(f)

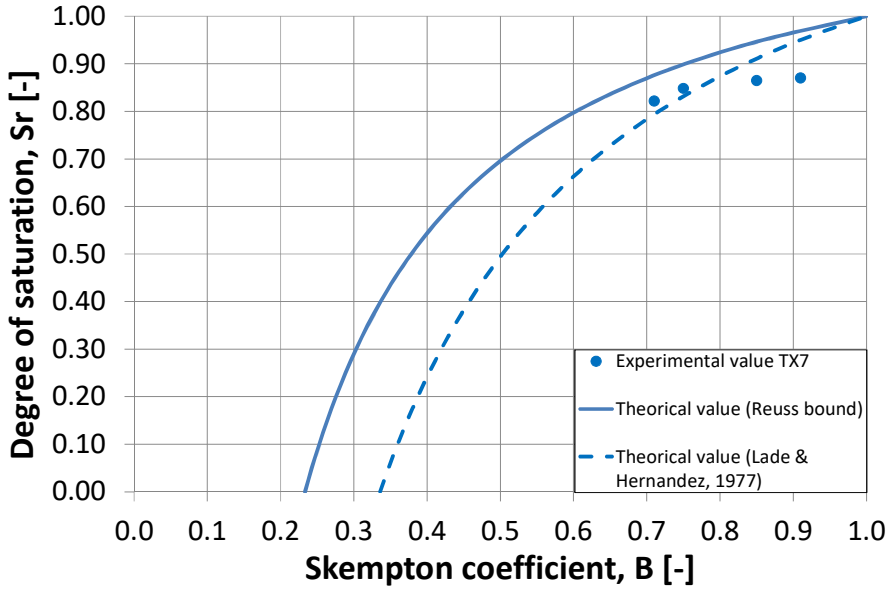

(g)

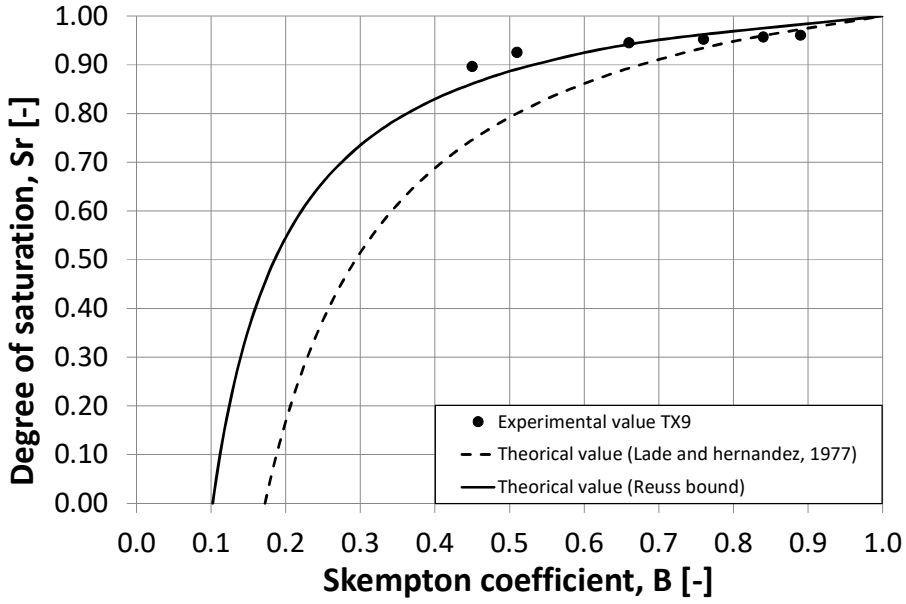

(h)

Fig. 7.39 - Comparison between *B-Sr* experimental values (dots), *B-Sr* theoretical relation proposed by Lade and Hernandez (dashed line) and Reuss bound (solid line) for externally compacted specimen: (a) TX1, (b) TX2 and moist tamped specimen (c) TX3, (d) TX4, (e) TX5, (f) TX6, (g) TX7, (h) TX9.

It is worth nothing that theoretical relationship proposed by Lade and Hernandez makes use both of bulk modulus of the soil skeleton K and the water pressure u_w. The latter one is the

water pressure reached at the last step of saturation phase. For this reasons, theoretical *B-Sr* relation proposed by Lade and Hernandez plotted in Fig. 7.39a-h should be compared just to the last experimental point of each test. It can be seen form Fig. 7.39 that, in many cases, theoretical Reuss bound is quite close to the theoretical curve proposed by Lade-Hernandez, especially for *B*-values higher than 0.6. Furthermore, all experimental points lies quite close to both theoretical relations. As previously shown for sand soils (Fig. 7.15), also for silty tailing Lade-Hernandez relation shows a small increase of degree of saturation with big variations of *B*-values (for *B*-values higher than 0.6). The estimation of *B-Sr* relation for test TX7 seems to be more precise by using Lade and Hernandez relationship instead of Reuss relationship.

The shifting with water pressure u_w of *B-Sr* relationship obtained by Lade and Hernandez equation, (i.e. test TX7) is shown in Fig. 7.40.

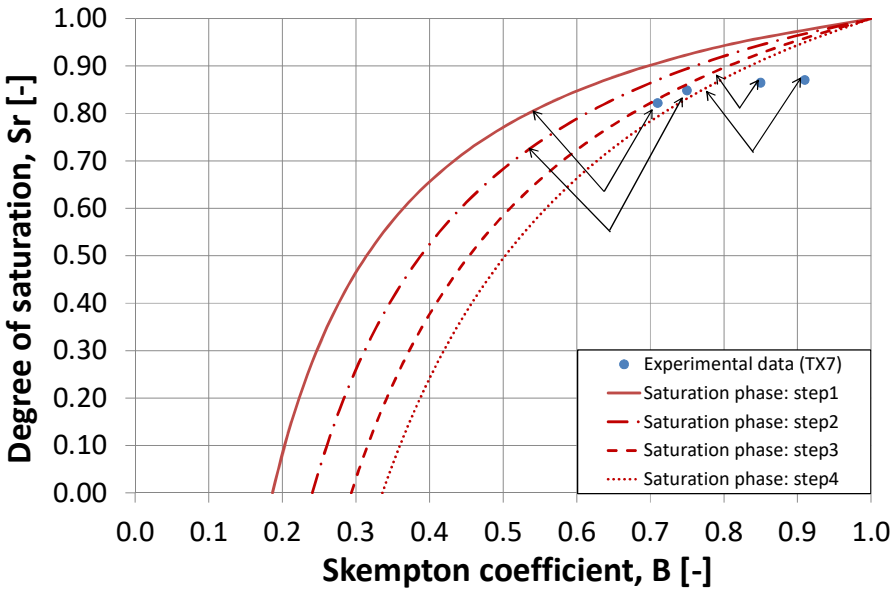

Fig. 7.40 - Theoretical relation *B-Sr* proposed by Lade and Hernandez at different water pressures at different steps during saturation phase (specimen TX7).

It can be clearly seen that the theoretical *B-Sr* curves moves at high *B*-values with increasing of water pressure. Each arrow connect the experimental point at its corresponding curve. Finally, due to the good agreement between experimental and theoretical data shown in Fig. 7.39 the estimations of Lade and Hernandez relationship or with the Reuss bound, represent good tools in order to predict the degree of saturation by knowledge of *B*-parameter.

7.6.9 Relationships between compression index and suction of unsaturated triaxial specimens

According to the water retention curve estimated by Gallipoli model (chapter 5), knowledge of void ratio and degree of saturation at the end of the consolidation phase allowed to estimate the corresponding suction of the sample. The compression lines in isotropic conditions during the consolidation phase allowed to compute the compression index at different suction levels.
Because of the initial loose state of the sample, the preconsolidation stress was supposed to be very low, so the isotropic compression occurred along the normal compression line. The compression index was obtained as:

$$\lambda(s=0) = -\frac{dv}{\ln\left(\frac{p'_B}{p'_A}\right)} \tag{7-27}$$

where *de* is the variation of void ratio, while p'_A and p'_B are the mean effective stresses between two reference states *A* and *B*.
The compression index of unsaturated specimens could be also obtained with the model proposed by Alonso *et al*. (1990) that was intended for unsaturated sands, clayey sand, sandy clays, low plasticity clays or silts as the soil tested in the current investigation. The Barcelona Basic Model gives an analytical expression describing the decreasing in soil stiffness (related to the compression index) with decreasing of suction:

$$\lambda(s) = b + d \cdot \ln(s) \tag{7-28}$$

or:

$$\lambda(s) = \lambda(0)\left[(1-r)e^{(-\beta s)+r}\right] \tag{7-29}$$

where *b*, *d* are constants, while in eq. 6-23b the term β is a parameter governing the rate of increase of soil stiffness with suction level and the constant *r* is related to the maximum stiffness of the soil:

$$r = \frac{\lambda(s \to \infty)}{\lambda(0)} \tag{7-30}$$

Within the investigated small suction range (given in Tab. 7.3), *b* and *d* parameters were obtained, by fitting eq. 7-28 to two data sets: TX1-TX2 (compacted specimens) and TX3÷TX9 (moist tamped specimens), respectively, $b = 0.084$, $d = -0.009$ and $b = 0.207$, $d = -0.144$.

Details in terms of suction *s*, void ratio e_C at the end of the consolidation phase and the compression index λ, of unsaturated triaxial samples tested in the current section are given in Tab. 7.3.

Tab. 7.3 - Estimated suction, void ratio and compression index of unsaturated triaxial samples TX1÷TX9.

Sample	s [kPa]	e_C [-]	λ(s) [-]
TX1	0.05 ÷ 1.0	0.94	0.09
TX2	~ 0.0	1.02	0.11
TX3	0.05 ÷ 1.0	0.82	0.29
TX4	0.05 ÷ 1.0	0.84	0.26
TX5	0.1 ÷ 0.5	0.71	0.42
TX6	0.2 ÷ 2.0	0.79	0.15
TX7	0.5 ÷ 5.0	0.78	0.41
TX8	-	-	-
TX9	0.2 ÷ 2.0	0.75	0.26

By analysing samples prepared with the same technique (sample TX1-TX2 and sample TX3÷TX9, Tab. 7.3), because of very similar saturation conditions, similar values of the compression index between samples TX1-TX2 and samples TX3-TX9 were expected. As can be observed in Tab. 7.3, in general terms this was obtained, except for sample TX5 and TX7. Indeed, compression index of sample TX5 and TX7 is higher than others and this it is supposed to be due to some in-homogeneities is their soil fabric.

7.7 SUMMARY AND FINAL CONSIDERATIONS

The high rate failures of tailing dams clearly demonstrates that a proper knowledge of static liquefaction resistance of tailing in unsaturated conditions is fundamental, not only for the coarser fraction but also for the finer grading, such as silt. For these reason, static liquefaction resistance of Stava silty tailings in unsaturated conditions or very close to saturated conditions was studied by performing triaxial tests with strain controlled shearing phase performed in undrained conditions. The moist tamped technique was widely adopted as the preparation method in order to better simulate the deposition technique within the basin. Also for tailings, the influence of preparation technique revealed to be an essential factor influencing the mechanical response. Furthermore, experimental results on Stava tailing clearly shown that degree of saturation is a key factor influencing the static liquefaction response, likely more important than the void ratio. Therefore, all samples saturated at *Sr* higher than 90%, independently from their (high) void ratio comprised between 0.71 and 0.84, liquefied. Hence, a limit value of about 90% of degree of saturation seems to represent a border between a state where static liquefaction can easily occur and a safe condition. For these reasons, a great care should be paid in order to avoid any factors leading to have a fast increase of phreatic level (degree of saturation and so *B*-value in laboratory testing) due to excessive rainfall/snowmelt or improper drainage, or a decrease of confinement within the dam (low density/high void ratio in laboratory testing) due to erosion phenomena. Hence, countermeasures aimed to avoid these phenomena (i.e. drainages or management) reveal to be fundamental for the stability of any tailing dam. Finally, in the current work, experimental results in terms of *B*-value and degree of saturation seems to be in good agreement with some theoretical *B*-*Sr* relationships that can be used as a predictive tool to estimate the degree of saturation reached during the saturation phase, especially for *B*-value higher than 0.6.

REFERENCES

1. Alonso E., Gens A. and Josa A. 1990. A constitutive model for partially saturated soils . Geotechnique **40** (3), 405–430.

2. Arab A., Belkhatir M. and Sadek M. 2015. Saturation Effect on Behaviour of Sandy Soil Under Monotonic and Cyclic Loading: A Laboratory Investigation, Geotechnical and Geological Engineering, Volume 34, Issue 1, pp 347–358.

3. Atigh E., Byrne P.M. 2004. Liquefaction flow of submarine slopes under partially undrained conditions: an effective stress approach. Can. Geotech. J. 41:154–165.

4. Been K. and Jefferies M.G. 1985. A state parameter for sands. Geotechnique, Vol. 35, No.2, pp. 99-112.

5. Bishop A.W. 1973. The influence of an undrained change in stress on the pore-pressure in porous media of low compressibility. Geotechnique. 23(3): 435-442.

6. Bouferra R. 2000. Etude en laboratoire de la liquefaction des sols, These de doctorat, Ecole Universitaire des Inge´nieurs de Lille USTLille, pp. 95-111.

7. Bouferra R. and Shahrour I. 2004. Influence of fines on the resistance to liquefaction of a clayey sand. Ground improvement, Vol. 8, No. 1, pp. 1-5.

8. Bouferra R., Benseddiq N. and Shahrour I. 2007. Saturation preloading effects on the cyclic behaviour of sand. Int. J. Geomech. 7(5):396–401.

9. Carrera A. 2008. Mechanical behaviour of Stava tailings. Ph.D. thesis, Politecnico di Torino.

10. Carrera A., Coop M. and Lancellotta R. 2011. Influence of grading on the mechanical behaviour of Stava tailings. Geotechnique, Vol. 61(11), pp. 935-946.

11. Chu J., Leong W.K. and Loke W.L. 2003. Discussion of “defining an appropriate steady state line for Marriespruit gold tailings”. Canadian Geotechnical Journal, Vol. 40, pp. 484-486.

12. Della N. 2010. Laboratory testing of the Monotonic behavior of partially saturated sandy soil. Earth Sci. Res. S J. Vol. 14,No. 2: 181-186.

13. Grozic J.L., Robertson P.K. and Morgenstern N.R. 1999. The behaviour of loose gassy sand. Can. Geotech. J. 36 (3), 482-492.

14. Grozic J.L., Nadim F. and Kvalstad T.J. 2005. On the undrained shear strength of gassy clays. Comput. Geotech. 32(7), 483-490. Robertson P.K., Morgenstern N.R. 1999. The behaviour of loose gassy sand. Can. Geotech. J. 36 (3), 482-492.

15. He J., Chu J. and Liu H. 2014. Undrained shear strength of desaturated loose sand under monotonic shearing. Soils and Foundations 54(4): 910-916.

16. Hossain A., Ronald D.A and Camp W. 2013. Correcting Liquefaction Resistance of Unsaturated Soil Using Wave Velocity, J. Geotech. Geoenviron. Eng., 2013, 139(2): 277-287.

17. Ishihara K. 1993. Liquefaction and flow failures during earthquakes. Geotechnique 43(3), 351-415.

18. Ishihara K. 1996. Soil Behaviour in Earthquake Geotechnics. Oxford University Press.

19. Ishihara K., Tsuchiya H., Huang Y., and Kamada K. 2001. Recent studies on liquefaction resistance of sand: effect of saturation. Proc., 4th Int. Conf. on Recent Advances in Geotech. Earthquake Engineering and Soil Dynamics, S. Prakash, ed., Missouri Univ. of Science and Technology, Rolla, MO.

20. Ishihara K., Tsukamoto Y. and Kamada K. 2004. Undrained behavior of near-saturated sand in cyclic and monotonic loading. In: Proceedings of conference, cyclic behavior of soils and liquefaction phenomena, 27–39.

21. Kokusho T (2000) Correlation of pore pressure B-value with p-wave velocity and poisson's ratio imperfectly saturated sand or gravel. Soils Foud. 40(4):95–102.

22. Kramer S.L. and Seed H.B. 1988. Initiation of soil liquefaction under static loading conditions. Journal of Geotechnical Engineering. 114(4):412-430.

23. Kuerbis R., Negussey D. and Vaid Y.P. 1988. Effect of gradation and fines content on the undrained response of sand. In Hydraulic fill structures. Edited by D.J.A. Van Zyl and S.G. Vick. Geotechnical Special Publication 21, American Society of Civil Engineers, New York, pp. 330–345.

24. Lade P.V. and Hernandez S.B. 1977. Membrane penetration effects in undrained tests. J. Geotech. Eng. Div. 103:109–125.

25. Lade P.V. and Yamamuro J.A. 1997. Effects of non-plastic fines on static liquefaction of sands. Canadian Geotechnical Journal, Vol. 34, pp. 918-928.

26. Martin G.R., Finn W.D.L. and Seed H.D. 1978. Effects of system compliance on liquefaction tests. J Geotech Eng Div 104(4):463–479.

27. Mathiroban S. and Grozic J. 2004. A model to predict the undrained behaviour of loose gassy sand. In: Proceedings of 57th Geotechnical conference, session 6G, 16–22.

28. Mullilis J.P., Townsend F.C. and Horz R.C. 1978. Triaxial testing techniques and sand liquefaction. ASTM STP 654 Dyn. Geotech. Test, pp. 265-279.

29. Okamura M. and Soga Y. 2006. Effects of pore fluid compressibility on liquefaction resistance of partially saturated sand. Soils Found. 46(5), pp. 695-700.

30. Pietruszczak S., Pande G. and Oulapour M. 2003. A hypothesis for mitigation of risk of liquefaction. Geotechnique 53(9): 833–838.

31. Pitman T.D., Robertson P.K. and Sego D.C. 1994. Influence of fines on the collapse of loose sands. Canadian Geotechnical Journal, Vol. 31, pp. 728-739.

32. Raghunadan M.E. and Ashish J. 2011. A study on the liquefaction resistance and dynamic properties of De-saturated sand. EJGE 16:109–122.

33. Reuss A. 1929. Berechnung der Fließgrenze von Mischkristallen auf Grund der Plastizit¨atsbedingung f¨ur Einkristalle. Z. Angew. Math. Mech., 9, pp. 49–58.

34. Robertson P.K., and Campanella R.G. 1985. Liquefaction potential of sands using the cpt. ASCE Journal of Geotechnical Engineering, 111(3): 384–403.

35. Seed H.B., Idriss I.M., and Arango I. 1983. Evaluation of liquefaction potential using field performance data. ASCE Journal of Geotechnical Engineering, 109(3): 458–482.

36. Shen C.K., Vrymoed J.L. and Uyeno C.K. 1977. The effects of fines on liquefaction of Sands. Proceedings of the Ninth International Conference on Soil Mech. and Found. Eng., Tokyo, Japan, Vol. 2, pp. 381-385.

37. Sherif A.M., Tsuchiya C. and Ishibashi I. 1977. Saturation effects on initial soil liquefaction. J. Geotech. Eng. Div. 103(8): pp. 914–917.

38. Skempton A. W. 1954. The pore pressure coefficients A and B. Geotechnique 4, No. 4, pp. 143–147.

39. Sladen J.A., D'Hollander R.D., Krahn J., 1985. The liquefaction of sands: a collapse surface approach. Canadian Geotechnical Journal, Vol. 22, pp. 564-578.

40. Tokimatsu K., and Yoshimi Y. 1983. Empirical correlation of soil liquefaction based on spt n-value and fines content. Soils and Foundations, 23(4): 57–74.

41. Troncoso J.H. and Verdugo R. 1985. Silt content and dynamic behavior of tailing sands. Proceedings of the 11th International Conference on Soil Mech. and Found. Eng., San Francisco, USA, Vol. 3, pp.1311-1314.

42. Vaid Y.P. and Sivathayalan S. 2007. Fundamental factors affecting liquefaction susceptibility of sands. Canadian Geotechnical Journal, Vol. 37, pp. 592-606.

43. Xia H. and Hu T. 1991. Effects of saturation and back pressure on sand liquefaction. J Geotech. Eng. 117(9):1347–1362.

44. Yamamuro J.A. and Lade P.L. 1997. Static liquefaction of very loose sands. Canadian Geotechnical Journal, Vol. 34, pp. 905-917.

45. Yang J. and Sato T. 2001. Analytical study of saturation effects on seismic vertical amplification of a soil layer. Geotechnique 51(2): pp. 161–165.

46. Yang J. 2002. Liquefaction resistance of sand in relation to P-wave velocity. Geotechnique 52(4): pp. 295–298.

47. Yang J., Savidis S. and Roemer M. 2004. Evaluating liquefaction strength of partially saturated sand. J Geotech. Geoenviron. Eng. ASCE 130(9): pp. 975–979.

48. Yang Z.X., Li X.S., Yang J. 2008. Quantifying and modelling fabric anisotropy of granular soils. Gèotechnique, Vol. 58, No. 4, pp. 237-248.

49. Yoshimi Y., Tanaka K., Tokimatsu K. 1989. Liquefaction resistance of partially saturated sand. Soils Found 29(3): pp.157–162.

Conclusions and future developments

The stability of tailings dams should be considered as one of the most relevant problem to guarantee the human safety and the efficiency of storage systems. The hydraulical behaviour of tailings in unsaturated conditions, especially above the phreatic surface at shallow depth in the vadose zone, affects the stability of tailings storage facilities in terms of mechanical strength. Shear strength is affected by changes of suction, so an accuracy in predicting the water retention behaviour is needed for a rigorous stability analysis of tailing dams. Indeed, a deep knowledge of the water retention behaviour is required for many practical applications, first of all in modelling the strength of tailings materials (i.e. shear strength), hydrological process (i.e. infiltration phenomena) together with problems related to in situ leaching installations, settlements around and in tailings ponds and the design of covers to limit the generation of acid leachate from sulfidic minerals during the design phases of tailings dams or during their long operation life. Furthermore, the heterogeneity of tailings and tailing dams claims for a detailed investigation of the dependency of the hydro-mechanical behaviour of soil on initial density and grain size distribution that can be studied by testing samples of different grading and void ratios, corresponding at different cross sections inside the basin. For these reasons, in the current research, an hydro-mechanical study of Stava tailings has been carried out in unsaturated conditions. All the water retention tests (chapter 5), the oedometer tests (chapter 6), the suction controlled triaxial tests (chapter 6) and the triaxial tests (chapter 7) were performed at Politecnico di Torino, Italy. Physical, chemical and mineralogical analysis (chapter 4) were performed at Centro de Desenvolvimento da Tecnologia Nuclear, in Belo Horizonte (Brazil). The proposed gamma ray, treatment aimed to simulate the ionizing radiations on the surface of unsaturated and saturated tailings, has been developed and carried out at Centro de Desenvolvimento da Tecnologia Nuclear.

An hydro-mechanical characterization of Stava tailings performed by Carrera (2008) represented the starting point of the current research. The soils investigated in this thesis are the same studied by Carrera (2008) in saturated conditions. Soil samples come from the lower portion of the upper Stava tailing dam collapsed in 1985, aimed to store the mineral wastes from the fluorite extraction. The particle size distribution gave two grading, a silt with a low content of clay and a fine sand. The embankment of Stava dams were mainly realized with the coarse fraction with a fine content ranging between 20% and 40%. Because of the deposition technique, the rest of the facility had a grading that become more silty from the embankment toward the decant pond. The failure of the dam caused a mixing of the two fractions, so they were separated in order to investigate their geotechnical behaviour. As for many tailings, also in this case, the silt fraction was generated by the crushing work of men, and thus it is constituted by minerals typical of sands rather than natural silts or clays, as it

has been revealed by the mineralogical analysis. Plasticity index, activity index and cohesion showed very little values.

After summarizing the main long-term processes acting on tailing materials, chapter 4 introduces the natural ionizing radiation from some radioactive isotopes of the soils, cosmic rays and ultraviolet rays from the sun, as an additional long-term process affecting tailing materials. A new gamma ray treatment was developed and proposed to simulate the ionizing radiations on the surface of tailing deposits, or in the tailing brick faces used for buildings or other economical purposes. Seventy years of low photon energy UV-rays exposition were simulated by seven days of high photon energy gamma-rays exposition. The long-term physical and chemical modifications could affect the hydraulic and mechanical behaviour of tailings with relevant economic consequences, so the grain size distribution was obtained by laser technique before and after the treatment in dry or wet conditions. True density determination, X-rays fluorescence, X-rays diffraction, energy x-rays spectroscopy, digital images analysis, surface determination and infrared spectroscopy technique tests were performed, before and after this ionizing treatment. From the chemical point of view, the current research demonstrated that Stava tailings have a certain stability. Adsorption tests revealed that the specific surface area of dry and wet irradiated specimen is 5.6% and 10% higher than those of not irradiated specimen. An increase of inner porosity for dry and wet irradiated samples was observed, while the true density didn't show any relevant changes in all three cases. X-ray fluorescence analysis exhibit little changes of metal concentration before and after treatments. In terms of metal composition, no modifications occur due to gamma-ray irradiation ageing test. An high concentration of fluorine, calcium and silicon was obtained from XRD analyses and confirmed by SEM analysis. If not irradiated sample's FTIR spectra and dry irradiated sample's spectra were compared, it was possible to observe the presence of new little peaks probably connected to the presence of weddellite and some new chemical bonds such as C-H (or C-H_3), and Si-Al-O. Also from the physical point of view, little changes were observed. A very small increase of silty fractions was observed, both after dry irradiation and after wet irradiation. No changes seemed to be evident if gamma ray treatment was carried out on dry or wet tailing samples. These results provided a good support to data obtained by laser particle analyser.
The small chemical variations are expected not to have any relevant consequences on the hydro-mechanical behaviour of the investigated soils. Indeed, the entity of variations experienced in grain size distributions and specific surface cannot influence the water retention curve, without appreciable consequences on the water retention and mechanical behaviour. It is worth to note that tested soils before gamma irradiation was exposed to natural solar radiations for twenty years before being collected in 2005. So it could have been undergo at chemical/physical modifications due to natural exposure at solar radiation prior its storage in 2005 and its analysing in 2016. These possible initial modifications could make the soil grains more stable, giving a justification about little chemical-physical variations before and after the gamma ray treatment. This investigation is aimed to give a starting point for a characterization method applicable to natural or wastes materials that can be re-used after their storage. Relevant changing in grain size distribution, specific surface and chemical composition due to ageing process, could affect the re-usage of these materials for economical purposes. It is observed that wet irradiation was performed in pure water to simplify the experimental program. In the site, tailings are mixed with water which contains heavy metals, contaminants, dissolved salts and residual chemicals from the mineralogical processes. So, in order to improve the affinity with the real environment, further wet irradiations tests could be carried out by using processing water. Additional tests can also be performed by increasing the photon energy emitted by gamma rays, in order to simulate a greater ionizing exposure period both on dry and wet specimens, or sandy-silty mixtures could be tested in order to take into account the heterogeneity of in situ tailings.

The hydraulic behavior of unsaturated tailings mixtures was studied in chapter 5 by means of water retention tests. The effects of grain size distribution and void ratio on Stava tailings were investigated in terms of water retention curve and expected pore size distribution by means of a campaign of suction controlled oedometer tests. The experimental results obtained in terms of water retention curve from a limited number of sample at different initial void ratio are then extended by means of the Gallipoli model in order to extend the hydraulic characterization to a larger domain of void ratio and to allow implementation in numerical modelling. Both variations in void ratio and grain size distribution have been demonstrated to affect main drying and wetting curves, and so the whole hydraulic behavior of tailings, with possible consequences in terms of shear strength. Due to the in-situ heterogeneity of tailing materials within the storage facility, the experimental results obtained from water retention tests represents different depth and vertical cross sections of the basin, and could be used in numerical modelling to better approach stability problems, allowing reliable predictions.

The hydro-mechanical behavior of unsaturated silt tailings was analysed in chapter 6 by means of suction controlled triaxial tests and 1D compression tests on unsaturated silt specimens. Aimed at investigating the dependency of preconsolidation stress and stiffness on suction, a campaign of 1D compression tests was performed on silt specimens in unsaturated conditions. Within the suction and stress interval investigated, the estimated preconsolidation stresses increased with suction. In a similar way, the stiffness of specimens shown an increase with suction.
An extensive campaign of suction-controlled triaxial tests was aimed to complete the water retention characterization and to study the hydro-mechanical response of the silt tailing in unsaturated conditions. After the consolidation phase at different net stresses, the shearing phase was performed at constant water content or at constant suction, in order to reach the Critical State and define a Critical State Line also in unsaturated conditions. A critical state condition was reached for almost the samples. The critical state was approached both from drying side and, in some cases, from the wetting side. Despite several trials, no tests have been successfully performed on very loose sample (initial void ratio higher than 0.80), due to experimental difficulties. These tests would provide additional data regarding an approach of the critical state from the wetting side. At these conditions of very low density, all the unsaturated triaxial silt samples collapsed because of the weight of the top cap and the load cell during the assemblage operations of the cell or during the suction equalization phase.
A possible interpretation of the hydro-mechanical behaviour by means of the water retention curve has been proposed. The water retention curve seems to play a relevant role in the mechanical response, acting as a domain. Indeed, the hydro-mechanical behaviour obtained from the suction controlled triaxial test in terms of s-Sr or s-e_w lies inside the two dimensional domain of the *WRC*. Then, the *CSL* in unsaturated conditions was compared with those obtained for the same soil tested by Carrera (2008) under saturated conditions. The two set of experimental data, in saturated and unsaturated conditions, are quite aligned, so a unique critical state line has been found. Also in the compressive plan, the Critical State Line for unsaturated samples is close to the Critical State Line for saturated samples. The model proposed by Gallipoli was successfully used to obtained the theorical void ratio at critical state in unsaturated conditions: theorical values are quite close to the experimental ones. Additional suction controlled triaxial tests could be performed at higher stress level in order to extend more the Critical State Line.

Because of the importance of the static liquefaction phenomenon with reference to tailing storage facilities in terms of collapses or stability problems, a deep knowledge of static liquefaction resistance of tailing in unsaturated conditions is essential, not only for the coarser fraction, but also for the finer grading, such as silt. The static liquefaction resistance

of Stava silt tailings, in unsaturated conditions or very close to saturated conditions, was investigated in chapter 7 by performing triaxial tests with undrained shearing in strain controlled conditions. This last experimental campaign was aimed at investigate the occurrence of the static liquefaction depending from three variables: the degree of saturation, the void ratio and the preparation technique. Also for tailings, the influence of preparation technique has been demonstrated to be an essential factor influencing the mechanical response. Even if looser, externally compacted specimens showed a strain-hardening behaviour differently from the denser moist tamped samples which exhibited a strain-softening behaviour. Furthermore, experimental results clearly shown that the degree of saturation is a fundamental factor influencing the static liquefaction response, probably more important than the void ratio. All samples saturated at *Sr* higher than 90%, independently from their void ratio, comprised between 0.71 and 0.84, liquefied. So, a limit value of about 90% of degree of saturation seems to represent a border value between a state where static liquefaction can easily occur, and safe conditions. This is the reason why, during the design phases and monitoring operations of tailings dams, a great care should be paid to avoid any factors leading to have a fast increase of the phreatic level due to excessive rainfall/snowmelt/improper drainage, or a decrease of confinement within the embankment due to erosion phenomena.

Finally, as demonstrated in the current research, the study of the hydraulical and mechanical properties of tailings and tailings dams in unsaturated conditions requires the use of several non-standard, sophisticated equipments and time-consuming experimental methodologies. Despite this, it is a substantial tool for assuring reliable predictions of the behaviour and stability of tailing dams.

Appendix

This appendix is aimed to give more details about some aspect of the chemical/physical characterization exposed in chapter 4.2 performed on Stava silty sample by means of gamma radiations bombardment carried out at Centro de Desenvolvimento da Tecnologia Nuclear in Belo Horizonte (Brazil). The long-term processes acting on tailing materials are firstly summarized. The sample preparation technique and some details about the gamma ray treatment performed in this research are exposed. Basic principles and sample preparation technique for each chemical/physical test are shown.

8.1 GAMMA RAY TREATMENT

8.1.1 Basic concepts of gamma-ray ray irradiation

Gamma rays are electromagnetic radiations having high energy, upper than 100keV, with short wavelength (10^{-12} m) and high frequency (10^{20}Hz). They are produced from naturally or artificial occurring radioactive isotopes and also by astronomical processes. Gamma rays (photons) don't involve moving of matter but only energy. When gamma radiation having intensity I_0 is incident on an absorber, the transmitted gamma ray intensity I follows the exponential Lambert-Beer equation:

$$I = I_0 \mathrm{e}^{-(\mu_l L)} \tag{8-1}$$

where μ_l is the linear attenuation coefficient (cm^{-1}) and L is the thickness of the absorber. Gamma rays interact with matter in three ways: photoelectric effect, Compton scattering or pair production (Fig. 8.1).

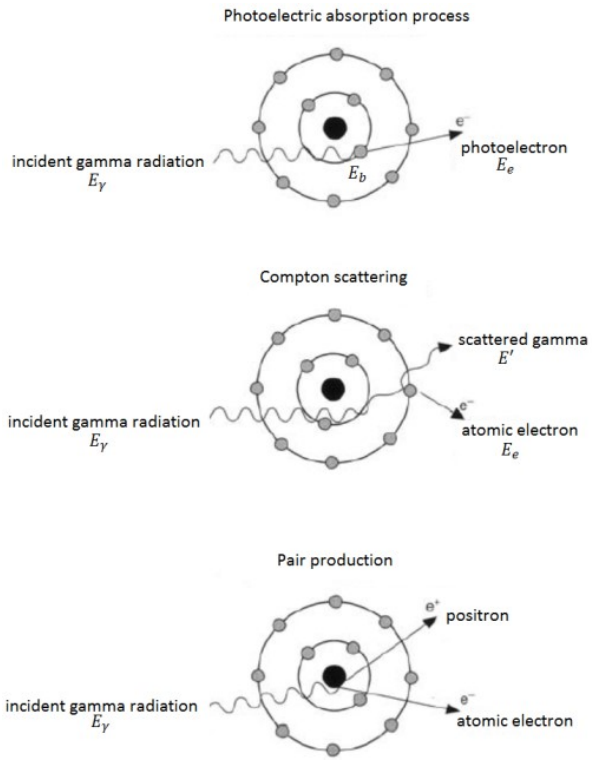

Fig. 8.1 - Gamma-rays interactions with matter (Gilmore, 2008).

In photoelectric absorption, the incident gamma photon can interact with a bound electron by losing all its energy in one interaction and ceasing to exist as gamma-ray. An electron is therefore emitted from the atom (ionization process) and then it moves through matter and loses its energy by excitation and ionization or Bremstrahlung. Some of the energy E_γ of the incident gamma-ray is used to overcome the electron binding energy E_b, a huge quantity of the remainder energy is given to the free electron in terms of kinetic energy E_e, while a small amount remains with the atom:

$$E_e = E_\gamma - E_b \tag{8-2}$$

The probability of photoelectric effect depends on the gamma ray energy E_γ, the electron binding energy and the atomic number Z of the atom

Compton scattering is a process where the gamma-ray interacts with a free or weakly bounded atomic electron, causing an increase in the energy of the freed electron, while a new gamma-ray (photon) with a smaller energy is then emitted. The electron interacts as in photoelectric absorption and becomes a free electron with kinetic energy E_e equal to the difference of the energy E_γ lost by incident gamma-ray and the electron binding energy E_b (eq. 8-3). Because E_b is very small if compared with E_γ, the kinetic energy of the atomic electron is very close to the energy of the incident gamma-ray:

$$E_e = E_\gamma - E' \tag{8-3}$$

where E' is the transferred to the electron during the interaction. The new gamma-ray can escape from the matter or can be absorbed through the photoelectric effect. The directions θ

of the freed electron and the scattered photon depend on the amount of energy transferred to the electron during the interaction.
If pair production effect occurs, high-energy gamma-rays having at least photon energy of 1.022MeV are absorbed and two particles are created: an electron and a positron. This type of effect has a threshold of 1.022MeV because that is the minimum energy required to create a positron and an electron. If gamma radiation has an energy higher than 1.022MeV the excess of energy is shared as kinetic energy between the positron and electron:

$$E_\gamma = 1.02\text{MeV} + E_{electron} + E_{positron} \tag{8-4}$$

The electron interacts with matter, as explained before, while the positron loses its energy through ionization or excitation. If it is stationary, the positron interacts with an electron creating two gamma rays with energies of 511keV each (annihilation radiation). These two gamma rays can escape or interact with matter through the Compton scattering or photoelectron effect.

8.1.2 Material and methods

The two tailing samples consists in silt fraction of Stava wastes. An amount of 500g of material was dried at 120°C for 24 hours. Stava loose sample named "dry irradiated" was placed into a plastic container that was surrounded by a crepe tape and aluminium foil containers (Fig. 8.2).

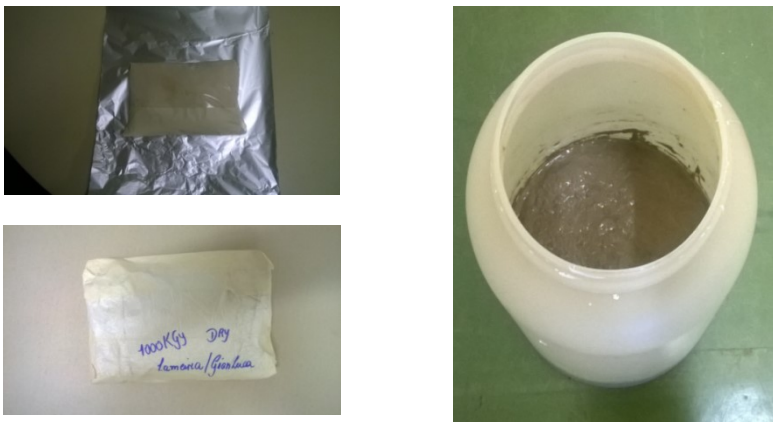

Fig. 8.2 - Dry irradiated (left) and wet irradiated (right) samples.

Finally the sample was placed into irradiation room, in contact to the cylinder containing the Cobalt-60 source. Stava sample named "wet irradiated" was added an amount of water corresponding to liquid limit (w_L=27,4%) in order to obtain a slurry. Than it was put into a rigid plastic flask and, as in the previous case, it was surrounded by a crepe tape and aluminium foil. The sample was placed into irradiation room, in contact to the cylinder containing the Cobalt-60 source. The irradiated dry sample is shown in Fig. 8.3.


(a)

(b)

Fig. 8.3 - Dry irradiated sample before (a) and after (b) gamma irradiation.

8.2 PARTICLE SIZE DISTRIBUTION BY LASER DIFFRACTION

8.2.1 Principles

The laser diffraction technique (LD) allows to indirectly measure particles having sizes between 0.02µm and 2000µm. Due to its accuracy, fast and fully automated usage, LD technique represents a good method for the examination of particle size distribution. The LD technique is based on the dependence of the particle size of the analysed sample from the spatial distribution of the scattered light. When a particle is illuminated by a laser beam, a complex laser diffraction phenomenon will be created as a stone hits the water surface, concentric rings of waves appear. Big stone will create higher, more intense and clearly separated waves than smaller stones. A similar phenomena occurs during LD tests: this technique allows to measure the intensities of diffracted rings and distances between them when particles are illuminated by a laser beam. The distance between diffracted rings is correlated to the declination angles from the direction of incident light. Beside diffraction, other phenomena (light scattering) occur when particles are hit by a laser beam: absorption and re-radiation, refraction and reflection. Furthermore, the light scattering mode, depends on the ratio of the particle diameter (D) to the wavelength (λ) of the incident laser beam, so depending on D/λ this phenomena can be classified as Fraunhofer ($\lambda<D$), Rayleigh ($\lambda>>D$) and Mie ($\lambda=D$) scattering.
Figure 8.4 gives a scheme of a LD instruments parts. The samples particles, dispersed in a suitable medium such as water, passes through a laser beam. Consequently, the light is scattered by the particles at typical spatial angles and a diffraction pattern is produced. The laser beam consists of two light sources (He-Ne) having different wavelengths:

- the blue laser is used for measuring the “small” particles;
- the red detects the “large” particles.

The diffraction pattern, typical of the particle size, is measured by detectors and the signal is then transformed to a particle size distribution based on an optical model.

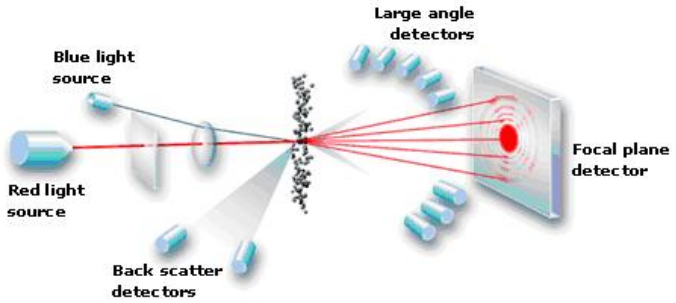

Fig. 8.4 - Working principle of particle laser diffractometer (Stojanovic and Markovic, 2012).

The translation of measured data acquired by the instrument into particle size distribution is usually performing by using different calculation methods among them Fraunhofer or Mie theory are the most applied. The use of Fraunhofer is more suitable for "large" particles, but there is a wide disagreement on where is the limit value between Mie and Fraunhofer method (Fig. 8.5): the range between 2µm and 100µm. The Mie theory provides the greatest accuracy for small particles, but this method needs the knowledge of the refraction index *n*.

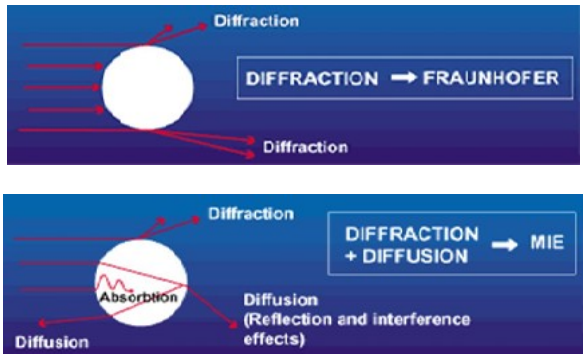

Fig. 8.5 - Fraunhofer method Vs Mie method (Stojanovic and Markovic, 2012).

The refractive index is a dimensionless parameter that quantitatively describes how a material refracts light and, for liquids, it can be easily obtained with a refractometer.

8.2.2 Sample preparation

The sample does not require any specific preparation technique. The dry and wet powder sample (about 15g) are well dispersed in a liquid media (water) into the apparatus (Fig. 8.6) in order to assure that the particles pass the laser beam in a homogeneous stream.

Fig. 8.6 - Particle laser diffractometer.

8.3 X-RAY FLUORESCENCE (WD-XRF, ED-ERF) AND ENERGY X-RAY SPECTROMETRY (EDS)

8.3.1 Principles

The X-ray fluorescence (XRF) and energy X-rays spectroscopy (EDS) are non-destructive technique that allow a qualitative and quantitative evaluation of the elemental composition of materials. These techniques make use of X-rays spectrum emitted by a pulverized, solid or liquid samples bombarded with a focused beam of high energy electromagnetic source, such as photons. The two methodological XRF techniques are:

- wavelength dispersive analysis (WD-XRF);
- energy dispersive analysis (ED-XRF).

X-ray fluorescence XRF and EDS techniques are based on the emission of x-rays spectrum by a soil sample bombarded with a beam of X-rays (XRF process) or electrons (EDS technique). If the primary energy of the incident X-rays or electrons is higher than or equal the binding energy of an atomic shell electron (K, L or M), electrons will be ejected from their shells and so vacancies will be created, making the atom excited. The transition from an excited state to a stable state with lower energy, occurs via two different processes:

- Auger effect;
- Photoelectric effect.

The occurrence probability of the two effects varies from an element to another: for element with high atomic number Z the photoelectric effect dominates, whereas the emission of an Auger electron is more likely for elements with low atomic numbers. The Auger process consists in the emission of an Auger electrons instead of X-rays, in order to reach a stable atomic configuration. The stable state can also be reached with the photoelectric effect, as in the current study. In this case, the atomic state transition is accompanied by a transfer of electron from outer shell (having higher energy E_m) to the inner shell (with binding energy E_n) where the vacancy was created. This electronic transition induces the emission of typical X-ray photon K_α or K_β, depending by the shell involved in the transition. Emitted X-rays are characterized by an amount of energy according to the Plank's law:

$$h\upsilon = E_m - E_n \tag{8-5}$$

where υ is the frequency of X-ray photon ($10^{-17} \div 10^{-19}$ s^{-1}) collected by a detector and then interpreted by a specific software. The so-called "critical excitation energy" E_c is defined as the minimum energy which bombarding photons or electrons must posses in order to create a vacancy and it shoul exceed at least two times the "incident electron energy" E_0.
Result is therefore a spectrum of emitted x-rays radiations consisting in a series of peaks characterized by a specific wavelength or energy (keV) and a typical intensity (a.u.) on x and y-axes, respectively. Every element has its own characteristic radiation that represent its fingerprint independent from its chemical environment.
The XRF and EDS techniques let to perform two types of analyses:

- qualitative analyses;
- quantitative analyses.

Aim of a qualitative analysis is the identification of the elements present in the unknown specimen by identifying the specific energies (ED-XRF and EDS) or wavelengths (WD-XRF) of the characteristic x-rays peaks appearing on the spectrum and compare them with energies or wavelengths from literature. The object of a quantitative analyses is the determination of the concentration of the elements by measuring peaks intensity for each element previously identified by qualitative analyses. When a sample containing a certain element of mass A is irradiated by EDS or XRF techniques, the intensity of the emitted radiation of A from the sample, depends on its concentration: the higher mass concentration of A results in a higher intensity or emitted radiation.

8.3.2 Sample preparation

In the current study the XRF technique was used. A small amount of dry and powdered sample (about 20g) and boric acid powder (about 40g) are pressed together under a load equal to 150kN (Fig. 7.7a) in order to create a cylinder 30mm diameter and 5mm height (Fig. 8.7b).


(a)
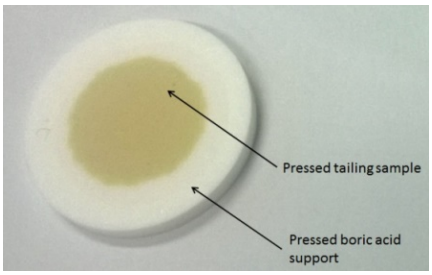

(b)

Fig. 8.7 - (a) Press and (b) specimen ready to be analysed with XRF technique.

The specimen is then placed into the XRF machine in order to perform the XRF analyses (Fig. 8.8).

Fig. 8.8 - XRF device used at CDTN laboratories.

8.4 SCANNING ELECTRON MICROSCOPE (EDS)

8.4.1 Principles

Energy Dispersive Spectroscopy technique (EDS) makes use of a scanning electron microscope (SEM) that allows observation of samples with a resolution of 1000 times higher than traditional optical microscopy. The scanning electron microscope (Fig. 8.9) uses the

EDS technique previously described: atoms of the sample are bombarded by an electron beam. The beam is focused by a lens system and deflected in order to scan a sample area to provide indications about chemical-physical composition, morphology and contamination of the surfaces of materials subjected to analysis. The electromagnetic radiation emitted by the bombarded atom is converted into energy (keV): the energy level achieved (keV) is specific of the element as in technique EDS, while the intensity is a function the mass concentration of the element within the sample and can be obtained by the area under the peak. The result is therefore a spectrum consisting peaks characterized by a specific emitted energy (x-axes) and a typical intensity (y-axes): a software, after identifying each peak, associates its features to the corresponding element. Finally, the interaction between the electron beam and the sample then produces the signals that are captured by suitable detectors and processed by means of specific software to form an image in grayscale.

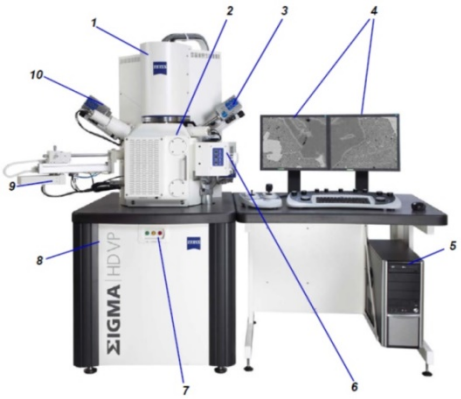

Fig. 8.9 - SEM microscope: 1) electron optical column, 2) specimen chamber, 3) EDS detector, 4) monitors, 5) personal computer, 6) 80mm airlock, 7) ON/STAND BY/OFF button 8) STEM detector 9) EDS detector.

8.4.2 Sample preparation

Because the SEM microscope makes use of EDS technique, the dry powder sample (less than 10g), is placed on a sample-holder and then it was metallized, i.e. made conductive to avoid the generation of electrostatic charges. In the current case, sample was metalized by using gold powder. Because the air does not allow the production of the beam, sample was placed under vacuum and placed into the SEM specimen chamber in order to perform the analysis.

8.5 QUANTIKOV IMAGE ANALIZER

8.5.1 Principles

Pictures acquired by SEM microscope were analysed by using Quantikov. This software, developed in 1996 at University of San Paolo by Professor Lucio Carlos Martins Pinto (CDTN, Belo Horizonte), represents a powerful tool for microstructural analysis and includes modules for digital image processing, geometric processing, graphics and hypertext moduli. SEM pictures are processed in order to obtain main parameters distribution in terms of surface, diameters and roundness of grains.
For a grain similar to a circle shape, roundness parameter will be close to 1, while elongated and narrow particles will show roundness parameter smaller than 0.3.

8.6 DENSITY DETERMINATION

8.6.1 Principles

True density determination technique of solid samples makes use of an ultra-gas pycnometer apparatus (Fig. 8.10) by operating on Archimedes 'principle of fluid displacement and Boyle's law. The fluid is usually an inert and ideal gas such as helium because, due of its small atomic dimensions, it assures a high penetration also into pores 0.25nm diameter.

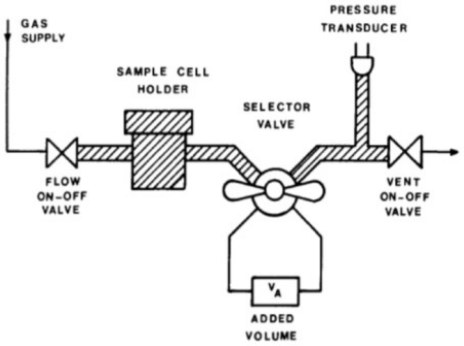

Fig. 8.10 - Schematic of the gas ultra-pycnometer (Chang, 1988).

The dashed area represents the first sealed chamber of the ultra-pycnometer, the so called cell volume (V_c). After purging with helium, if the solenoid valves is open, the system reaches ambient pressure (P_a), so according to Boyle's law the state will be:

$$P_a V_c = nRT_a \tag{8-6}$$

where R is the gas constant, T_a is the ambient temperature expressed in Kelvin degrees and n is the number of moles of gas occupying the cell vulme. When a solid sample having grain volume V_S is put into the sample cell, the state of the system can be expressed as:

$$P_a(V_c - V_s) = n_1 RT_a \tag{8-7}$$

where $n_1$is the number of moles of gas occupying the $(V_c - V_S)$ volume. If the system is pressurized with a pressure P_2 higher than P_a the system will resut:

$$P_2(V_c - V_S) = n_2 RT_a \tag{8-8}$$

where n_2 is the number of moles of gas occupying the $(V_c - V_S)$ volume. When the selector valve is open to connect the first chamber (cell volume V_c) to the second chamber (add volume V_A), the pressure will decrease from to P_2 to P_3, where n_A is the numbers of moles contained in the add volume V_A:

$$P_3(V_c - V_S - V_A) = n_2 RT_a + n_A RT_a \tag{8-9}$$

By using $P_a V_a$ instead of $n_A RT_a$, eq. 8-8 becomes:

$$P_3(V_c - V_p - V_A) = n_2 R T_a + P_a V_A \tag{8-10}$$

After manipulating eq. 8-9, the unknown total volume of grains (V_s) can be obtained:

$$V_S = V_c + \frac{V_A}{1 - \frac{P_2}{P_3}} \tag{8-11}$$

where V_c and V_A are known from the initial calibration process with the sample cell empty, while P_2 and P_3 are measured after putting the sample. Finally, the true density of the sample (ρ_T) is obtained by the ratio between the volume of the sample without taking into account inner (close and open) pores and its mass m_p:

$$\rho_T = \frac{m_p}{V_S} \tag{8-12}$$

The calibration of the added volume is carried out by performing two pressurizations. The first one by repeating the procedure previously described and by measuring the pressures P'_2 and P'_3 without sample in the sample cell (V_p=0) and the second one by putting a calibration sphere (V_{cal}) in the sample cell. The calibration of the sphere is considered satisfied if its density computed by the instrument will be equal to 1.

8.6.2 Sample preparation

Before putting a certain amount (20g) of dry silt sample into the properly box (Fig. 8.11, left and centre), material must be carefully weighed and then put into the ultra-pycnometer (Fig. 8.11 right), according to the procedure previously described.

Fig. 8.11 - Dried silty sample (left, middle) and gas ultra-pycnometer 1000 (right).

The soil sample should be dried and powdered. A suitable calibration sphere is used for calibration of added volume and cell volume (Fig. 8.12).

Fig. 8.12 - Different sizes of the calibration spheres.

8.7 SURFACE AREA DETERMINATION

8.7.1 Principles

The gas adsorption technique is the most widely used method for indirect determination of the surface area of powder material. Most atoms making up a solid are bound on all sides by other atoms in the bulk of the solid, but atoms on the surface are incompletely bounded. Due to van der Waals forces, these surface atoms are more reactive and they can attract gas, vapour/liquids in order to satisfy the imbalance of atomic forces (Fig. 8.13a). Referring this phenomena, all gas adsorption techniques are based on adsorption that represents a process for which the solute adheres to a solid surface due to the unbalanced forces acting on surface atoms.

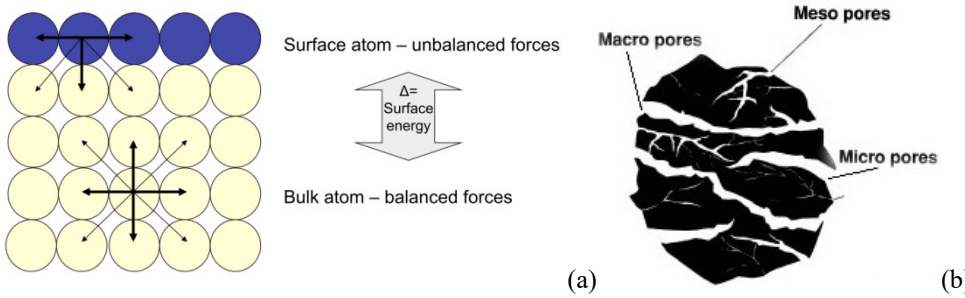

Fig. 8.13 - (a) Unbalanced surface atoms and balanced bulk atoms and (b) schematic drawing of micro, meso and macropores inside a grain of active carbon (Rouquerol *et al.,* 2007 and Reis *et al.*, 2002).

All of specific surface area tests and pores size distributions are carried out depending the size of the pores of the solid sample (Fig. 8.13b). Pores are classified according to their sizes, macropores (pores > 50nm diameter), mesopores (pores 2÷50nm diameter) and micropores (pores < 2nm diameter), respectively.

BET method is the main technique for evaluation the specific area of a powder solid sample by calculation of volume V_m of the adsorbed gas, usually nitrogen, corresponding to a monomolecular layer on the surface of the sample. Developed by Brunauer-Emmett-Teller, the measure is carried out at the temperature of liquid nitrogen (77K), consisting in the evaluation of volume V_m of gas adsorbed by solid sample at different pressures P, lower than saturation pressure P_s. After calibration and pre-treatment processes, solid powder is cooled under vacuum to cryogenic temperature. Adsorptive gas is dosed to the solid powder in controlled increments and after each dose of adsorptive, the pressure is allowed to equilibrate, so the adsorbed quantity of gas is computed. The adsorbed quantity at each pressure/temperature defines an adsorption isotherm, from which the quantity of gas required to form a monolayer over the external surface of the powder is determined. Known the area covered by each adsorbed gas molecule, the surface area can be obtained. The amount of gas adsorbed can be measured by a volumetric or continuous flow procedure. In both cases, when the gas is adsorbed by the sample, the Brunauer-Emmett-Teller (BET) equation holds when $\frac{P_0}{P}$ is in the range of 0.05÷0.3:

$$\frac{1}{W\left(\frac{P_0}{P}-1\right)} = \frac{1}{W_m C} + \frac{C-1}{W_m C}\left(\frac{P_0}{P}\right) \tag{8.13}$$

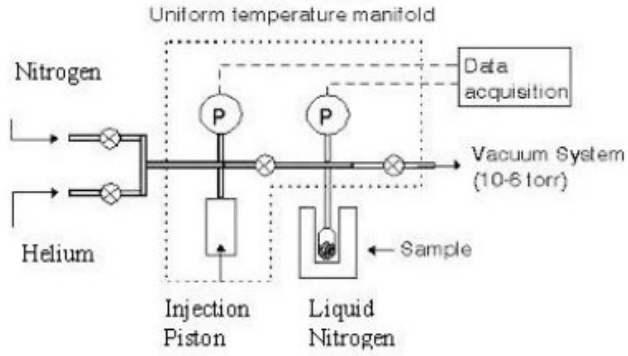

Fig. 8.14 - Schematic draw of apparatus using BET technique (Rouquerol *et al.,* 2007).

where P is the partial vapour pressure of adsorbate gas in equilibrium with the surface, P_0 is the saturated pressure of the adsorbate gas at -196°C, W is the measured weight of gas adsorbed at a relative pressure $\frac{P_0}{P}$, W_m is the computed weight of gas adsorbed in a monolayer of surface coverage , C is a dimensionless constant related to the energy of adsorption in the first adsorbed layer. This value is related to the magnitude of the adsorbent/adsorbate interactions C for nitrogen is equal to 50÷250. By considering y as the dependent variable, x the independent variable, i the intercept and s the slope, BET equation can be considered as linear relation where:

$$\frac{1}{W\left(\frac{P_0}{P}-1\right)} = y \tag{8.14}$$

$$\left(\frac{P_0}{P}\right) = x \tag{8.15}$$

$$\frac{1}{W_m C} = \mathrm{i} \tag{8.16}$$

$$\frac{C-1}{W_m C} = s \tag{8.17}$$

By using eq. 8-14, eq. 8-17, eq. 8-13 can be rewritten in the simple form:

$$y = sx + i \tag{8-18}$$

BET eq. 8-12 or eq. 8-17 can be used for determination of the surface area of powder sample, by applying two different methods multi-point BET method or single-point BET method. In the current research the first approach was adopted. In multi-point BET the value of W is measured at each of not less than 3 imposed values of P_0/P. Then, a linear plot of y versus x is obtained, so the values of intercept i and slope s are known. The data are considered acceptable if the correlation coefficient (*r)* of the linear regression is upper than 0.9975. From eq. 8-16 and eq. 8-17 weight of a monolayer of adsorbate gas constituting a monolayer of surface coverage is given:

$$W_m = \frac{1}{s+i} \tag{8-19}$$

The total surface area is obtained:

$$S_t = \frac{W_m N A_{cs}}{M} \tag{8-20}$$

where N is the Avogadro's number ($6.022 \cdot 10^{23}$ molecules/mol), M is the molar mass/molecular weight of the adsorbate gas (for nitrogen $M = 28 \cdot 1.66 \cdot 10^{-27} kg$), A_{CS} is the molecular cross section of the adsorbate molecule (for nitrogen at 77K $A_{cs} = 0.162 nm^2$). Considering w as the sample weight, the specific area S of the powder sample is then obtained:

$$S = \frac{S_t}{w} \tag{8-21}$$

The total pore volume of grains is derived from the amount of the measured vapor adsorbed V_{ads} at a relative pressure close to unity, by assuming that the pores are then filled with liquid adsorbate. The volume of nitrogen adsorbed V_{ads} can be converted to the volume of liquid nitrogen V_{liq} contained in the pores using this equation:

$$V_{liq} = \frac{P_a V_{ads} V_m}{RT} \tag{8-22}$$

where P_a is the ambient pressure, T is the ambient temperature and V_m is the molar volume of the adsorbate gas (for nitrogen V_m=34.7cm^3/mol). Since pores which would not be filled below $\frac{P}{P_0} \approx 1$ have a negligible contribution to the total pore volume, the average pore size can be estimated from the pore volume, so for cylindrical pore, the average pore diameter is given:

$$d_p = \frac{4 V_{liq}}{S} \tag{8-23}$$

The equipment calibration is carried out by using α-alumina cylinders. Specific surface area obtained for α-alumina must be within the range specified for the reference standard of α-alumina.

8.7.2 Sample preparation

After equipment calibration, the specific surface area test was performed on the tailing sample. The tared sample container was precisely weighed and a quantity of the test dry powder. A pre-treatment was performed in order to remove any gases and vapours that have been physically adsorbed onto the sample surface, by outgassing the sample under reduced pressure. Heating (150°C) may also be employed as long as there is no effect on the physical or chemical properties of the sample. After the pre-treatment is completed, the sample container with the sample was precisely weighed and the mass of the tared container measured previously, was subtracted in order to obtain the mass of the test powder.
A fixed quantity of the adsorbate gas was taken (Fig. 8.15a) and introduced into the sample container that has been chilled by immersion in liquid nitrogen (Fig. 8.15b). The adsorbate gas was adsorbed on the powder sample, while the pressure decreased until gas/solid adsorption reached to a new equilibrium. The volume of gas adsorbed was calculated from the difference between the volume of adsorbate gas that was introduced and the volume of unabsorbed gas remaining in the void volume. The void volume can be measured by using helium either before or after the adsorption measurements are performed.

(a)

(b)

Fig. 8.15 - (a) BET apparatus and (b)tailing samples just before immersion into liquid nitrogen.

For multiple-point BET method, specific surface area was calculated by repeating 3 measurements or more of the volume adsorbed, under a relative equilibrium pressure of the adsorbate gas in the range from 0.05 to 0.3. For the single-point method, one measurement of the volume adsorbed was performed under a relative pressure of close to 0.3.

8.8 MINERALOGICAL ANALISIES

8.8.1 Principles

X-ray diffraction technique (XRD) is based on the emission of electromagnetic radiation, consisting in x-rays beams, by an exciter source. Incident x-rays beams, having a defined wavelength λ much lower than that of the light (0.1÷2A), propagate in a straight line and they are refracted by the reticular nature of the crystals, that from the dispersive medium, by meaning the diffracted x-rays beam is connected to the nature of the sample's constituents. The electromagnetic incident radiation, having a known wavelength λ, will be diffracted in a direction in order to satisfy Bragg equation (1913):

$$n\lambda = 2d\text{sen}\theta \tag{8-24}$$

where n is the diffraction order, θ the angle between incident beam and diffraction plane, while d is the distance (Angstrom) between two crystal planes. As a consequence, the incident beam is diffracted into a radiation that depends on the wavelength, angle of incidence and the inter-planar distance of the grids constituents the crystal structure and the diffracted radiation will emerge under an angle 2θ with respect to the direction of the incident beam.

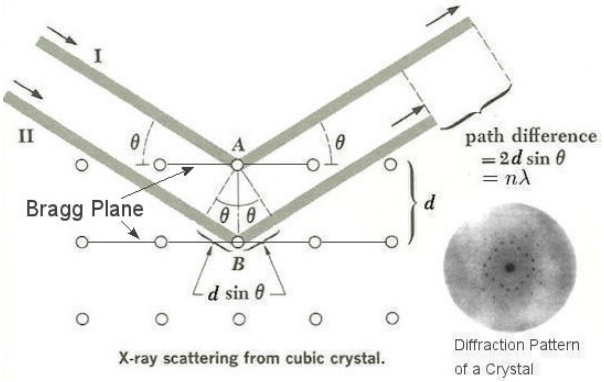

Fig. 8.16 - Incident and reflected X-Ray beam on crystal planes having distance *d*, described by Bragg's equation (Black, 2005).

In order to measure the full spectrum, sample and detector undergo a rotation equal to θ and 2θ, respectively. In this way, detector is always in the right position for collecting the diffracted beams, according to the various angles that are related to the inter-planar distance of the crystal structure.

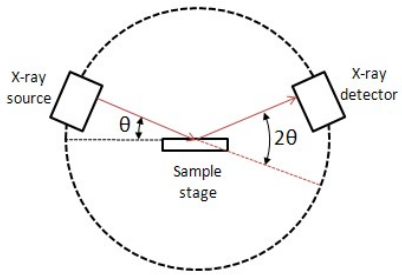

(a)

(b)

Fig. 8.17 - Working principle (a) and XRD diffractometer used at CDTN laboratories (b).

8.8.2 Sample preparation

The adopted technique is the "powder method", so the oven dried sample (120°C, 24 hours) is powdered and a small quantity (10g) and then placed into a circular sample-holder. The top surface of the sample should be well smoothed and the sample is put into the XRD diffractometer in order to perform the analyses.

Fig. 8.18 - Dry irradiated and wet irradiated Stava tailings into sample-holder before XRD analyses.

8.9 FOURIER TRANSFORM INFRARED SPECTROSCOPY

8.9.1 Principles

Fourier transform infrared spectroscopy (FTIR) technique is a powerful tool for qualitative and quantitative identification either organic or inorganic chemicals, impurities and percent crystallinity by using infrared radiation (IR) through a solid, liquid or gaseous samples. When a certain material is IR irradiated, absorbed infrared radiation excites molecules into a higher vibrational state. The wavelength (or frequency) of IR absorbed by a specific molecule depends on the energy difference between excited vibrational and the at-rest states. FTIR spectroscopy measures the wavelength at which the sample absorbs and also the intensities (transmittance) of these absorptions. Resulting absorbed wavelengths are typical of its molecular structure: IR radiation produced by the source hits the beam splitter where it is partly directed towards two mirrors. One of them is stationary, while the other one is moved at a constant rate during data acquisition. IR beams are then reflected by mirrors, so they are recombined at the beam splitter. After the two beams reflected by the mirrors recombine, they will travel different distances and the recombination will lead to constructive and destructive interference. The result will be an interferogram. Subsequently the recombined IR beams pass through the sample and are acquired by the detector that records all wavelengths in the IR range. After the recombined beam has passed through the sample the detector will record the Fourier transform of the IR spectrum of the sample. Data obtained are then processed by a computer that performs an additional Fourier transform to back-transform the interferogram into an IR spectrum.
The result is a series of peaks into a two dimension plot (spectrum) in which *y* and *x* axes are represented by transmittance (a.u.) and wavenumber (cm^{-1}) of sample absorption, respectively. The region from 4000÷400 wavenumbers is referred to as the fingerprint region and every peak, characterized by a certain wavenumbers and transmittance, is specific for each material so this allows computerized data searches within reference libraries to identify the chemical composition. The wavenumbers are used for the identification of the sample's chemical make-up due to the fact that chemical functional groups are responsible for the absorption of radiation at different frequencies, while the percentage concentration of each component can be obtained based on the intensity of the absorption.

8.9.2 Sample preparation

Tailing material should be dried (120°C, 24 hours), powdered and dispersed in KBr. A cylindrical sample (8mm diameter, 1mm thickness) is then realized under vacuum, by using a a press in order to apply a load corresponding to six tons (Fig. 8.19a and Fig. 8.19b).

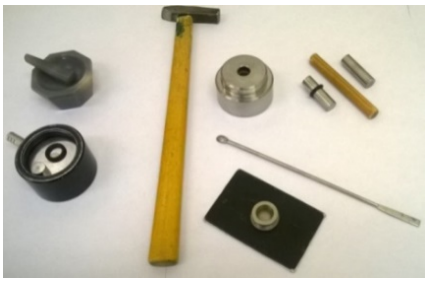
(a)

(b)

Fig. 8.19 - (a) Instruments for sample preparation and (b) press and vacuum pump.

The sample is then put into the sample-holder and placed within the FTIR spectrometer (Fig. 8.20) in order to perform the analysis.

Fig. 8.20 - FTIR spectrometer “Arid Zone”.

REFERENCES

1. Black S. 2005. Domesticating the Crystal: Sir Lawrence Bragg and the Aesthetics of "X-ray Analysis," Configurations, **13**: pp. 256-257.

2. Chang C.S. 1988. Measuring Density and Porosity of Grain Kernels using a Gas Pycnometer," Cereal Chemist, **65**: pp. 13-15.

3. Gilmore G. 2008. Practical Gamma-Ray Spectrometry, 2nd edition, John Wiley & Sons, Ltd.

4. Reis S.C., Vasconcelos V., Leiteb M.C. and Vasconcelosb W.L. 2002. Development of a Computer Application to Simulate Porous Structures, Materials Research, **5**: pp. 275-279.

5. Rouquerol J., Llewellyn P.L. and Rouquerol F. 2007. Is the BET equation applicable to microporous adsorbents?, Characterization of porous solids VII, Studies in surface science and catalysis, Elsevier, pp. 49-56.

6. Stojanovic Z. and Markovic S. 2012. Determination of Particle Size Distribution by Laser Diffraction, Technics-New Materials, **21**: pp. 11-20.